Universidad de Alcalá

Escuela Politécnica Superior

Departamento de Electrónica

CONTRIBUTIONS TO CASCADE LINEAR CONTROL STRATEGIES APPLIED TO GRID-CONNECTED VOLTAGE-SOURCE CONVERTERS

PH.D. THESIS

Author: Ana Rodríguez Monter

Supervisors: Dr. Emilio José Bueno Peña
Dr. Aurelio García Cerrada

July 2013

DEPARTAMENTO DE ELECTRÓNICA
Edificio Politécnico
Campus Universitario s/n
28805 Alcalá de Henares (Madrid)
Teléfono: 91 885 65 40
Fax: 91 885 65 91
eldep@depeca.uah.es

Dr. Juan Jesús García Domínguez, Director del Departamento de Electrónica de la Universidad de Alcalá,

INFORMA: Que la Tesis Doctoral titulada "**Contributions to cascade linear control strategies applied to grid-connected Voltage-Source Converters"** presentada por Dña. Ana Rodríguez Monter, y dirigida por los doctores D. Emilio José Bueno Peña y D. Aurelio García Cerrada, cumple con todos los requisitos científicos y metodológicos, para ser defendida ante un Tribunal, según lo indicado por la Comisión Académica del Programa de Doctorado.

Alcalá de Henares, 27 de Mayo de 2013

Fdo. Juan Jesús García Domínguez

Universidad de Alcalá

DEPARTAMENTO DE ELECTRÓNICA
Edificio Politécnico
Campus Universitario s/n
28805 Alcalá de Henares (Madrid)
Teléfono: 91 885 65 40
Fax: 91 885 65 91
eldep@depeca.uah.es

Dr. Emilio José Bueno Peña, Profesor Titular de la Universidad de Alcalá, y
Dr. Aurelio García Cerrada, Profesor Propio Ordinario de la Universidad Pontificia de Comillas,

INFORMAN: Que la Tesis Doctoral titulada "**Contributions to cascade linear control strategies applied to grid-connected Voltage-Source Converters"** presentada por Dña. Ana Rodríguez Monter, y realizada bajo la dirección de los doctores D. Emilio José Bueno Peña y D. Aurelio García Cerrada, dentro del campo de la aplicación de los VSCs como interfaces entre la red eléctrica y sistemas de generación de energía eléctrica, reúne los méritos de calidad y originalidad para optar al Grado de Doctor.

Alcalá de Henares, 27 de Mayo de 2013

Fdo. Emilio José Bueno Peña

Fdo. Aurelio García Cerrada

Abstract

The work developed in this Thesis is aimed at optimizing the behavior of Voltage-Source Converters (VSCs) when used as an interface with the grid, in order to demand or deliver energy to the grid with the best possible quality, and meeting the standards. To this end, this Thesis focuses on the field of cascade linear systems applied to the control of VSCs connected in shunt mode with the grid through an L-filter, especially in connections to weak grids and in two topics: (i) tracking of grid current harmonics and rejection of grid voltage harmonics, and (ii) control of PCC voltage in an unbalanced condition. For this purpose, contributions to current control and PCC voltage control are made in this work.

Among the existing techniques for implementing the current control for harmonic compensation, two of the most used are resonant and repetitive controllers both in stationary and synchronous reference frames. A thorough study of different existing structures to implement them is carried out, showing the frequency-adaptive algorithm for each of these structures and analyzing their computational load. Basic guidelines for the programming of such controllers are given. The current control scheme is studied and characterized in order to establish a comparison among the different structures.

After studying in depth the current control of a grid-connected VSC, the second control to analyze is the PCC voltage controller. The presence of an unbalanced voltage at the PCC results in the appearance of a negative sequence current component, which deteriorates the control performance when applying conventional control techniques. STATCOMs are well-known to be a power application capable of carry out the PCC voltage regulation in distribution lines that may suffer from grid disturbances. This Thesis proposes a novel voltage controller in synchronous reference frame to compensate an unbalanced PCC voltage by means of a STATCOM, allowing an independent control of both positive and negative voltage sequences. Several works have been proposed in this line but they were not able to compensate an unbalance in the PCC voltage. Furthermore, this novel controller includes aspects as antiwindup and *droop control* to improve the control-system performance.

Several experimental tests have been carried out to analyze the performance of the current controllers discussed in the Thesis. All of them have been tested under the same conditions of power, voltage and current. These tests aim at characterizing the transient response, steady-state response, behavior under frequency jumps and computational load of the current controllers.

Resumen

El trabajo desarrollado en esta Tesis se centra en optimizar el comportamiento de *Voltage-Source Converters* (VSCs) cuando son utilizados como interfaz con la red eléctrica, tanto para absorber como para entregar energía de la red con la mejor calidad posible y cumpliendo con los estándares. Para tal fin, esta Tesis se centra en el control de sistemas lineales conectados en cascada aplicados al control de VSCs conectados en paralelo con la red eléctrica a través de un filtro L, especialmente en conexiones con redes débiles y en dos líneas de trabajo: (i) seguimiento de armónicos de las corrientes de red y rechazo de armónicos de las tensiones de red, y (ii) control de la tensión del PCC en caso de desequilibrio. Para ello, esta Tesis realiza contribuciones en el área del control de corriente y control de la tensión del PCC.

De entre las técnicas existentes para implementar el control de corriente para compensación armónica, dos de las más utilizadas son el control resonante y el control repetitivo, tanto en ejes de referencia estacionarios como síncronos. Se ha realizado un exhaustivo estudio de diferentes estructuras para implementar tales controles, mostrando su algoritmo adaptativo en frecuencia para cada una de ellas y analizando su carga computacional. Además, se han facilitado directrices básicas para su programación en un DSP. Se ha analizado también el esquema de control de corriente para establecer una comparación entre las diferentes estructuras.

Después de estudiar en profundidad el control de corriente de un VSC conectado a la red eléctrica, el segundo control a analizar es el control de tensión del PCC. La presencia de una tensión desequilibrada en el PCC da lugar a la aparición de una componente de corriente de secuencia negativa, que deteriora el comportamiento del sistema de control cuando se emplean las técnicas de control convencionales. Los STATCOMs son bien conocidos por ser una aplicación de potencia capaz de llevar a cabo la regulación de la tensión en el PCC en líneas de distribución que pueden ser susceptibles de sufrir perturbaciones. Esta Tesis propone el uso de un controlador de tensión en ejes de referencia síncronos para compensar una tensión desequilibrada a través de un STATCOM, permitiendo controlar independientemente tanto la secuencia positiva como la secuencia negativa. Además, este controlador incluye aspectos como un mecanismo de antiwindup y *droop control* para mejorar su comportamiento.

Se han realizado varias pruebas experimentales para analizar las características de los controladores de corriente abordados en esta Tesis. Todas ellas han sido realizadas bajo las mismas condiciones de potencia, tensión y corriente, de modo que se pueden extraer resultados comparativos. Estas pruebas pretenden caracterizar la respuesta transitoria, la respuesta en régimen permanente, el comportamiento frente a saltos de frecuencia y la carga computacional de los controladores de corriente estudiados.

Agradecimientos

Después de una trayectoria investigadora de seis años en el grupo GEISER de la Universidad de Alcalá, desde que comenzara con el Proyecto Fin de Carrera hasta la Tesis Doctoral, muchas han sido las personas que he ido conociendo a lo largo de este camino. En estas líneas quiero mostrar mi más sincera gratitud a todas aquellas que me han ayudado a crecer personal y profesionalmente y que, al final y al cabo, han hecho que todos estos años valgan la pena.

Quiero agradecer especialmente todo el apoyo, paciencia y formación que me ha dado uno de mis directores de Tesis, Emilio Bueno, sin el cual todos estos años de trabajo en el grupo no habrían sido posible. Por las largas horas de trabajo que hemos pasado juntos, por sus consejos tanto técnicos como humanos, por preocuparse siempre por mí, por los buenos momentos en el laboratorio y por todo lo que me ha enseñado. Igualmente, quiero agradecer a mi codirector de Tesis, Aurelio García-Cerrada, el soporte recibido durante estos años de Tesis.

También quiero agradecer la enorme colaboración proporcionada por Carlos Girón en la implementación en el DSP de los algoritmos desarrollados, por estar siempre dispuesto a ayudar y animarme cuando lo necesitaba. A Javier Roldán, del ICAI, por su inestimable ayuda en la implementación del RC-IP en la plataforma experimental.

A todos los que han ido pasando por el grupo de investigación y con los que he compartido innumerables horas en la universidad, como Christina, Santi, Francisco Javier, Paco, Miguel, Inés, Iván, Álvar, Jorge, Fernando, Mouhai, Manu, etc. De cada uno de vosotros he aprendido algo y de todos vosotros me llevo un gran recuerdo. Además de otros compañeros que, a pesar de no pertenecer al mismo grupo de investigación, han conseguido hacer más llevaderos todos estos años de trabajo. Laura, Arancha, Carlos Julián, etc., todos vosotros me habéis aguantado en mis días malos y con todos he compartido inquietudes y alegrías.

A todos mis amigos de fuera de la universidad por conseguir hacerme desconectar y sacarme una sonrisa, sobre todo en los últimos meses cuando los nervios y el estrés comenzaron a aflorar. Por haberos preocupado constantemente por mí, sobre todo Ana, Elena, Laura, David, Almudena y Álvaro.

También quiero agradecer a Marta Marrón que en su día, allá por el 2007, pensara en mí para formar parte de este grupo de investigación. Tal vez hoy no estaría aquí si no fuera por ella. Así mismo, agradecer a Ernesto Martín las largas charlas mantenidas cuando no sabía qué rumbo tomar. Muchos son los profesores del departamento de Electrónica a los que tengo especial cariño, por interesarse siempre por cómo me va cada vez me ven por los pasillos y por los buenos recuerdos que tengo de sus clases, como Álvaro Hernández, Francisco Javier Meca, Ignacio Bravo, José Luis Lázaro, Manuel Ocaña, Fernando Naranjo, etc.

Y por último, y no por ello menos importante, a toda mi familia, por estar siempre pendientes de mí y por estar más orgullosos que nadie de mis logros y progresos. En especial, a mis padres, Jesús y Elena, y a mi hermano, Jorge, porque han sufrido más que nadie mis largas noches de trabajo y me han enseñado que, en esta vida, todo se consigue con esfuerzo y dedicación. Vosotros, más que nadie, me habéis dado ánimo, valor y apoyo para seguir adelante cuando más lo necesitaba.

A mis padres, Jesús y María Elena,
y a mi hermano, Jorge,
por estar a mi lado en los buenos
y en los malos momentos.

"Don't cry because it's over, smile because it happened"

Glossary

1. Abbreviations.

Fig.	Figure.

2. Acronyms.

AFC	Adaptive Feedforward Cancelation.
APF	Active Power Filter.
BE	Backward Euler.
bin2	FIR filter implemented with a binomial filter of order 2.
DSC	Delayed Signal Cancelation.
DSP	Digital Signal Processor.
DSOGI	Dual Second Order Generalized Integrator.
DVR	Dynamic Voltage Restorer.
EKF	Extended Kalman Filter.
FE	Forward Euler.
FIR	Finite Impulse Response.
FLL	Frequency-Locked Loop.
FOH	Triangle approximation (non-causal First-Order Hold)
FPGA	Field Programmable Gate Array.

GI	Generalized Integrator.
ham16	FIR filter implemented with a Hamming-window filter of order 16.
HVDC	High Voltage Direct Current.
IMP	Impulse-Invariant transformation.
KF	Kalman Filter.
LV	Low Voltage.
MPZ	Matched Pole-Zero transformation.
MV	Medium Voltage.
NPC	Neutral-Point Clamped.
PCC	Point of Common Coupling.
PF	Power Factor.
PI	Proportional Integral.
PLL	Phase-Locked Loop.
PNSC	Positive Negative Sequence Calculation.
p.u.	Per unit
PWM	Pulse-Width Modulation.
RC-IP	Repetitive Controller based on the Inverse of the Plant.
RC-DCT	Repetitive Controller based on Discrete Cosine Transform.
RC-FFDP	Repetitive Controller based on Feedback and Feedforward Delay Paths.
SOGI	Second Order Generalized Integrator.
SOGI-LLN	Second Order Generalized Integrator with Lead-Lag Network.
SOGI-QSG	Second Order Generalized Integrator – Quadrature-Signal Generation.
SRF-PLL	Synchronous Reference Frame – Phase-Locked Loop.
STATCOM	Static Synchronous Compensator.
THD	Total Harmonic Distortion.
THPWM	PWM with Third Harmonic injection.
TPW	Tustin with Prewarping transformation.
TUS	Tustin transformation (bilinear transformation).
UPFC	Unified Power Flow Controller.

VSC	Voltage-Source Converter.
VSI	Voltage-Source Inverter.
WTHD	Weighted Total Harmonic Distortion.
ZOH	Zero-Order Hold.

3. Symbols.

^	Estimated value.
$\lfloor x \rfloor$	Largest integer not greater than x.
ε	Error signal.
θ	PCC phase angle.
$\vec{\psi}$	PCC flux vector.
ξ	Damping coefficient.
C_{DC}	Capacitance of the DC-link capacitors.
C_{DC1}	Capacitance of the upper DC-link capacitor in a three-level NPC.
C_{DC2}	Capacitance of the lower DC-link capacitor in a three-level NPC.
$conj(\ )$	Complex conjugate.
$\vec{e}$	Ideal grid voltage.
f_o	Resonant frequency.
f_1	Grid fundamental frequency.
f_s	Sampling frequency.
GM	Gain margin.
h	Harmonic order.
$\vec{\imath}$	PCC current.
i_{DC1}	Grid-side DC-link current.
i_{DC2}	Load-side DC-link current.
$[k]$	Discrete variable.
k_{aw}	Antiwindup gain.
k_i	Integral gain.

k_p	Proportional gain.
$\mathcal{L}$	Laplace transform.
L	Inductance of the grid filter.
L_g	Inductance of the grid impedance.
$\mathbb{N}$	Natural number.
P	Active power.
PM	Phase margin.
Q	Reactive power.
R	Resistance of the grid filter.
R_g	Resistance of the grid impedance.
(t)	Continuous variable.
t_s	Settling time.
T_s	Sampling period.
T_{sw}	Switching period.
$\vec{u}^*$	Reference PCC voltage for the modulator.
$\vec{u}$	PCC voltage.
$\vec{v}$	VSC output voltage.
u_{DC}	DC-link voltage.
u_{DC}^+	Upper DC-link voltage in the three-level NPC.
u_{DC}^-	Lower DC-link voltage in the three-level NPC.
ω_n	Natural pulsation.
ω_o	Resonant pulsation.
ω_1	Grid fundamental pulsation.
$\mathbb{Z}$	Integer number.
$\mathcal{Z}$	z-transform

4. Subscripts.

$\alpha\beta$	Variable in $\alpha\beta$-axes.

dq	Variable in *dq*-axes.
g	Grid.
L	Load.
lim	Limited value.

5. Superscripts.

+	Positive sequence.
-	Negative sequence.
*	Reference value.

Summary

Abstract i

Resumen iii

Agradecimientos v

Glossary ix

Summary xv

1. Introduction 1
1.1. Introduction 1
1.1.1. Consequences of the development of power electronics 2
1.1.2. Energy production model 3
1.1.3. Voltage-Source Converter (VSC) 4
1.2. Grid-connected VSCs 5
1.2.1. Applications 6
1.2.1.1. Shunt Active Power Filter (APF) 6
1.2.1.2. Dynamic Voltage Restorer (DVR) 7
1.2.1.3. Static Synchronous Compensator (STATCOM) 7
1.2.1.4. Unified Power Flow Controller (UPFC) 8
1.2.1.5. High-Voltage Direct Current (HVDC) transmission 9
1.3. Objectives 10
1.4. Structure of the Thesis 11
1.5. Conventions adopted in the development of the Thesis 12
1.6. Published papers 13

2. State of the art 19
2.1. Control of grid-connected converters to compensate harmonics 19
2.1.1. Harmonic current compensation 20
2.1.1.1. Resonant control 20
2.1.1.2. Repetitive control 22
2.1.2. Calculation of reference currents 24
2.2. Control of grid-connected converters to perform PCC voltage control 24
2.3. Contributions 25
2.3.1. Current control 25
2.3.2. PCC voltage control 27

3. Control of grid-connected converters 29
3.1. Overview of the control of a VSC connected in shunt mode with the grid through an L-filter 29
3.1.1. Active power control 32
3.1.1.1. Active power controller 32
3.1.1.2. DC-link voltage controller 33
3.1.2. Reactive power control 35
3.1.2.1. Reactive power controller 35
3.1.2.2. PCC voltage controller 35
3.1.2.3. Power factor controller 36
3.1.3. Current controller 36
3.2. Current control 41
3.2.1. Calculation of reference currents in case of unbalanced grid conditions 41
3.2.1.1. Stationary reference frame ($\alpha\beta$-axes) 42
3.2.1.2. Synchronous reference frame (dq-axes) 46
3.2.1.3. Comparison 49
3.2.2. Limitation of references 50
3.3. Grid synchronization and monitoring 51
3.3.1. Phase-Locked Loop (PLL) 52
3.3.2. Frequency-Locked Loop (FLL) 56
3.3.3. Kalman Filter (KF) 57
3.3.3.1. Fundamentals of the KF 57
3.3.3.2. Application to grid synchronization and monitoring 59
3.3.4. Extended Kalman Filter (EKF) 62
3.3.4.1. Fundamentals of the EKF 62
3.3.4.2. Application to grid synchronization and monitoring 65
3.3.5. Comparison 67
3.4. Conclusions 67

4. Current control based on resonant controllers 69
4.1. Introduction 69

4.2. Second Order Generalized Integrator (SOGI) 72
4.2.1. Continuous-time domain 72
4.2.2. Discrete-time domain 73
4.2.2.1. Individual discretization of the integrators 73
4.2.2.2.. Difference equation of the controller 76
4.2.3. Frequency-adaptive algorithm and computational burden 79
4.3. Second Order Generalized Integrator with Lead-Lag Network (SOGI-LLN) 81
4.3.1. Continuous-time domain 81
4.3.2. Discrete-time domain 83
4.3.3. Frequency-adaptive algorithm and computational burden 84
4.4. Adaptive Feedforward Cancelation (AFC) 84
4.4.1. Discrete-time domain 84
4.4.2. Frequency-adaptive algorithm and computational burden 86
4.5. Current control scheme 87
4.6. Conclusions 92

5. Current control based on repetitive controllers 93
5.1. Introduction 93
5.2. Generic plug-in Repetitive Controller based on the Inverse of the Plant (RC-IP) 96
5.2.1. Discrete-time domain 96
5.2.2. Frequency-adaptive algorithm and computational burden 100
5.3. Repetitive Controller based on Feedback and Feedforward Delay Paths (RC-FFDP) 104
5.3.1. Continuous-time domain 104
5.3.2. Discrete-time domain 108
5.3.3. Frequency-adaptive algorithm and computational burden 112
5.4. Repetitive Controller based on Discrete Cosine Transform (RC-DCT) 113
5.4.1. Discrete-time domain 113
5.4.2. Frequency-adaptive algorithm and computational burden 115
5.5. Current control scheme 118
5.6. Conclusions 121

6. PCC voltage control 125
6.1. Introduction 125
6.2. Grid modeling under unbalanced conditions 127
6.3. Control scheme 129
6.3.1. Active and reactive power control 130
6.3.2. PCC voltage control 131
6.3.3. dq to $\alpha\beta$ transformation and calculation of $\alpha\beta$-axes reference current 133
6.3.4. Current controller 133
6.4. Online adaptation of the DC-link reference voltage 134
6.5. Sampling mode when working with an L-filter 135
6.6. Simulation results 137

6.7. Conclusions 141

7. Experimental results 143
7.1. Performance indicators 143
7.1.1. Transient response 143
7.1.2. Steady-state response 144
7.2. Experimental setup 144
7.3. Experimental tests 147
7.3.1. Connection to the laboratory grid 148
7.3.1.1. Specifications of the laboratory grid 148
7.3.1.2. Transient response 149
7.3.1.2.1. Abrupt step in positive reactive power reference 149
7.3.1.2.2. Abrupt step in negative reactive power reference 156
7.3.1.3. Steady-state response 156
7.3.2. Connection to the programmable AC voltage source 157
7.3.2.1. Specifications of the AC voltage source 157
7.3.2.2. Behavior under frequency jumps 158
7.3.2.2.1. Frequency jump from 50 to 45 Hz 158
7.3.2.2.1.1. Results for P + SOGI 159
7.3.2.2.1.2. Results for RC-DCT 162
7.3.2.2.2. Frequency jump from 50 to 55 Hz 164
7.3.2.2.2.1. Results for P + SOGI 164
7.3.2.2.2.2. Results for RC-DCT 167
7.3.3. Execution time 169
7.3.3.1. Analysis of the execution time of repetitive controllers 169
7.3.3.2. Comparison of the execution time of all tested current controllers 169
7.4. Conclusions 170

8. Conclusions and future works 173
8.1. Conclusions 173
8.2. Future works 175
8.2.1. Current control 175
8.2.2. PCC voltage control 176

References 179

1

Introduction

This introductory chapter presents the current problems regarding the depletion of traditional energy sources and the environmental pollution involved, and the reasons that led to the flourishing of renewable energies. This situation has been accompanied by a great development of power electronics, being the Voltage Source Converter (VSC) one of the most common power converters nowadays. Their main applications are briefly explained, as well as an outline of the control system of a VSC. Thus, the motivations and objectives of this Thesis are introduced.

1.1. Introduction.

Satisfying our energy needs over the coming decades will be a big challenge. Our own fossil fuel resources are running out fast, fuel prices are increasing and the environment is suffering as result of our current energy supply structure. In 2030 the European Union (EU) will be importing 84% of its gas, 59% of its coal and 94% of its oil [Zervos and Kjaer, 2008].

Several analyses show that the massive use of fossil fuels to supply current energy needs is also problematic in the short term, due to environmental pollution and the limitations of these resources [Bueno, 2005]. Globally, the energy sector emits 26 billion tones of CO_2 each year and electricity production alone accounts for 41% of emissions. The International Energy Agency expects CO_2 emissions in 2030 to have increased by 55% to reach more than 40 billion tones of CO_2 per year. The share of emissions coming from electricity production will increase to 44% in 2030, reaching 18 billion tones of CO_2 [Zervos and Kjaer, 2008]. Fig. 1.1 shows the world energy consumption according to Mitsubishi Electric. It also shows the global trend of electricity consumption in the next 25 years, and the percentage that represents of the total value of energy. This study reveals that by 2020 both electricity generation and energy consumption will double, and electrification of end-consumption will be multiplied by five [Carroll, 2005]. One solution to reduce the consumption of fossil fuels is the generation of electricity from renewable energies.

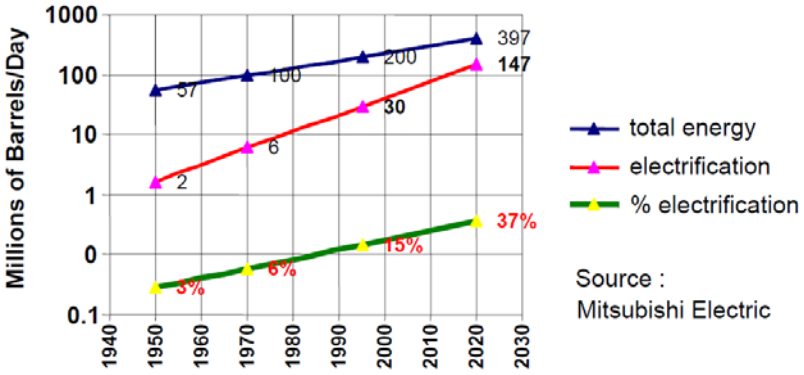

Fig. 1.1. World energy consumption.

In the last few years, renewable energies have experienced one of the largest growth in percentage (over 30% per year) compared with the growth of coal and lignite energy [Teodorescu, *et al.*, 2011]. A huge step forward was taken in March 2007, as the 27 EU Heads of State unanimously adopted a binding target of 20% of energy to come from renewables by 2020 [Clifford, 2007]. In January 2008, the European Commission released its draft legislation on renewable energies, which proposes a stable and flexible EU framework and should ensure a massive expansion of wind energy in Europe.

Therefore, power electronics has become one of the areas with higher activity and development in recent years, supported by technology advances in semiconductor devices such as Insulated Gate Bipolar Transistors (IGBTs) and Gate Commutated Thyristors (GCTs) [Wu, 2006]. To a large extent, this is due to lower manufacturing costs, which has helped increasing the use of new and better power electronics devices. Nowadays, only 15 % of electricity flows via electronics but, as the demand for electrical energy increases, high-power energy conversion systems based on power electronics are more necessary. Besides, they have to be electronically controlled. The development of high-power converters is more feasible for Medium Voltage (MV) conversion. This has been economically and technologically possible from the last ten years, and in the coming years MV conversion is expected to grow faster than Low Voltage (LV) conversion [Carroll, 2005].

1.1.1. Consequences of the development of power electronics.

Since power electronics was introduced in the late 1960s, nonlinear loads that consume non-sinusoidal current have increased significantly. In some cases, they represent a very high percentage of the total load. Today, it is common to find a house without linear loads such as conventional incandescent lamps. In most cases, these lamps have been replaced by electronically controlled fluorescent lamps. In industrial applications, an induction motor that can be considered as a linear load in steady state is now equipped with a rectifier and inverter for the purpose of achieving adjustable-speed control. The induction motor together with its

driver is no longer a linear load [Akagi, *et al.*, 2007].

Hence, problems related to nonlinear loads have significantly increased with the proliferation of power electronics equipment. Modern equipment behaves as a nonlinear load drawing a significant amount of harmonic current from the power network. Thus, power systems in some cases have to be analyzed under non-sinusoidal conditions.

Due to this situation, nowadays current regulation plays a key role in modern power electronic AC conversion systems such as variable speed drive systems, reactive power controllers and active filter systems [Holmes, *et al.*, 2009]. For uninterruptible power supplies [Mattavelli, *et al.*, 2004a], high bandwidth current control is essential to achieve good dynamic response, when the system supplies nonlinear loads such as diode rectifiers, while for grid-connected systems [Chen and Hsu, 2008], accurate current control is important to effectively regulate real- and reactive-power flow between the grid and the inverter. However, irrespective of the application, the essential concept of a current regulator is always to compare a measured load current against a reference target, and use the difference ("error") between these two quantities to adjust the switching of the associated power electronic converter so as to minimize this tracking error. Specifically, the primary goals of a current regulator can be summarized as [Rowan and Kerkman, 1986; Kazmierkowski and Malesani, 1998]:

- Minimize the steady-state magnitude and phase error, preferably achieving zero steady-state error;
- Accurately track the commanded reference current during transient changes. This requires a control system with as high a bandwidth as possible, to achieve the best possible dynamic response;
- Limit the peak current, to avoid overload conditions;
- Minimize low-order harmonics in the load current, and compensate for DC-link voltage ripple, dead-time delays, semiconductor device voltage drops and other practical second-order effects associated with the inverter operation.

Achieving these goals, particularly for AC current regulators, has proved to be very challenging problem for several decades, and has been the subject of substantial research effort throughout this period.

1.1.2. Energy production model.

A change in the energy production model has taken place, moving from a *centralized* model (Fig. 1.2a) to another *distributed* or *decentralized* (Fig. 1.2b) [Cóbreces, 2009]. The

centralized structure and the few generation points induce severe design vulnerabilities into the system. A few network points support a big generation responsibility and, in the case of a fault in some of the biggest generation nodes, the probability of a chained fault is higher than it should, even in the presence of back-up systems. Another limitation is its low efficiency regarding the distance from energy producers to energy consumers. As displayed in Fig. 1.2a, energy is always flowing from power plants, through the transmission and distribution system, to power consumers as domestic and industrial facilities. The information flows in the opposite direction: the system operator acquires the available consumption data and sends commands to the generation points in order to balance electricity production.

On the other hand, the *distributed* generation scheme is characterized by a bidirectional power flow and information that allows a more powerful control of the power system. It allows the integration of extensive small distributed power sources, placed, or not, close to end users. It also allows its integration with large-scale central power generation, the participation of small producers in the electric market, the introduction of quality of service concepts in energy delivery, the ability to increase grid efficiency by equalizing power consumption along the day, etc. [Cóbreces, 2009].

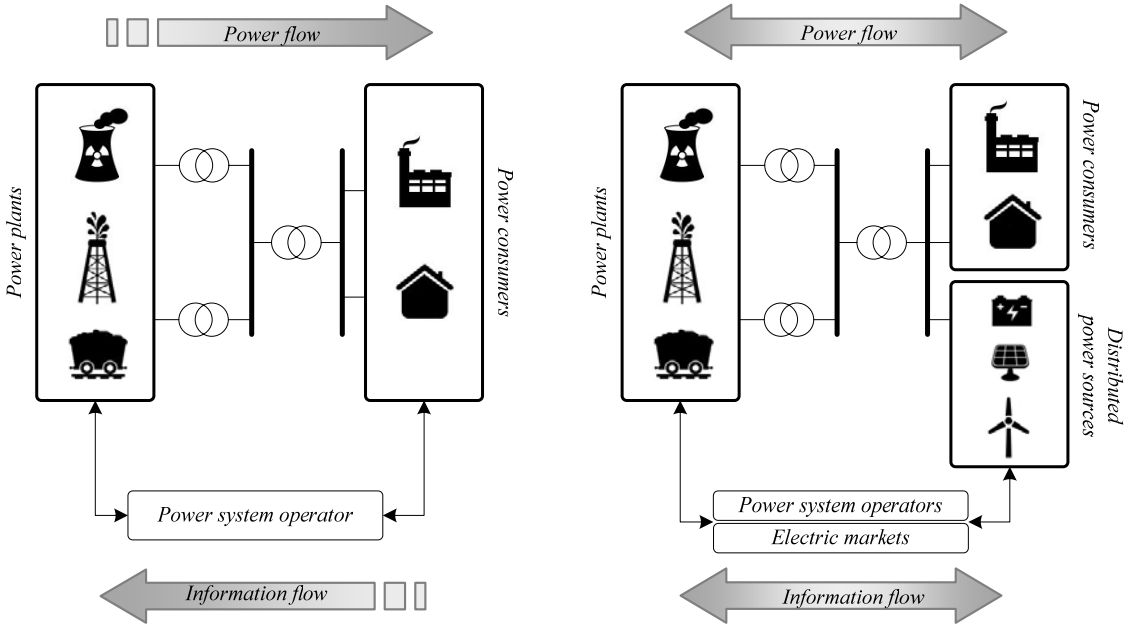

Fig. 1.2. Traditional vs. distributed generation.

1.1.3. Voltage Source Converter (VSC).

In the MV market, the various topologies have evolved with components, design, and reliability. The two major types of converters are known as VSC and Current Source

Converter (CSC). In industrial markets, the VSC design has proven to be more efficient, has higher reliability and faster dynamic response, and is capable of running motors without de-rating [Van Der Meulen and Maurin, 2010].

When connected to the grid, VSCs should achieve a low Total Harmonic Distortion (THD) of AC currents $(\vec{\imath}_g)$ and a controllable phase shift in the converter output voltage with respect to the grid voltage $(\vec{e}_g)$. From the viewpoint of power balance, this means that the fundamental harmonic of the active and reactive power should be controlled and the other harmonics of the active and reactive power should be zero. Furthermore, the VSC used as active rectifier also interfaces the DC load. Thus, the VSC must be controlled to have a controllable DC component of the DC-link voltage (U_{DC}) and the remaining harmonics close to zero, whether the DC load is linear, nonlinear, passive or active [Bueno, 2005].

The grid-filter selection is important because it affects the dynamic behavior of the system, the cost of it and the quality of the energy delivered to the grid. The aim is to obtain a given attenuation at the switching frequency (or a certain frequency depending on the standards and harmonic regulations) with the lowest possible cost. The simplest option from the viewpoint of converter assembly and controller design is to use an L-filter, but the fact of achieving a sinusoidal line current at relatively low switching frequencies implies a very high cost. LC- or LCL-filters present very high attenuation for harmonics caused by the PWM, even for moderate switching frequencies (below 2.5 kHz, approximately), and with lower costs. The criteria for designing the filter components can be found in different standards of IEC, IEEE, etc. [Lindgren, 1998].

1.2. Grid-connected Voltage-Source Converters.

This type of converter has different applications, for example:

- Active front-end rectifiers.
- Industry: excitation of motors, pumps, etc. that can be found in paper-production industries, petrochemical industries, etc.
- Transmission and distribution of energy: wind farms, VSC-HVDC, STATCOMs, active filters, high-power UPS, etc.
- Drive: grid-side converters and machine-side converters.

A brief explanation of some of the most typical applications of grid-connected VSCs is given in the next section.

1.2.1. Applications.

1.2.1.1. Shunt active power filter (APF).

The concept of shunt active filtering was first introduced by Gyugyi and Strycula in 1976 [Gyugyi and Strycula, 1976]. The shunt APF is a power conditioner used for compensation of harmonic current from nonlinear loads, and it is usually connected very near to this kind of loads [Akagi*, et al.*, 2007]. The shunt APF has the task of detecting the load current harmonics and generating a current that cancels out that harmonic current, leaving the fundamental current only to be supplied by the utility grid [Rodríguez*, et al.*, 2009; Rodríguez*, et al.*, 2010]. They have shown an efficient performance, being a robust and optimal solution to carry out this objective. Its basic configuration and control scheme are depicted in Fig. 1.3.

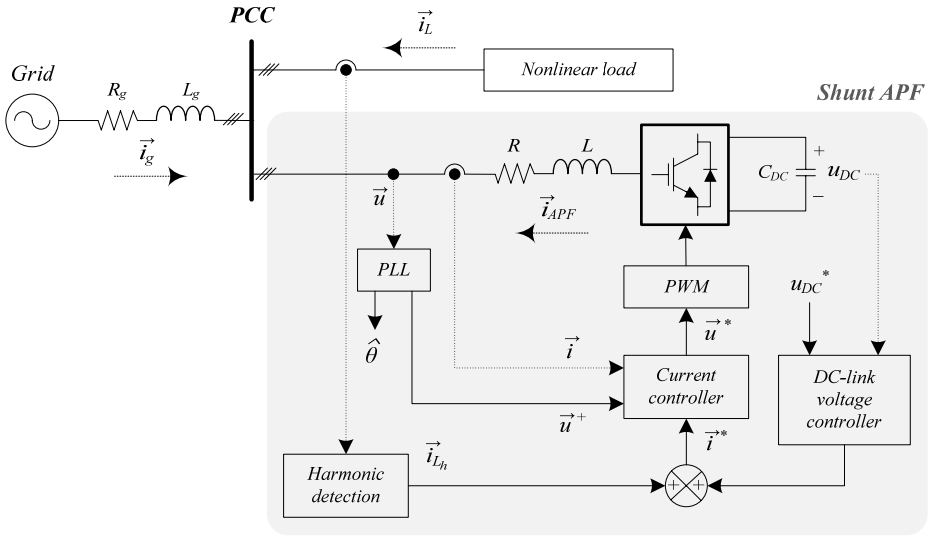

Fig. 1.3. Block diagram of a shunt APF and its generic control scheme.

In short, the shunt APF can be viewed as a short-circuit for the harmonic frequencies and as an open-circuit for fundamental frequency imposed by the grid. It is the ideal compensator for nonlinear loads that behave as current sources. If the load behaves as a harmonic voltage source, the shunt APF can also be used but it is recommended to insert an inductance in series with the non-linear load [Akagi, 2005]. This way, the nonlinear load can be expressed by its equivalent Norton and be represented as current source connected in parallel with an inductance.

APFs can solve problems of harmonic and reactive power simultaneously. APFs consisting of VSIs and a DC capacitor have been researched and developed for improving the power factor and stability of transmission systems. APFs have the ability to adjust the amplitude of the synthesized AC voltage of the inverters by means of PWM or by control of the DC-link

voltage, thus drawing either leading or lagging reactive power from the supply. APFs are an up-to-date solution to power quality problems [Özdemir, *et al.*, 2003].

1.2.1.2. Dynamic voltage restorer (DVR).

Significant deviations from the nominal voltage are a problem for sensitive consumers in the grid system. Interruptions are generally considered to be the worst case with the load disconnected from the supply. Voltage dips are characterized by a reduction in voltage, but the load is still connected to the supply. They are in most cases considered less critical compared to interruptions, but they typically occur more frequently. Voltage dips have in several cases been reported as a threat to sensitive equipment and have resulted in shutdowns, loss of production and a hence a major cost burden [Nielsen, *et al.*, 2001].

The DVR is a power electronics device conceived to restore the voltage waveform when a voltage dip occurs [Roldán-Pérez, *et al.*, 2011]. The DVR can be implemented at both a LV level as well as a MV level; and gives an opportunity to protect high power applications from voltage dips. It uses a series-connected topology to add voltage to the PCC when a voltage dip is detected, as shown in Fig. 1.4. This aims to protect critical loads against voltage dips [Nielsen, *et al.*, 2004]. The DVR usually consists of an injection transformer, which is connected in series with the distribution line, a VSI-PWM which is connected to the secondary of the injection transformer and an energy storage device connected at the DC-link of the inverter bridge [Vilathgamuwa, *et al.*, 1999].

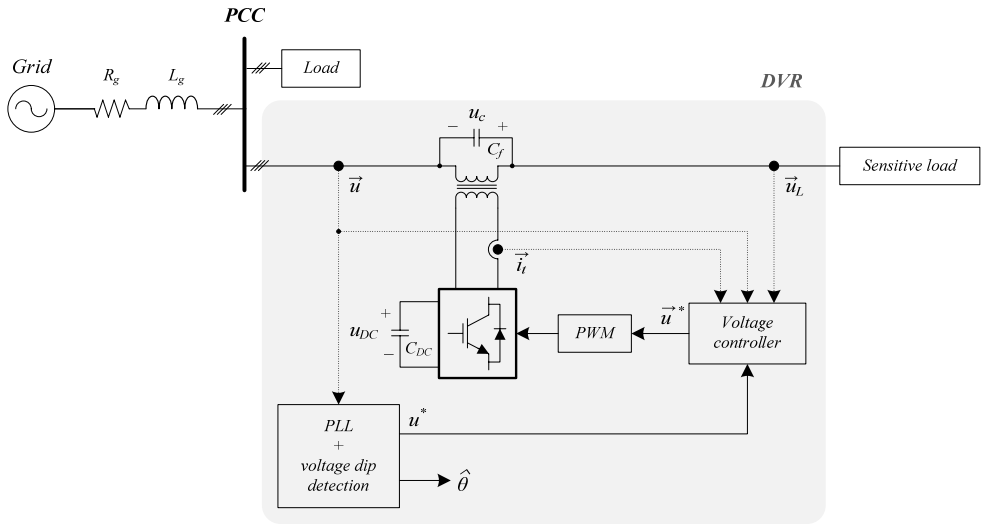

Fig. 1.4. Block diagram of a DVR and its generic control scheme.

1.2.1.3. Static synchronous compensator (STATCOM).

The STATCOM is a Flexible AC Transmission System (FACTS) device [Hingorani, 1991;

Hingorani and Gyugyi, 2000]. Its prime function is to exchange reactive power with the host AC system. In an electric power transmission system, the STATCOM can be used to increase the line power transmission capacity [Hingorani and Gyugyi, 2000], to enhance the voltage/angle stability [Mihalic, *et al.*, 1993], or to damp the system oscillatory modes [Gronquist, *et al.*, 1995]. In a distribution system, the STATCOM is mainly used for voltage regulation [Schauder, *et al.*, 1997]; however, it can also supply real power to the loads in the case of a blackout if it is augmented with an energy storage device, for example, a battery storage system. Moreover, the STATCOM may also be employed to balance a distribution network by compensating for load unbalances [Yazdani and Iravani, 2010]. The generic block diagram of a STATCOM is represented in Fig. 1.5 along with its control scheme.

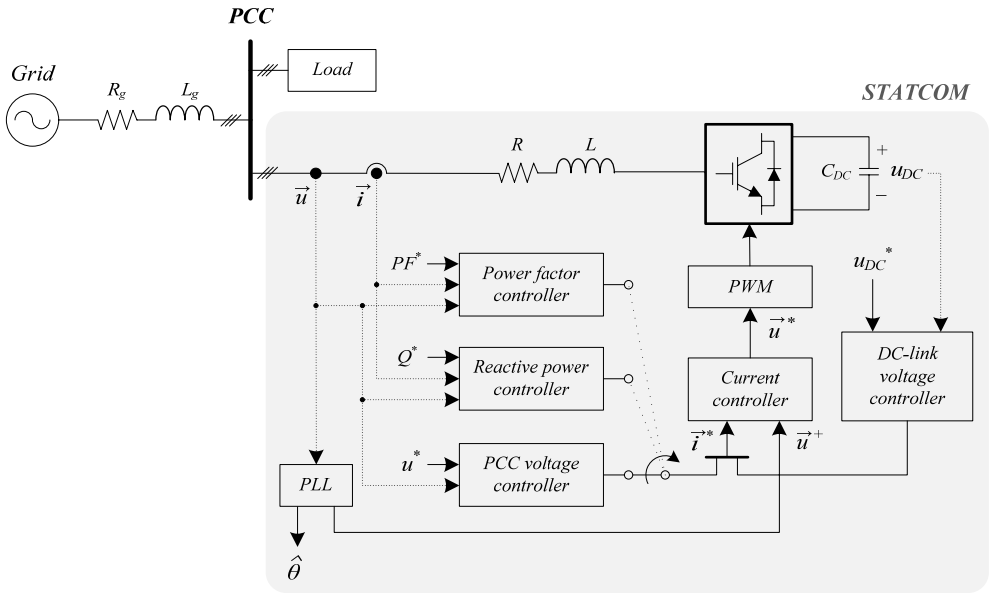

Fig. 1.5. Block diagram of a STATCOM and its generic control scheme.

1.2.1.4. Unified power flow controller (UPFC).

The possibility of controlling power flow in an electric power system without generation rescheduling or topology changes can improve the power system performance [Hingorani, 1991]. By use of controllable components, the line flows can be changed in such a way that thermal limits are not exceeded, losses minimized, stability margins increased, contractual requirements fulfilled, etc. without violating the economic generation dispatch [Noroozian, *et al.*, 1997].

The Unified Power Flow Controller (UPFC) is a device in FACTS family which consists of series and shunt connected VSCs, as shown in Fig. 1.6. Combined series and shunt power conditioners are formed by two VSCs connected back-to-back through a common DC-link. Usually, the AC output of one converter is inserted in series with the power system, whereas the AC output of the second one is connected in parallel. Although two CSCs could be

employed in its basic configuration, it is common to use two VSCs connected back-to-back through a common DC-link [Akagi*, et al.*, 2007].

The UPFC performs power flow control, reactive power compensation and voltage regulation. It can control the active (real) and reactive (imaginary) power through a transmission line and simultaneously regulate the voltage at an AC network. It is a very fast acting device with high performance and flexibility.

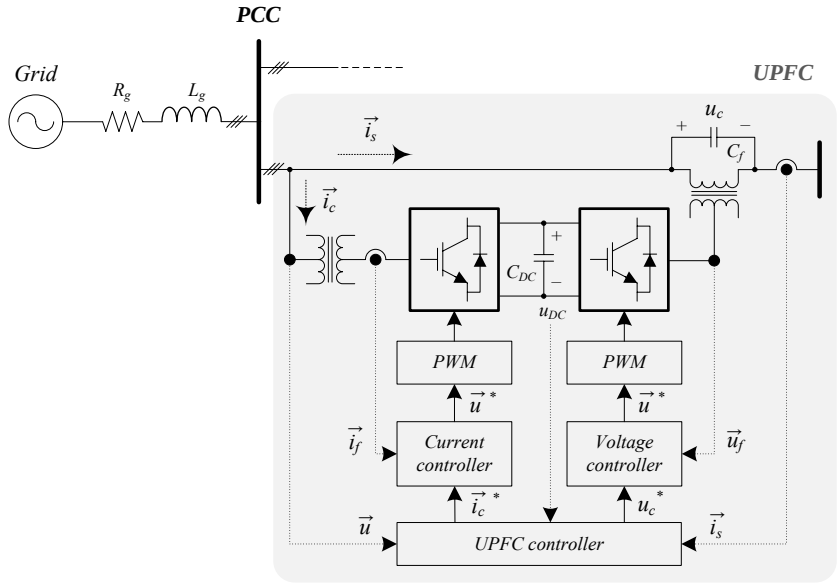

Fig. 1.6. Block diagram of a UPFC and its generic control scheme.

1.2.1.5. High-voltage direct-current (HVDC) transmission.

HVDC transmission is widely recognized as being advantageous for long-distance bulk-power delivery, asynchronous interconnections and long submarine cable crossings [Bahrman and Johnson, 2007]. VSC-based HVDC (or simply VSC-HVDC) is gradually gaining ground to CSC-based HVDC (CSC-HVDC) due to the weaknesses of the latter: (i) a relatively strong AC grid is required for commutation, so blackstart is not possible; (ii) it is not possible to perform control of reactive power (the stations always consume reactive power); (iii) power direction reversal requires DC voltage reversal, so that extruder polymer cables cannot be used; (iv) filters, both on AC and DC side, need to be large; and (v) the transformers need DC insulation, which is translated into expensive specialized transformers [Norrga, 2011]. The basic scheme of one of its topologies, namely, back-to-back VSC-HVDC, is shown in Fig. 1.7.

The particular advantages of VSC-HVDC can be summarized as follows: (i) it is possible to perform a rapid and independent of active and reactive power; (ii) there is no need for a strong grid; (iii) power direction reversal is carried out by means of a DC current reversal; (iv)

lightweight, less expensive, extruded polymer cables can be used, which make DC grids more feasible; and (v) smaller AC and DC filters are required compared to those of CSC-HVDC.

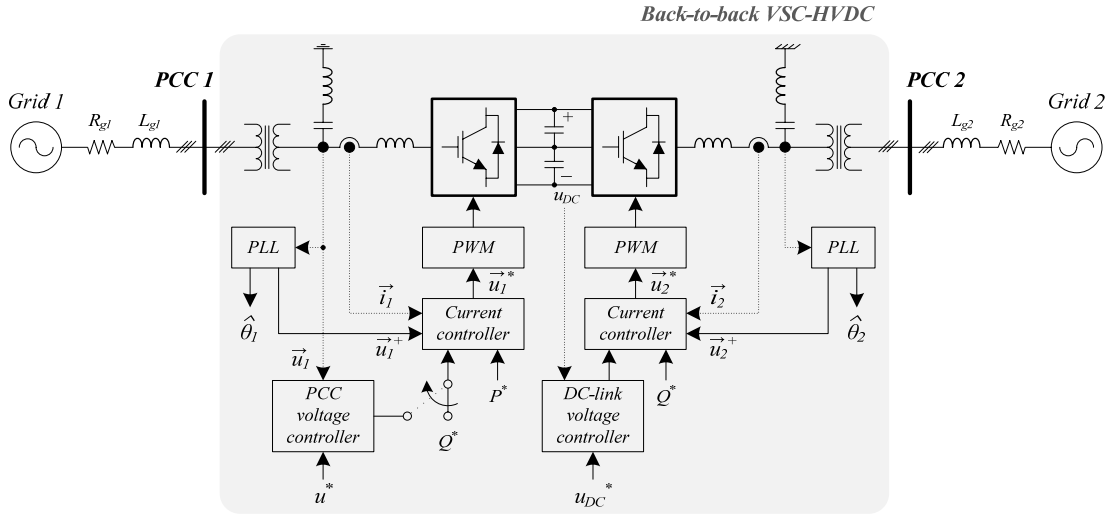

Fig. 1.7. Block diagram of a back-to-back VSC-HVDC and its generic control scheme.

1.3. Objectives.

This thesis aims to improve the behavior of VSCs connected in shunt mode with the grid through an L-filter, especially in connections to weak grids and in two topics: (i) tracking of grid current harmonics and rejection of grid voltage harmonics, and (ii) control of PCC voltage in an unbalanced condition. These improvements entail:

- Development of current control algorithms that are able of both reducing the harmonic content of the grid current and maintaining the selectivity of the current control against frequency drifts, ensuring the stability of the system. Such frequency drifts can mean a big loss in performance capability of the controllers, both low-level and high-level controllers, significantly worsening the quality of the power delivered to the grid.
- Analysis and optimization of the computational burden of all current controllers discussed in the Thesis. The digital implementation of the converter control is a very important aspect as the viability of the project may depend on a proper use of the resources of the digital platform.
- Experimental testing with all current controllers addressed in the Thesis under the same conditions of power, voltage and current, so that a comparison of their performance can be established.
- Development of methods for calculating reference currents suitable for weak

grids, where the grid voltage may be unbalanced and thus contain a negative sequence component. This negative sequence also appears in the grid current and, in order to be rejected, proper reference currents for the current controller are needed.

- Improvement of the behavior of the control of the voltage at the PCC, so that it is possible to have control over the negative sequence level and counteract possible harmful effects in the converter.

1.4. Structure of the Thesis.

The Thesis is structured in the following chapters:

- *Chapter 2.*

  Chapter 2 presents a review of knowledge of linear control techniques applied to VSCs, focusing in current control and PCC voltage control. The objectives of the Thesis are listed next. These goals focus on making contributions to the behavior of VSCs in the presence of frequency drifts, harmonics, unbalanced grid voltages, etc. as well as to optimize the digital implementation of the current control.

- *Chapter 3.*

  In first place, an overview of the control scheme of a VSC connected to the grid through an L-filter is given in chapter 3. Calculation of reference currents and their limitation are also tackled in this chapter, concluding with a review of grid-frequency estimation methods.

- *Chapter 4.*

  Among the existing techniques for implementing the current control for harmonic compensation, two of the most used are resonant control and repetitive control. This chapter focuses on the first one, making a thorough study of different existing structures to implement it, showing the frequency-adaptive algorithm for each of these structures and analyzing their computational load. The current control scheme is studied and characterized in order to establish a comparison among the different structures.

- *Chapter 5.*

  While the previous chapter covers one of the two current control techniques studied in this Thesis, chapter 5 does the same with the second technique, namely, repetitive control.

- *Chapter 6.*

Chapter 6 addresses the PCC voltage control. To do so, the grid model under unbalanced conditions is mathematically analyzed, distinguishing between positive and negative sequences. This allows developing a novel PCC voltage control with independent control of both sequences. Finally, simulation results show the effectiveness of this controller.

- *Chapter 7.*

  Several experimental tests have been carried out to analyze the performance of the current controllers discussed in chapters 4 and 5. All of them have been performed under the same conditions, so that conclusions can be drawn about their suitability for different power applications. These tests aim at characterizing the transient response, steady-state response, behavior under frequency jumps and computational load of the current controllers.

- *Chapter 8.*

  Chapter 8 summarizes the conclusions obtained during the development of the Thesis, and future work lines arise from these.

1.5. Conventions adopted in the development of the Thesis.

In this Thesis, all transformations from *abc*-axes to *αβ*-axes, and vice versa, are accomplished by means of a power-invariant transformation (Table 1.1). Besides, *dq*-axes are oriented so that the *d*-axis coincides with the flux vector of the PCC $(\vec{\psi})$, and therefore the PCC voltage vector is located in the *q*-axis of the *dq*-plane. The graphical representation of the location of these vectors is shown in Fig. 1.8.

TABLE 1.1. TRANSFORMATIONS BETWEEN *ABC*-AXES AND *αβ*-AXES.

$\boldsymbol{abc \rightarrow \alpha\beta\gamma}$	$\boldsymbol{\alpha\beta\gamma \rightarrow abc}$
$T_{abc\rightarrow\alpha\beta\gamma} = \sqrt{\frac{2}{3}}\begin{bmatrix} 1 & -1/2 & -1/2 \\ 0 & \sqrt{3}/2 & -\sqrt{3}/2 \\ 1/\sqrt{2} & 1/\sqrt{2} & 1/\sqrt{2} \end{bmatrix}$	$T_{\alpha\beta\gamma\rightarrow abc} = \sqrt{\frac{2}{3}}\begin{bmatrix} 1 & -1/2 & -1/2 \\ -1/2 & \sqrt{3}/2 & 1/\sqrt{2} \\ -1/2 & -\sqrt{3}/2 & 1/\sqrt{2} \end{bmatrix}$

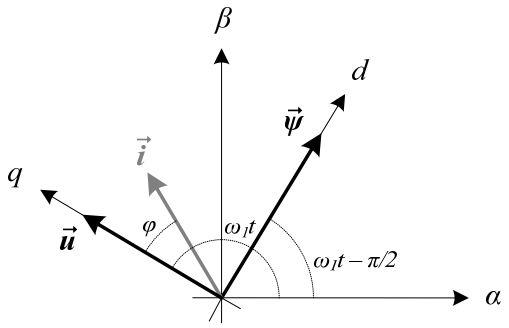

Fig. 1.8. Location of the PCC voltage vector and PCC flux vector in *dq*-axes.

1.6. Published papers.

Most of the results shown in this Thesis have been presented at different conferences. The most significant are displayed chronologically in this section. A brief description of their contents is made and, in case that the work has been included in this Thesis, the corresponding part of the document is indicated.

1. A.Rodríguez, E.Bueno, C.Girón, F.J.Rodríguez, and Á.Mayor, "PCC unbalanced voltage control using a STATCOM," *pending of acceptance for IECON'13*.

This paper proposes a novel voltage controller in synchronous reference frame to compensate an unbalanced PCC voltage by means of a STATCOM, allowing an independent control of both positive and negative voltage sequences. Furthermore, this controller includes aspects as antiwindup and droop control to improve the control system performance. This work has been included in chapter 6.

2. A.Rodríguez, F.Huerta, E.Bueno, and F.J.Rodríguez, "Analysis and Performance Comparison of Different Power Conditioning Systems for SMES-Based Energy Systems in Wind Turbines," *Energies*, vol. 6, Mar. 2013, pp. 1527-1553.

This article studies the performance of three SMES-based systems that differ in the topology of power converter, namely, a two-level VSC, a three-level VSC and a two-level CSC, giving special attention to the analysis of the converter power losses. The tuning of the parameters of the active power controller, reactive power controller and DC-link voltage controller is carried out as in section 3.1.

3. F.Huerta, D.Pizarro, S.Cóbreces, F.J.Rodríguez, C.Girón, and A.Rodriguez, "LQG servo controller for the current control of LCL grid-connected Voltage-Source

Converters," *IEEE Trans. Industrial Electronics*, vol. 59, no. 11, Nov. 2012, pp. 4272-4284.

This paper addresses the study of another type of current control strategy for VSCs connected to the grid through an LCL-filter, i.e. LQG servo control. This control technique will serve as a basis for future work lines, which will entail the application of resonant and repetitive controllers to perform LQG servo control.

4. A.Rodríguez, M.Moranchel, E.Bueno, and F.J.Rodríguez, "Tuning of resonant controllers applied to the current control of Voltage-Source Converters," 38th Annual Conference of the IEEE Industrial Electronics Society (IECON'12), 25-28 Oct. 2012, pp. 4444-4449.

The tuning of the resonant controllers that has been applied in chapter 4 is based on this work. Simulation and experimental results are provided in order to compare their performance in a grid whose harmonic content includes harmonic sixth, analyzing typical control parameters such as settling time, maximum overshoot and steady-state error.

5. M.Rizo, A.Rodríguez, F.J.Rodríguez, E.Bueno, and M.Liserre, "Different approaches of Stationary Reference Frames Saturators," 38th Annual Conference of the IEEE Industrial Electronics Society (IECON'12), 25-28 Oct. 2012, pp. 2233-2238.

This work is focused on developing different novel techniques achieving different grades of distortion and bandwidth in function of the control loop structure and system requirements. These are the techniques that have been applied to limit the reference currents for the current control, as indicated in section 3.2.2.

6. J.Valero, E.Bueno, P.Ledesma, H.Amarís, and A.Rodríguez, "Dynamic Performance of a STATCOM under Grid Disturbances for Two Different Linear Controllers," 38th Annual Conference of the IEEE Industrial Electronics Society (IECON'12), 25-28 Oct. 2012, pp. 355-360.

The aim of this paper is to present a comparative stability study between vectorial control (VC) and power-synchronization control (PSC) related to a STATCOM under different grid disturbances. Both of them are linear control methods of grid-connected VSCs. The tuning of the parameters of the VC controllers is carried out as in section 3.1.

7. A.Rodríguez, M.Rizo, E.Bueno, F.J.Rodríguez, A.Garcés, and M.Molinas, "Analysis and performance comparison of different power conditioning systems for SMES-based energy systems in wind turbines," 3rd International Symposium on Power Electronics for Distributed Generation Systems (PEDG'12), 25-28 Jun. 2012, pp. 527-533.

This paper analyzes and compares the performance of three SMES-based systems that differ in the topology of power converter, namely, a two-level VSC, a three-level VSC and a two-level CSC. The tuning of the parameters of the active power controller, reactive power controller and DC-link voltage controller is carried out as in section 3.1.

8. A.Rodríguez, C.Girón, V.Sáez, M.Rizo, E.Bueno, and F.J.Rodríguez, "Analysis of Repetitive-Based Controllers for Selective Harmonic Compensation in Active Power Filters," 36th Annual Conference of the IEEE Industrial Electronics Society (IECON'10), 7-10 Nov. 2010, pp. 2013-2018.

This paper realizes an exhaustive analysis and comparative study of the different existing techniques up to now in order to develop repetitive controllers applied to selective harmonic compensation in shunt active power filters. The paper also explains the importance of having a correct and accurate model of the plant in order to ensure stability and good performance of the entire system, justifying the method used to carry out the design of such model. This is the basis for chapter 5.

9. V.Sáez, A.Rodríguez, M.Rizo, E.Bueno, Á.Hernández, and F.J.Rodríguez, "Fixed Point Implementation of IIR Filters using Delta Operator applied to distributed power generation systems," 36th Annual Conference of the IEEE Industrial Electronics Society (IECON'10), 7-10 Nov. 2010, pp. 1709-1714.

In this paper, a study of IIR filter quantification and delta operator is carried out. As an example, fixed-point implementation of second order generalized integrators (SOGIs) is realized, whose results show the advantages of using delta operator. The study of the discretization techniques of the SOGI is the basis for the analysis made in section 4.2.2.

10. M.Rizo, A.Rodríguez, E.Bueno, S.Cóbreces, and F.J.Rodríguez, "Low Voltage Ride-Through of Wind Turbine based on Interior Permanent Magnet Synchronous Generators Sensorless Vector Controlled," 2nd IEEE Energy Conversion & Expo (ECCE'10), 12-16 Sep. 2010, pp. 2507-2514.

This paper is focused on satisfying Low Voltage Ride-Through (LVRT) restrictions

controlling both active and reactive powers delivered to the grid according to the more relevant grid codes. The control of the grid-side converter is based on the scheme described in section 3.

11. A.Rodríguez, C.Girón, V.Sáez, E.Bueno, F.J.Meca, and F.J.Rodríguez, "Stability Issues of Current Controllers based on Repetitive-Based Control and Second Order Generalized Integrators for Active Power Filters," IEEE International Symposium on Industrial Electronics (ISIE'10), 4-7 Jul. 2010, pp. 2593-2598.

This paper analyzes the robustness and stability of two current controller schemes for shunt active power filters, based on repetitive controllers and proportional + resonant controllers using SOGIs connected in parallel. The detailed analysis of these controllers has been included in chapters 4 and 5.

12. V.Sáez, A.Martín, M.Rizo, A.Rodríguez, E.Bueno, Á.Hernández, and A.Mirón, "FPGA implementation of grid synchronization algorithms based on DSC, DSOGI-QSG and PLL for distributed power generation systems," IEEE International Symposium on Industrial Electronics (ISIE'10), 4-7 Jul. 2010, pp. 2765-2770.

Several grid-synchronization algorithms are implemented in an FPGA in this work. These algorithms have been included in chapter 3, regarding grid-frequency estimation methods.

13. A.Rodríguez, C.Girón, M.Rizo, V.Sáez, E.Bueno, and F.J.Rodríguez, "Comparison of Current Controllers based on Repetitive-Based Control and Second Order Generalized Integrators for Active Power Filters," 35th Annual Conference of the IEEE Industrial Electronics Society (IECON'09), 3-5 Nov. 2009, pp. 7-12.

In this paper, two current controller schemes, based on repetitive controllers and proportional+resonant controllers using second order generalized integrators connected in parallel, are proposed and compared for shunt active power filters. The objectives of this paper are to analyze both controllers in continuous and discrete time; to study how to tune the parameters of the controllers and other auxiliary elements like a PI controller in the case of repetitive controllers; to show questions related to real-time implementation for the two cases; and, finally, to present some experimental and comparative results. All these studies have been included in chapters 4 and 5.

14. E.Bueno, S.Cóbreces, F.J.Rodríguez, F.Huerta, M.Gálvez, A.Rodríguez, and

F.A.S.Neves, “Optimal proposal to mitigate the problems produced by the acquisition of noisy signals in the control of grid-converters,” 34th Annual Conference of the IEEE Industrial Electronics Society (IECON’08), 10-13 Nov. 2008, pp. 297-302.

This work proposes different algorithms, as digital filters and Kalman filters, which have as objective reduce the noise to the input of converter controllers. In this way, the quality of the current grids improves considerably. The study of the plant model for the DC-link voltage controller has been included in section 3.1.1.2, whereas the study of the plant model for the current controller has been included in section 3.1.3.

2

State of the art

The work developed in this Thesis is aimed at optimizing the behavior of VSCs when used as an interface with the grid, in order to demand or deliver energy to the grid with the best possible quality, and meeting the standards. To this end, this Thesis focuses on the study and improvement of current control and PCC voltage control, both forming part of a cascade linear control system. These improvements are especially useful in VSCs connected to weak grids, but they are also applicable to strong grids.

Thus, this chapter is divided into three parts. The first part deals with the control of grid-connected converters to compensate harmonics, making a review of the contributions made in the field of current control implemented by means of resonant control and repetitive control. The second part addresses the control of grid-connected converters to perform PCC voltage control, showing the evolution of the controllers designed for this purpose. In the third part, from the general lines indicated in the previous paragraph and the analysis of the issues not covered by the references shown in the literature survey, a detailed description of the main contributions of the Thesis is presented.

2.1. Control of grid-connected converters to compensate harmonics.

The proper control of the harmonic content of grid currents is becoming more important in the last decades due to the increasing number of nonlinear loads connected to the distribution network, such as adjustable speed drives (ASDs), arc furnaces, switched mode power supply (SMPS), uninterruptible power supply (UPS) systems, battery chargers, etc. [Bhattacharya*, et al.*, 2009]. These nonlinear loads draw fluctuating and harmonic currents from the utility grid, producing several problems such as additional heating in the power system components, voltage distortion, poor power factor, possible excitement of resonances or undesirable interactions in the power system. This expansion of nonlinear devices is accelerated by the research in power electronics [Yazdani and Iravani, 2010]. Therefore, power harmonics and their effects on power quality are a topic of concern.

The way in which power electronics-based applications deal with the possible presence of harmonic currents is by means of current control. Whether the primary purpose of the application is to compensate the harmonic content of the grid current or not, all power converter-based applications require a selective current control that allows eliminating unwanted frequency components that can be found in the utility grid. Several techniques can be found in the technical literature for carrying out this control [Kazmierkowski and Malesani, 1998], developed first in *abc*-axes and, subsequently, in stationary (*αβ*) and synchronous (*dq*) reference frames [Zargari and Joos, 1995; Mattavelli, 2001; Zmood*, et al.*, 2001]. The work [Schauder and Caddy, 1982] was one of the first to explain the control in *dq*-axes applied to AC machines. A few years later, this same structure in *dq*-axes was applied to the control of PWM inverters in the work [Rowan and Kerkman, 1986].

2.1.1. Harmonic current compensation.

2.1.1.1. Resonant control.

Conventional Proportional-Integral (PI) controllers are not able to obtain zero steady-state error under sinusoidal inputs due to the finite gain presented at the operating frequency [Yuan*, et al.*, 2000], creating unavoidable steady-state amplitude and phase errors [Zmood*, et al.*, 2001]. Resonant control originally emerges as an alternative to PI controllers to perform the current control of power converters without the need for an *αβ0* to *dq0* transformation. Resonant control obtains a theoretical infinite gain at the frequency of interest, also called resonant frequency f_o (hence the name). Issues relating to the practical implementation of these controllers on digital platforms obviously prevent them from behaving ideally, but a wise choice of the appropriate discretization technique (design by emulation) or the direct design of the controller in discrete time can minimize the differences between the behavior of the controller in continuous time and in discrete time.

The Generalized Integrator (GI) formally introduced in [Yuan*, et al.*, 2002] was one of the first proposals of resonant control, showing how it was capable of compensating both positive and negative sequences of the input signal and how to compensate multiple harmonics by adding several resonant controllers in parallel. Besides, the effect of proportional and integral gains on the control performance was also analyzed. This GI derived in the well-know Second Order Generalized Integrator (SOGI), where the only difference with respect to the original was the inclusion of a gain ω in the numerator. The fact of adding this gain made the resonant controller a more general structure that could be used in current control of grid converters taking into account the changes in the gain, and also in tasks related to grid synchronization [Rodríguez*, et al.*, 2008].

A scheme developed from the SOGI in order to generate quadrature-signals is the SOGI-

QSG [Rodríguez, *et al.*, 2006]. The SOGI has the disadvantage of having an infinite gain at the resonant frequency, which can make the system unstable. The SOGI-QSG presents a finite gain at the desired frequencies and an adjustable bandwidth through a specific gain (usually defined as k_s); hence, a current control scheme based on SOGI-QSGs will not be able to achieve zero steady-state error due to this finite gain but the stability of the system will be assured [Rodríguez, *et al.*, 2012]. The work [Zmood and Holmes, 2003] already posed an approximation to the SOGI-QSG structure. The authors justified that an ideal integrator is often approximated by a low-pass transfer function due to finite precision in digital systems and, when transforming it to a band-pass transfer function centered at ω, the resulting transfer function also had an adjustable bandwidth and finite gain at the resonant frequency ω. By means of an optimal tuning of the design parameters the steady-state error can be minimized but its results are not very satisfactory in comparison to other current control techniques. This is the reason why this current control technique has not been covered in this Thesis.

As stated earlier, the SOGI introduces an infinite gain at the resonant frequency that can make the system unstable as it does not make any control in the phase lag introduced. Thus, some modifications were made to the original SOGI in order to control the phase shift in the works [García-Cerrada, *et al.*, 2004; Pinzón-Ardila, 2007]. This technique was applied to the voltage control of a Voltage Source Inverter (VSI) and it consisted of the addition of a lead-lag network to a SOGI to modify the phase shift introduced by the current controller. In this Thesis, this technique receives the name of Second Order Generalized Integrator with Lead-Lag Network (SOGI-LLN). An interesting study of the tradeoff between selectivity and system speed was also made in these works [García-Cerrada, *et al.*, 2004; Pinzón-Ardila, 2007].

Another technique of resonant control found in technical literature is Adaptive Feedforward Cancelation (AFC). In its early applications it was employed in mechanical systems [Ludwick, 1999; Byl, *et al.*, 2005; Bodson, 2005] to reject periodic disturbances that are harmonics of some fundamental frequency. A discrete time AFC was designed to control the output voltage of a full-bridge DC-AC inverter in the work [Malo and Griñó, 2008] following the loop-shaping approach presented in [Byl, *et al.*, 2005], accompanied by a complete study of the controller behavior in the vicinity of the resonant frequency and a design guide of its parameters.

Regarding compensation of multiple harmonics, the current control scheme proposed in [Bojoi, *et al.*, 2005] is widely used due to its benefits. It is implemented in a mixed reference frame, since it is formed by a resonant controller tuned at the fundamental frequency f_o in stationary reference frame ($\alpha\beta$-axes) and a set of resonant controllers tuned at the harmonic frequencies $6kf_o$ ($k \in \mathbb{Z}$) in synchronous reference frame (dq-axes) connected in parallel with the first one. The fact of transforming the error signal of the current controller from stationary

to synchronous reference frame makes possible halving the number of resonant controllers needed to compensate the harmonics of the input signal. If a current control implemented in *dq*-axes is desired, it would be as simple as replacing the SOGI tuned at f_o by a PI controller.

2.1.1.2. Repetitive control.

Repetitive control has its origins in the works of Inoue *et al.* in the early eighties [Inoue*, et al.*, 1981a; Inoue*, et al.*, 1981b], where the authors provided the first discussion of this new method of control. These papers describe the theoretical basis of repetitive control in terms of Laplace transforms, which was completed in subsequent papers [Hara and Yamamoto, 1985; Nakano and Hara, 1986; Omata*, et al.*, 1987].

The Internal Model Principle (IMP) [Francis and Wonham, 1975] was first cited in the literature as the mathematical basis of repetitive control in [Hara*, et al.*, 1985], which states that a model of the reference input must be included into the stable closed-loop transfer function, so that perfect reference tracking in steady-state can be expected. Two fundamental assumptions of repetitive control theory are that the input is periodic and that the control system without the repetitive control loop is asymptotically stable [Broberg and Molyet, 1994].

The discrete time analysis of a generic repetitive controller with zero phase error was first carried out in [Tomizuka, 1987]. This work dealt with the presence of uncancellable zeros in the controlled plant, e.g. unstable zeros, so that the plant output cannot follow arbitrary desired trajectories. To achieve a superior tracking, a feedforward controller was added to the feedback controller. These two controllers can be designed simultaneously or separately. An adaptive version of this repetitive controller was posed in [Tsao and Tomizuka, 1987], where the adaptive feedforward controller was used to let the output of a plant with stable and unstable zeros track a time-varying desired output without any phase error.

In practice, the generic scheme of a repetitive controller usually makes the system unstable as it amplifies many high-order harmonics, while the system to be controlled usually has a limited bandwidth [Pinzón-Ardila, 2007]. This is the reason why a change had to be made to the original model. The concept of *plug-in* implementation was first introduced in [Tomizuka*, et al.*, 1988], a novel concept that enables a repetitive controller to be inserted prior to the standard controller in a feedback loop to reduce periodic errors. This allows implementation of repetitive control to be accomplished after the original feedback system is fully stabilized and tested [Broberg and Molyet, 1992]. Furthermore, a plug-in controller has the advantage that the standard controller can be designed without special consideration for the repetitive nature of the input/disturbance; instead the designer can concentrate his efforts on other aspects like robustness and noise rejection, for example [Tomizuka*, et al.*, 1988].

Since the basic repetitive controller amplifies infinite harmonics in continuous time or up to the Nyquist frequency in discrete time, a low-pass filter is added to stabilize the system. This filter is assumed to be asymptotically stable and its cutoff frequency cannot be too high because of stability and noise considerations [Broberg and Molyet, 1992]. It should be avoided to introduce a high gain at the switching frequency, which would lead to fluctuations in the system. Thenceforth, the plug-in repetitive controller consists of a generator of the reference input, a low-pass filter and a user-defined function. The latter is based on the inverse of the plant model if the plant is a minimum-phase system [Griñó and Costa-Castelló, 2005; García-Cerrada*, et al.*, 2007; Griñó*, et al.*, 2007]. Otherwise other alternatives are explained in [Broberg and Molyet, 1992; Broberg and Molyet, 1994]. Such repetitive control amplifies all harmonics of the input signal, which may lead to a waste of control effort and a reduction of system robustness without improving system performance [Griñó*, et al.*, 2007]. A frequency-adaptive algorithm for the repetitive controller studied in [García-Cerrada*, et al.*, 2007] was analyzed in [Roldán-Pérez*, et al.*, 2011].

A repetitive controller based on the Discrete Cosine Transform (DCT) filter was proposed in [Mattavelli and Marafao, 2004]. The strength of this new implementation is that the specific harmonics to be compensated can be selected by means of an offline calculation of the DCT coefficients, thus eliminating the need for a low-pass filter. Therefore, its complexity is independent of the number of harmonics to be compensated, and it features less sensitivity to rounding and quantization effects which is very well suited to digital implementations. However, the plant model is not taken into account in the design of the plug-in repetitive controller and the consequences are that dynamics of the plant will not be compensated and may affect the control behavior to a larger extent in comparison to other current control techniques.

Another option proposed to try to solve the problem of multiple harmonics amplified by the basic repetitive control is discussed in [Escobar*, et al.*, 2007]. A repetitive controller based on a pure delay line in a negative feedback configuration plus a feedforward path is proposed in this work, which is capable of compensating only the odd harmonics of the input signal. Obviously, this controller also needs a low-pass filter to ensure system stability. Later, the authors improved this scheme to develop a repetitive controller capable of compensating only the typical harmonics in power systems, i.e. those of order $6k \pm 1$ ($k \in \mathbb{Z}$) [Escobar*, et al.*, 2009]. The new repetitive controller was based on two feedback delay paths and a feedforward delay path. This work also delves into the digital implementation of the controller, explaining how to compensate the delay introduced by the low-pass filter and how to avoid potential instabilities due to the infinite gain introduced at the resonant frequencies.

A similar scheme to the above was developed in [Loh*, et al.*, 2008]. It is also based on feedback and feedforward delay paths but it is capable of compensating the harmonics of order $6k$ ($k \in \mathbb{Z}$). Moreover, it is combined with a proportional + resonant controller in

stationary reference frame. The authors of this paper claimed that the basic schemes of [Escobar, *et al.*, 2007], although proven to be effective, still face the complication of unintentional noise amplification caused by its implicit inclusion of an integrator. This is the reason why they made a different use of this "embedded" integrator, proving mathematically that it can be used for compensating all grid harmonic disturbances if the phase angle is synchronized with the distorted grid, including those with frequencies $+(6k-1)f_o$ and $-(6k+1)f_o$ (although at a reduced gain), where f_o is the fundamental frequency.

2.1.2. Calculation of current references.

The calculation of reference currents determines the signals the current control must track, using the measurements in the electrical system [Chang, 2001]. Traditionally, calculation of the current references does not take into account if the PCC voltage is unbalanced or not [Akagi, *et al.*, 2007; Rodríguez, *et al.*, 2009; Yazdani and Iravani, 2010]. That is, the current references generated are always balanced regardless of the state of the grid since the PCC voltage components employed in their calculation are not divided into positive and negative sequence. In some cases this may endanger the stability of the system as it introduces an oscillation in the DC-link voltage and harmonic currents [Kang and Sul, 1997], resulting in poorer performance or even device rupture if protection systems are not properly designed. This situation takes special importance in isolated and weak AC systems, where it is more likely that the PCC voltage is affected by connecting and disconnecting loads, faults in power stations, wind fluctuations, etc.

Active and reactive power references used in the calculation of these current references depend on the power application, and can (i) be set by the grid operator, (ii) depend on the power consumed by the load or (iii) be provided by a high-level controller [Sood, 2004; Pinzón-Ardila, 2007].

2.2. Control of grid-connected converters to perform PCC voltage control.

The control of voltage levels is accomplished by controlling the production, absorption and flow of reactive power at all levels in the system. The generating units provide the basic means of voltage control, although additional means are usually required to control voltage throughout the system [Kundur, 1994]. The possibility of generating or absorbing controllable reactive power with various power electronic switching converters has long been recognized [Schauder, *et al.*, 1997]. Among the devices used for this purpose, those who perform an *active* compensation can be found, i.e. sources or sinks of reactive power such as shunt capacitors, shunt reactors, synchronous condensers and static compensators (STATCOMs). The reactive power absorbed/supplied by them is automatically adjusted so as to maintain voltages of the buses to which they are connected. Together with the generating units, they

establish voltages at specific points in the system [Kundur, 1994].

Unbalances such as magnitude fluctuation and phase deviation are typical in current industrial AC power systems, and the effects of unbalances should be precisely assessed because voltage unbalances produce undesirable power ripple of low order frequencies which result in current harmonics and poor DC-link voltage regulation. Therefore if unbalances are not compensated adequately, larger size of DC-link filter should be used [Kang and Sul, 1997].

Some of the first mathematical analysis of an unbalanced PWM converter were carried out in [Enjeti, *et al.*, 1989; Enjeti and Ziogas, 1990; Moran, *et al.*, 1992]. The work [Enjeti, *et al.*, 1989] also presented a new algorithm to selectivity cancel the generated second harmonic component by suitably counter unbalancing the converter switch gating signals (switching functions). The appearance of such second order harmonic component has been explained by the cross product term between the positive sequence component of the converter PWM switching function and the negative sequence component of the input voltage. But this paper was mainly focused on the theoretical analysis of PWM harmonic patterns and failed to suggest a practical control method.

The work [Vincenti and Jin, 1994] proposed an unbalanced transfer matrix in terms of input phase voltage that was implemented with the positive and negative sequence components of input source. It was presented as a simple feedforward input unbalance correction method. In the work [Kang and Sul, 1997], based on the concept of real time power theory, a counter-unbalancing control strategy was proposed for the unbalanced voltage PWM converter. The proposed algorithm tries to improve the performance of DC-link voltage regulation by eliminating the oscillating part of the line currents.

2.3. Contributions.

The contributions of this Thesis are made in the field of linear cascade systems applied to the control of VSCs connected in shunt mode with the grid through an L-filter, especially in weak grids and in two topics: (i) tracking of grid current harmonics and rejection of grid voltage harmonics, and (ii) control of PCC voltage in an unbalanced condition. For this purpose, contributions in the field of current control and PCC voltage control are made in this Thesis. These contributions are detailed in the following two sections.

2.3.1. Current control.

In first place, an exhaustive theoretical study is made for two techniques for implementing current controllers, namely, resonant control and repetitive control. Basic guidelines for the

tuning of their parameters are provided. Each of these control techniques can be implemented according to different structures, which are analyzed and compared from the viewpoint of selective harmonic compensation, frequency-adaptation and transient response.

Frequency drifts may take place in weak grids, seriously affecting the controller's performance and introducing an error in the reference voltage obtained. Therefore, the frequency-adaptive algorithm corresponding to all the studied control structures is posed. In the case of resonant control, this is a fairly straightforward procedure, whereas in the case of repetitive control the computational burden is considerably high, even when the controller is non-frequency-adaptive. Therefore, special attention has also been given to the implementation of these algorithms in commercial digital platforms, such as digital signal processors (DSPs).

The previous analysis shows the importance of performing a precise synchronization and monitoring of the grid, so that four techniques are reviewed to do so. They are based on a Phase-Locked Loop (PLL), Frequency-Locked Loop (FLL), Kalman Filter (KF) and Extended Kalman Filter (EKF).

Another point that helps improving the controller's performance is the limitation of reference currents before applying them to the current controller. This topic has no greater complication when working with constant references because a simple linear saturator works properly, but this is no longer useful when working sinusoidal references, since a distorted reference would be obtained. Thus, an alternative limitation technique is studied in this Thesis when working with sinusoidal references.

As for the calculation of reference currents for the current controller, traditional techniques always lead to the generation of balanced currents, despite of the state of the grid. Thus, if the grid voltage is unbalanced, a negative sequence will also appear in the grid current with the consequent adverse effects for the elements of the converter. A solution for this problem involves the compensation of the negative sequence of the grid current; hence an unbalanced current reference is needed. Alternative techniques for this calculation are proposed in this Thesis, both in synchronous reference frame (dq-axes) and stationary reference frame ($\alpha\beta$-axes).

Lastly, all current controllers addressed in the Thesis have been tested in the same experimental setup and under the same conditions of power, voltage and current, so that a comparison of their performance can be established. These tests have been classified into three groups, namely, characterization of the transient response, characterization of the steady-state response and behavior under a frequency jump. This allows carrying out a complete comparison of the current controllers that facilitates the specification of the most suitable current controller for each power application. These results will define future work lines and

the conclusions derived from this work.

2.3.2. PCC voltage control.

The presence of an unbalanced voltage at the PCC results in the appearance of a negative sequence current component that deteriorates the control performance. This Thesis proposes a novel voltage controller in synchronous reference frame to compensate an unbalanced PCC voltage by means of a STATCOM, allowing an independent control of both positive and negative voltage sequences. For this purpose, the grid model in case of an unbalanced voltage is obtained, which allows obtaining the plant model to develop the controller and studying its corresponding dynamics and interactions.

3

Control of grid-connected converters

The control of a shunt-connected VSC is usually based on a cascade linear control system due to its benefits, such as independent tuning of each controller and higher robustness to uncertainty. Two levels of control can be differentiated within this control scheme, which are low-level and high-level control. As a previous step to the following chapters, where the study of the current controller and PCC voltage controller is carried out, this chapter shows an overview of the generic control scheme of a VSC connected in shunt with the grid through an L-filter. The two controllers mentioned above can be located within this scheme.

Calculation of reference currents and their limitation are also tackled in this chapter. The proposed matrices allow generating unbalanced currents when a negative sequence is present in the grid current. This possibility was not available in traditional techniques.

Lastly, another topic that is essential for the later study of the current control and the development of frequency-adaptive algorithms is grid synchronization. Furthermore, it is also essential to develop control schemes that are able to work irrespective of the grid nominal frequency, i.e. in $50\ Hz$ or $60\ Hz$ grids. Four methods are discussed and compared by means of simulation results. Two of them have been employed to obtain the experimental results of this Thesis.

Therefore, this chapter addresses a number of issues that are basic to the subsequent development of the remaining chapters.

3.1. Overview of the control of a VSC connected in shunt mode with the grid through an L-filter.

An overview of the general control scheme in *dq*-axes of a VSC connected in shunt with the grid through an L-filter is depicted in Fig. 3.1:

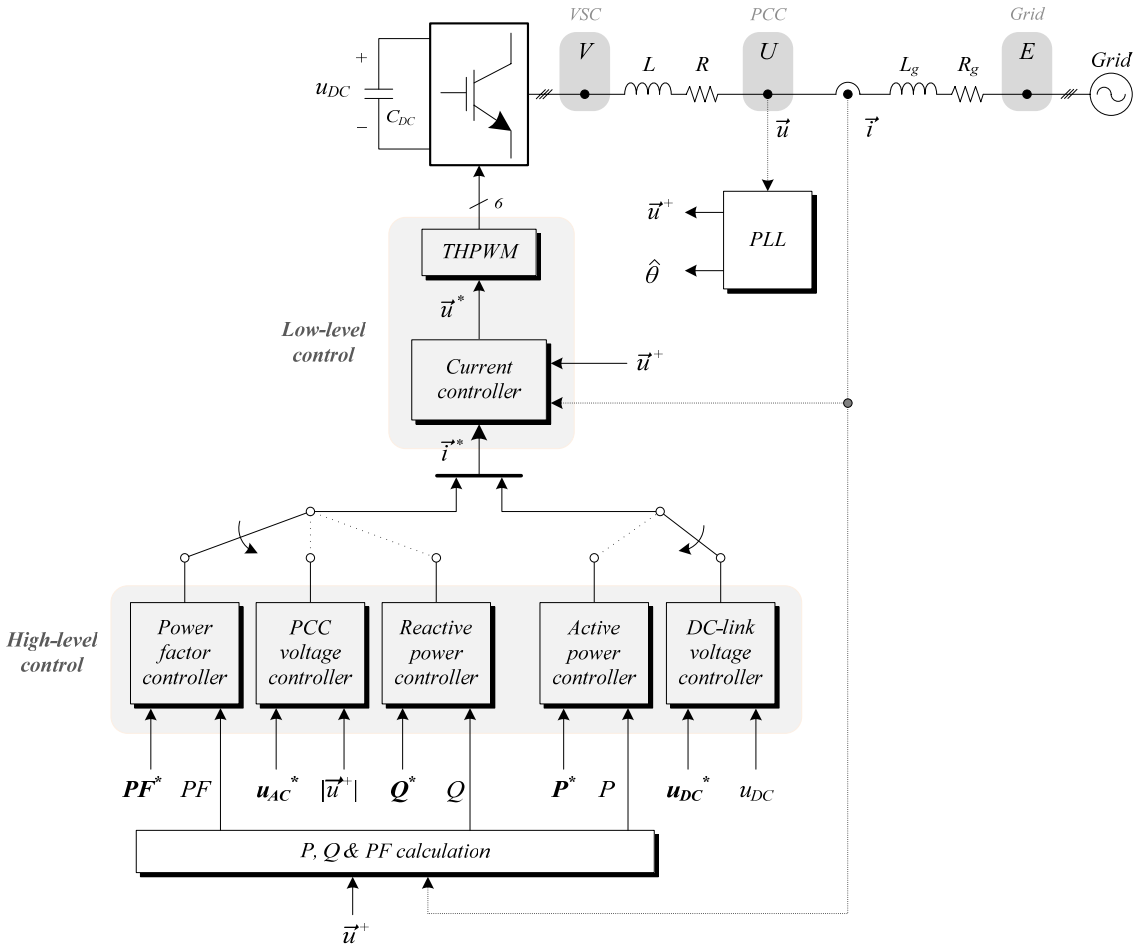

Fig. 3.1. Overview of the general control scheme of a VSC connected in shunt with the grid through an L-filter.

It consists of a cascade control, i.e. the output from one controller is the reference command to another. With this control configuration each controller is usually tuned one at a time with a minimum of modeling effort, their tuning parameters have a direct effect, they tend to be insensitive to uncertainty and the need for control links is reduced [Skogestad and Postlethwaite, 2005].

In this cascade control system, two levels of control can be differentiated:

- *High-level control.*

  It generates the reference currents for the current controller. The high-level controllers can be classified into two groups: active power control and reactive power control. Within the first group, active power controller and DC-link voltage controller can be found; within the second group, reactive power controller, PCC voltage controller and power factor controller are located. Since they work with constant signals, a PI controller is enough to obtain zero steady-state error.

- *Low-level control.*

  It is performed by the current controller and the modulation strategy.

  The current controller receives as inputs the reference currents generated by the high-level control, the grid current, the feedforward of the PCC voltage positive sequence and, optionally, the limited reference voltage to use it in an anti-windup scheme. For the sake of simplicity, the latter has not been included in the scheme of Fig. 3.1. One of the design requirements in cascade control systems is that the settling time of the low-level control must be at least ten times lower than that of the high-level control ($t_s|_L \leq 10 \cdot t_s|_H$, where t_s means settling time and the subscripts $_L$ and $_H$ stand for low-level and high-level controller, respectively). In other words, the low-level controller must be at least ten times faster than the high-level controller, so that the inner controller may be omitted in the design of the outer.

  As for the modulation, one of the most widely utilized strategies for controlling the AC output of power electronic converters is the technique known as Pulse-Width Modulation (PWM), which varies the duty cycle of the converter switches at a high frequency to achieve a target average low-frequency output voltage or current [Holmes and Lipo, 2003].

  A major limitation with the three-phase converter modulation is the reduced maximum peak fundamental output line voltage of $\sqrt{3}\,u_{DC}$ that can be obtained compared to the available DC-link voltage [Holmes and Lipo, 2003]. The converter fundamental line voltage can also be increased by adding a third harmonic component to the three-phase sinusoidal modulating wave without causing overmodulation. Overmodulation is known to produce low-frequency baseband distortion and is to be avoided if possible. This modulation technique is known as Third Harmonic injection PWM (THPWM) [Wu, 2006]. This third harmonic component does not affect the fundamental output line voltage, since the common mode voltages cancel between the phase legs, but it does reduce the peak size of the envelope of each phase leg voltage. A $15\,\%$ increase in modulation index can be achieved by simply including a one-sixth third harmonic injection into the fundamental reference waveforms [Holmes and Lipo, 2003].

  There are other popular modulation techniques, among which is Space Vector Modulation (SVM). An advantage of the SVM is the instantaneous control of switching states and the freedom to select vectors in order to balance the neutral point in a Neutral Point Clamped (NPC) converter. Additionally, one can realize output voltages with almost any average value by using the nearest three vectors, which is the method that results in the best spectral performance [Celanovic, 2000].

Other important parts of the control scheme are:

- *Grid synchronization and monitoring.*

  Grid synchronization is an important and necessary task, linked to the converter control due to the need to synchronize the delivery of the desired power with that in the power system. Under certain circumstances, a jump in the grid phase angle may occur, requiring a quick and accurate detection of the phase angle for reliable power delivery. Moreover, during grid faults, especially unbalanced faults, the negative sequence component of the voltage influences the phase angle detection, leading to an oscillation at a frequency twice the fundamental in the estimated phase angle. Therefore, the algorithm in charge of detecting the grid phase angle needs to be robust under disturbances.

  Due to the demands on the limit values of voltage and frequency published in the grid codes, grid monitoring plays an important role in deciding when to disconnect the generation system from the grid. In the same way as a synchronization algorithm, a monitoring algorithm may also be affected by grid perturbations, giving erroneous values to the control and, thus, leading to an undesired tripping.

  Nowadays, the most used technique is the PLL, which is further studied in section 3.5.1.

This general control scheme can suffer variations depending on the application, but it shows the basic controllers that can be found in any practical case. For example, the control of a STATCOM does not perform an active power control, since the active power is already controlled by the DC-link voltage control. Even the calculation of reference currents can be accomplished in different ways, as will be explained in section 3.2. The active and reactive power references can be set by the operator or be dependent on other parameters, such as grid codes, load power (like in APFs), etc.

3.1.1. Active power control.

3.1.1.1. Active power controller.

The block diagram of the active power controller is shown in Fig. 3.2. The proportional constant of the PI controller is related to the transformation of active power to active current reference, whereas the integral constant helps achieve zero steady-state error in the event of model mismatch and disturbances. Therefore, the parameter tuning is focused on settling time and controller bandwidth.

In many cases, this controller is omitted and the active current reference is calculated by a

simple division. However, in certain applications it is necessary to ensure that, in the face of a change in the active power, the new current reference will reach steady-state within a predetermined maximum time and with certain characteristics in regard to transient response. The active power controller is responsible for such performance.

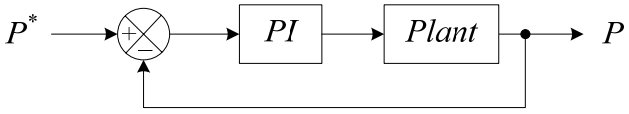

Fig. 3.2. Active power controller.

3.1.1.2. DC-link voltage controller.

The DC-link is modeled as an ideal capacitor. Fig. 3.3 represents the dynamic equivalent circuit of the DC-link [Bueno, 2005].

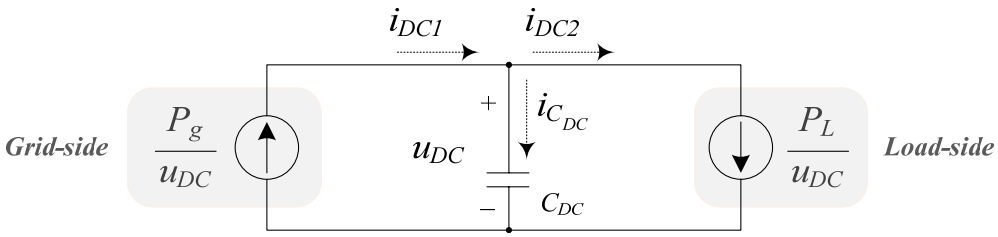

Fig. 3.3. Dynamic equivalent circuit of the DC-link.

The DC-link model based on the energy stored in the capacitor has been used. The temporal drift of the energy stored in the capacitor is equal to the instantaneous subtraction of the grid power and load power with the energy transfer signs shown in Fig. 3.3. This is expressed as:

$$\frac{1}{2}C_{DC}\frac{du_{DC}^2}{dt} = P_g - P_L = u_q i_q - P_L \tag{3.1}$$

To transform the above equation into a first order system a new variable $W = u_{DC}^2$ is introduced [Ottersten, 2003], obtaining the expression:

$$\frac{1}{2}C_{DC}\frac{dW}{dt} = u_q i_q - P_L \tag{3.2}$$

which is a linear differential equation that describes the behavior of the system in Fig. 3.3. From this, it is possible to perform a linear control of the DC-link voltage for a VSC

connected to the grid through an L-filter or LCL-filter using the energy stored in the capacitor as control variable [Hur*, et al.*, 2001; Ottersten, 2003]. Therefore, a controller for W is sought.

The plant transfer function of (3.2) in continuous time is given by:

$$G_{DC}(s) = \frac{W}{i_q}(s) = \frac{2u_q}{sC_{DC}} \tag{3.3}$$

and its corresponding block diagram is shown in Fig. 3.4. The value and sign of P_L depends on the type of load that is connected to the DC-link of the VSC. Because of this, P_L is considered a perturbation in the design of the controller.

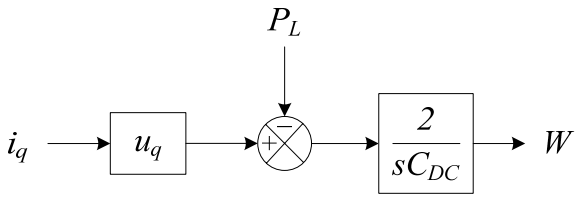

Fig. 3.4. Plant transfer function of the DC-link voltage controller in continuous time, using the model based on the energy stored in the DC-link capacitor.

Nevertheless, the PCC voltage u_q may suffer variations under grid perturbations; therefore it is not desirable to have it in the plant model. To solve this, a division by u_q is placed before the plant model and the tuning is carried out without taking into account this parameter in (3.3).

The DC-link voltage controller only needs information about the error on u_{DC}^2 to generate the reference i_q^*. As mentioned before, it consists of a PI controller and its parameters are tuned without taking into account the inner current controller. To do so, the Zero-Order Hold (ZOH) method has been applied to the plant to obtain its discrete time version:

$$G_{DC}(z) = \frac{2T_s}{C_{DC}(z-1)} \tag{3.4}$$

The PI controller can be expressed in pole-zero form as:

$$C(z) = k_{P_{DC}} \frac{z-\alpha}{z-1} \tag{3.5}$$

where $\alpha = 1 - \left(k_{I_{DC}} T_s / k_{P_{DC}}\right)$, $k_{P_{DC}}$ is the proportional gain and $k_{I_{DC}}$ is the integral gain. The open-loop transfer function has two poles placed at $z_p = 1$ and a zero placed at $z_z = \alpha$. Depending of the controller gain, the closed loop system $G_{CL}(z)$ can have two conjugate poles as shown. In this case, the general form of the denominator polynomial of $G_{CL}(z)$ is:

$$den\{G_{CL}(z)\} = \left(z - \rho e^{j\vartheta}\right)\left(z - \rho e^{-j\vartheta}\right) = z^2 - (2\rho\, cos\, \vartheta)z + \rho^2 \tag{3.6}$$

where $\rho = e^{-\xi\omega_n T_s}$, $\vartheta = \omega_n T_s\sqrt{1-\xi^2}$, ω_n is the natural pulsation and ξ is the damping coefficient. To avoid a large overvoltage in u_{DC}, the damping coefficient has to be chosen as $\xi \geq 1/\sqrt{2}$. From settling time and damping coefficient values, ω_n can be calculated with the expression $t_s \approx 4.6/\xi\omega_n$ for a second order system. To verify these conditions, $k_{P_{DC}}$ and α have to take the next values:

$$k_{P_{DC}} = \frac{(1-\rho\cos\vartheta)C_{DC}}{T_s} \tag{3.7}$$

$$\alpha = \frac{1-\rho^2}{2(1-\rho\cos\vartheta)} \tag{3.8}$$

and then $k_{I_{DC}} = (1-\alpha)k_{P_{DC}}/T_s$.

3.1.2. Reactive power control.

3.1.2.1. Reactive power controller.

The block diagram of the reactive power controller is shown in Fig. 3.5. Analogously to the active power controller, the reactive power controller is not used in many cases and the reactive current reference is calculated with a division. However, in certain applications it is necessary to ensure that, in the face of a change in the reactive power, the new current reference will reach steady-state within a predetermined maximum time and with certain characteristics in regard to transient response. The reactive power controller is responsible for such performance.

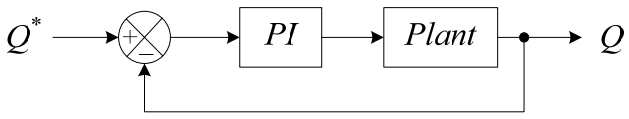

Fig. 3.5. Reactive power controller.

3.1.2.2. PCC voltage controller.

PCC voltage control is one of the main tasks in power applications like STATCOMs. PCC voltage may suffer large variations in weak grids due to the non-negligible value of its grid impedance, thus affecting other devices connected to the same grid with possible harmful

consequences. Therefore, the control of PCC voltage is a topic of paramount importance in weak grids. This voltage control is usually applied to the root mean square (RMS) value of the PCC voltage, without distinguishing between positive and negative sequence. This Thesis proposes a PCC voltage controller in chapter 6 that controls independently both sequences, so that the consequences of having a negative sequence flowing through the power system can be minimized.

3.1.2.3. Power factor controller.

A very important aspect of the systems connected to the grid is to select a proper power factor according to the grid demands [Hassaine*, et al.*, 2009]. The most efficient systems are those that allow variations in the active and reactive power injected into the grid, depending on the power grid requirements [Barbosa*, et al.*, 1998; Huang and Pai, 2001; Wu*, et al.*, 2005]. A unity power factor is desired in many power electronics applications, being the power factor controller in charge of such achievement.

3.1.3. Current controller.

Current control can be performed according to different control techniques. Two of the currently most used techniques are tackled in this thesis, namely, resonant control and repetitive control. Such techniques are studied in depth in chapters 4 and 5, respectively, where their possible implementations are studied, their main features are analyzed and their frequency-adaptive algorithm is developed.

Besides, the current control scheme can be implemented in two types of reference frames: stationary reference frame ($\alpha\beta$-axes) or synchronous reference frame (dq-axes). The first one deals with sinusoidal signals, whereas the second one deals with constant signals. Each of them has its own advantages and drawbacks, which can be categorized as follows:

- *Computational burden.*

  It is similar in both cases, considering that $dq \rightarrow \alpha\beta$ and $\alpha\beta \rightarrow dq$ transformations are employed in both schemes. PCC voltage always has to be converted to dq-axes in order to use it in the grid synchronization algorithm.

- *Feedforward of the PCC voltage.*

  A feedforward of the PCC voltage is added to the output of the current controller, i.e. to the reference voltage for the modulator, so that the initial transient of the current controller (at the start-up of the control system) is minimized, the windup of the integrators is avoided and, this way, the control system remains stable. This feedforward can be either the PCC voltage positive sequence (which is obtained

from a SRF-PLL) or simply the total PCC voltage in *dq*-axes. Two case scenarios can be distinguished to explain the effect of this feedforward: a VSC interfaced with (i) a stiff grid and (ii) a weak grid.

If the VSC is interfaced with a stiff grid, it has been proved that the PLL dynamics are decoupled from those of the rest of the system and the operating point [Yazdani and Iravani, 2010]; therefore, the fact of applying a feedforward of the PCC voltage positive sequence to the current controller does not alter its dynamics, irrespective of the reference frame.

If the VSC is interfaced with a weak grid, the dynamic response of the PLL includes transient components that are functions of the grid current [Yazdani and Iravani, 2010]. In *αβ*-axes, $\vec{u}_{\alpha\beta}^{+}$ it is obtained by transforming the PCC voltage from *abc* to *αβ*-axes and applying a sequence detection algorithm, which depends on the estimated grid frequency. In *dq*-axes, in order to obtain $\vec{u}_{dq}^{+}$ it is necessary to transform $\vec{u}_{\alpha\beta}^{+}$ to *dq*-axes, making use of the phase angle estimated by the PLL. This situation does not influence the steady-state operation of the current controller, not even the start-up of the control system since all input signals are blocked until the PLL is phase-locked, but it takes special importance in case of grid disturbances such as voltage dips.

- *Calculation of reference currents.*

  A current controller implemented in *αβ*-axes facilitates the calculation of reference currents to compensate certain effects in the DC-link of the converter, such as oscillations due to unbalanced grid voltages. Moreover, it is able to remove unwanted currents generated by the oscillating part of the reactive power $(\tilde{q})$. These issues are further detailed in section 3.2.

- *Limitation of reference currents.*

  It is easier to limit constant references with the use of a linear saturator. But the fact of working in *dq*-axes does not always entail working with constant references, as in the case of harmonic compensation. When limiting a sinusoidal reference, a special care has to be taken to not linearly saturate it, which would lead to the appearance of high-order harmonics. Therefore, the limitation in *αβ*-axes or *dq*-axes is quite similar when the references are not constant. This topic is addressed in section 3.3.

- *Anti-windup mechanism.*

  The same scheme is used in both reference frames. A linear saturator is applied to the reference voltage, and the subtraction of the limited and non-limited reference is added to the integral path of the controller that compensates the lowest-order harmonic. For instance, this is the PI controller in a current controller in *dq*-axes.

- *Negative sequence compensation.*

  Resonant controllers are able to compensate both positive and negative sequence of its input signal, whereas repetitive controllers either compensate a certain set of harmonics or can be designed to compensate the desired harmonics. Grid disturbances like unbalanced voltages introduce negative sequence in the PCC voltage, i.e. an harmonic of order $h = -1$.

  Regarding resonant control, a current controller developed in *αβ*-axes is able to compensate this negative sequence by means of the resonant controller tuned at ω_1. On the contrary, a current controller developed in *dq*-axes needs an extra resonant controller tuned at $2\omega_1$ to compensate it (the harmonic of order -1 turns into order $+2$ after applying a transformation to positive *dq*-axes), thus increasing the computational burden and reducing the stability margins.

  As for repetitive control, each implementation compensates a different set of harmonics. For instance, some of them compensate harmonics of order $6k$ ($k \in \mathbb{Z}$, so that they are unable to track or reject the negative sequence; others compensate harmonics order $6k \pm 1$, therefore they already include a resonant gain at $h = -1$; and, finally, other repetitive controllers compensate a set of user-defined harmonics without increasing the controller complexity, which make them suitable for a wider range of applications.

- *Behavior under frequency variations.*

  A current controller working in *αβ*-axes is more sensitive to frequency variations than that in *dq*-axes when it comes to the tracking of the fundamental component, which is the component of higher level. The reason is that the calculation of reference currents in *dq*-axes involves the use of the PCC voltage phase angle, thus adapting them to the grid frequency. For example, Fig. 3.6 shows the result of applying a frequency jump from 50 to $51.5\ Hz$ at $t = 1\ s$ and from 51.5 to $50\ Hz$ at $t = 1.5\ s$ to two different controllers: (i) a SOGI tuned at $h = 1$ implemented in *αβ*-axes (left column) and (ii) a PI controller implemented in *dq*-axes (right column). The reference currents in *abc*-axes are three sinusoidal signals with amplitude $1\ p.u.$, subsequently transformed to *αβ* and *dq*-axes. The errors obtained in *αβ*-axes (ε_α and ε_β) reach a level of $0.5\ p.u.$, whereas the errors in *dq*-axes (ε_d and ε_q) are almost negligible, with the exception of the transients.

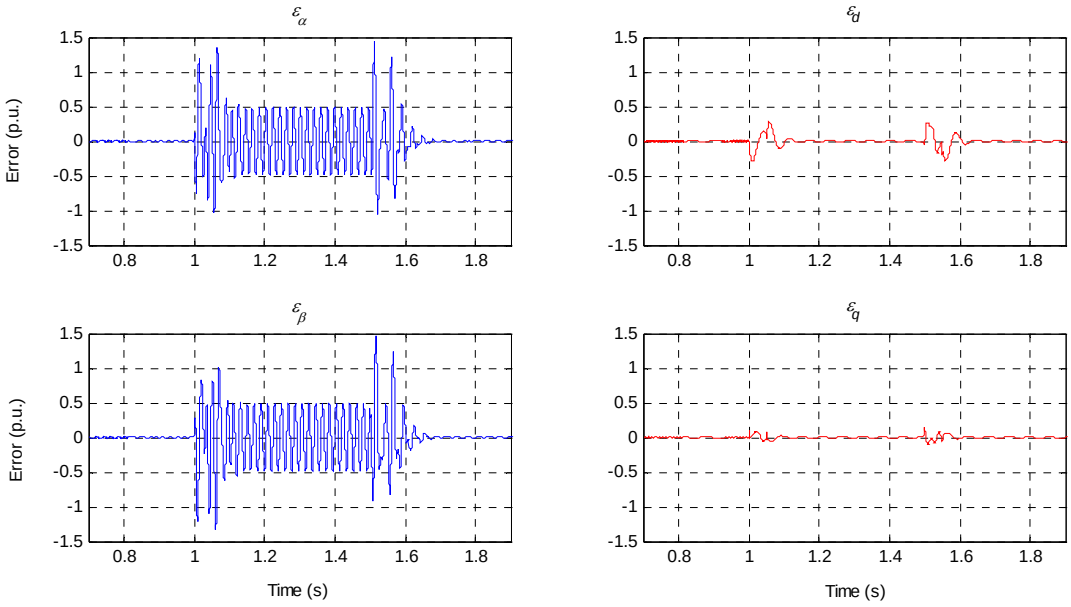

Fig. 3.6. Error signals obtained after applying a frequency jump from 50 to 51.5 Hz at $t = 1\ s$ and from 51.5 to 50 Hz at $t = 1.5\ s$ to two different controllers: (a) a SOGI tuned at $h = 1$ implemented in $\alpha\beta$-axes and (b) a PI controller implemented in dq-axes (right column).

A correct and accurate plant model is necessary to design, tune and simulate a current controller, as a previous step to its implementation in a digital platform. Two options are available when designing the current control of a VSC connected in shunt with the grid through an L-filter, whose block diagrams in dq-axes and $\alpha\beta$-axes are shown in Fig. 3.7 and Fig. 3.8, respectively.

The first one (Fig. 3.7) is the traditional and widely used transfer function for a VSC connected to the grid through an L-filter, $G(s) = 1/(R + Ls)$, where L is the filter inductance and R is the parasitic resistance, plus the PCC voltage and the cross-coupling between axes. The PWM converter reference ($u^*_{\alpha\beta}$ or u^*_{dq}) is kept constant over each sampling interval, so the power converter can be assumed to be a ZOH circuit. Therefore, the inductive filter discrete time model should be obtained through the ZOH method [Sedighy, *et al.*, 2000; Akagi, *et al.*, 2007].

The second one (Fig. 3.8) is based on the previous scheme, and a feedback loop with a PI controller has been added in order to increase the system speed [Malo and Griñó, 2008]. In both cases, the block z^{-1} represents the computational delay associated to the control implementation on the digital platform.

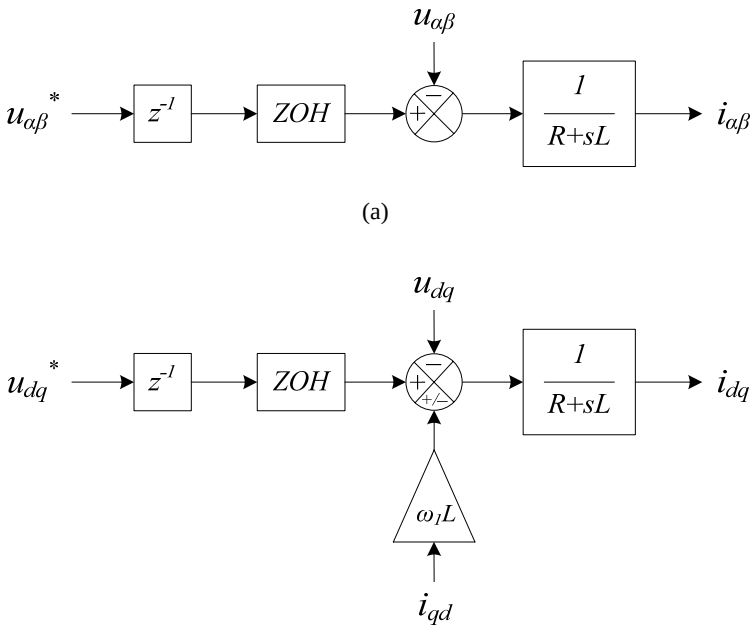

Fig. 3.7. Traditional plant model (a) in *αβ*-axes and (b) in *dq*-axes.

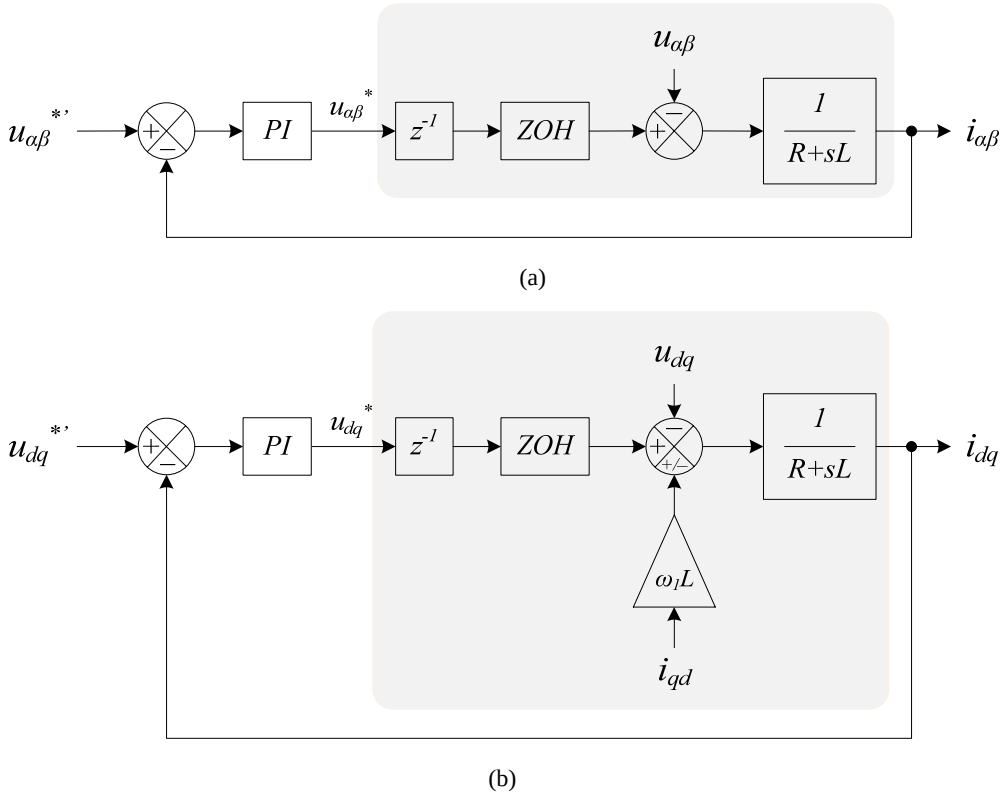

Fig. 3.8. Modified plant model including a feedback loop with a PI controller (a) in *αβ*-axes and (b) in *dq*-axes.

The problem with the second model is that the magnitude in the Bode diagram of the open-loop transfer function (including the current controller) shows less attenuation at the non-resonant frequencies than the first model. Ideally, this should not be a major drawback when working with nonlinear loads since only harmonics of order $6k \pm 1$ ($k \in \mathbb{Z}$) would appear, but the truth is that the rest of harmonics are very low but not exactly zero. This leads to a slightly higher steady-state error, although the settling time is lower.

Therefore, if constraints regarding settling time are very restrictive, a reduction over 30% in the settling time can be achieved by means of the second plant model [Rodríguez*, et al.*, 2012]. On the other hand, if these specifications are more flexible and a more accurate performance is required, the first plant model is the desired one. This last case is tackled in this Thesis.

3.2. Current control.

3.2.1. Calculation of reference currents in case of unbalanced grid conditions.

To date, the method of calculation of reference currents in a grid-connected VSC always led to the generation of balanced currents, independently of the grid state. This method may lead to problems when an unbalance in the PCC voltage occurs. In particular, a harmful oscillation in the DC-link voltage appears when the grid voltage is composed of both positive and negative sequence that can damage system components and even destabilize the system.

To solve this, it is necessary to perform a decomposition of the voltages and currents on positive and negative sequence, so that the level of each sequence of the reference currents is appropriate. This methodology is developed both in $\alpha\beta$ and dq-axes, analyzing their characteristics and comparing their performance by means of simulation results. To do so, a case scenario with a STATCOM of nominal power $100\ kVA$ connected to the grid through an L-filter and no load connected to the PCC has been considered. The reactive power reference has been set to $Q^* = 25\ kVAr$. An ideal grid voltage with $20\ \%$ of negative sequence and harmonic 5^{th} and 7^{th} as depicted in Fig. 3.9 has been applied in the simulations, being the grid impedance parameters $L_g = 0.1\ mH$ and $R_g = 0.5\ m\Omega$.

As stated in the comparison of current control in $\alpha\beta$ and dq-axes carried out in section 3.1.3, the best choice to compensate the negative sequence is a resonant controller tuned at the grid fundamental frequency and implemented in $\alpha\beta$-axes, since it compensates both positive and negative sequences of its input signal. Thus, this current control scheme has been used to compare the effects of applying each of the methods of calculation of reference currents described in the next sections.

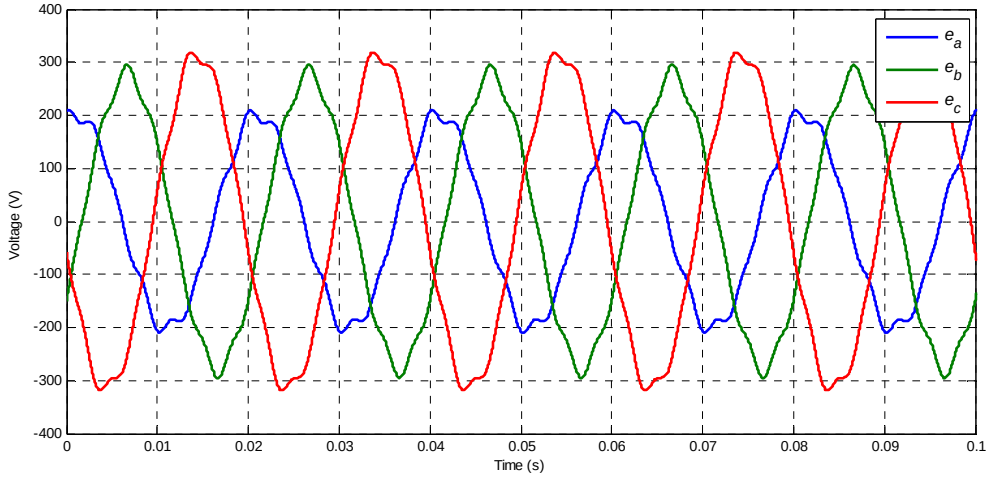

Fig. 3.9. Ideal grid voltage used in simulation to test the methods of calculation of reference currents.

3.2.1.1. Stationary reference frame (*αβ*-axes).

The traditional method of calculation of reference currents in *αβ*-axes is described by (3.9). From now on, this method will be called *αβ_2×2*, since the matrix of voltages has dimension *2×2*. The block diagram of this calculation method connected to the current controller is shown in Fig. 3.10. The limitation of references may be included, both in current and voltage references. The limitation of $u^*_{\alpha\beta}$ would be applied to the current controller to use it in an anti-windup scheme. In a general case when no load is connected to the PCC, this method always gives rise to balanced currents even if the PCC voltage is unbalanced.

$$\begin{bmatrix} i^*_\alpha \\ i^*_\beta \end{bmatrix} = \frac{1}{(u^+_\alpha)^2 + (u^+_\beta)^2} \begin{bmatrix} u^+_\alpha & u^+_\beta \\ u^+_\beta & -u^+_\alpha \end{bmatrix} \begin{bmatrix} P^* \\ Q^* \end{bmatrix} \tag{3.9}$$

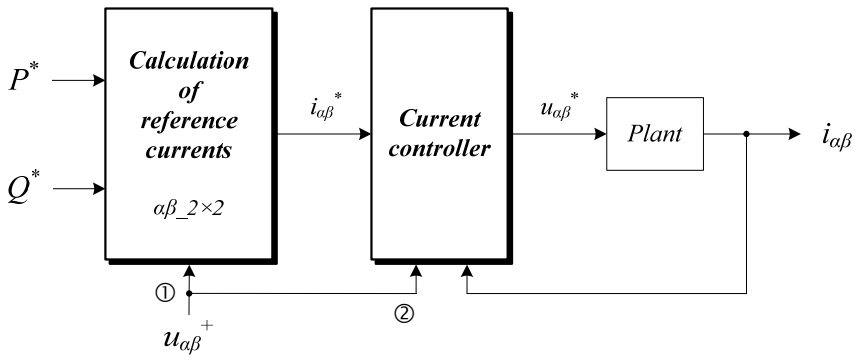

Fig. 3.10. Calculation of reference currents based on *αβ_2×2* connected to the current controller.

In the current control scheme depicted above and in the following, the voltage employed in the calculation of reference currents is always the PCC voltage positive sequence. When the

grid voltage is balanced, the positive sequence matches the PCC voltage, i.e. $\vec{u}_{\alpha\beta} \equiv \vec{u}^{+}_{\alpha\beta}$. Therefore, in steady-state operation there is no difference between using $\vec{u}_{\alpha\beta}$ or $\vec{u}^{+}_{\alpha\beta}$ if the grid voltage is balanced.

However, the PCC voltage can be decomposed into positive and negative sequences when there is an unbalance. Fig. 3.11 shows its corresponding simulation results after applying different combinations of $\vec{u}_{\alpha\beta}$ and $\vec{u}^{+}_{\alpha\beta}$ to the calculation of reference currents in (3.9) (marked as ① in Fig. 3.10) and to the feedforward of the PCC voltage in the current controller (marked as ② in Fig. 3.10). The time intervals corresponding to each combination are indicated below the figure. This figure reveals that the only combinations that work well are when are applying the PCC voltage positive sequence in ①, since the other combinations give rise to distorted reference currents (Fig. 3.11a) and distorted grid current (3.11c). There is always an oscillation in the DC-link voltage (Fig. 3.11b).

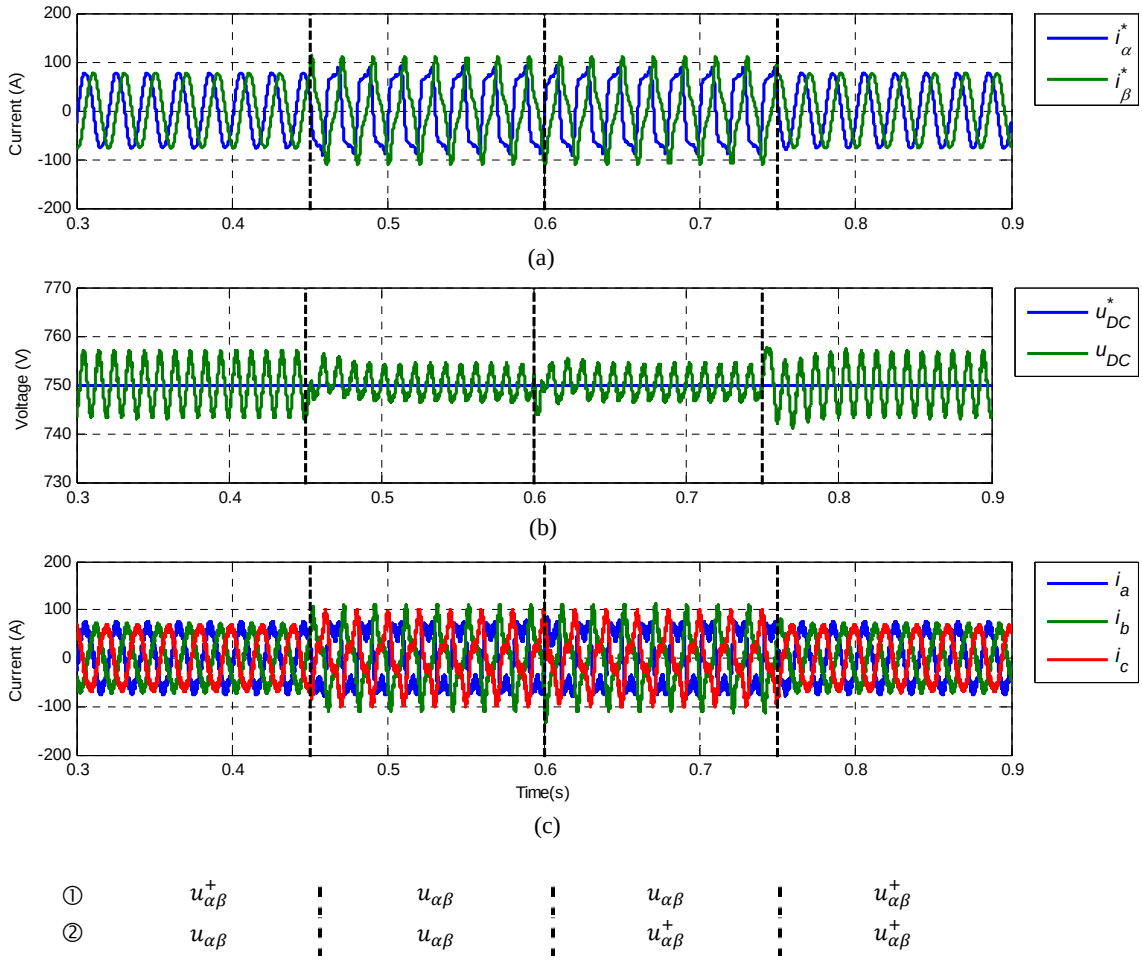

Fig. 3.11. Simulation results calculating the reference currents by means of *αβ_2×2*. Different combinations of PCC voltage are used in the calculation of reference currents (marked as ① in Fig. 3.10) and in the feedforward of the PCC voltage in the current controller (marked as ②). (a) Reference currents in *αβ*-axes; (b) DC-link voltage and its reference; (c) grid current.

To justify the following method of calculating reference currents, the apparent power in $\alpha\beta$-axes is expressed in (3.10), decomposing both voltages and currents in their respective positive and negative sequences.

$$\begin{aligned}\vec{S} &= \left(\vec{u}^{+}_{\alpha\beta} + \vec{u}^{-}_{\alpha\beta}\right) \cdot conj\left(\vec{i}^{+}_{\alpha\beta} + \vec{i}^{-}_{\alpha\beta}\right) \\ &= \left(u^{+}_{\alpha} + ju^{+}_{\beta} + u^{-}_{\alpha} + ju^{-}_{\beta}\right) \cdot \left(i^{+}_{\alpha} - ji^{+}_{b} + i^{-}_{\alpha} - ji^{-}_{\beta}\right)\end{aligned} \tag{3.10}$$

The terms obtained after operating on (3.10) can be grouped as shown in (3.11), where P_0 is the constant active power, Q_0 is the constant reactive power, and $P_{2\omega}$ and $Q_{2\omega}$ are two terms corresponding to the oscillation of P and Q at twice the fundamental frequency. The value of these terms is shown in Table 3.1. It clearly shows that, if there is not negative sequence, the oscillating terms $P_{2\omega}$ and $Q_{2\omega}$ are null.

$$\vec{S} = P_0 + P_{2\omega} + j(Q_0 + Q_{2\omega}) \tag{3.11}$$

TABLE 3.1. COMPONENTS OF $\vec{S}$ IN $\alpha\beta$-AXES.

Active power	
$\boldsymbol{P_0}$	$u^{+}_{\alpha}i^{+}_{\alpha} + u^{+}_{\beta}i^{+}_{\beta} + u^{-}_{\alpha}i^{-}_{\alpha} + u^{-}_{\beta}i^{-}_{\beta}$
$\boldsymbol{P_{2\omega}}$	$u^{+}_{\alpha}i^{-}_{\alpha} + u^{+}_{\beta}i^{-}_{\beta} + u^{-}_{\alpha}i^{+}_{\alpha} + u^{-}_{\beta}i^{+}_{\beta}$
Reactive power	
$\boldsymbol{Q_0}$	$-u^{+}_{\alpha}i^{+}_{\beta} + u^{+}_{\beta}i^{+}_{\alpha} - u^{-}_{\alpha}i^{-}_{\beta} + u^{-}_{\beta}i^{-}_{\alpha}$
$\boldsymbol{Q_{2\omega}}$	$-u^{+}_{\alpha}i^{-}_{\beta} + u^{+}_{\beta}i^{-}_{\alpha} - u^{-}_{\alpha}i^{+}_{\beta} + u^{-}_{\beta}i^{+}_{\alpha}$

Table 3.1 can be rearranged in matrix form as shown in (3.12):

$$\begin{bmatrix} P_0 \\ Q_0 \\ P_{2\omega} \\ Q_{2\omega} \end{bmatrix} = \begin{bmatrix} u^{+}_{\alpha} & u^{+}_{\beta} & u^{-}_{\alpha} & u^{-}_{\beta} \\ u^{+}_{\beta} & -u^{+}_{\alpha} & u^{-}_{\beta} & -u^{-}_{\alpha} \\ u^{-}_{\alpha} & u^{-}_{\beta} & u^{+}_{\alpha} & u^{+}_{\beta} \\ u^{-}_{\beta} & -u^{-}_{\alpha} & u^{+}_{\beta} & -u^{+}_{\alpha} \end{bmatrix} \cdot \begin{bmatrix} i^{+}_{\alpha} \\ i^{+}_{\beta} \\ i^{-}_{\alpha} \\ i^{-}_{\beta} \end{bmatrix} \tag{3.12}$$

Positive and negative sequence currents are calculated as shown in (3.13) (canceling the oscillating components $P_{2\omega}$ and $Q_{2\omega}$, and applying the references P^* and Q^*), to finally calculate the reference currents in accordance with (3.14).

$$\begin{bmatrix} i_\alpha^+ \\ i_\beta^+ \\ i_\alpha^- \\ i_\beta^- \end{bmatrix} = \begin{bmatrix} u_\alpha^+ & u_\beta^+ & u_\alpha^- & u_\beta^- \\ u_\beta^+ & -u_\alpha^+ & u_\beta^- & -u_\alpha^- \\ u_\alpha^- & u_\beta^- & u_\alpha^+ & u_\beta^+ \\ u_\beta^- & -u_\alpha^- & u_\beta^+ & -u_\alpha^+ \end{bmatrix}^{-1} \cdot \begin{bmatrix} P^* \\ Q^* \\ 0 \\ 0 \end{bmatrix} \tag{3.13}$$

$$\begin{bmatrix} i_\alpha^* \\ i_\beta^* \end{bmatrix} = \begin{bmatrix} i_\alpha^+ + i_\alpha^- \\ i_\beta^+ + i_\beta^- \end{bmatrix} \tag{3.14}$$

Calculating the inverse of a square matrix of order 4 as the one shown in (3.13) is not so straightforward, even more considering the implications of its digital implementation. Nevertheless, by means of symbolic computation software it is possible to obtain directly the equations for the calculation of the reference currents, which are shown in (3.15) and (3.16).

$$\begin{bmatrix} i_\alpha^+ \\ i_\beta^+ \\ i_\alpha^- \\ i_\beta^- \end{bmatrix} = \begin{bmatrix} a_0 & a_1 \\ a_1 & -a_0 \\ b_0 & b_1 \\ b_1 & -b_0 \end{bmatrix} \cdot \begin{bmatrix} P^* \\ Q^* \end{bmatrix}$$

$$\begin{aligned} a_0 &= (u_\alpha^+)^3 - u_\alpha^+ (u_\alpha^-)^2 + u_\alpha^+ \left(u_\beta^+\right)^2 + u_\alpha^+ \left(u_\beta^-\right)^2 - 2u_\alpha^- u_\beta^+ u_\beta^- \\ a_1 &= \left(u_\beta^+\right)^3 + (u_\alpha^+)^2 u_\beta^+ + (u_\alpha^-)^2 u_\beta^+ - \left(u_\beta^-\right)^2 u_\beta^+ - 2u_\alpha^+ u_\alpha^- u_\beta^- \\ b_0 &= (u_\alpha^-)^3 - (u_\alpha^+)^2 u_\alpha^- + u_\alpha^- \left(u_\beta^+\right)^2 + u_\alpha^- \left(u_\beta^-\right)^2 - 2u_\alpha^+ u_\beta^+ u_\beta^- \\ b_1 &= \left(u_\beta^-\right)^3 - (u_\alpha^+)^2 u_\beta^- + (u_\alpha^-)^2 u_\beta^- + \left(u_\beta^+\right)^2 u_\beta^- - 2u_\alpha^+ u_\alpha^- u_\beta^+ \end{aligned} \tag{3.15}$$

$$\begin{bmatrix} i_\alpha^* \\ i_\beta^* \end{bmatrix} = \frac{1}{k} \cdot \begin{bmatrix} i_\alpha^+ + i_\alpha^- \\ i_\beta^+ + i_\beta^- \end{bmatrix}$$

$$\begin{aligned} k = {} & (u_\alpha^+)^4 + (u_\alpha^-)^4 + \left(u_\beta^+\right)^4 + \left(u_\beta^-\right)^4 - 2(u_\alpha^+)^2 (u_\alpha^-)^2 + 2(u_\alpha^+)^2 \left(u_\beta^+\right)^2 \\ & + 2(u_\alpha^+)^2 \left(u_\beta^-\right)^2 + 2(u_\alpha^-)^2 \left(u_\beta^+\right)^2 + 2(u_\alpha^-)^2 \left(u_\beta^-\right)^2 + 2\left(u_\beta^+\right)^2 \left(u_\beta^-\right)^2 \\ & - 8u_\alpha^+ u_\alpha^- u_\beta^+ u_\beta^- \end{aligned} \tag{3.16}$$

From now on, this method will be called *αβ_4×4*, since the matrix of voltages in (3.13) has dimension *4×4*. The block diagram of this calculation method connected to the current controller is shown in Fig. 3.12. In a general case when no load is connected to the PCC and under unbalanced conditions, this method leads to an unbalanced current.

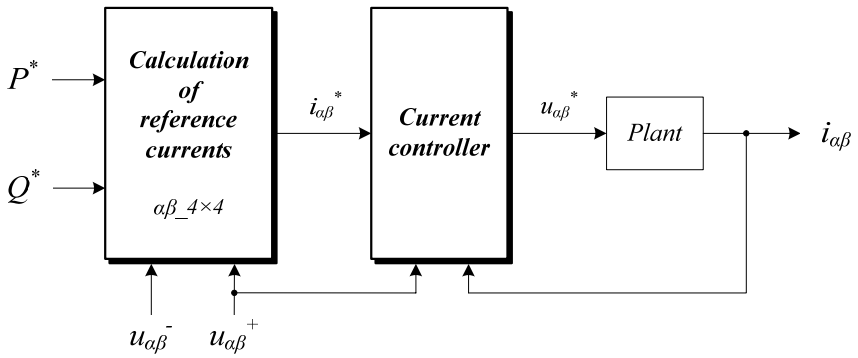

Fig. 3.12. Calculation of reference currents based on *αβ_4×4* connected to the current controller.

3.2.1.2. Synchronous reference frame (*dq*-axes).

The traditional method of calculating reference currents in *dq*-axes is described by (3.17). Henceforth, this method will be called *dq_2×2*. The block diagram corresponding to its connection to the current controller is shown in Fig. 3.13. In a general case when no load is connected to the PCC, this method always results in balanced currents, irrespective of the balanced or unbalanced condition of the grid voltage.

$$\begin{bmatrix} i_d^* \\ i_q^* \end{bmatrix} = \begin{bmatrix} 0 & 1/u_q^+ \\ 1/u_q^+ & 0 \end{bmatrix} \begin{bmatrix} P^* \\ Q^* \end{bmatrix} \tag{3.17}$$

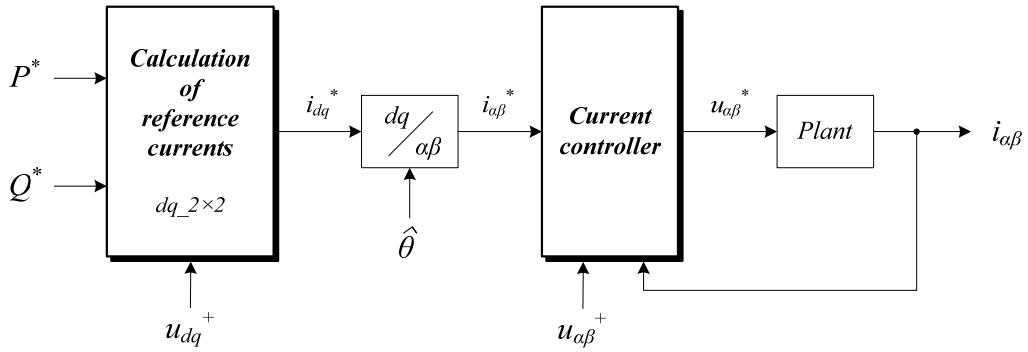

Fig. 3.13. Calculation of reference currents based on *dq_2×2* connected to the current controller.

Similarly to what was done in the previous section in *αβ*-axes and to justify the following calculation method, called *dq_4×4* in this Thesis, the apparent power in *dq*-axes is expressed in (3.18), decomposing both voltages and currents in their respective positive and negative sequences. In this equation, P_0 is the constant active power, Q_0 is the constant reactive power and the terms due to the unbalanced voltage are split into two parts, one corresponding to the terms with cosine ($P_{2\omega(c)}$ and $Q_{2\omega(c)}$) and another with sine ($P_{2\omega(s)}$ and $Q_{2\omega(s)}$). The real power exchanged between the VSC and the grid sets the DC-link voltage, u_{DC}. To keep u_{DC}

constant, the terms $P_{2\omega(c)}$ and $P_{2\omega(s)}$ must be zero. The expressions of all these terms are collected in Table 3.2.

$$\begin{aligned}\vec{S} &= \left(\vec{u}_{dq}^{+}e^{j\omega_1 t} + \vec{u}_{dq}^{-}e^{-j\omega_1 t}\right)\cdot conj\left(\vec{i}_{dq}^{+}e^{j\omega_1 t} + \vec{i}_{dq}^{-}e^{-j\omega_1 t}\right)\\ &= \left(P_0 + P_{2\omega(c)}\,cos(2\omega_1 t) + P_{2\omega(s)}\,sin(2\omega_1 t)\right)\\ &+ j\left(Q_0 + Q_{2\omega(c)}\,cos(2\omega_1 t) + Q_{2\omega(s)}\,sin(2\omega_1 t)\right)\end{aligned} \tag{3.18}$$

TABLE 3.2. COMPONENTS OF $\vec{S}$ IN dq-AXES.

Active power	
$\boldsymbol{P_0}$	$u_d^+ i_d^+ + u_q^+ i_q^+ + u_d^- i_d^- + u_q^- i_q^-$
$\boldsymbol{P_{2\omega(c)}}$	$u_d^- i_d^+ + u_q^- i_q^+ + u_d^+ i_d^- + u_q^+ i_q^-$
$\boldsymbol{P_{2\omega(s)}}$	$u_q^- i_d^+ - u_d^- i_q^+ - u_q^+ i_d^- + u_d^+ i_q^-$
Reactive power	
$\boldsymbol{Q_0}$	$u_q^+ i_d^+ - u_d^+ i_q^+ + u_q^- i_d^- - u_d^- i_q^-$
$\boldsymbol{Q_{2\omega(c)}}$	$u_q^- i_d^+ - u_d^- i_q^+ + u_q^+ i_d^- - u_d^+ i_q^-$
$\boldsymbol{Q_{2\omega(s)}}$	$-u_d^- i_d^+ - u_q^- i_q^+ + u_d^+ i_d^- + u_q^+ i_q^-$

Table 3.2 can be rearranged in matrix form as shown in (3.19):

$$\begin{bmatrix} P_0 \\ P_{2\omega(c)} \\ P_{2\omega(s)} \\ Q_0 \\ Q_{2\omega(c)} \\ Q_{2\omega(s)} \end{bmatrix} = \begin{bmatrix} u_d^+ & u_q^+ & u_d^- & u_q^- \\ u_d^- & u_q^- & u_d^+ & u_q^+ \\ u_q^- & -u_d^- & -u_q^+ & u_d^+ \\ u_q^+ & -u_d^+ & u_q^- & -u_d^- \\ u_q^- & -u_d^- & u_q^+ & -u_d^+ \\ -u_d^- & -u_q^- & u_d^+ & u_q^+ \end{bmatrix} \cdot \begin{bmatrix} i_d^+ \\ i_q^+ \\ i_d^- \\ i_q^- \end{bmatrix} \tag{3.19}$$

To obtain the equivalent equation to (3.13), it would be necessary to calculate the inverse of the voltage matrix in (3.19). However, it is not possible since it is not a square matrix. The upper square matrix of order 4 is chosen to compensate for possible fluctuations in the active power, and thus avoiding an oscillation in u_{DC}. The terms $Q_{2\omega(c)}$ and $Q_{2\omega(s)}$ are not compensated. Trying to control these oscillating reactive powers only deteriorates the control performance, thus they are allowed to run freely.

The resulting equations to calculate the reference currents are (3.20) and (3.21), and the

block diagram showing its connection to the current controller is shown in Fig. 3.14.

$$\begin{bmatrix} i_d^+ \\ i_q^+ \\ i_d^- \\ i_q^- \end{bmatrix} = \begin{bmatrix} u_d^+ & u_q^+ & u_d^- & u_q^- \\ u_d^- & u_q^- & u_d^+ & u_q^+ \\ u_q^- & -u_d^- & -u_q^+ & u_d^+ \\ u_q^+ & -u_d^+ & u_q^- & -u_d^- \end{bmatrix}^{-1} \cdot \begin{bmatrix} P^* \\ 0 \\ 0 \\ Q^* \end{bmatrix} \tag{3.20}$$

$$\begin{bmatrix} i_d^* \\ i_q^* \end{bmatrix} = \begin{bmatrix} i_d^+ + i_d^- \\ i_q^+ + i_q^- \end{bmatrix} \tag{3.21}$$

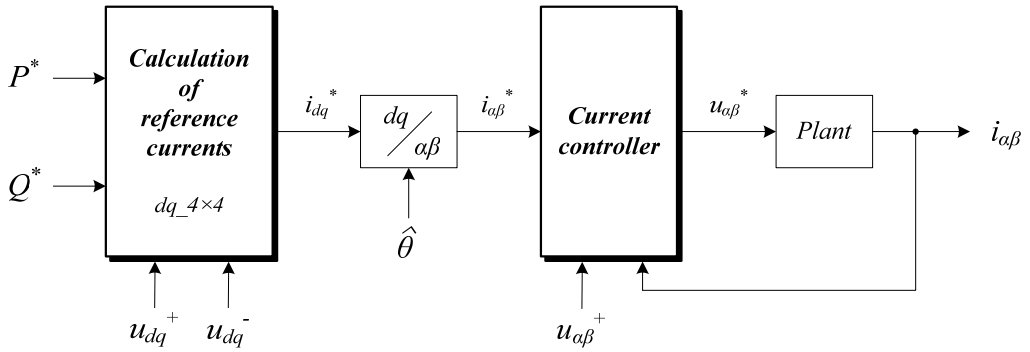

Fig. 3.14. Calculation of reference currents based on *dq_4×4* connected to the current controller.

Analogously to what was done in the previous section with the calculation in *αβ*-axes, symbolic computation has been used to directly obtain the expressions for calculating the reference currents in *dq*-axes, and avoid the calculation of the inverse matrix in (3.20). The resulting equations are shown in (3.22) and (3.23). Compared to those obtained in *αβ*-axes (section 3.2.1), these only need a few multiplications and additions. Furthermore, the computational burden can be minimized knowing that $u_d^+ = 0$ due to the PLL synchronization.

$$\begin{bmatrix} i_d^+ \\ i_q^+ \\ i_d^- \\ i_q^- \end{bmatrix} = \begin{bmatrix} u_d^+ & u_q^+ \\ u_q^+ & -u_d^+ \\ -u_d^- & u_q^- \\ -u_q^- & -u_d^- \end{bmatrix} \cdot \begin{bmatrix} P^*/k_1 \\ Q^*/k_2 \end{bmatrix} \tag{3.22}$$

$$k_1 = -(u_d^+)^2 - \left(u_q^+\right)^2 + (u_d^-)^2 + \left(u_q^-\right)^2$$

$$k_2 = (u_d^+)^2 + \left(u_q^+\right)^2 + (u_d^-)^2 + \left(u_q^-\right)^2$$

$$\begin{bmatrix} i_d^* \\ i_q^* \end{bmatrix} = \begin{bmatrix} i_d^+ + i_d^- \\ i_q^+ + i_q^- \end{bmatrix} \tag{3.23}$$

3.2.1.3. Comparison.

Fig. 3.15 shows the simulation results of the performance obtained by the four methods of calculation of reference currents studied in the two previous sections. Remember that the ideal unbalanced grid voltage of Fig. 3.9 has been applied.

It is obvious that the traditional methods, namely, *αβ_2×2* and *dq_2×2*, are not suitable when the grid voltage is unbalanced. An oscillation in the DC-link voltage is introduced (Fig. 3.15b) and, thus, the oscillating active power $P_{2\omega}$ has a non-zero value (Fig. 3.16c). This term has been calculated according to Table 3.1.

Regarding *αβ_4×4*, a reduction of around 25 % in the DC-link voltage oscillation magnitude is achieved, at the expense of introducing harmonics of order $2k-1$ ($k \in \mathbb{Z}$) in the reference currents (Fig. 3.15a). This is due to the multiple operations carried out with the PCC voltage sequences in (3.15) and (3.16). Its effect is reflected in the constant active power P_0 (Fig. 3.16a) by means of an oscillation.

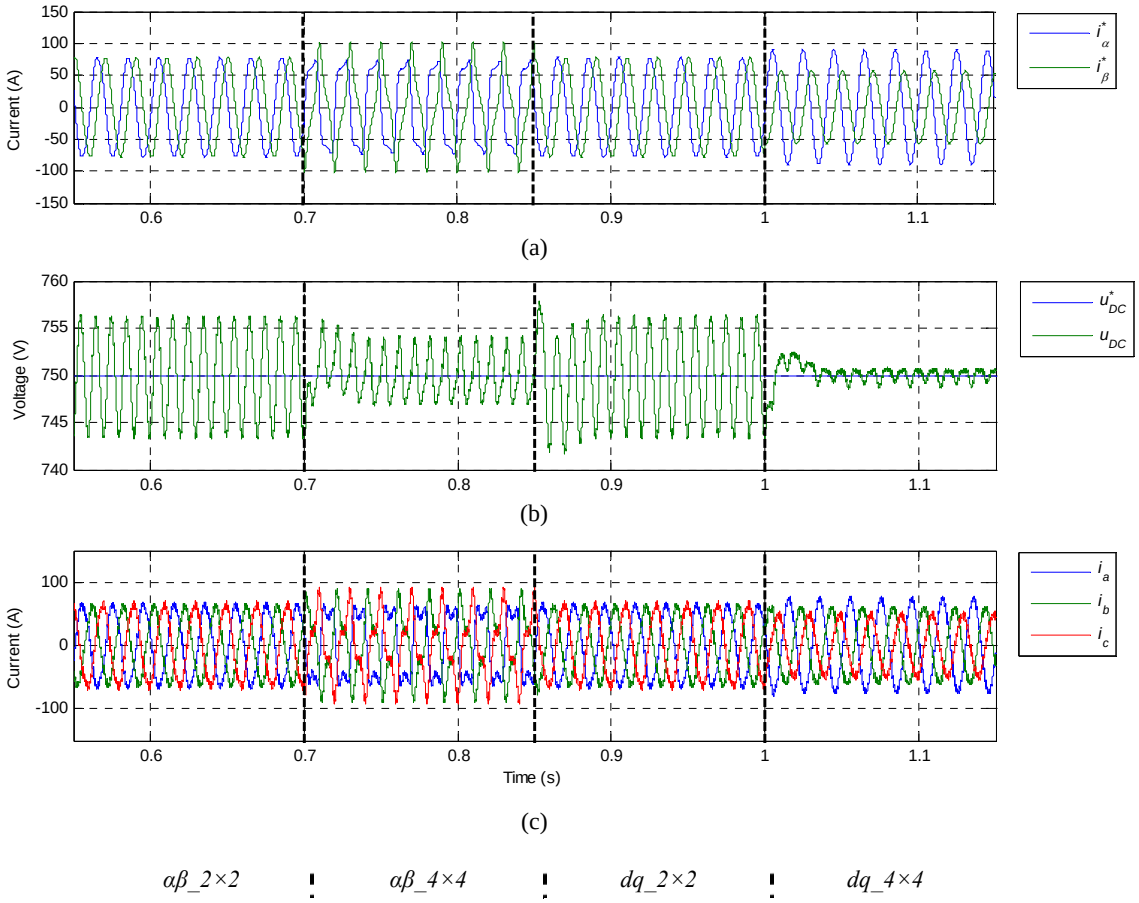

Fig. 3.15. Simulation results of the performance obtained by the methods of calculation of reference currents indicated above. (a) Reference currents in *αβ*-axes; (b) DC-link voltage and its reference; (c) grid current.

As for *dq_4×4*, it shows the best results. The DC-link voltage oscillation is minimized as well as the oscillating active power. It is the only method that provides unbalanced reference currents without harmonic content (under conditions of no load and no grid harmonics), as seen in Fig. 3.15a. Furthermore, the constant active and reactive powers are kept to a minimum.

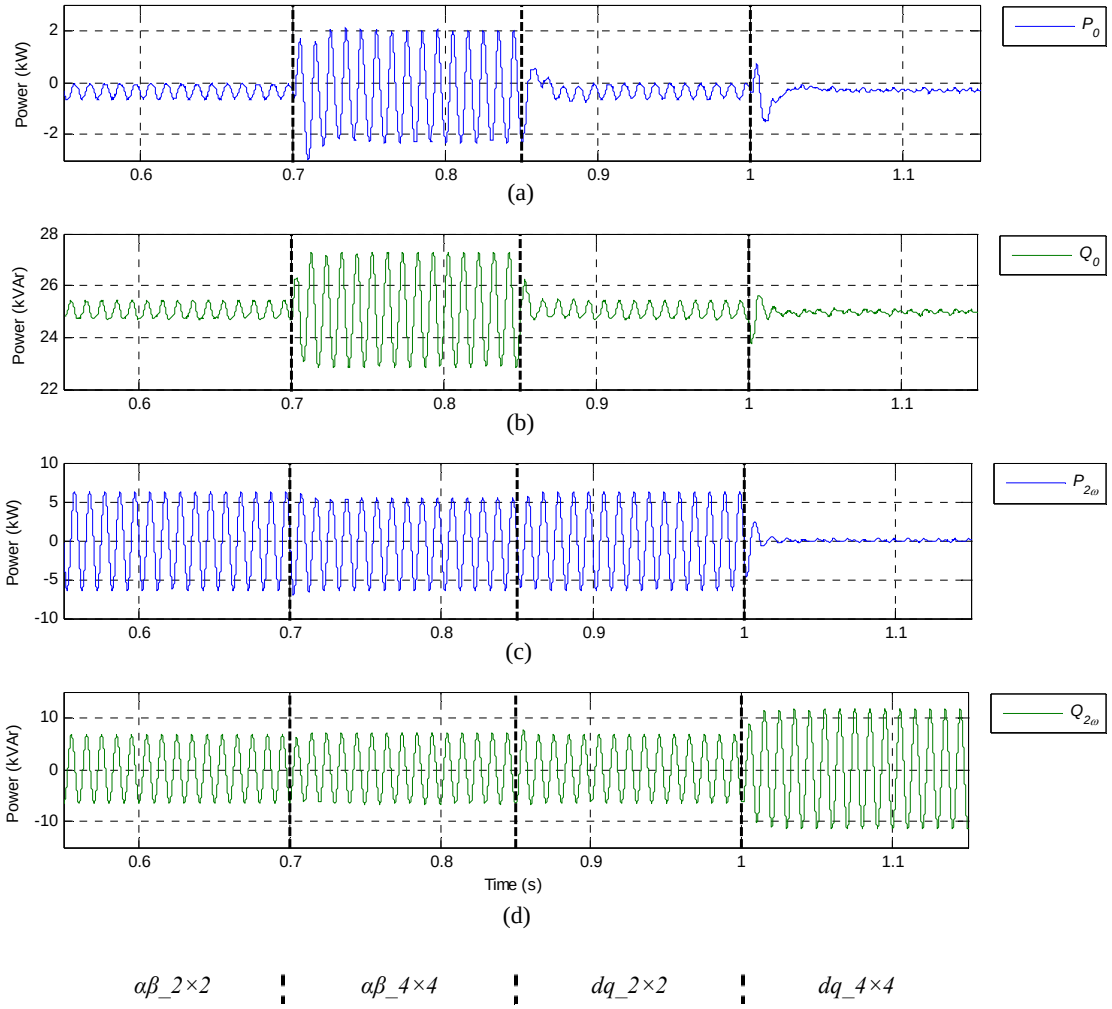

Fig. 3.16. Simulation results of the performance obtained by the methods of calculation of reference currents indicated above. (a) Constant active power; (b) constant reactive power; (c) oscillating active power; (d) oscillating reactive power.

3.2.2. Limitation of references.

The limitation technique of reference currents influences the control performance. If the limitation level is not set properly, the actuation limit of the whole control system can be reduced.

To limit a constant reference, a linear saturator can be applied. The drawback is that each limitation level is independent to the other axis, thus in some cases the operation range of the converter is not fully used. Another possibility is to use limitation levels dependent to each other, giving more priority to one of the axes and/or sequences if necessary in the case of overcurrent.

To limit a sinusoidal reference, the limitation techniques proposed in [Rizo*, et al.*, 2012] can be applied. Two different structures were tackled, achieving different grades of distortion and bandwidth in function of the control loop structure and system requirements. These two structures differ in the way they calculate the limited reference current $\vec{i}^*_{lim}$ when the reference magnitude $|\vec{i}^*|$ exceeds the maximum level $I_{\max}$: (i) Proportional Saturation (PS) of both components, in which a reduction factor is applied to both components, and (ii) saturation Maximizing the trajectory Area (MA), in which the new limited vector reference optimizes the area available between the limit circle and the input trajectory ellipse. Fig. 3.17 explains graphically the operation of both limiting techniques according to the level of unbalance of the reference.

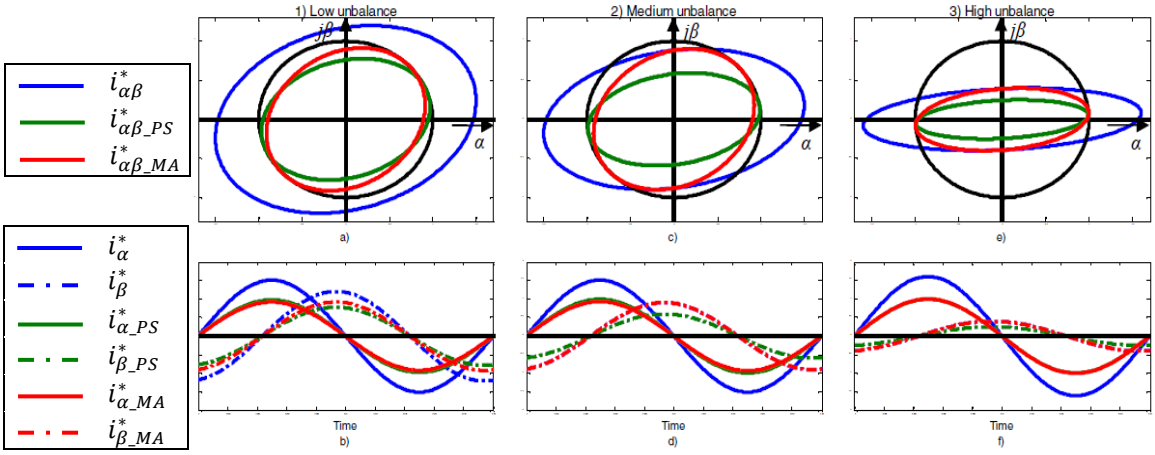

Fig. 3.17. Vector trajectories and temporal waveforms of PS and MA strategies under three unbalance levels: low (a and b), medium (c and d) and high (e and f) [Rizo*, et al.*, 2012].

3.3. Grid synchronization and monitoring.

This section presents several techniques to perform the grid synchronization and monitoring. To do so, the grid frequency has to be estimated, which is necessary to develop frequency-adaptive current controllers, as will be discussed in the next chapters. Particularly, four methods will be tackled here: Phase-Locked Loop (PLL), Frequency Locked-Loop (FLL), Kalman Filter (KF) and Extended Kalman Filter (EKF).

3.3.1. Phase-Locked Loop (PLL).

Nowadays, the PLL [Chung, 2000] is the most common technique in order to extract the phase angle of the PCC voltage, from which the frequency is obtained. It is usually implemented in synchronous reference frame (*dq*-axes) and its simplest scheme is shown in Fig. 3.18. This block diagram corresponds to a "Synchronous Reference Frame – Phase Locked Loop" (SRF-PLL). In this representation, the angular position in this reference frame is controlled by means of a feedback loop that controls the *d*-component of the PCC voltage. Hence, in steady-state the *q*-component represents the amplitude of the voltage vector and its phase is determined by the output of the feedback loop, as represented in Fig. 3.19.

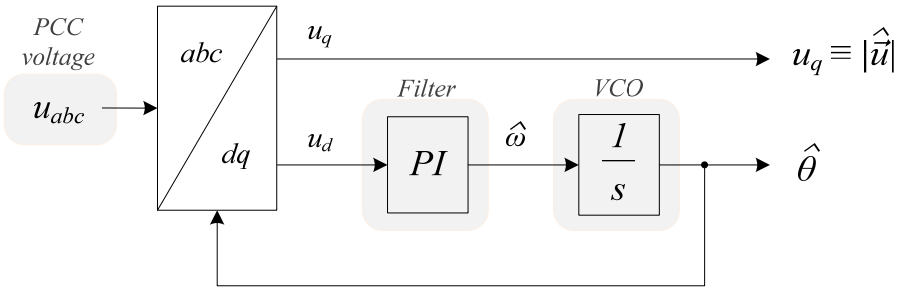

Fig. 3.18. General structure of a SRF-PLL for three-phase systems.

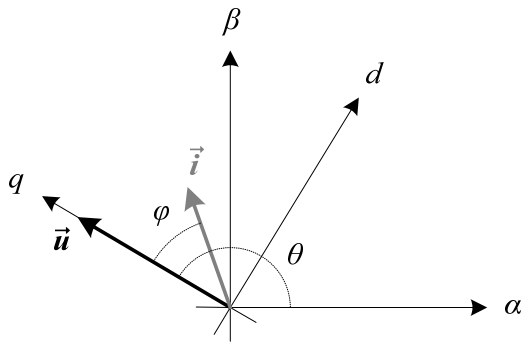

Fig. 3.19. Location of the grid voltage vector in *dq*-frame for the scheme of Fig. 3.1.

There is a first step in which the PCC voltage, expressed in *abc*-axes, is transformed into the *dq*-axes by means of the Park transformation for three-phase three-wire systems. The corresponding transformation matrix is shown in (3.24), where k is a constant that depends on whether a power-invariant $\left(k = \sqrt{2/3}\right)$ or amplitude-invariant $(k = 2/3)$ transformation is required. In second place, the filter loop is implemented with a controller, generally a PI controller because a satisfactory behavior in the regulation of DC variables is obtained to control the synchronization variable (*d* or *q*) [Blaabjerg, *et al.*, 2006]. The output of this controller is the estimated grid pulsation $\hat{\omega}$. Lastly, the Voltage-Controlled Oscillator (VCO) consists of an integrator, whose output is the estimated phase angle $\hat{\theta}$ and it is applied to the

"abc/dq" block to perform the *abc* to *dq* transformation (zero-sequence component is not taken into account).

$$T_{abc\to dq} = k \cdot \begin{bmatrix} cos\,\hat{\theta} & cos\left(\hat{\theta} - \frac{2\pi}{3}\right) & cos\left(\hat{\theta} + \frac{2\pi}{3}\right) \\ -sin\,\hat{\theta} & -sin\left(\hat{\theta} - \frac{2\pi}{3}\right) & -sin\left(\hat{\theta} + \frac{2\pi}{3}\right) \end{bmatrix} \tag{3.24}$$

Once the basic structure has been analyzed, a simple second stage has to be added to obtain the grid frequency from a SRF-PLL. It is a first-order low-pass filter with a low cutoff frequency, between 1 and 25 Hz, connected to the output of the PI controller and followed by a division by 2π, given that $f = \omega/2\pi$. The reason of including this filter is, since the spectral content of the estimated frequency $\hat{f}$ should be a DC-component, a low-pass filter helps to obtain a cleaner and smoother value if a perturbation is present in the system. In the experimental results carried out in this Thesis, the value of the low-pass filter cutoff frequency has been chosen as 1 Hz, so that the transients after applying a frequency jump are easily observable and the estimated grid frequency has a low distortion.

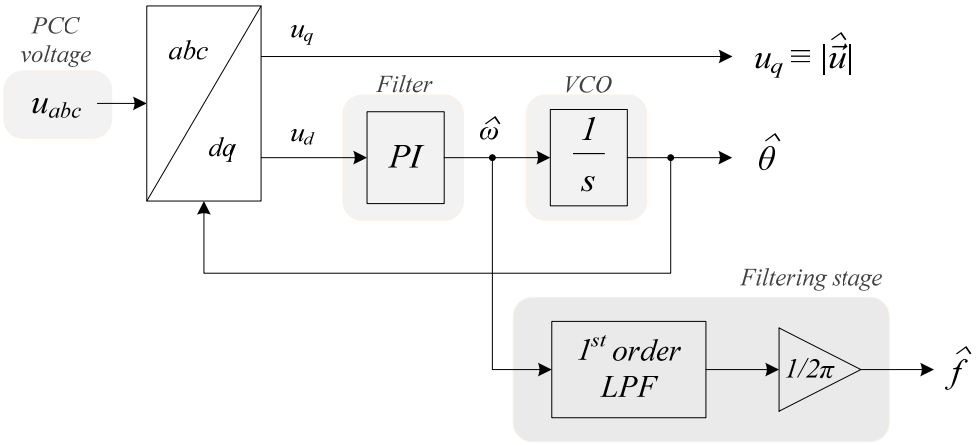

Fig. 3.20. Structure based on SRF-PLL to perform grid synchronization and monitoring.

This algorithm presents a good rejection of grid harmonics, voltage dips and any other kind of perturbations, but additional improvements are required to deal with an unbalanced grid voltage. The harmonics produced by the negative sequence will be spread along the PLL and will be reflected in the extracted phase angle. To avoid this, different filtering techniques are needed in order to filter the negative sequence. Therefore, the PLL will properly estimate the phase angle during unbalanced conditions.

Two configurations formed by a PLL and a sequence-separation algorithm are shown in Fig. 3.21. Both schemes of Fig. 3.21 are based in the same equations, which are shown in (3.25a) and (3.25b), and where q is the quadrature operator whose value is $q = e^{-j\frac{\pi}{2}}$.

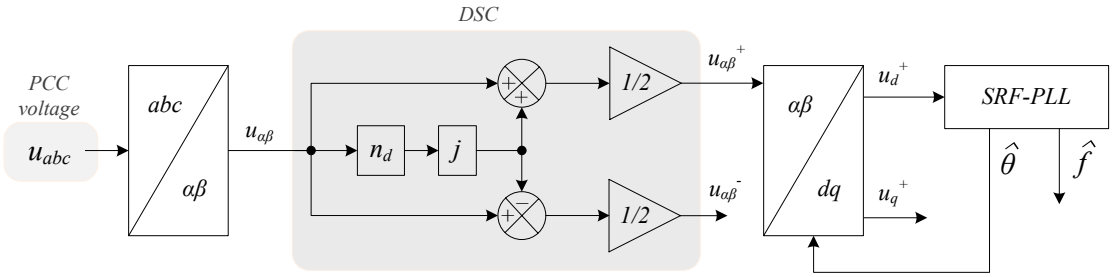

(a)

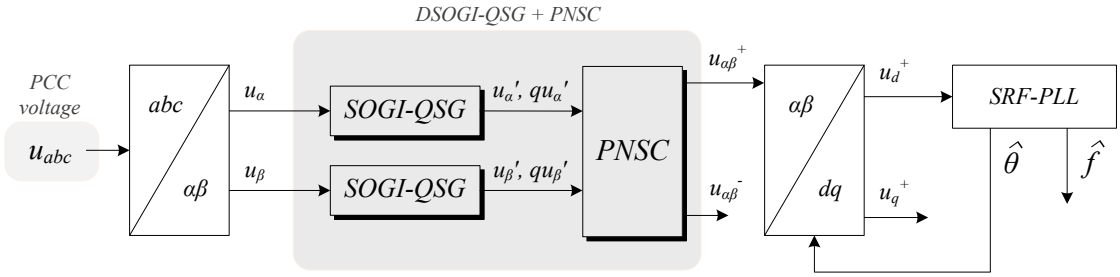

(b)

Fig. 3.21. Improvement of the SRF-PLL by means of two different sequence-separator methods, giving rise to (a) DSC-PLL and (b) DSOGI-PLL.

$$\vec{u}_{\alpha\beta}^{+}(t) = \frac{1}{2} \cdot \begin{bmatrix} 1 & -q \\ q & 1 \end{bmatrix} \cdot \vec{u}_{\alpha\beta}(t) \tag{3.25a}$$

$$\vec{u}_{\alpha\beta}^{-}(t) = \frac{1}{2} \cdot \begin{bmatrix} 1 & q \\ -q & 1 \end{bmatrix} \cdot \vec{u}_{\alpha\beta}(t) \tag{3.25b}$$

The block diagram of Fig. 3.21a uses a Delayed Signal Cancellation (DSC) [Saccomando and Svensson, 2001; Svensson*, et al.*, 2007] to separate positive and negative sequences in *αβ*-axes, being the positive sequence the one which is transformed to *dq*-axes to make the PLL synchronization either with the positive *d*-sequence or with the positive *q*-sequence. It receives the name of DSC-PLL. This algorithm uses a delay of a quarter-period of the fundamental frequency (5 ms for 50 Hz).

The block diagram of Fig. 3.21b uses a Dual Second Order Generalized Integrator-Quadrature Signal Generator (DSOGI-QSG) plus a Positive-Negative Sequence Calculation (PNSC), forming the DSOGI-PLL [Rodríguez*, et al.*, 2006]. The SOGI-QSG is represented in Fig. 3.22 and it is based on the SOGI, which is deeply studied in chapter 4, and it obtains two outputs: one in phase with the input (v') and another in quadrature (qv'). The continuous-time transfer functions for each output correspond to (3.26a) and (3.26b), respectively. A phase difference of 90° is obtained at $\pm f_o$. Besides, $v'/v(s)$ behaves as a band-pass filter and

the bandwidth is determined by the value of k_s, whereas $qv'/v(s)$ behaves as a low-pass filter. When detecting the positive sequence, the DSOGI-PLL behaves as a low-pass filter for the positive sequence input voltage and as a Notch filter for the negative sequence input voltage. With these signals, the PNSC algorithm is able to calculate the positive and negative sequences of the PCC voltage.

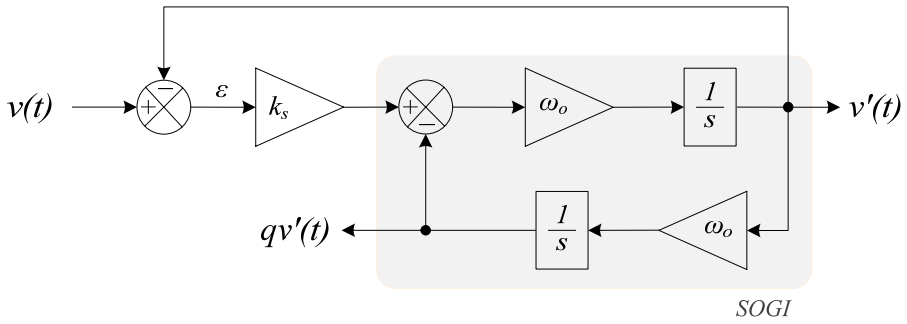

Fig. 3.22. SOGI-QSG in continuous time.

$$\frac{v'}{v}(s) = \frac{k_s \omega_o s}{s^2 + k_s \omega_o s + \omega_o^2} \tag{3.26a}$$

$$\frac{qv'}{v}(s) = \frac{k_s \omega_o^2}{s^2 + k_s \omega_o s + \omega_o^2} \tag{3.26b}$$

According to (3.25a), the α-component of the PCC voltage positive sequence can be expressed as:

$$u_\alpha^+(s) = \frac{1}{2}\left(u'_\alpha(s) - q u'_\beta(s)\right) = \frac{1}{2}\left(\frac{v'}{v}(s) + \frac{qv'}{v}(s)\right) u_\alpha(s) \tag{3.27}$$

whereas the β-component is in general related to the α-component by:

$$u_\beta(s) = -\frac{s}{\omega} u_\alpha(s) \tag{3.28}$$

Substituting (3.26a) and (3.26b) into (3.27), the transfer function of the α-axis positive sequence is shown in (3.29).

$$\frac{u_\alpha^+}{u_\alpha}(j\omega) = \frac{1}{2} \frac{k_s \widehat{\omega}(\omega + \widehat{\omega})}{k_s \widehat{\omega}\omega + j(\omega^2 - \widehat{\omega}^2)} \tag{3.29}$$

3.3.2. Frequency-Locked Loop (FLL).

The FLL [Rodríguez, *et al.*, 2006] is a frequency-adaptive loop that is used along with a standard PLL to detect the frequency and phase of the PCC voltage. Its control loop does not use neither the phase angle nor trigonometric functions, and a signal with the same frequency as the input signal is obtained at its output. It depends on one of the most stable grid variables, the grid frequency.

The Dual SOGI-FLL (DSOGI-FLL), whose block diagram is shown in Fig. 3.23, is a simple and effective method to obtain the grid frequency. For three-phase systems, it consists of a DSOGI-QSG (as the one used in the previous section to form a DSOGI-PLL), a PNSC algorithm, a FLL that estimates the grid frequency and a SRF-PLL that estimates the PCC phase angle. Besides, the estimated grid pulsation is used as input to the DSOGI-QSG. The structure of the FLL block is shown in Fig. 3.24, where ε is an error signal obtained from the SOGI-QSG for the α-component (see Fig. 3.22), γ is a constant, ω_{ff} is the feedforward of the grid pulsation and $\hat{\omega}$ is the estimated grid pulsation.

Since this structure is also based on a DSOGI-QSG, it also behaves as a low-pass filter for the positive sequence input voltage and as a Notch filter for the negative sequence input voltage.

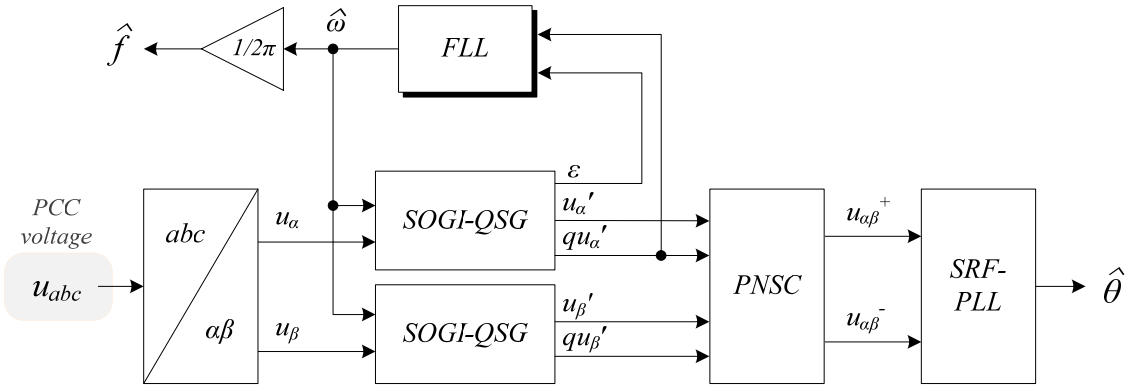

Fig. 3.23. Structure based on FLL to perform grid synchronization and monitoring, giving rise to DSOGI-FLL.

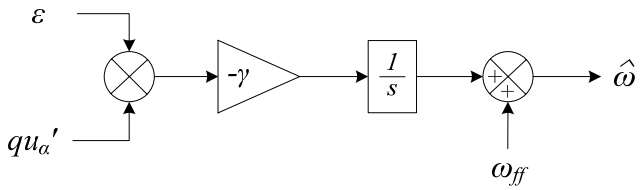

Fig. 3.24. FLL in continuous time.

3.3.3. Kalman Filter (KF).

3.3.3.1. Fundamentals of the KF.

The KF is a set of mathematical equations that provides an efficient computational (recursive) means to estimate the state $x \in \Re^n$ of a discrete-time controlled process, implementing a predictor-corrector type estimator that is *optimal* in the sense that it minimizes the estimated error covariance. The filter is very powerful in several aspects: it supports estimations of past, present, and even future states, and it can do so even when the precise nature of the modeled system is unknown [Welch and Bishop, 1995]. It is well suited for online applications [Girgis*, et al.*, 1991].

The process is governed by the linear stochastic difference equation:

$$x_{k+1} = A_k x_k + B_k u_{k+1} + w_k \tag{3.30}$$

with a measurement $z \in \Re^m$ that is:

$$z_k = C_k x_k + v_k \tag{3.31}$$

where $C_k x_k \equiv y_k$ are the only observable variables.

The random variable w_k represents the discrete variation of the state variables due to an input white noise sequence, whereas the random variable v_k is an $m \times 1$ measurement noise vector assumed to be a white sequence with known covariance structure and uncorrelated with the w_k sequence [Girgis*, et al.*, 1991]. They have the normal probability distributions given by (3.32a) and (3.32b).

$$p(w) \sim N(0, Q) \tag{3.32a}$$

$$p(v) \sim N(0, R) \tag{3.32b}$$

In practice, the *process noise covariance* Q and *measurement noise covariance* R matrices might change with each time step or measurement, however here they are assumed to be constant [Welch and Bishop, 1995].

The $n \times n$ matrix A_k in the difference equation (3.30) is the state transition matrix, which relates the state at the previous time step $k-1$ to the state at the current step k, in the absence of either a driving function or process noise. The $n \times l$ matrix B_k is the control application matrix, which relates the optional control input $u \in \Re^l$ to the state x. The $m \times n$ matrix C_k in

the measurement equation (3.31) is the observation matrix, which relates the state to the measurement z_k.

The *a priori* state estimate at step $k+1$ given knowledge of the process prior to step $k+1$ is defined as $\hat{x}_{k+1/k} \in \Re^n$, and the *a posteriori* state estimate at step $k+1$ given measurement z_{k+1} is defined as $\hat{x}_{k+1/k+1} \in \Re^n$. The *a priori* and *a posteriori* estimate errors can be defined as:

$$e_{k+1/k} = x_{k+1} - \hat{x}_{k+1/k} \tag{3.33a}$$

$$e_{k+1/k+1} = x_{k+1} - \hat{x}_{k+1/k+1} \tag{3.33b}$$

The *a priori* and *a posteriori* estimate error covariances are defined by (3.34a) and (3.34b), respectively:

$$P_{k+1/k} = E\left[e_{k+1/k}\, e_{k+1/k}^T\right] \tag{3.34a}$$

$$P_{k+1/k+1} = E\left[e_{k+1/k+1}\, e_{k+1/k+1}^T\right] \tag{3.34b}$$

With these definitions, the *a posteriori* state estimate is calculated as a linear combination of an *a priori* estimate $\hat{x}_{k+1/k}$ and a weighted difference between an actual measurement z_{k+1} and a measurement prediction $\left(z_{k+1} - C_{k+1}\hat{x}_{k+1/k}\right)$ as shown below in (3.35).

$$\hat{x}_{k+1/k+1} = \hat{x}_{k+1/k} + K_{k+1}\left(z_{k+1} - C_{k+1}\hat{x}_{k+1/k}\right) \tag{3.35}$$

The matrix K_{k+1} in (3.35) is chosen to be the gain or *blending factor* that minimizes the *a posteriori* error covariance equation (3.34b).

The basic idea of the KF algorithm is shown in Fig. 3.25, where the evolution of the state variables is represented. On the left side we find the state variable at instant k $(\hat{x}_k)$, whereas on the right side we locate the state variable at instant $k+1$ $\left(\hat{x}_{k+1/k+1}\right)$, showing how the predicted state variable $\left(\hat{x}_{k+1/k}\right)$ is corrected by means of the measurement (z_{k+1}).

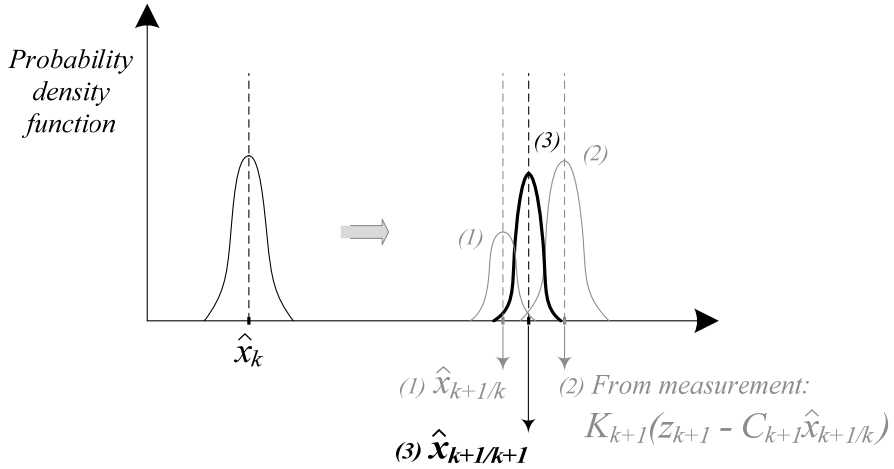

Fig. 3.25. Evolution of the state variables in the KF algorithm (left side: state variable at instant k ($\hat{x}_k$); right side: state variable at instant $k+1$ ($\hat{x}_{k+1/k+1}$), showing the contributions of the predicted state variable ($\hat{x}_{k+1/k}$) and the measurement (z_{k+1})).

The algorithm of the KF is shown in Fig. 3.26. The first task during the measurement update is to compute the Kalman gain, K_{k+1}. The next step is to actually measure the process to obtain z_{k+1}, and then to generate an *a posteriori* state estimate $\hat{x}_{k+1/k+1}$ by incorporating the measurement. The final step is to obtain an *a posteriori* error covariance estimate $P_{k+1/k+1}$.

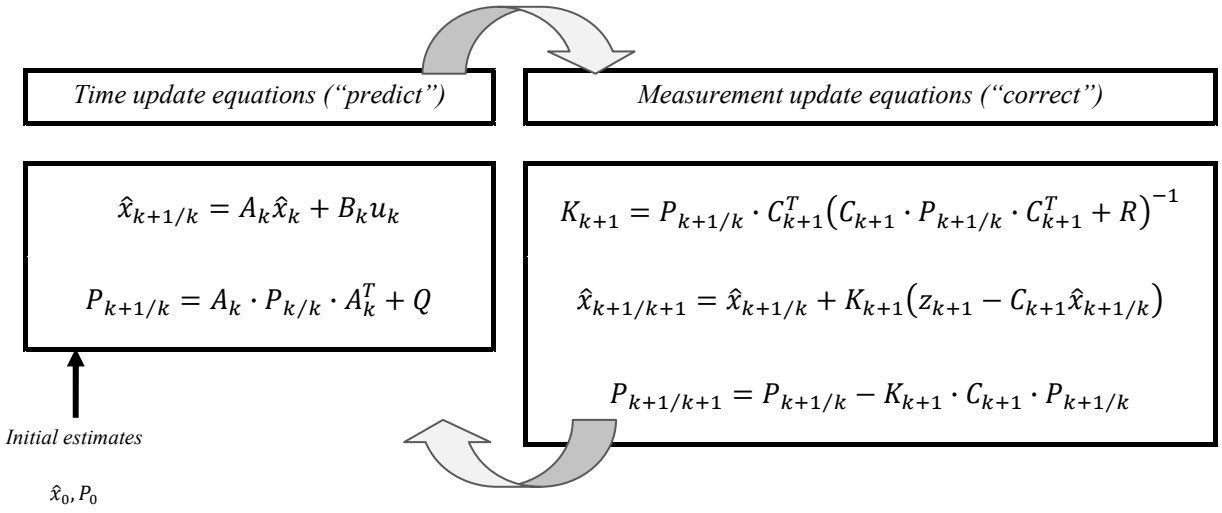

Fig. 3.26. Set of equations of the KF.

3.3.3.2. Application to grid synchronization and monitoring.

Fig. 3.27 shows the block diagram of the KF-based grid synchronization and monitoring method. Its input is the PCC voltage in *abc*-axes and is composed of four stages or blocks,

namely, (i) *abc* to *αβ* transformation, (ii) KF, (iii) PNSC and (iv) a SRF-PLL. Its outputs are the estimated grid frequency and estimated phase angle, which can be necessary for the operation of the converter control. The KF receives as inputs the *αβ*-components of the PCC voltage and its output provides four voltages, two of which are in phase with the input (u'_α, u'_β) and the other two are in quadrature (qu'_α, qu'_β). With these signals, the PNSC calculates the positive and negative sequences according to (3.25), which are applied to the PLL to estimate the grid frequency. This PLL may include an algorithm to decide which of the two sequences is the predominant and synchronize with it.

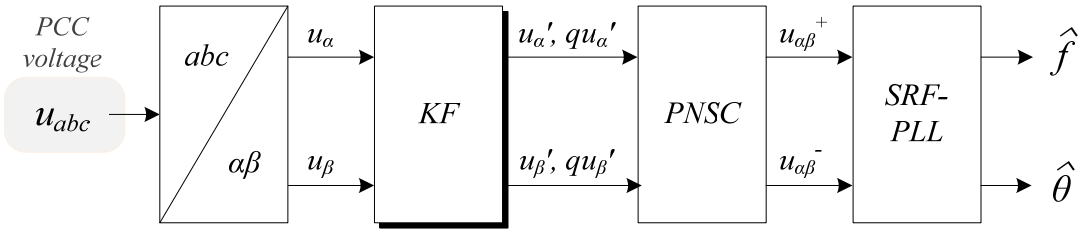

Fig. 3.27. Structure based on KF to perform grid synchronization and monitoring.

Therefore, it is necessary to model the process that obtains an output in phase with the input and another one in quadrature. A state variable representation of a signal with time-varying magnitude using a stationary reference is considered. Let us consider a noise-free discrete signal:

$$s[t_k] = A[t_k]\, cos[\omega t_k + \theta] \tag{3.36}$$

where $A[t_k]$ is the amplitude, ω is the pulsation and t_k is the sampling instant, given by the sampling frequency. At the instant $t_{k+1} = t_k + \Delta t$, the sinusoidal signal can be expressed as [Girgis*, et al.*, 1991]:

$$s[t_{k+1}] = A[t_{k+1}]\, cos[\omega_1 t_{k+1} + \theta] = A[t_{k+1}]\, cos[\omega_1 t_k + \omega_1 \Delta t + \theta] \tag{3.37}$$

and the following states can be considered:

$$x1_k = A[t_k]\, cos[\omega_1 t_k + \theta] \tag{3.38a}$$

$$x2_k = A[t_k]\, sin[\omega_1 t_k + \theta] \tag{3.38b}$$

The signal $s[t_{k+1}]$ can be written as:

$$\begin{aligned} s[t_{k+1}] = x1_{k+1} \\ &= A[t_{k+1}]\,cos[\omega_1 t_k + \theta]\,cos[\omega_1 \Delta t] \\ &- A[t_{k+1}]\,sin[\omega_1 t_k + \theta]\,sin[\omega_1 \Delta t] \\ &= x1_k\,cos[\omega_1 \Delta t] - x2_k\,sin[\omega_1 \Delta t] \end{aligned} \tag{3.39}$$

And the state variable $x2$ can be written at the time instant t_{k+1} as:

$$\begin{aligned} x2_{k+1} = A[t_{k+1}]\,cos[\omega_1 t_k + \theta]\,sin[\omega_1 \Delta t] + A[t_{k+1}]\,sin[\omega_1 t_k + \theta]\,cos[\omega_1 \Delta t] \\ = x1_k\,sin[\omega_1 \Delta t] + x2_k\,cos[\omega_1 \Delta t] \end{aligned} \tag{3.40}$$

This way, the state variable representation is given by:

$$\begin{bmatrix} x1_{k+1} \\ x2_{k+1} \end{bmatrix} = \begin{bmatrix} cos(\omega_1 \Delta t) & -sin(\omega_1 \Delta t) \\ sin(\omega_1 \Delta t) & cos(\omega_1 \Delta t) \end{bmatrix} \begin{bmatrix} x1_k \\ x2_k \end{bmatrix} + \begin{bmatrix} v1_k \\ v2_k \end{bmatrix} \tag{3.41}$$

For this representation to be valid, it is assumed that $A[t_k] = A[t_{k+1}]$, which will introduce an error. This is why this model is called *stationary reference model*.

It is straightforward to see that the states $x1$ (3.38a) and $x2$ (3.38b) are in quadrature. Therefore, four states are needed to represent $u'_\alpha\ (x1),\ qu'_\alpha\ (x2),\ u'_\beta\ (x3)$ and $qu'_\beta\ (x4)$. The resulting state variable representation for the KF implementation is shown in (3.42) – (3.45), where ω_o is the grid pulsation.

$$\begin{bmatrix} u'_{\alpha_{k+1}} \\ qu'_{\alpha_{k+1}} \\ u'_{\beta_{k+1}} \\ qu'_{\beta_{k+1}} \end{bmatrix} = A_k \begin{bmatrix} u'_{\alpha_k} \\ qu'_{\alpha_k} \\ u'_{\beta_k} \\ qu'_{\beta_k} \end{bmatrix} + B_k u_{k+1} + w_k \tag{3.42}$$

$$A_k = \begin{bmatrix} cos(\omega_1 T_s) & -sin(\omega_1 T_s) & 0 & 0 \\ sin(\omega_1 T_s) & cos(\omega_1 T_s) & 0 & 0 \\ 0 & 0 & cos(\omega_1 T_s) & -sin(\omega_1 T_s) \\ 0 & 0 & sin(\omega_1 T_s) & cos(\omega_1 T_s) \end{bmatrix} \tag{3.43}$$

$$B_k = [0 \quad 0 \quad 0 \quad 0]^T \tag{3.44}$$

$$C_k = [1 \quad 0 \quad 1 \quad 0] \tag{3.45}$$

The measurement matrix is shown in (3.46), where u_α and u_β are the $\alpha\beta$-components of the PCC voltage.

$$z_k = \begin{bmatrix} u_\alpha \\ u_\beta \end{bmatrix} \tag{3.46}$$

As for the KF parameters:

- *Initial estimation of the state vector* $(\hat{x}_0)$.

  As the KF model is not based on any previous measure, $\hat{x}_0$ can be initialized to an array of zeros. This implies the existence of an initialization period in which the estimate will not be accurate.

- *Initial covariance matrix* (P_0).

  The estimate is more accurate when the trace of the matrix P_k is minimal [Ma and Girgis, 1996], this being a diagonal matrix, reaching the conclusion that the most appropriate value for the diagonal values of the matrix initial error covariance is $10\ V^2$.

- *Measurement noise variance matrix* (R).

  The noise variance is chosen constant and with value $0.05\ V^2$, as this is the typical value of the noise present in grid signal measurements in normal environments [Girgis*, et al.*, 1991; Farach*, et al.*, 1993].

- *State variable variance matrix* (Q).

  It has also been chosen with the constant value $0.05\ V^2$ [Girgis*, et al.*, 1991; Meliopoulos*, et al.*, 1994].

3.3.4. Extended Kalman Filter (EKF).

3.3.4.1. Fundamentals of the EKF.

The KF addresses the general problem of trying to estimate the state $x \in \Re^n$ of a discrete-time controlled process that is governed by a linear stochastic difference equation, whereas frequency estimate entails a non-linear process. A KF that linearizes about the current mean and covariance is referred to as an EKF.

The estimation around the current estimate can be linearized using the partial derivatives of the process and measurement functions to compute estimates even in the face of non-linear relationships. As said before, the process to be estimated has a state vector $x \in \Re^n$, but the process is now governed by the non-linear stochastic difference equation:

$$x_{k+1} = f(x_k, u_{k+1}, w_k) \tag{3.47}$$

with a measurement $z \in \Re^m$ that is:

$$z_k = h(x_k, v_k) \tag{3.48}$$

where the random variables w_k and v_k represents the process and measurement noise, respectively. In this case, the non-linear function f in the difference equation (3.47) relates the state at the previous time step k to the state at the current time step $k+1$. It includes as parameters any driving function u_{k+1} and the zero-mean process noise w_k. The non-linear function h in the measurement equation (3.48) relates the state x_k to the measurement z_k.

In practice, the individual values of the noise w_k and v_k at each time step are not known. However, the state and measurement vectors can be approximated without them as:

$$\hat{x}_{k+1/k} = f(\hat{x}_k, u_{k+1}, 0) \tag{3.49}$$

and

$$\hat{z}_{k+1} = h\left(\hat{x}_{k+1/k}, 0\right) \tag{3.50}$$

where $\hat{x}_{k+1/k+1}$ is some *a posteriori* estimate of the state (from a previous time step $k+1$).

It is important to note that a fundamental flaw of the EKF is that the distributions (or densities in the continuous case) of the various random variables are no longer normal after undergoing their respective non-linear transformations. The EKF is simply an *ad hoc* state estimator that only approximates the optimality of Bayes' rule by linearization. Some interesting work has been done in [Julier and Uhlmann, 1997] in developing a variation to the EKF, using methods that preserve the normal distributions throughout the non-linear transformations.

To estimate a process with non-linear difference and measurement relationships, the new governing equations that linearize an estimate about (3.49) and (3.50) are shown next:

$$x_{k+1} \approx \hat{x}_{k+1/k} + F_k(x_k - \hat{x}_k) + W w_k \tag{3.51}$$

$$z_{k+1} \approx \hat{z}_{k+1} + C_{k+1}\left(x_{k+1} - \hat{x}_{k+1/k}\right) + V v_{k+1} \tag{3.52}$$

where:

- x_{k+1} and z_{k+1} are the actual state and measurement vectors,
- $\hat{x}_{k+1/k}$ and $\hat{z}_{k+1}$ are the approximate state and measurement vectors from (3.49) and (3.50),
- $\hat{x}_{k+1/k+1}$ is an *a posteriori* estimate of the state at step $k+1$,
- the random variables w_k and v_k represent the process and measurement noise,
- F_k is the Jacobian matrix of partial derivatives of f with respect to x, that is

$$F_k \Longrightarrow F_{[i,j]} = \frac{\partial f_{[i]}}{\partial x_{[j]}}(\hat{x}_k, u_{k+1}, 0) \tag{3.53}$$

- W_k is the Jacobian matrix of partial derivatives of f with respect to w,

$$W_k \Longrightarrow W_{[i,j]} = \frac{\partial f_{[i]}}{\partial w_{[j]}}(\hat{x}_k, u_{k+1}, 0) \tag{3.54}$$

- C_k is the Jacobian matrix of partial derivatives of h with respect to x,

$$C_k \Longrightarrow C_{[i,j]} = \frac{\partial h_{[i]}}{\partial x_{[j]}}\left(\hat{x}_{k+1/k}, 0\right) \tag{3.55}$$

- V_k is the Jacobian matrix of partial derivatives of h with respect to v,

$$V_k \Longrightarrow V_{[i,j]} = \frac{\partial h_{[i]}}{\partial v_{[j]}}\left(\hat{x}_{k+1/k}, 0\right) \tag{3.56}$$

The prediction error is defined as:

$$\tilde{e}_{x_k} \equiv x_{k+1} - \hat{x}_{k+1/k} \tag{3.57}$$

and the measurement residual,

$$\tilde{e}_{z_k} \equiv z_{k+1} - \hat{z}_{k+1} \tag{3.58}$$

Since it is not possible to have access to x_{k+1} (the actual state vector) in (3.57) and, in the

other hand, it is possible to have access to z_{k+1} (the actual measurement that is used to estimate x_{k+1}) in (3.58), the following governing equations for an error process are shown in (3.59) and (3.60).

$$\tilde{e}_{x_k} \approx A_k(x_k - \hat{x}_k) + \varepsilon_{k+1} \tag{3.59}$$

$$\tilde{e}_{z_k} \approx C_{k+1}\tilde{e}_{x_k} + \eta_{k+1} \tag{3.60}$$

where ε_{k+1} and η_{k+1} represent new independent random variables having zero mean and covariance matrices $\sigma_{\varepsilon_{k+1}} = WQW^T$ and $\sigma_{\eta_{k+1}} = VRV^T$. The previous equation has a format similar to the description of the model of a linear system, so it is going to be taken as a starting point to develop the EKF. In this case, the state vector is the estimation error of the system $\tilde{e}_{x_k}$, which is also the one desired to be null. With all this, the control equation is:

$$\hat{e}_{k+1} = K_{k+1} \cdot \tilde{e}_{z_k} \tag{3.61}$$

Moreover, the equation of the *a posteriori* estimation of the original state vector is now defined as:

$$\hat{x}_{k+1/k+1} = \hat{x}_{k+1/k} + \hat{e}_{k+1} \tag{3.62}$$

and substituting (3.61) into (3.62):

$$\hat{x}_{k+1/k+1} = \hat{x}_{k+1/k} + K_{k+1} \cdot \tilde{e}_{z_k} = \hat{x}_{k+1/k} + K_{k+1} \cdot (z_{k+1} - \hat{z}_{k+1}) \tag{3.63}$$

To complete the EKF, it is defined the gain of the estimator K_{k+1} in a way that it minimizes the prediction error of $\hat{e}_{k+1}$ and the covariance matrix of the estimation error P from the previous ones. Fig. 3.28 shows the algorithm of the EKF.

3.3.4.2. Application to grid synchronization and monitoring.

The application of an EKF to grid synchronization and monitoring is based on the same model as the KF. The difference is that now the SRF-PLL is only needed to estimate the grid phase angle, since the grid frequency is estimated by means of the EKF. Fig. 3.29 shows the block diagram of this method. Its input is the PCC voltage in *abc*-axes and is composed of three stages or blocks, namely, (i) *abc* to *αβ* transformation, (ii) EKF and (iii) SRF-PLL. The EKF outputs are the in-phase and quadrature signals with respect to its input and the estimated grid pulsation ($\hat{\omega}$). The estimated grid frequency is simply obtained by dividing $\hat{\omega}$ by 2π.

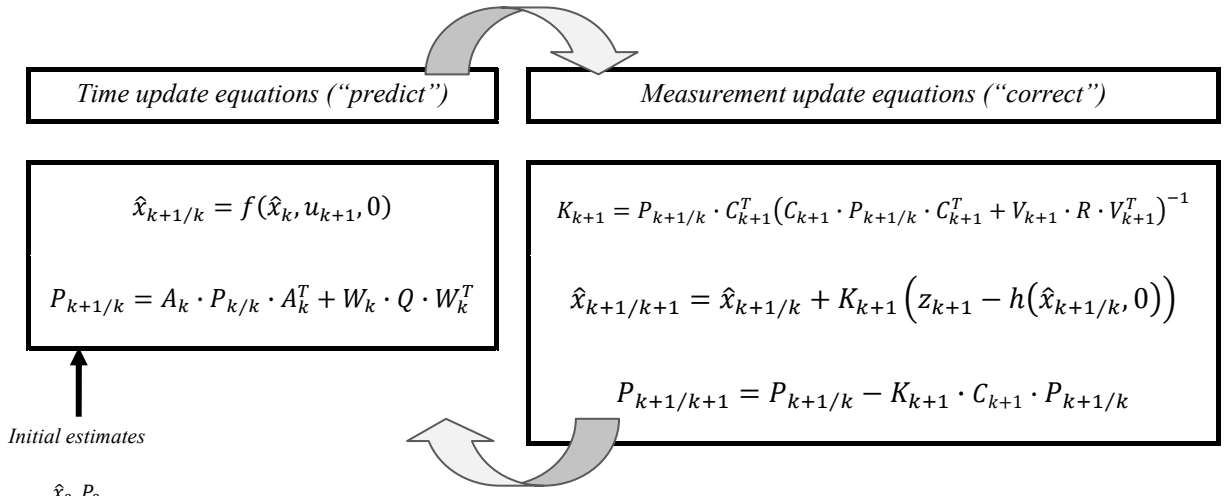

Fig. 3.28. Set of equations of the EKF.

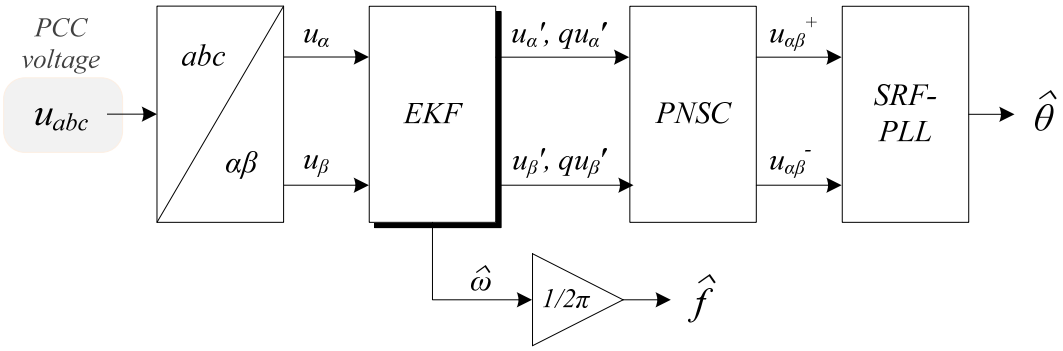

Fig. 3.29. Structure based on EKF to perform grid synchronization and monitoring.

The state variable representation is given by (3.64) – (3.68).

$$\begin{bmatrix} u'_{\alpha_{k+1}} \\ qu'_{\alpha_{k+1}} \\ u'_{\beta_{k+1}} \\ qu'_{\beta_{k+1}} \\ \widehat{\omega}_{k+1} \end{bmatrix} = A_k \begin{bmatrix} u'_{\alpha_k} \\ qu'_{\alpha_k} \\ u'_{\beta_k} \\ qu'_{\beta_k} \\ \widehat{\omega}_k \end{bmatrix} + B_k u_{k+1} + w_k \tag{3.64}$$

$$A_k = \begin{bmatrix} cos(\omega_1 T_s) & -sin(\omega_1 T_s) & 0 & 0 & 0 \\ sin(\omega_1 T_s) & cos(\omega_1 T_s) & 0 & 0 & 0 \\ 0 & 0 & cos(\omega_1 T_s) & -sin(\omega_1 T_s) & 0 \\ 0 & 0 & sin(\omega_1 T_s) & cos(\omega_1 T_s) & 0 \\ 0 & 0 & 0 & 0 & 1 \end{bmatrix} \tag{3.65}$$

$$B_k = [0 \quad 0 \quad 0 \quad 0 \quad 0]^T \tag{3.66}$$

$$C_k = [1 \quad 0 \quad 1 \quad 0 \quad 0] \tag{3.67}$$

$$F_k = \begin{bmatrix} cos(\omega_1 T_s) & -sin(\omega_1 T_s) & 0 & 0 & T_s(-sin(\omega_1 T_s)\cdot x1 - cos(\omega_1 T_s)\cdot x2) \\ sin(\omega_1 T_s) & cos(\omega_1 T_s) & 0 & 0 & T_s(cos(\omega_1 T_s)\cdot x1 - sin(\omega_1 T_s)\cdot x2) \\ 0 & 0 & cos(\omega_1 T_s) & -sin(\omega_1 T_s) & T_s(-sin(\omega_1 T_s)\cdot x3 - cos(\omega_1 T_s)\cdot x4) \\ 0 & 0 & sin(\omega_1 T_s) & cos(\omega_1 T_s) & T_s(cos(\omega_1 T_s)\cdot x3 - sin(\omega_1 T_s)\cdot x4) \\ 0 & 0 & 0 & 0 & 1 \end{bmatrix} \tag{3.68}$$

3.3.5. Comparison.

A simulation in MATLAB/Simulink® has been carried out to compare the performance of the four grid synchronization and monitoring methods studied in the previous sections in order to estimate the grid frequency. A special attention is given at this parameter since it is necessary to develop frequency-adaptive current controllers. Fig. 3.30 shows the results of applying an abrupt frequency jump from 50 to 45 Hz and from 50 to 55 Hz to each structure.

This figure reveals that the KF-based method has the largest overshoot and settling time; the EKF-based method is an intermediate option in terms of response speed but it presents the highest noise in the estimated frequency; and the PLL and FLL have a very similar response, as well as showing the lowest overshoot and fastest response. Therefore, the grid synchronization algorithms that have been implemented in the control platform of the experimental setup are the PLL-based (DSOGI-PLL) and FLL-based (DSOGI-FLL).

3.4. Conclusions.

In first place, this chapter has briefly analyzed the general control scheme of a VSC connected in shunt with the grid through an L-filter, showing the possible controllers that it may contain and their function.

Special attention has been given to the current controller. An exhaustive comparison of the main characteristics of a current controller implemented in $\alpha\beta$ and dq-axes has been carried out, yielding that the most suitable configuration for compensating the negative sequence caused by an unbalanced grid voltage is a resonant controller tuned at ω_o implemented in $\alpha\beta$-axes.

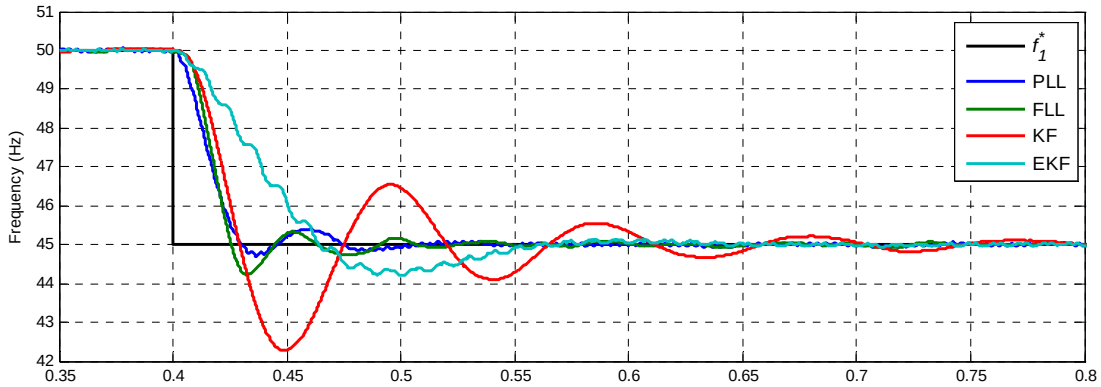

(a)

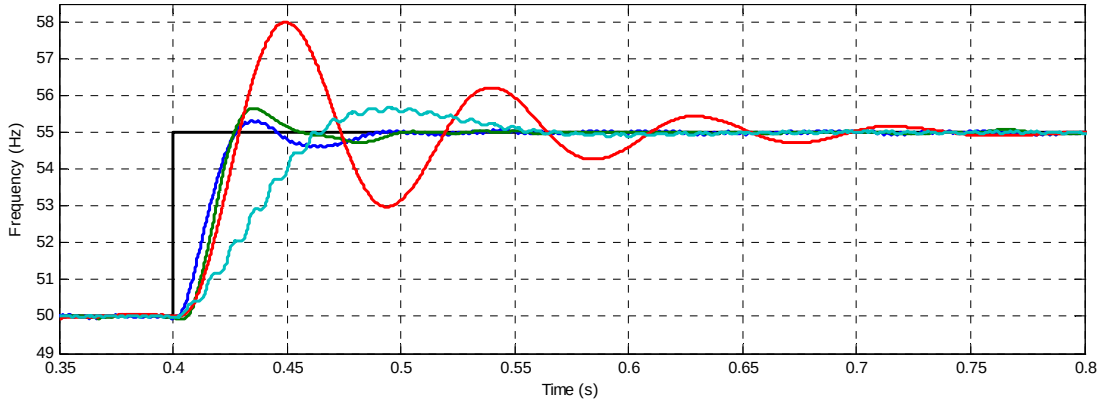

(b)

Fig. 3.30. Grid frequency estimated by the PLL, FLL, KF and EKF, along with the reference value f_1^*, when an abrupt jump in the grid frequency is applied (a) from 50 to 45 Hz and (b) from 50 to 55 Hz.

The study of the calculation of reference currents has been focused on this type of current controller. This chapter has analyzed and compared the performance of four different methods of calculation of reference currents, showing that the one named as *dq_4×4* achieves the best performance in terms of reduction of DC-link voltage oscillation and oscillating active power.

Lastly, an overview of grid synchronization and monitoring techniques has been presented. The four techniques studied have been compared by means of a simulation where an abrupt frequency jump of $\pm 5\ Hz$ has been applied to them, resulting in a better performance of the PLL-based (section 3.3.1) and FLL-based (section 3.3.2) techniques when estimating the grid frequency. Therefore, these two techniques are the ones that have been digitally implemented in the experimental setup to test the frequency-adaptive current controllers developed in the next chapters.

4

Current control based on resonant controllers

Once the current controller has been located inside the control scheme of a VSC in the previous chapter, this is the first chapter of two intended to study two techniques to implement selective harmonic control, namely, resonant control and repetitive control. Therefore, this chapter addresses the study of resonant control.

A thorough analysis of various structures for performing this type of control in power converters is provided, regardless of the application. Each structure is studied both in continuous and discrete time and its corresponding frequency-adaptive algorithm is proposed. The comparison of the performance of each current control scheme is carried out considering a VSC connected in shunt with the grid through an L-filter. Practical details of their digital implementation are also tackled.

4.1. Introduction.

Conventional PI controllers are not able to obtain zero steady-state error under sinusoidal inputs due to its finite gain at non-zero frequencies [Yuan*, et al.*, 2002]. The resonant control originally emerges as an alternative to PI controllers to perform the current control of power converters without the need for an *αβ0* to *dq0* transformation. Thus, no grid synchronization mechanism is needed.

The resonant control obtains a theoretical infinite gain at the frequency of interest. This frequency is also called resonant frequency ($f_o = \omega_o/2\pi\ Hz$) and hence the name of this control. Several works [Mattavelli, 2001; Zmood*, et al.*, 2001; Zmood and Holmes, 2003] have described the resonant control as a displacement of the frequency spectrum of an ideal integrator. This modulation process is shown in Fig. 4.1, where the frequency spectrum is shifted to either side of the origin of frequencies and is centered on the resonant angular frequencies $\pm\omega_o\ rad/s$. In other words, the resonant control is the result of applying the frequency-shift transformation described by (4.1) [Zmood*, et al.*, 2001], where $C_I(s) = 1/s$ is

an ideal integrator, yielding the corresponding transfer function in continuous time described by (4.2).

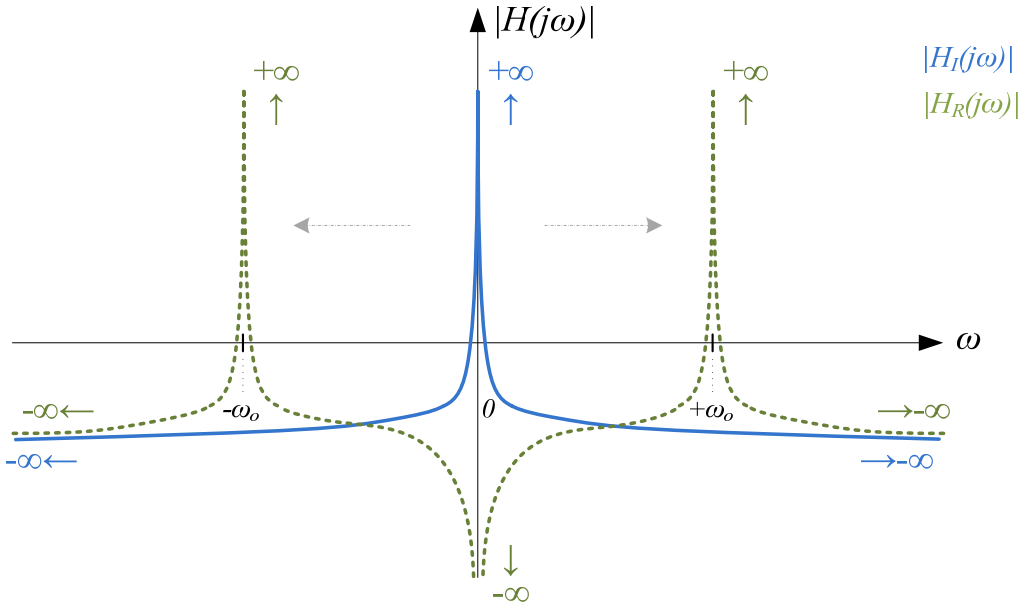

Fig. 4.1. Modulation process that illustrates how resonant control $(H_R(j\omega))$ is derived from integral control $(H_I(j\omega))$ in continuous time. The green and blue arrows indicate where the magnitude of the frequency response tends to.

$$C_R(s) = C_I(s + j\omega_o) + C_I(s - j\omega_o) \tag{4.1}$$

$$C_R(s) = \frac{2s}{s^2 + \omega_o^2} \tag{4.2}$$

Since a resonant controller presents an infinite gain at the frequencies $\pm f_o$, it is able to track (or reject) a sinusoidal signal of frequency f_o with zero steady-state error. This is verified by means of Internal Model Principle (IMP) [Francis and Wonham, 1975], which states that closed-loop characteristic polynomial of a controller achieves a theoretical perfect tracking (or rejection) of the input signal $x(t)$ if the denominator of its Laplace transform $C_R(s)$ contains the denominator of the input signal $X(s)$. It is straightforward to observe that the denominators of resonant controller $C_R(s)$ in (4.2) and cosine Laplace transform $G_{cosine}(s)$ in (4.3) are equal.

$$G_{cosine}(s) = \frac{s}{s^2 + \omega_o^2} \tag{4.3}$$

Starting from this point, many researchers have worked on the design and improvement of different techniques for implementing resonant controllers capable of guaranteeing the stability of the system, even under distorted and unbalanced operating conditions. These techniques can be divided into three categories according to their characteristics at the resonant frequency:

- Resonant control with infinite gain and no phase control at the resonant frequency,
- Resonant control with finite gain and no phase control at the resonant frequency,
- Resonant control with infinite gain and phase control at the resonant frequency.

In the first category we find the Second Order Generalized Integrator (SOGI) [Yuan*, et al.*, 2002; Rodríguez*, et al.*, 2006]. It has an excellent selectivity but in applications where several harmonics have to be compensated, such as an Active Power Filter (APF), the fact of adding more SOGIs in parallel may endanger the system stability. This is due to the lack of phase control of this controller. Some alternatives arise to tackle this problem, which are grouped in the second and third categories.

In the second category, the Second Order Generalized Integrator for Quadrature-Signal Generation (SOGI-QSG) can be found [Rodríguez*, et al.*, 2006]. Its main characteristic is its finite gain at the resonant frequency. This ensures the control stability at the expense of having a very poor performance when it comes to compensation of several harmonics. Therefore, this controller has not been addressed in this Thesis.

Finally, some of the most interesting techniques are covered in the third category. They allow controlling the phase of the open-loop system at the resonant frequency and, by extension, the phase margin. Two techniques are investigated inside this group: Second Order Generalized Integrator with Lead-Lag Network (SOGI-LLN) and Adaptive Feedforward Cancellation (AFC). Both techniques have formerly been applied to the voltage control of a Voltage Source Inverter (VSI) in the works [García-Cerrada*, et al.*, 2004; Malo and Griñó, 2008], and they are now applied to the current control of a VSC connected in shunt with the grid through an L-filter.

These controllers may present different forms but the purpose of all of them is to achieve the maximum possible gain at the resonant frequency while ensuring the system stability with a gain and phase margins reasonable. Their characteristics, parameter tuning and current control schemes are detailed in this chapter, as well as the study of the best digital implementation for each controller. Furthermore, the frequency-adaptive algorithm of each technique is also provided.

4.2. Second Order Generalized Integrator (SOGI).

4.2.1. Continuous-time domain.

The work [Yuan*, et al.*, 2002] introduced the concept of Generalized Integrator (GI) for sinusoidal signals, emphasizing its ability to compensate both positive and negative sequences of the input signal, whereby one GI in the stationary reference frame is equivalent to two ideal integrators in the synchronous reference frame.

A little modification respect to the original topology was presented in [Rodríguez*, et al.*, 2006] for its subsequent use in quadrature-signal generation, giving rise to the so-called SOGI. The difference between the GI described by (4.2) and the SOGI described by (4.4) is the gain. Thus, this structure is more general and can be used both in current control of grid converters taking into account the changes in the gain and in tasks related to grid synchronization [Rodríguez*, et al.*, 2008]. The new transfer function has two poles placed at $\pm j\omega_o$ and a zero in the origin, exactly equal to (4.2). Its continuous time block diagram is represented in Fig. 4.2, where $x(t)$ is the input signal, ε is the error signal and $y(t)$ is the output signal.

$$C_{SOGI}(s) = \frac{s\omega_o}{s^2 + \omega_o^2} \tag{4.4}$$

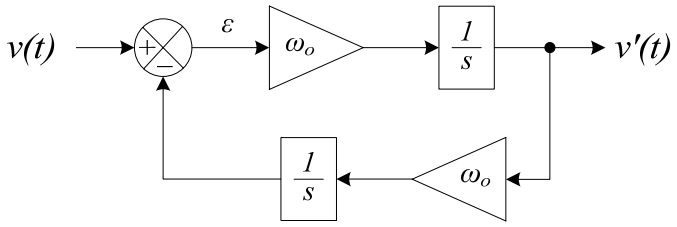

Fig. 4.2. Continuous time SOGI.

The Bode diagram of the SOGI in Fig. 4.3a shows an infinite gain at $\pm f_o = \pm 50\ Hz$ and an inversion of the phase at each zero and pole of the controller, whose locations are shown in the pole-zero map of Fig. 4.3b. Its phase diagram presents zero phase at $\pm f_o$ and $\pm \pi/2\ rad$ at the rest of the frequencies. One of the main characteristics of the SOGI is that it presents a very narrow bandwidth around the resonant frequency f_0, i.e. it is very selective. It also rejects the DC component, since it has a zero placed at $s = 0$ (4.4), thereby it shows an infinite attenuation at $f = 0$. The transfer function has another zero at infinite, hence the magnitude diagram tends to negative values (in dB) when *s* approaches $\pm\infty$. Note that although in a typical Bode diagram the frequency scale is logarithmic, in this case a linear scale has to be used in order to represent the negative frequencies.

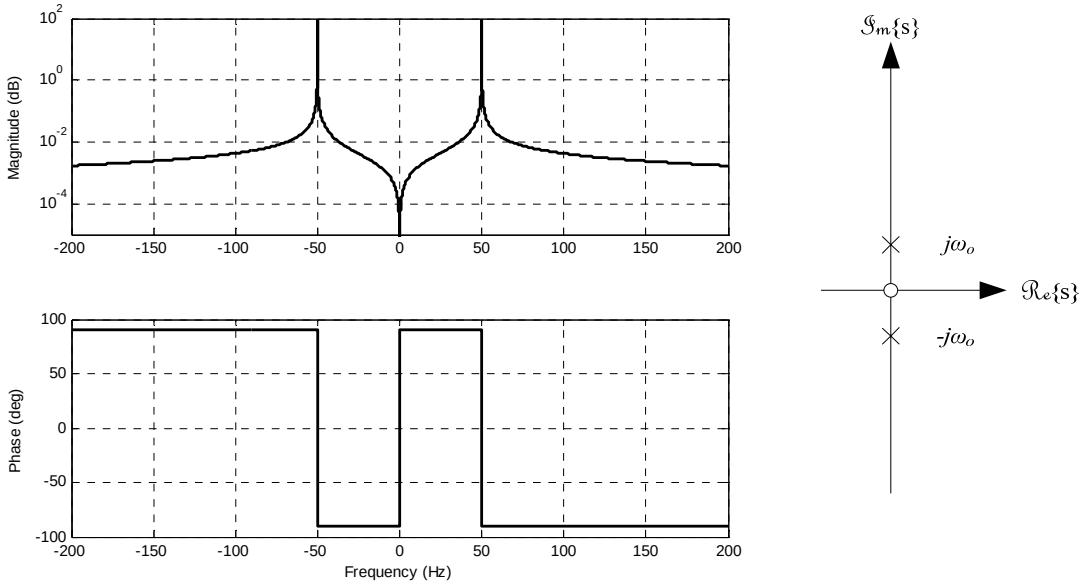

(a) (b)

Fig. 4.3. (a) Bode diagram and (b) pole-zero map of the SOGI in continuous tine.(b)

4.2.2. Discrete-time domain.

There are two options to digitally implement a SOGI: (1) one based on the individual discretization of each continuous time integrator of Fig. 4.2 and (2) another one based on the difference equation of the controller.

4.2.2.1. Individual discretization of the integrators.

For the first option, the discrete integrators of Table 4.1 are employed. The work [Rodríguez*, et al.*, 2008a] presents a set of possible configurations of the discrete SOGI depending on the type of discrete integrator used in the direct gain (from ε to $y(t)$) and the feedback gain (from $y(t)$ to ε).

TABLE 4.1. DISCRETE INTEGRATORS.

Type of integrator	*z-domain equation*	*Difference equation*
Forward Euler	$T(z) = \frac{T_s z^{-1}}{1 - z^{-1}}$	$y[n] = T_s x[n-1] + y[n-1]$
Backward Euler	$T(z) = \frac{T_s}{1 - z^{-1}}$	$y[n] = T_s x[n] + y[n-1]$
Tustin	$T(z) = \frac{T_s}{2} \cdot \frac{1 + z^{-1}}{1 - z^{-1}}$	$y[n] = \frac{T_s}{2}(x[n] + x[n-1]) + y[n-1]$

One of the best configurations is represented in Fig. 4.4, in which backward Euler (BE) integrators are used both in the direct and feedback gains (from now on, BE & BE configuration) and the computational delay is also taken into account, which models the inherent delay produced in the programming process. Its behavior is described by (4.5) and the comparison with the continuous time SOGI is represented in the Bode diagram of Fig. 4.5 for the harmonics of order $h = 1, 7$ and 13. These diagrams show that, as the harmonic order increases, the poles displacement from their ideal locations is higher. This displacement also depends on T_s, as shown in Fig. 4.6 for the fundamental harmonic. The effects described in these two figures are summarized in Fig. 4.7, where the resonant frequency deviation ($\Delta f = f_o' - f_o$, where f_o is the ideal resonant frequency and f_o' is the displaced resonant frequency) is expressed in terms of harmonic order h and sampling period T_s. It can be stated that this discretization option is not suitable when high-order harmonics have to be compensated.

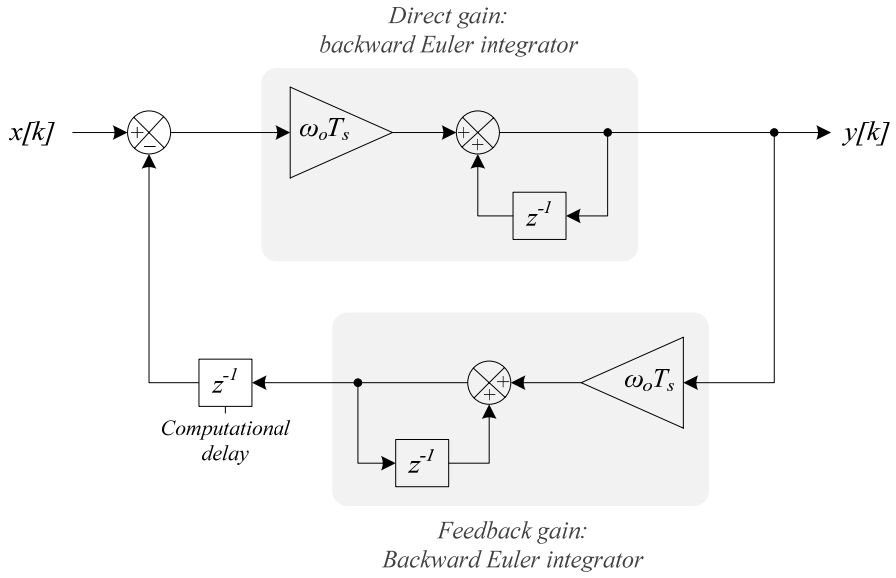

Fig. 4.4. SOGI in discrete time (BE & BE configuration).

$$C_{SOGI}(z) = \frac{\omega_o T_s z(z-1)}{(z-1)^2 + \omega_o^2 T_s^2 z} \tag{4.5}$$

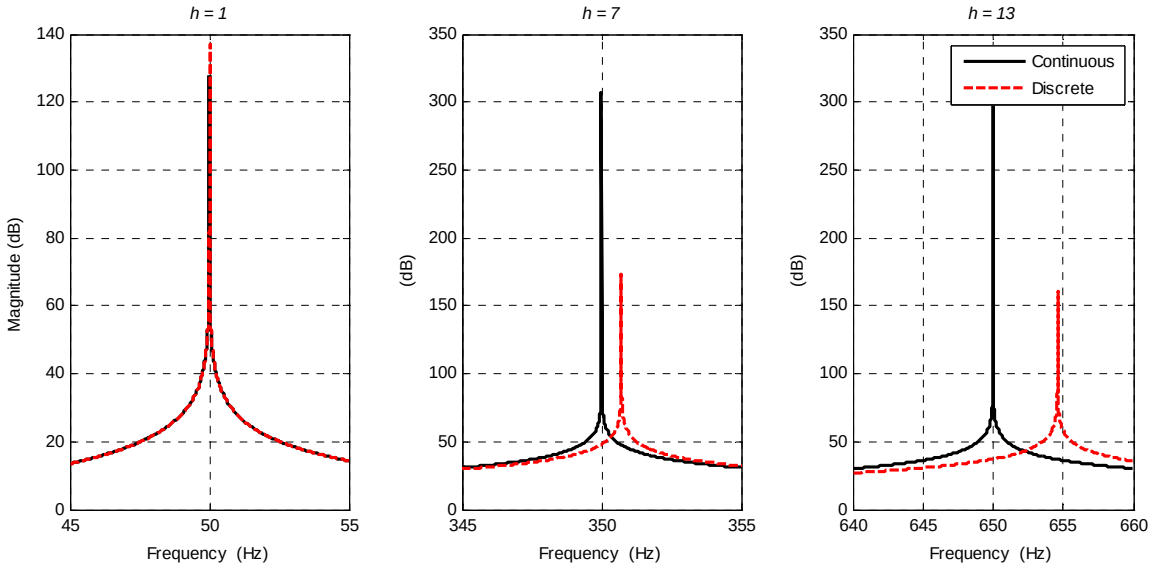

Fig. 4.5. Bode diagram of the SOGI in continuous and discrete time (BE & BE configuration for $T_s = 100\ \mu s$). From left to right: $h = 1$, $h = 7$ and $h = 13$.

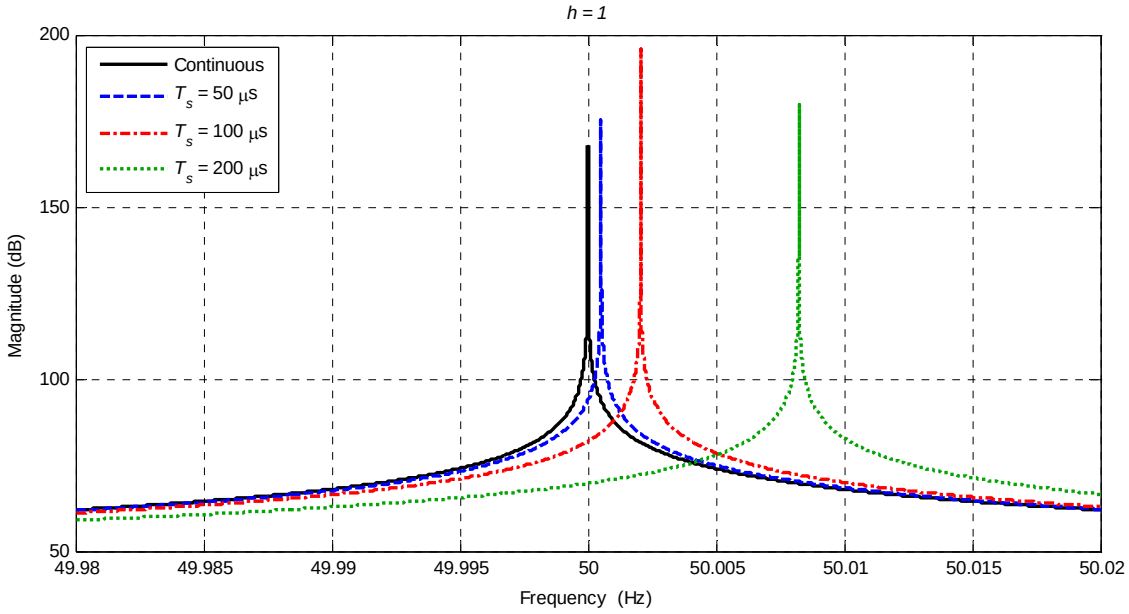

Fig. 4.6. Bode diagram of the SOGI (h = 1) in continuous and discrete time (BE & BE configuration), showing the effect of increasing the sampling period T_s.

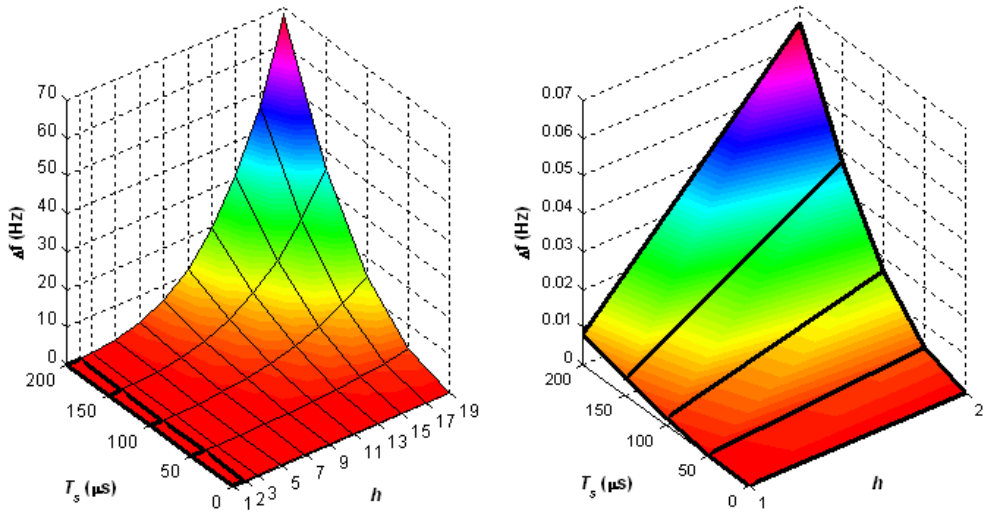

Fig. 4.7. Relationship between resonant frequency deviation Δf, sampling period T_s and harmonic order h in the SOGI in discrete time (BE & BE configuration). Right-side diagram represents a zoom of the left-side diagram into the low-order harmonics $h = 1, 2$.

4.2.2.2. Difference equation of the controller.

Regarding the second option for discretizing the continuous time SOGI, Table 4.2 collects the most common discretization techniques for continuous time transfer functions and their correspondence between the s-plane and the z-plane. The result of applying these techniques to the continuous time SOGI of (4.4) is shown in Table 4.3, where k' in the Matched Pole-Zero (MPZ) transformation is adjusted in order to have a certain gain for some concrete frequencies.

All discrete SOGIs in Table 4.3 present a general structure like the one described by (4.6), where $X(z)$ and $Y(z)$ are the z-transforms of the input and output signals, respectively, and each coefficient depends on the applied discretization method (some of them can be zero). Therefore, the output of each discrete SOGI can be obtained by means of (4.7). It is advisable to normalize the controller coefficients respect to b_0, so that the division $1/b_0$ can be avoided when implementing the controller in a digital platform.

$$\frac{Y}{X}(z) = \frac{a_0 - a_1 z^{-1} - a_2 z^{-2}}{b_0 - b_1 z^{-1} - b_2 z^{-2}} \tag{4.6}$$

$$y[k] = \frac{1}{b_0}(a_0 x[k] - a_1 x[k-1] - a_2 x[k-2] + b_1 y[k-1] + b_2 y[k-2]) \tag{4.7}$$

TABLE 4.2. METHODS FOR DISCRETIZING CONTINUOUS TIME TRANSFER FUNCTIONS.

Method	*Relation*	*Notation*
Forward Euler (FE)	$s = \frac{1 - z^{-1}}{T_s z^{-1}}$	$C_{FE}(z)$
Backward Euler (BE)	$s = \frac{1 - z^{-1}}{T_s}$	$C_{BE}(z)$
Tustin (TUS)	$s = \frac{2}{T_s} \cdot \frac{1 - z^{-1}}{1 + z^{-1}}$	$C_{TUS}(z)$
Tustin with prewarping (TPW)	$s = \frac{\omega_0}{tan\left(\frac{\omega_0 T_s}{2}\right)} \cdot \frac{1 - z^{-1}}{1 + z^{-1}}$	$C_{TPW}(z)$
Zero-Order Hold (ZOH)	$H(z) = (1 - z^{-1}) \cdot \mathbb{Z}\left\{\mathcal{L}^{-1}\left\{\frac{H(s)}{s}\right\}\right\}$	$C_{ZOH}(z)$
Triangle approximation (noncausal First-Order Hold, FOH)	$H(z) = \frac{(z-1)^2}{T_s z} \cdot \mathbb{Z}\left\{\mathcal{L}^{-1}\left\{\frac{H(s)}{s^2}\right\}\right\}$	$C_{FOH}(z)$
Matched pole-zero (MPZ)	$z = e^{T_s s}$	$C_{MPZ}(z)$
Impulse-invariant (IMP)	$H(z) = \mathbb{Z}\{\mathcal{L}^{-1}\{H(s)\}\}$	$C_{IMP}(z)$

Similarly to Fig. 4.7, Fig. 4.8 shows the effect of h and T_s in the resonant frequency displacement Δf with this type of discretization. There are four pairs of diagrams, two on the top and two on the bottom, each of them corresponding to (i) forward Euler (FE), (ii) backward Euler (BE), (iii) Tustin (TUS) and (iv) Tustin with prewarping (TPW), Zero-Order Hold (ZOH), triangle approximation (noncausal first-order hold, FOH), MPZ and impulse-invariant (IMP) methods. In each pair of diagrams, the one on the right is a zoom of the one on the left into the low-order harmonics $h = 1$ and 2. The difference between each pair of diagrams lies in its pole locus.

The worst results are obtained with FE and BE methods. This is because these techniques introduce damped poles, which do not assure perfect tracking [Zmood and Holmes, 2003]. Poles must be placed in the unit circumference, which corresponds to a zero damping factor (infinite gain). FE maps the poles outside of the unit circle, whereas BE moves them toward the origin, causing a damping factor different from zero [Yepes*, et al.*, 2010].

TABLE 4.3. DISCRETE TIME TRANSFER FUNCTIONS OF THE SOGI.

Method	***z-domain equation***
Forward Euler (FE)	$C_{FE}(z) = \omega_o T_s \cdot \frac{z-1}{z^2 - 2z + \omega_o^2 T_s^2 + 1}$
Backward Euler (BE)	$C_{BE}(z) = \frac{\omega_o T_s}{1+\omega_o^2 T_s^2} \cdot \frac{z^2 - z}{z^2 - \frac{2}{1+\omega_o^2 T_s^2} z + \frac{1}{1+\omega_o^2 T_s^2}}$
Tustin (TUS)	$C_{TUS}(z) = \frac{2\omega_o T_s}{4+\omega_o^2 T_s^2} \cdot \frac{z^2 - 1}{z^2 + \frac{2\omega_o^2 T_s^2 - 8}{4+\omega_o^2 T_s^2} z + 1}$
Tustin with prewarping (TPW)	$C_{TPW}(z) = \frac{sin(\omega_o T_s)}{2} \cdot \frac{z^2 - 1}{z^2 - 2\,cos(\omega_o T_s)\,z + 1}$
Zero-Order Hold (ZOH)	$C_{ZOH}(z) = sin(\omega_o T_s) \cdot \frac{z-1}{z^2 - 2\,cos(\omega_o T_s)\,z + 1}$
Triangle approximation (noncausal First-Order Hold, FOH)	$C_{FOH}(z) = \frac{1 - cos(\omega_o T_s)}{\omega_o T_s} \cdot \frac{z^2 - 1}{z^2 - 2\,cos(\omega_o T_s)\,z + 1}$
Matched pole-zero (MPZ)	$C_{MPZ}(z) = k' \cdot \frac{z-1}{z^2 - 2\,cos(\omega_o T_s)\,z + 1}$
Impulse-invariant (IMP)	$C_{IMP}(z) = \omega_o T_s \cdot \frac{z^2 - cos(\omega_o T_s) z}{z^2 - 2\,cos(\omega_o T_s)\,z + 1}$

Despite being one of the most used discretization techniques in practical applications, TUS transformation introduces a pole displacement. In fact, it introduces the highest pole displacement of the discretization techniques that obtains undamped poles, namely: ZOH, FOH, TUS, TPW, IMP, MPZ and BE & BE. The latter also introduces a displacement, but to a lower extent.

In order to decide which method accomplishes a better discretization, the controller phase in the vicinity of the resonant frequency is analyzed in Fig. 4.9. The pairs of techniques that have the same phase are TPW & FOH (red lines) and ZOH & MPZ (green lines). This last pair has an extra phase shift at f_o compared to the continuous time phase (black line), which is indicated in this figure as δ_1 in *zoom 1* and δ_2 in *zoom 2*. Furthermore, this phase lag becomes greater as $\omega_o T_s$ increases. Therefore, the implementation of a SOGI by means of these two techniques may lead to instability and should be avoided. Concerning TPW & FOH, they show the most similar behavior to the continuous transfer function. IMP (blue line) has the advantage of introducing less phase lag at the rest of frequencies, thereby allowing for a larger phase margin. However, other facts have to be taken into account. Impulse-invariant mapping introduces a shift in the DC gain of the discretized system. In addition, it introduces a phase

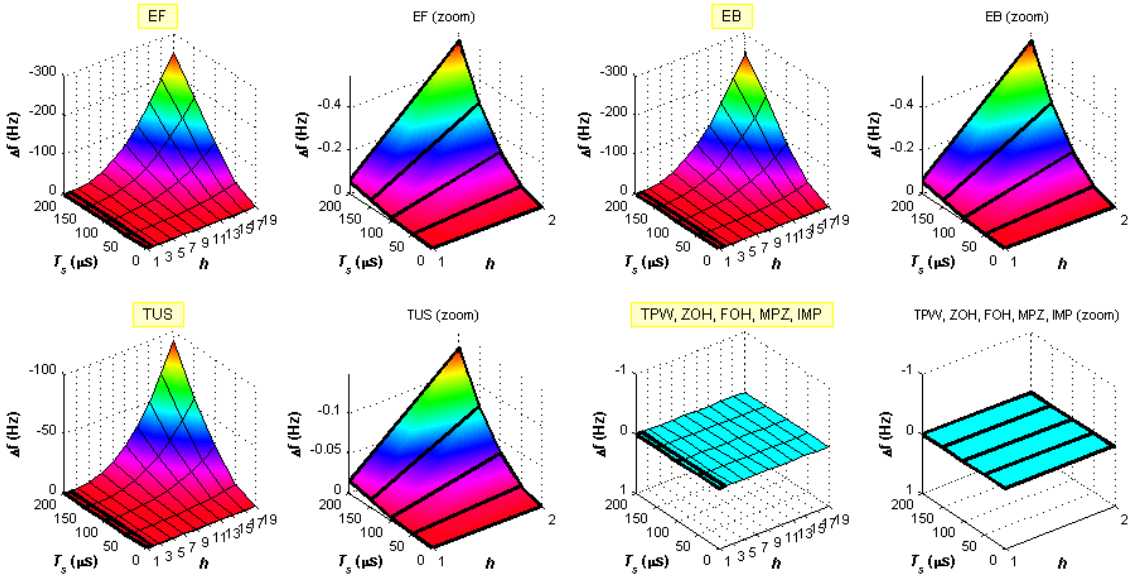

Fig. 4.8. Relationship between resonant frequency deviation Δf, sampling period T_s and harmonic order h in the SOGI in discrete time (difference equation). In each pair of diagrams, right-side diagram represents a zoom of the left-side diagram into the low-order harmonics $h = 1, 2$.

mismatch at higher frequencies. The phase mismatch results from alias effects and this effect becomes more pronounced as T_s increases [Franklin, *et al.*, 1998].

In conclusion, the most suitable techniques for discretizing a SOGI are Tustin with prewarping and triangle approximation (noncausal first-order hold) methods.

4.2.3. Frequency-adaptive algorithm and computational burden.

The structure based in individual discretization of integrators is usually considered as the most suitable for performing frequency-adaptation, since no explicit trigonometric functions are needed [Yepes, *et al.*, 2010]. Nevertheless, current high-speed digital platforms such as Digital Signal Processors (DSPs) and Field Programmable Gate Arrays (FPGAs) are capable of carrying out a few trigonometric functions without jeopardizing the total execution time. It has already been proved that the discrete SOGI based on discrete integrators is not a suitable option when compensating several harmonics (section 4.2.2.1), hence it is worth implementing a discrete SOGI with one of the two discretizing techniques selected in the previous section in applications like APFs.

The way to implement the frequency-adaptive algorithms is quite straightforward once we have the difference equation for both TPW and FOH (Table 4.3). Both discrete transfer functions $C_{TPW}(z)$ and $C_{FOH}(z)$ can be generally expressed as:

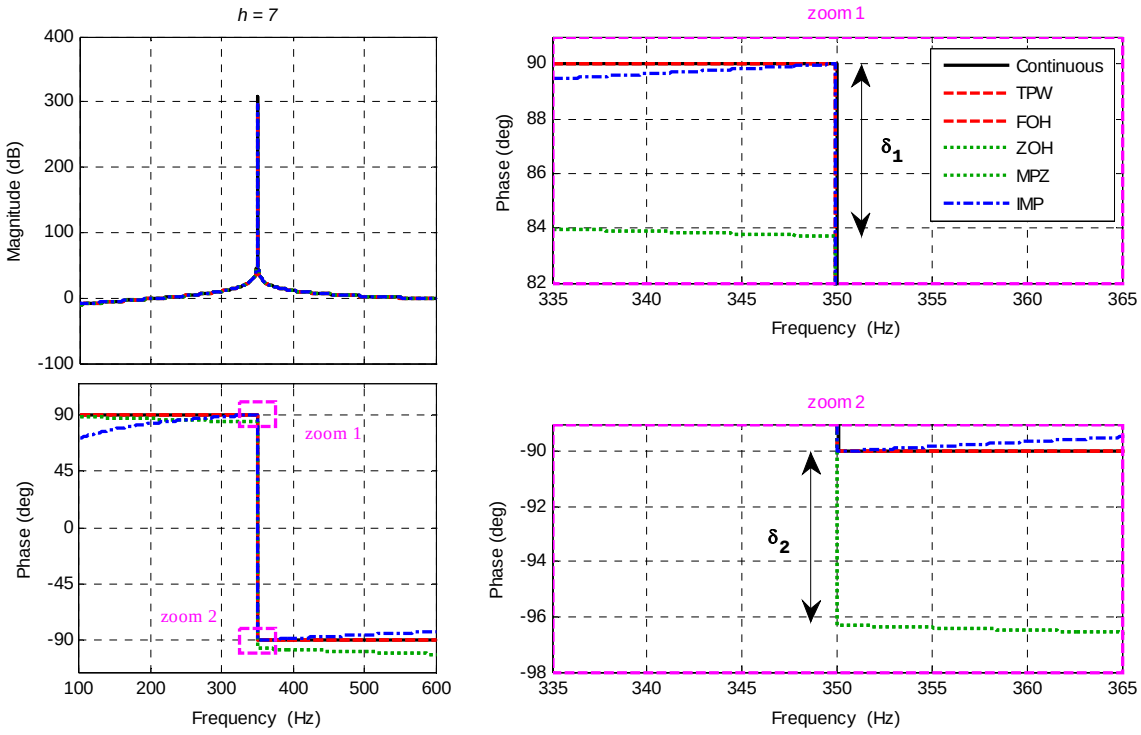

Fig. 4.9. Bode diagram of the discrete SOGIs that have undamped poles: TPW, FOH, ZOH, MPZ and IMP. Special attention is given to the vicinity of the resonant frequency $f_o = 350\ Hz$ (zooms 1 and 2). δ_1 and δ_2 indicates the extra phase shift (in degrees) added by ZOH and MPZ techniques at the resonant frequency.

$$C(z) = \frac{a(1 - z^{-2})}{1 - bz^{-1} + z^{-2}} \tag{4.8}$$

where $a|_{TPW} = sin(\omega_o T_s)/2,\ a|_{FOH} = 1 - cos(\omega_o T_s)/\omega_o T_s,\ b = 2\,cos(\omega_o T_s)$ for both techniques and $\omega_o = h\hat{f}$. From (4.8) it is simple to obtain their difference equation (4.9), whose schematic representation is depicted in Fig. 4.10.

$$y[k] = a \cdot (x[k] - x[k-2]) + b \cdot y[k-1] - y[k-2] \tag{4.9}$$

In some cases, calculation of trigonometric functions can be avoided by using look-up tables. In the case at handle, the values of coefficients a and b are so small that tables with a very high accuracy would be necessary, i.e. with large sizes. If the digital platform has enough available memory, this option can be considered. The type of memory has to be taken into account as well, since the access times may differ from one to another and influence the execution time.

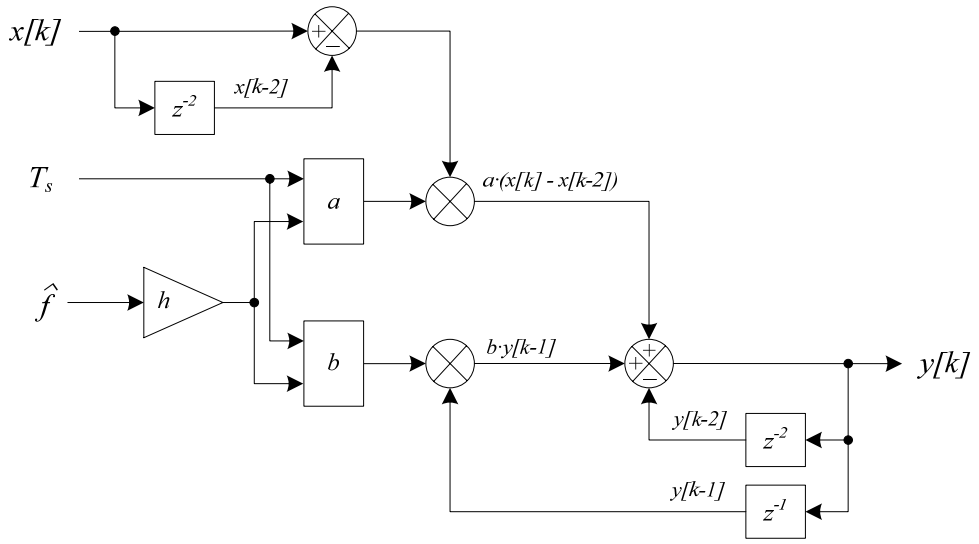

Fig. 4.10. Frequency-adaptive SOGI for both TPW and FOH discretization methods.

Regarding computational burden, both methods perform n times the multiplication $\omega_o T_s = 2\pi h \hat{f} T_s$ and a trigonometric function ($sin(\omega_o T_s)$ or $cos(\omega_o T_s)$) in the calculation of coefficient a, where n is the number of harmonics to be compensated. TPW also performs a multiplication ($a|_{TPW} = \mathbf{0.5} \cdot sin(\omega_o T_s)$) and FOH performs a subtraction and a division ($a|_{FOH} = (\mathbf{1} - cos(\omega_o T_s))/\boldsymbol{\omega_o T_s}$), which leads to a slightly higher computational burden. Obviously, this type of implementation results in an increased consumption of resources, but can be addressed by most of today's digital processors. Note that the factor $\omega_o T_s$ involves only the multiplications of two terms, $\hat{f}$ and $2\pi h T_s$. The latter is stored in the processor memory as a single value.

4.3. Second Order Generalized Integrator with Lead-Lag Network (SOGI-LLN).

4.3.1. Continuous-time domain.

As stated earlier, controllers like SOGI, which introduce an infinite gain at the resonant frequency, can make the system unstable as they do not make any control in the phase lag introduced. Thus, some modifications can be made to the original SOGI in order to control the phase shift. This technique was presented in [García-Cerrada*, et al.*, 2004] and it was applied to the voltage control of a VSI. In this Thesis, this type of controller is adapted to the current control of a VSC connected in shunt with the grid through an L-filter.

Fig. 4.11 shows the connection of the lead-lag network $\left(C_a(s)\right)$ to the SOGI plus the integral gain k_{ih} $\left(C_b(s)\right)$. The transfer function on the resulting structure is given by (4.10). The lead-lag network controls the phase shift by means of the parameters f and α_c.

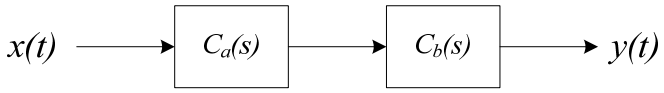

Fig. 4.11. SOGI-LLN in continuous time.

$$C(s) = \frac{1 + \frac{\alpha_c}{\omega_o} s}{1 + f\frac{\alpha_c}{\omega_o} s} \cdot \frac{k_{ih}\omega_o s}{s^2 + \omega_o^2} = C_a(s) \cdot C_b(s) \tag{4.10}$$

The design of $C_a(s)$ can be based on the frequency response of the open-loop transfer function. It is useful to calculate $C_a(s)$ together with k_{ih} to achieve the required phase margin (Pm) at the gain-crossover frequency (ω_h' in p.u.):

$$C_a(j\omega_h') = -\frac{e^{jPm}}{G(j\omega_h')C_b(j\omega_h')} \tag{4.11}$$

where $G(s)$ is the continuous-time plant transfer function, $G(s) = 1/(R + Ls)$. It can be easily seen that there are two gain-crossover frequencies: one smaller than ω_o and another one bigger than ω_o. The phase margin should be set at the frequency at which the Nyquist frequency plot of the open-loop system is closer to -1 in the complex plane to guarantee the required stability margin. In any case, the use of a first-order system like $C_a(s)$ limits the possible phase lead (or lag) to something less than 90° [García-Cerrada*, et al.*, 2004].

Two equations (magnitude and phase) with three unknowns (k_{ih}, α_c and f) can be extracted from (4.10). The parameter f is usually set following this rule: set $f < 1$ if a phase lead is needed and $f > 1$ if a phase lag is needed. This design method is carried out for each SOGI-LLN, being the resulting design equations (4.12) to (4.14).

The phase margin Pm and the gain-crossover pulsation ω_h can be set independently for each harmonic. The selectivity of each SOGI-LLN decreases as ω_h increases, but the controller becomes faster and the settling time decreases. Therefore, a trade-off between accuracy and system speed has to be made when choosing the controller parameters. With these parameters, the Bode diagram and pole-zero map of the continuous time SOGI-LLN is represented in Fig. 4.12.

$$k_{ih} = -\frac{\left(\omega_o^2 - \omega_h^2\right)\sqrt{R^2 + (\omega_h L)^2}}{\omega_h \omega_o} \sqrt{\frac{1 + (f\alpha_c\omega_h)^2}{1 + (\alpha_c\omega_h)^2}} \tag{4.12}$$

$$\alpha_c = \frac{\omega_h(1-f) \pm \sqrt{\left(\omega_h(1-f)\right)^2 + 4x^2 f\omega_h^2}}{2xf\omega_h^2} \tag{4.13}$$

$$x = \tan\left(Pm + \pi/2 + atan(\omega_h L/R)\right) \tag{4.14}$$

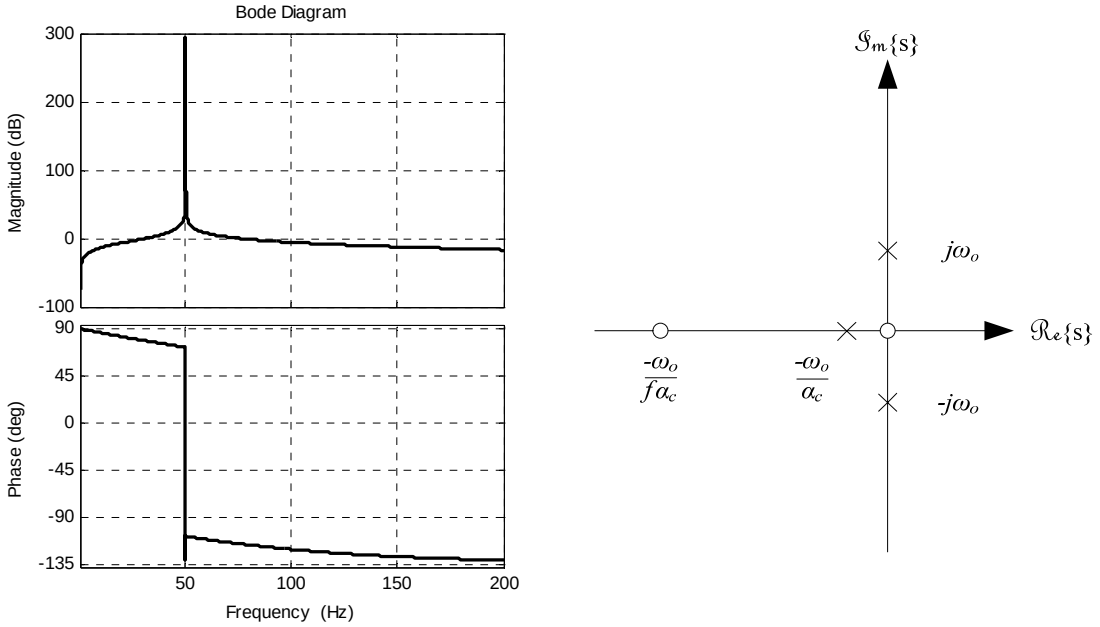

Fig. 4.12. (a) Bode diagram and (b) pole-zero map of the SOGI-LLN in continuous time.

4.3.2. Discrete-time domain.

The most critical part of this controller is $C_b(s)$, which includes the SOGI, since the selectivity of the controller at the resonant frequency must be assured. Consequently, the discretization methods employed in the SOGI-LLN are the same as the ones selected in Section 4.2.2.2 for the SOGI.

Among FOH and TPW, it is convenient to choose the discretization technique that obtains the simplest coefficients calculation. This is achieved by TPW, whose mathematical expression for the discrete SOGI-LLN is shown in Table 4.4. The order of the controller is larger than the SOGI due to lead-lag network added.

TABLE 4.4. DISCRETE TIME TRANSFER FUNCTION OF THE SOGI-LLN.

Method	*z-domain equation*
Tustin with prewarping (TPW)	$C_{TPW}(z) = \frac{k_{ih}\sin(\omega_o T_s)}{2} \cdot \frac{a_0 + a_1 z^{-1} + a_2 z^{-2} + a_3 z^{-3}}{b_0 + b_1 z^{-1} + b_2 z^{-2} + b_3 z^{-3}}$ $a_0 = -a_2 = a + b$ $a_1 = -a_3 = a - b$ $a = \sin\left(\frac{\omega_o T_s}{2}\right)$ $b = \omega_o \alpha_c \cos\left(\frac{\omega_o T_s}{2}\right)$

4.3.3. Frequency-adaptive algorithm and computational burden.

Looking at the design equations of the SOGI-LLN ((4.12) to (4.14)), it is clear that this resonant controller is not suitable for frequency-adaptation. Its equations involve the use of several multiplications, divisions, powers and square roots. This computational burden is even higher as the number of harmonics to compensate increases, which makes it non-viable.

Therefore, this resonant controller is only a good choice when no frequency-adaptation is required and its coefficients are calculated offline.

4.4. Adaptive Feedforward Cancellation (AFC).

4.4.1. Discrete-time domain.

The AFC was directly studied in discrete time in [Malo and Griñó, 2008] and it was applied to a voltage control of a DC-AC voltage inverter, based on the work [Byl*, et al.*, 2005]. In this Thesis it is applied to the current control of a VSC connected in shunt with the grid through an L-filter.

This controller shows a good performance in order to selectively track periodic input signals. In continuous time, the advantage on the use of the AFC control structure lies in the placement of an infinite gain on the open-loop transfer function at the desired ω_o pulsation by means of the $R_o(s)$ resonator [Malo and Griñó, 2008]. By following the IMP, perfect tracking at such frequency can be expected. Its discrete time behavior is described by (4.15) and represented in Fig. 4.13, where $H(z)$ is a backward Euler integrator. The Bode diagram of the resonator $R_1(z)$ is shown in Fig. 4.14. The main difference between the continuous and the discrete time realizations of the AFC controller resides in the construction of the $R_o(z)$ resonator modules. In (4.15), k_{ih} is the integral gain and φ_o is the phase shift parameter for

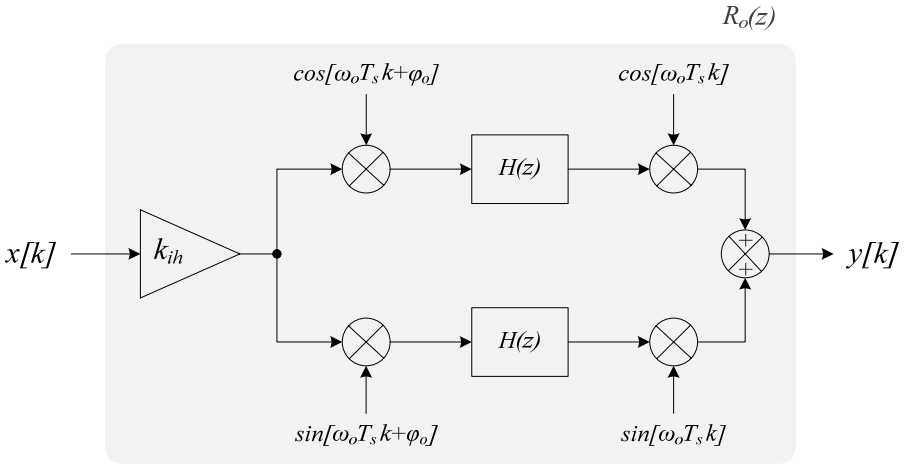

Fig. 4.13. AFC in discrete time.

$$R_o(z) = k_{ih}\frac{\cos(\varphi_o)\,z^2 - \cos(\omega_o T_s + \varphi_o)\,z}{z^2 - 2\cos(\omega_o T_s)\,z + 1} \tag{4.15}$$

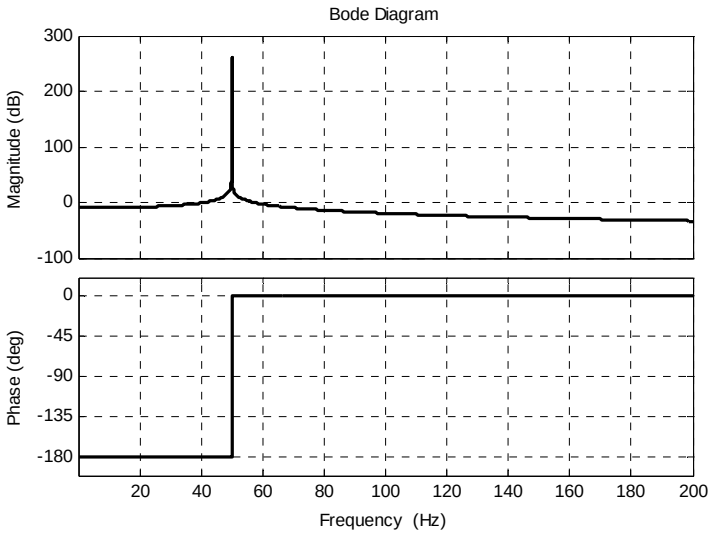

Fig. 4.14. Bode diagram of the AFC in discrete time.

the h^{th} resonator in radians.

The analysis of (4.15) in the vicinity of ω_o yields that the phase shift of the resonator at the resonant pulsation ω_o is:

$$\angle R_o\left(e^{j\omega_o T_s}\right) = -\varphi_o \tag{4.16}$$

Besides, the phase shift in (4.15) and (4.16) has to be chosen as:

$$\varphi_o = \angle G(z_o) \tag{4.17}$$

where $z_o = e^{j\omega_o T_s}$ and $G(z)$ is the discrete time plant model without taking into account the computational delay. Therefore, this tuning guideline allows achieving zero phase in the open-loop transfer function at the resonant pulsation ω_o.

The integral gain is related to steady-state error and the settling time. The bigger it is, the faster the system is and the lower the steady-state error, but a lower gain and phase margin is achieved.

Since this controller is directly designed in discrete time, the discrete transfer function of the plant $G(z)$ is used to calculate the controller parameters. This transfer function is described by (4.18).

$$G(z) = \frac{b}{z - a} \tag{4.18}$$

where $a = e^{-(RT_s/L)}$ and $b = (1 - a)/R$.

4.4.2. Frequency-adaptive algorithm and computational burden.

The discrete transfer function $R_o(z)$ of (4.15) can be generally expressed as:

$$C(z) = \frac{a - bz^{-1}}{1 - bz^{-1} + z^{-2}} \tag{4.19}$$

where $a = cos(\varphi_o)$, $b = \cos(\omega_o T_s + \varphi_o)$ and $c = 2\,cos(\omega_o T_s)$. From (4.19) it is simple to obtain its difference equation (4.20), whose schematic representation is depicted in Fig. 4.15.

$$y[k] = k_{ih} \cdot (a \cdot x[k] - b \cdot x[k-1]) + c \cdot y[k-1] - \ y[k-2] \tag{4.20}$$

It has been assumed that the only modifiable parameters of the AFC are k_{ih} and ω_o, but the plant phase at the resonant frequency (φ_o) also depends on the frequency. However, the change that this parameter is going to suffer due to frequency variations can be considered negligible, since the phase of this type of plants does not change so abruptly. Furthermore, the maximum frequency drift that a VSC must handle generally does not exceed 2 or 3 Hz.

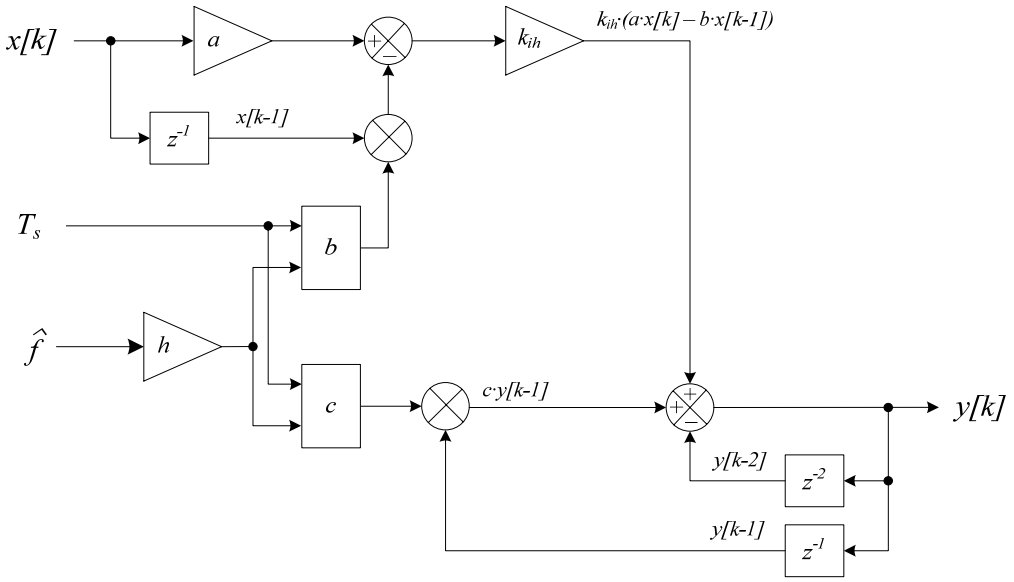

Fig. 4.15. Frequency-adaptive AFC.

4.5. Current control scheme.

The generic current control scheme based on resonant controllers that has been used in this Thesis is shown in Fig. 4.16, both in $\alpha\beta$-axes (Fig. 4.16a) and dq-axes (Fig. 4.16b). Usually, the configuration based on a resonant controller plus a proportional gain in parallel is called as *proportional + resonant control*. Table 4.5 compares the main features of these two implementations specifying their input signals, output signal, controllers employed, usage of antiwindup mechanism and compensation of cross-coupling between axes.

The active current component needed to keep charged the DC-link capacitor at a specified voltage and the compensation the reactive current is carried out by the PI controller in dq-axes and the resonant controller ω in $\alpha\beta$-axes. The proportional constant of the PI controller is adjusted in order to help decreasing the settling time. Similarly, a proportional constant k_p is added to the resonant controller ω for the same purpose.

The blocks 6ω, 12ω and 18ω correspond to the resonant controllers tuned at $h = 6, 12$ and 18, respectively. They all include an integral gain and can be implemented with any of the structures studied in this chapter, namely, SOGI, SOGI-LLN and AFC.

Due to the transformation of the current or the error signal to dq-axes, the order of the typical harmonics in a power system suffers the transformations indicated in Table 4.6. For example, the negative-sequence harmonic of order 5 turns into negative-sequence harmonic of order 6, whereas the positive-sequence harmonic of order 7 turns into positive-sequence harmonic of order 6. Since resonant controllers are able to compensate both positive and negative sequences of its input signal, only a resonant controller tuned at $h = 6$ is needed to

TABLE 4.5. COMPARISON OF THE FEATURES OF THE CURRENT CONTROL SCHEMES IMPLEMENTED IN $\alpha\beta$ AND dq-AXES.

	αβ-axes	***dq-axes***
Inputs	Reference current, $i^*_{\alpha\beta}$ Measured current, $i_{\alpha\beta}$ Limited voltage reference, $u^*_{\alpha\beta\_lim}$ PCC voltage positive sequence, $u^+_{\alpha\beta}$ Estimated PCC phase angle, $\hat{\theta}$	Reference current, i^*_{dq} Measured current, i_{dq} Limited voltage reference, $u^*_{dq\_lim}$ PCC voltage positive sequence, u^+_{dq}
Output	Reference voltage, $u^*_{\alpha\beta}$	Reference voltage, u^*_{dq}
Controllers	Proportional constant, k_p Resonant controllers, $\omega, 6\omega, 12\omega, 18\omega$	PI controller Resonant controllers, $6\omega, 12\omega, 18\omega$
Antiwindup	Yes, applied to the integral path of ω	Yes, applied to the integral path of PI
Compensation of cross-coupling between axes	Not required	Yes
Compensation of negative sequence	Performed by resonant controller ω	Necessary to add 2ω in parallel

TABLE 4.6. HARMONIC SEQUENCES IN THREE-PHASE POWER SYSTEMS.

Harmonic order in αβ-axes	***Harmonic order in dq-axes rotating at ω_o***
Positive and negative sequence: 1	0
Negative sequence: $6k-1$ $(k \in \mathbb{Z}-\{0\})$	Negative sequence: $6k$ $(k \in \mathbb{Z}-\{0\})$
Positive sequence: $6k+1$ $(k \in \mathbb{Z}-\{0\})$	Positive sequence: $6k$ $(k \in \mathbb{Z}-\{0\})$

compensate both harmonics. Therefore, the fact of working in dq-axes allows halving the number of resonant controllers needed compared to $\alpha\beta$-axes.

The Bode diagram of the open-loop transfer function is a graphical and useful tool to compare the performance of several systems as a previous study. This diagram is represented in Fig. 4.17a for a current control scheme in dq-axes (compensating the harmonics of order $h = 0, 6, 12$ and 18) based on each of the resonant controllers previously studied. The frequency range goes from $1\,Hz$ to $f_s/2\ Hz$ (Nyquist frequency), being the sampling frequency $f_s = 10\ kHz$. All of them present gain peaks at the resonant frequencies, which are

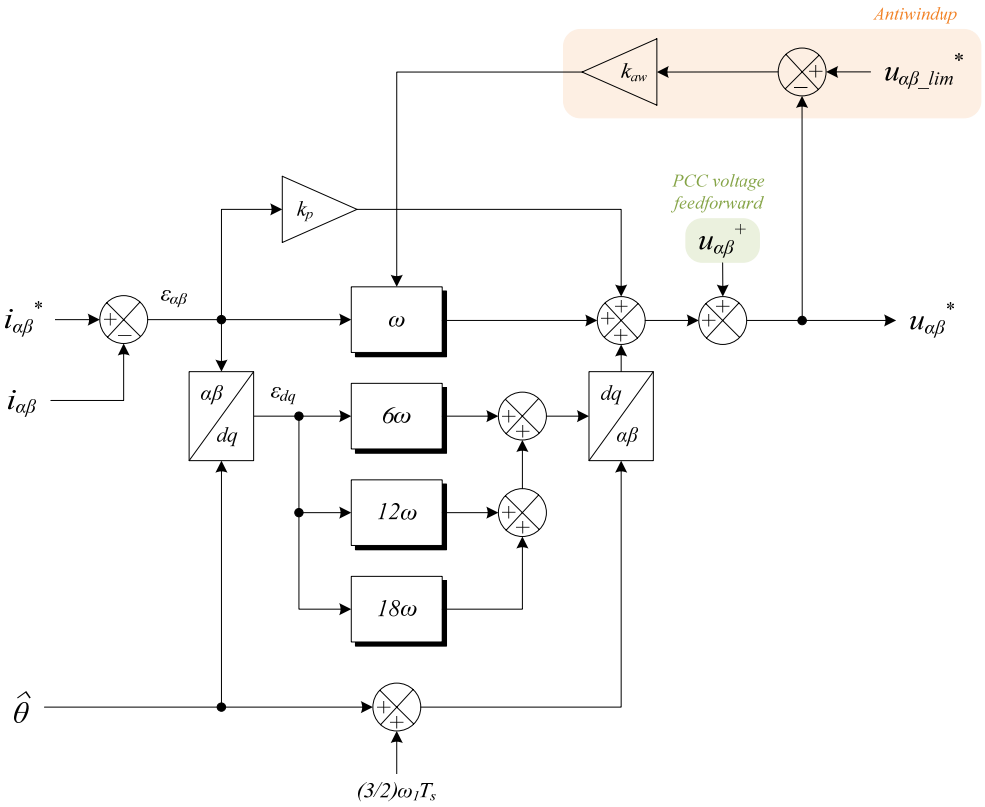

(a)

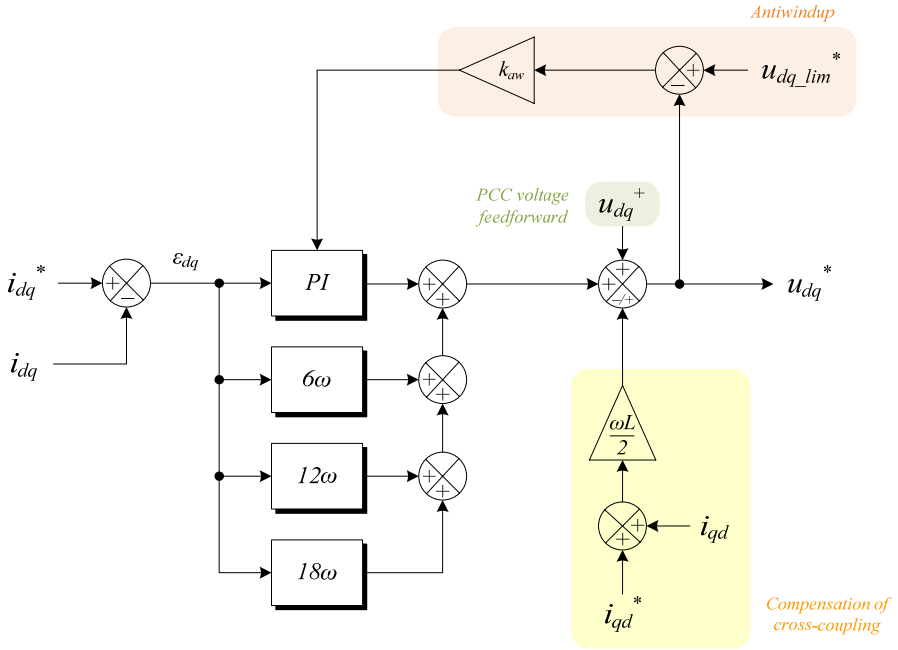

(b)

Fig. 4.16. Current control scheme based on resonant controllers in (a) $\alpha\beta$-axes and (b) dq-axes.

at $300\ Hz$ $(h = 6)$, $600\ Hz$ $(h = 12)$ and $900\ Hz$ $(h = 18)$. They also show a very high DC gain, since the current control scheme includes an integrator. SOGI and SOGI-LLN (both discretized with TPW, since the differences with FOH are almost negligible) are the ones that have higher gains at the resonant peaks, while AFC has higher selectivity around these resonant frequencies. Furthermore, AFC also presents lower gain at the frequencies between the resonant frequencies.

The Nyquist diagram of each open-loop transfer function is represented in Fig. 4.17b (and a zoom in the stability margins in Fig. 4.17c), showing the weak point of the SOGI. It has the lowest phase margin $(15.7°)$, whereas SOGI-LLN and AFC have almost the same $((24.9°)$ and $(24.2°)$, respectively). As the number of harmonics to compensate increases, the phase margin becomes even lower. The same conditions operates on the gain margin: $2.35\ dB$ (SOGI), $3.17\ dB$ (SOGI-LLN) and $3.45\ dB$ (AFC).

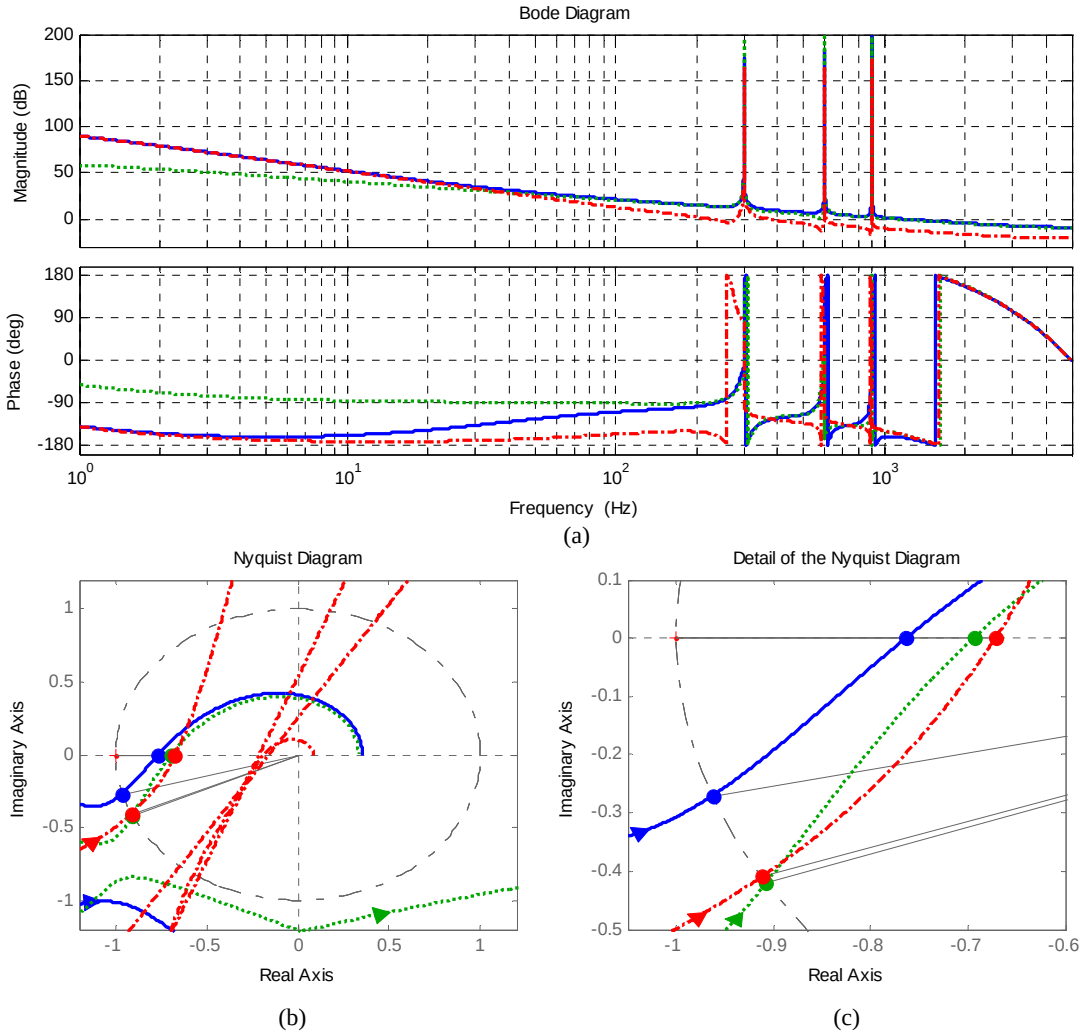

Fig. 4.17. (a) Bode diagram of the open-loop transfer function, (b) Nyquist diagram of the open-loop transfer function, (c) zoom of the Nyquist diagram in the stability margins of the current control scheme in *dq*-axes $(h = 0, 6, 12, 18)$ based on SOGI (discretized with TPW), SOGI-LLN (discretized with TPW) and AFC.

Fig. 4.18 shows the error signals in dq-axes after applying an amplitude jump of 150 % at $t = 0.5\ s$ to the harmonics (a) $h = 1$, (b) $h = 1, 5, 7$, (c) $h = 1, 11, 13$ and (d) $h = 1, 17, 19$. The amplitude level for each harmonic is $1/h\ p.u.$ This clearly shows that the AFC obtains the highest selectivity at the expense of having the highest settling time. Both SOGI and SOGI-LLN have similar behaviors under these circumstances.

All the performance and stability indicators described in the above paragraphs are collected in Table 4.7. These values numerically verify what has been stated in the preceding paragraphs by means of the settling time, maximum overshoot and minimum gain and phase margins. The settling time has been calculated as the time after which the output remains within $\pm 2\%$ (when the input is a unity step). SOGI-LLN is placed in an intermediate place, with a settling time of 16.7 ms and an overshoot of 65.32 %. The SOGI has a settling time of 13.3 ms and an overshoot of 86.31 %.

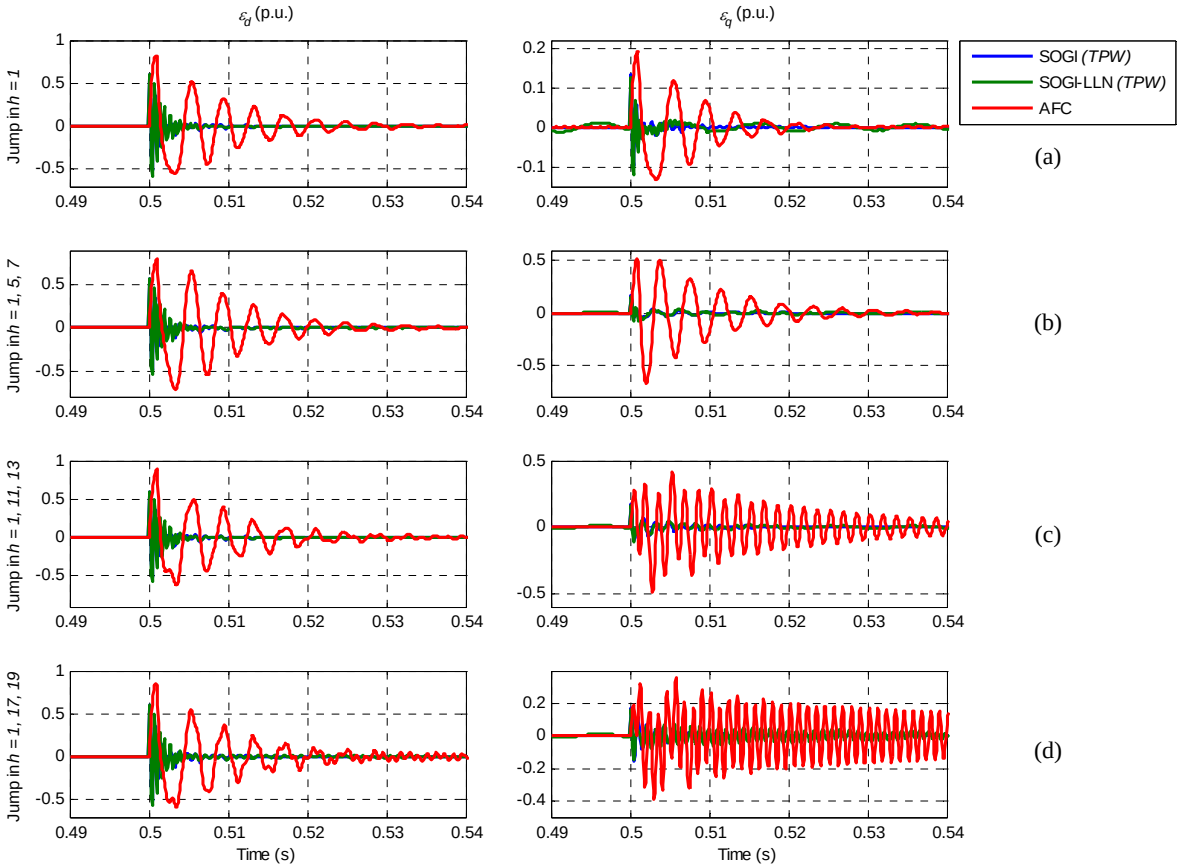

Fig. 4.18. Simulation results: error in dq-axes after applying an amplitude jump of 150 % at $t = 0.5\ s$ to the harmonics (a) $h = 1$, (b) $h = 1, 5, 7$, (c) $h = 1, 11, 13$ and (d) $h = 1, 17, 19$ to a current control scheme based on resonant controllers connected in parallel (tuned at $h = 6, 12, 18$): SOGI (discretized with TPW), SOGI-LLN (discretized with TPW) and AFC.

TABLE 4.7. PERFORMANCE AND STABILITY INDICATORS OF THE CURRENT CONTROL SCHEME BASED ON RESONANT CONTROLLERS TO COMPENSATE THE HARMONICS OF ORDER $h = 0, 6, 12$ AND 18.

	SOGI	***SOGI-LLN***	***AFC***
Settling time, t_s	13.3 ms	16.7 ms	30.5 ms
Maximum overshoot (%)	86.31 %	65.32 %	31.07 %
Gain margin, GM (dB)	2.35 dB	3.17 dB	3.45 dB
Phase margin, PM (°)	15.7°	24.9°	24.2°

4.6. Conclusions.

Three structures to implement a resonant controller have been analyzed and studied, namely, SOGI, SOGI-LLN and AFC. The last two emerged as a solution to the stability problems of the SOGI, caused by its infinite gain at the resonant frequency and a lack of phase control.

The most commonly used discretization techniques have been applied to the digitalization of the SOGI and SOGI-LLN, showing that the so-called TPW and FOH methods obtain the discrete time models that better match the continuous time model.

As the number of harmonics to compensate increases, provided that system stability is assured, SOGI-LLN arises as the desired option due to its low steady-state error and phase control capabilities. SOGI-LLN also has one of the highest overshoots; hence if this is not permissible, AFC is a good tradeoff.

With regard to the implementation of the frequency-adaptive version of these controllers, SOGI-LLN is not a viable option due to the high complexity of the calculation of its parameters, whereas SOGI and AFC are simple to implement. They both entail the calculation of a few trigonometric operations, but they do not suppose a high consumption of resources and their digital implementation is feasible. As for the SOGI, the digital implementation based on the individual discretization of the integrators is no longer valid when performing harmonic compensation due to the pole displacement introduced by this configuration.

5

Current control based on repetitive controllers

The analysis of one of the two types of current control covered in this thesis, which is resonant control, was carried out in Chapter 4. This chapter does the same with repetitive control, which in recent years has experienced great development thanks to its goodness and the evolution of digital processors.

The result of use of repetitive control is increased tracking precision and a reduction in the effects of physical imperfections or changes in parameters of the devices or associated transducers [Broberg and Molyet, 1992]. The different ways to implement the repetitive control have been grouped into three categories: (i) repetitive control based on the inverse of the plant (RC-IP), (ii) repetitive control based on feedback and feedforward delay paths (RC-FFDP) and (iii) repetitive control based on Discrete Cosine Transform (RC-DCT).

5.1. Introduction.

To track a sinusoidal signal with harmonic pulsation ω_o without steady-state error it is necessary to design a regulator with poles in $s = \pm j\omega_o$. However, a periodic function of period T has many sinusoidal components with pulsations $h\omega_1$ ($h \in \mathbb{Z}$), where $\omega_1 = 2\pi/T$ is the fundamental pulsation of the reference periodic signal and h is the harmonic order. The Internal Model Principle (IMP) [Francis and Wonham, 1975] states that if the open-loop system contains the reference-generating polynomial and the closed-loop is stable, then the regulated output will track the reference signal asymptotically (in steady-state) and the tracking is robust [Dorf and Bishop, 1991]. In addition, in stable closed-loop systems, a disturbance is cancelled exactly in steady-state if its generating polynomial is also included [Goodwin, *et al.*, 2001]. In continuous time domain, the desired reference-generating polynomial is $1 - e^{-sT}$ using the Laplace transform. Therefore, a controller that is capable of tracking multiple poles placed at $h\omega_1$ in continuous time domain is described by (5.1):

$$C(s) = \frac{C_N(s)}{1 - e^{-sT}} \tag{5.1}$$

where $C_N(s)$ is the numerator of the controller and has no zeros that can be cancelled with its poles. As mentioned before, this controller tracks in closed-loop the harmonics and the continuous component of the input periodic signal $x(t)$. It can be implemented as a positive feedback of the transfer function e^{-sT}, as shown in Fig. 5.1. If the block e^{-sT} were placed in the feedback path instead of the direct path, the controller would have the same poles and the same phase at the pulsations $h\omega_1$, but the gain of the open-loop transfer function at the interharmonic frequencies would be higher. Thus, it is preferable to place this block in the direct path to minimize the gain introduced at undesired frequencies.

From the point of view of frequency response, the repetitive loop has an infinite gain to all frequencies that are multiples of $1/T\ Hz$, as shown in Fig. 5.2, starting at zero frequency, which also performs the function of a pure integrator. It introduces zero phase shift at these frequencies. This ensures disturbance rejection and zero steady-state error for signals with spectral content at these frequencies.

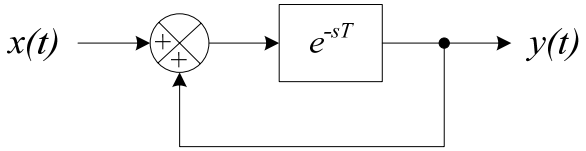

Fig. 5.1. Fundamental repetitive controller in continuous time.

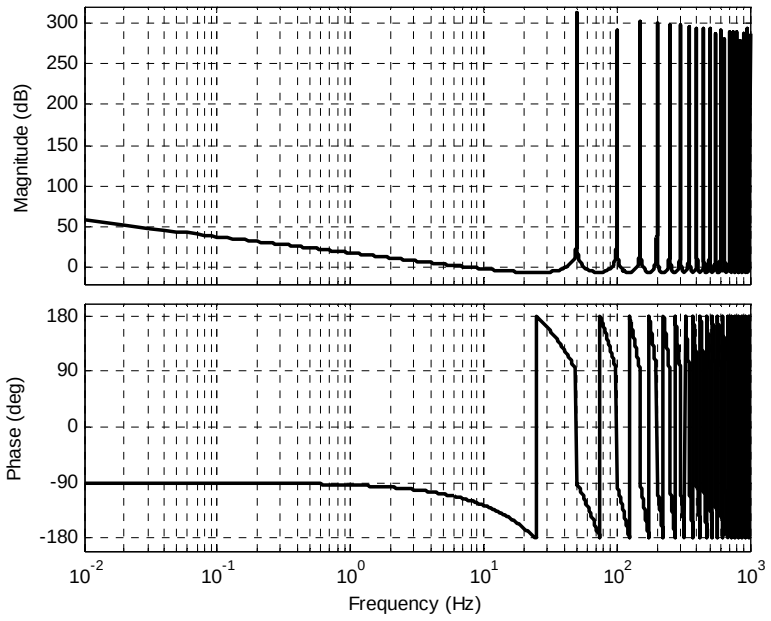

Fig. 5.2. Bode diagram of the fundamental repetitive controller in continuous time.

In discrete time domain, the desired reference-generating polynomial is $1 - z^{-N}$ using the z- transform, where $N = \lfloor T/T_s \rfloor$ is a natural number proportional to the fundamental period of the grid (T) and inversely proportional to the sampling period (T_s). Recalling (5.1), a controller can be designed in discrete time with N poles on the unit circle as:

$$C(z) = \frac{C_N(z)}{1 - z^{-N}} \tag{5.2}$$

where $C_N(z)$ is the numerator of the controller and has no zeros that can be cancelled with its poles. Note that this controller can eliminate harmonics of the periodic input signal $x[k]$ up to the Nyquist pulsation ($\pi/T_S\ rad/s$), including the continuous component of the input signal $x[k]$. This transfer function can be implemented as a positive feedback of the transfer function z^{-N} as shown in Fig. 5.3, with the delay block placed in the direct path for the same reason as the continuous time case. The Bode diagram of this controller is represented in Fig. 5.4, which shows that the differences between the implementation in continuous and discrete time are practically negligible.

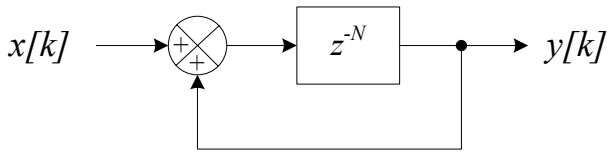

Fig. 5.3. Fundamental repetitive controller in discrete time.

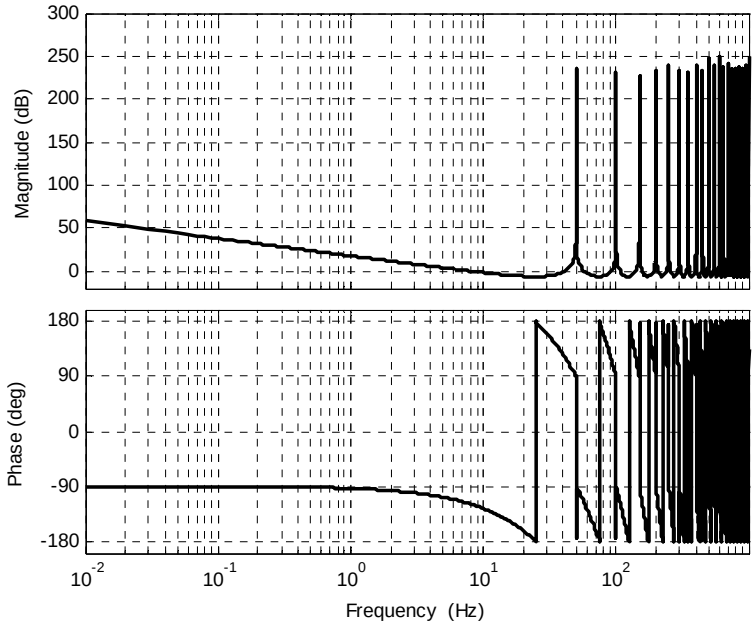

Fig. 5.4. Bode diagram of fundamental repetitive controller in discrete time.

In practice, this scheme usually makes the system unstable as it amplifies many high-order harmonics, while the system to be controlled usually has a limited bandwidth [Pinzón-Ardila, 2007]. This is the reason why a change has to be made in the original model. The concept of *plug-in* implementation was first introduced in [Tomizuka, *et al.*, 1988], a novel concept that enables a repetitive controller to be inserted prior to the standard controller in a feedback loop to reduce periodic errors. This allows implementation of repetitive control to be accomplished after the original feedback system is fully stabilized and tested [Broberg and Molyet, 1992]. This scheme is represented in Fig. 5.5.

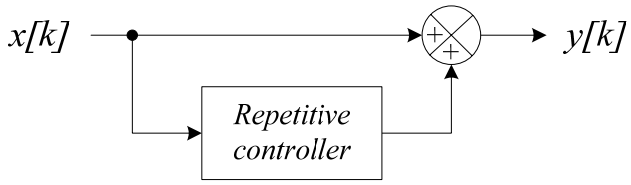

Fig. 5.5. Plug-in implementation of a repetitive controller.

5.2. Repetitive Controller based on the Inverse of the Plant (RC-IP).

5.2.1. Discrete-time domain.

The repetitive controller based on the inverse of the plant (RC-IP) was first studied in discrete time in the works [Broberg and Molyet, 1992] and [Zhou and Wang, 2001]. Later on, it was applied to the current control of a three-phase shunt active power filter in the work [García-Cerrada, *et al.*, 2007], being its scheme the one described in Fig. 5.6 (notice the plug-in configuration). This controller compensates all harmonics of its input signal $x[k]$, i.e. $h = k$ ($k \in \mathbb{Z}$).

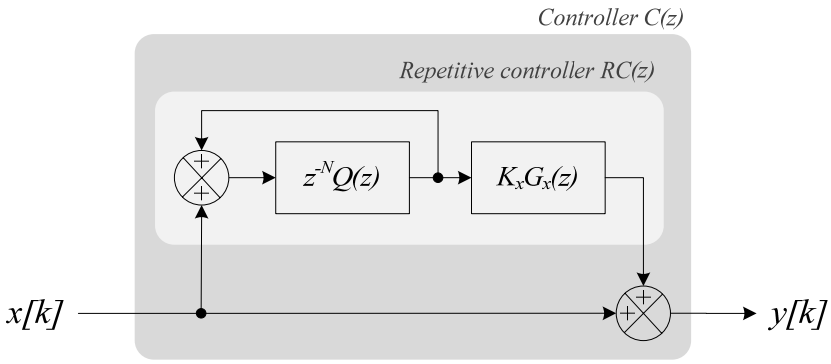

Fig. 5.6. RC-IP in discrete time.

The plug-in repetitive controller $C(z)$ is defined by (5.3), where $Q(z)$ is a low pass filter, K_x is a positive constant gain and $G_x(z)$ is a user-defined transfer function chosen so as to

ensure a stability margin of the system.

$$C(z) = \frac{1 - z^{-N}Q(z) + z^{-N}Q(z)K_x G_x(z)}{1 - z^{-N}Q(z)} \tag{5.3}$$

The method of calculating $G_x(z)$ gives rise to the name of this repetitive controller. The transfer function $G_p(z)$ is calculated as shown in (5.4), where $P(z)$ is the exact discrete time model of the plant to be controlled (*basic servo plant*), possibly with some additives placed like an inner control loop.

$$G_p(z) = \frac{P(z)}{1 + P(z)} \tag{5.4}$$

The transfer function $G_x(z)$ is obtained as the inverse of the estimated $G_p(z)$ $\left(\hat{G}_p(z)\right)$ if it is a minimum-phase system [Broberg and Molyet, 1992; Hillerström, 1994], as described by (5.5). If $\hat{G}_p(z)$ is not minimum-phase, i.e. there are zeros outside the unit circle in the z-plane, $\hat{G}_p^{-1}(z)$ will be unstable [Harnefors and Nee, 1998].

$$G_x(z) = \hat{G}_p^{-1}(z) = \frac{1 + \hat{P}(z)}{\hat{P}(z)} \tag{5.5}$$

The transfer function $\hat{P}(z)$ is an estimated model of the basic servo plant $P(z)$, whose accuracy and stability will also depend on the system. Moreover, if $\hat{G}_p(z)$ does not model accurately the frequency response of $G_p(z)$, the adjust of K_x can not ensure stability. In order to give some stability margin, K_x is chosen as $0 < K_x < 1$ but it cannot be very small because the smaller it is, the slower the closed-loop response is [Zhou and Wang, 2002]. This problem can be addressed by making $Q(z)$ a low pass filter with $Q\left(e^{j\omega T_s}\right) = 1$ only as long as $\hat{G}_p^{-1}(z)$ is accurate so that the IMP is satisfied. Its cutoff frequency must allow passing all expected harmonic frequencies of the periodic input signal with a unit gain and zero phase shift. This ideal situation would allow complete elimination of periodic disturbances within the ideal filter bandwidth. The cutoff frequency cannot be too high because of stability and noise considerations [Broberg and Molyet, 1992]. It should be avoided to introduce a high gain at the switching frequency, which would lead to fluctuations in the system. The low pass filter is assumed to be asymptotically stable, i.e. all its poles are located inside the unit circle in the z-plane (with radius less than 1).

A possible proposal for $Q(z)$ is a typical finite-impulse response (FIR) filter, calculated with a Hamming window, cutoff frequency $f_c = 1500\,Hz$ (this allows a harmonic compensation until order 30), sampling frequency $f_s = 10\,kHz$, order $W = 16$ and non-causal (as well as $G_x(z)$), although the complete algorithm is causal and implementable as a

single transfer function. Fig. 5.7 compares the Bode diagram of the open-loop system when $Q(z)$ is causal and when not. A causal filter would produce a shift of the resonance peaks with respect to the harmonic frequencies, with a consequent increase in the error of the obtained current. Therefore, zero phase at the harmonic frequencies is not achieved either. The result of using a Hamming-window FIR filter with order $W = 16$ is shown in the Bode diagram of the repetitive controller $RC(z)$ of Fig. 5.8.

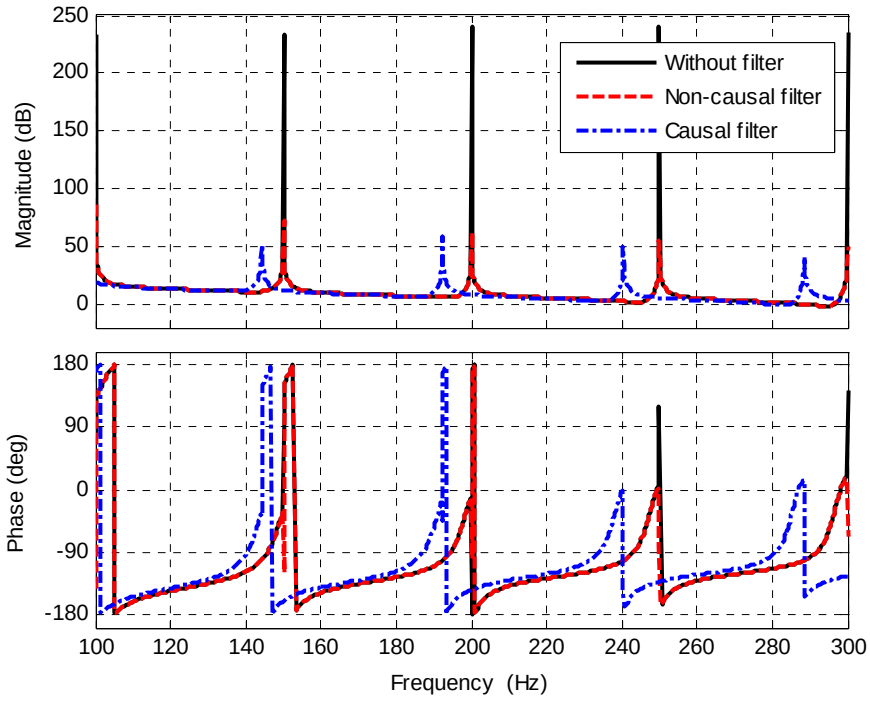

Fig. 5.7. Detail of the Bode diagram of the open-loop system in three cases: without filter $Q(z)$, with non-causal filter and with causal filter.

A 2^{nd} order non-causal binomial FIR filter $(Q(z) = 0.25z + 0.5 + 0.25z^{-1})$ was proposed in [García-Cerrada, *et al.*, 2007], being chosen a non-causal filter for the same reasons as the previous filter. The implementation based on a Hamming-window-based FIR filter achieves lower steady-state error, which is justified with Fig. 5.9 because this one introduces lower attenuation at the desired frequencies in the band pass than a binomial filter.

As for the reason for the introduction of a plug-in controller in the control loop is worth mentioning that in [Zhou and Wang, 2002] it is shown that if N is large, the plug-in implementation with a PI controller in $P(z)$ follows the DC component of the reference signal faster than without the plug-in structure.

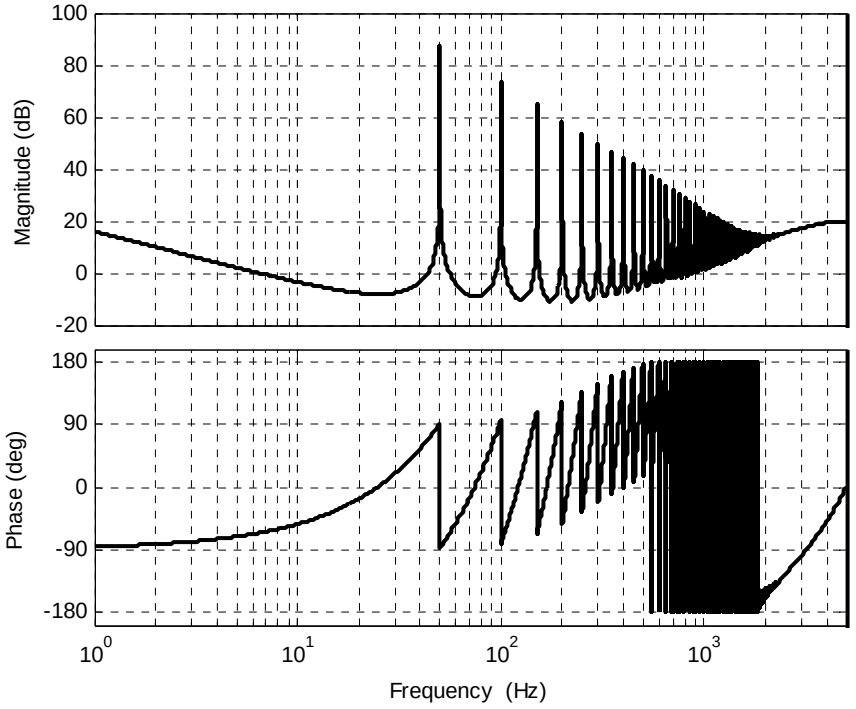

Fig. 5.8. Bode diagram of $RC(z)$ in Fig. 5.6 (RC-IP) with a Hamming-window filter of order 16.

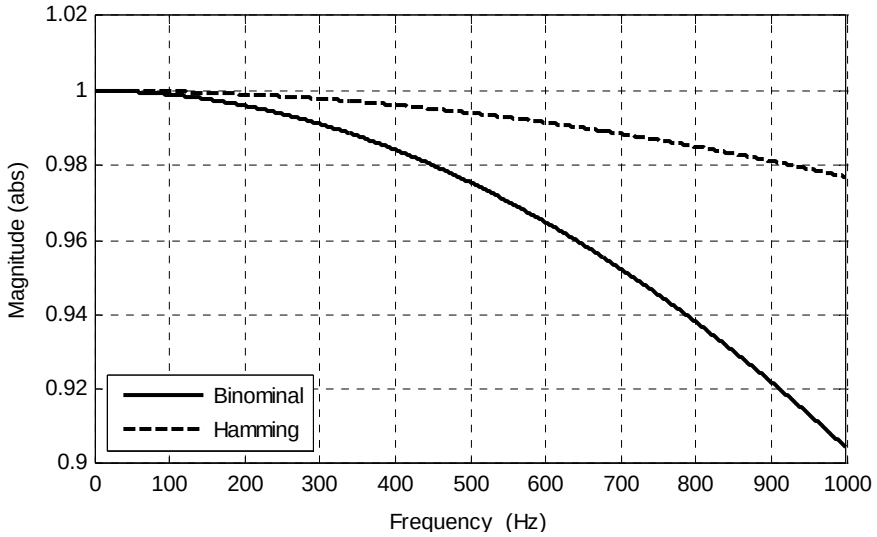

Fig. 5.9. Comparison of the Bode diagrams of a binomial FIR filter and a Hamming-window-based FIR filter.

In [Griñó, *et al.*, 2007] this same scheme was realized but with some modifications (Fig. 5.10). The repetitive controller has the task of filtering only the odd harmonics since often they are the only ones that appear in power systems, hence the inclusion of the delay block $z^{-N/2}$, demonstrating the position of its poles in the fundamental frequency and its odd harmonics in [Griñó and Costa-Castelló, 2005].

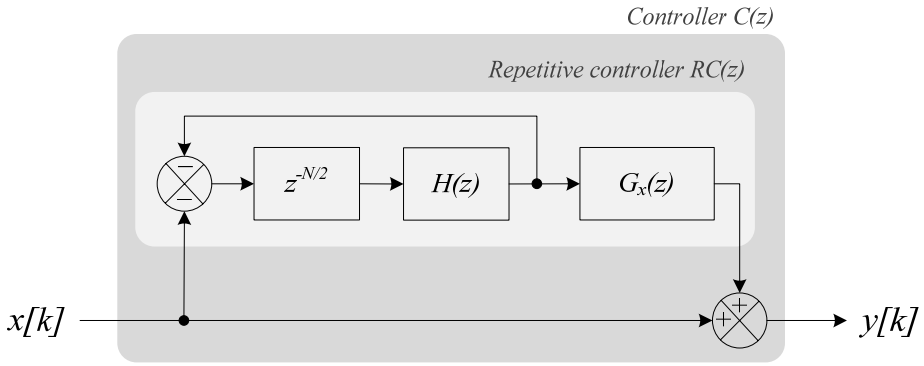

Fig. 5.10. Discrete model of the RC-IP analyzed in [Griñó, *et al.*, 2007].

5.2.2. Frequency-adaptive algorithm and computational burden.

A frequency-adaptive proposal for RC-IP was presented in the work [Roldán-Pérez, *et al.*, 2011] applied to a DVR. The plug-in controller is shown in Fig. 5.11, and it is based on Fig. 5.6. A new transfer function $L(z)$ is added to the repetitive controller to compensate the possible frequency variations. The original structure of this controller was designed to work with a value of N such that $N = T/T_s \in \mathbb{N}$ but, in cases where the new frequency is such that $N \notin \mathbb{N}$, $L(z)$ models the decimal part of this parameter by means of a discretized first order Padé approximation. Recalling that the transfer function of the fundamental repetitive controller in continuous time is described by (5.6) and knowing that the grid fundamental period can be expressed by (5.7), where $0 < l_e < 1$, the new transfer function of the repetitive controller in continuous time can be written as shown in (5.8).

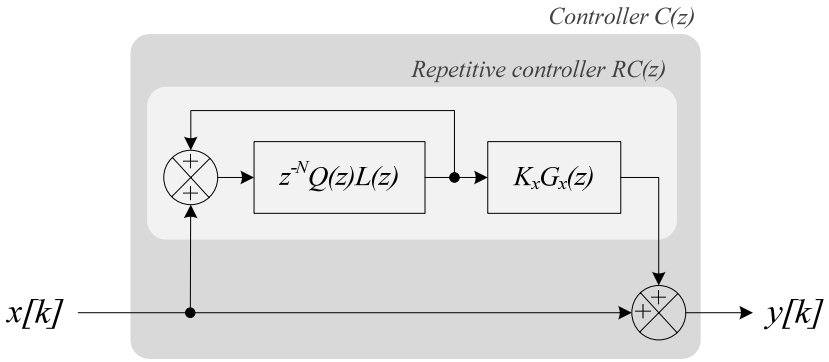

Fig. 5.11. Frequency-adaptive RC-IP in discrete time studied in [Roldán-Pérez, *et al.*, 2011].

$$C(s) = \frac{e^{-sT}}{1 - e^{-sT}} \tag{5.6}$$

$$T = NT_s + l_e T_s \tag{5.7}$$

$$C(s) = \frac{e^{-sNT_s} e^{-sl_e T_s}}{1 - e^{-sNT_s} e^{-sl_e T_s}} \tag{5.8}$$

The term e^{-sNT_s} in (5.8) corresponds to a delay z^{-N} in discrete time, whereas the term $e^{-sl_e T_s}$ can be discretized with Tustin approximation according to [Roldán-Pérez, *et al.*, 2011], yielding (5.9). The effect of the inclusion of $L(z)$ plus the recalculation of N is the adaptation of the frequency spectrum to the new grid frequency, moving the gain peaks to the new harmonic frequencies.

$$L(z) = \frac{(1 - l_e) + (1 + l_e) z^{-1}}{(1 + l_e) + (1 - l_e) z^{-1}} \tag{5.9}$$

The new transfer function of the controller $C(z)$ is described by:

$$C(z) = \frac{1 - z^{-N} Q(z) L(z) + z^{-N} Q(z) L(z) K_x G_x(z)}{1 - z^{-N} Q(z) L(z)} \tag{5.10}$$

There are two options for implementing the RC-IP in a digital platform, regardless of whether frequency-adaptation is performed or not: (i) based on the discrete transfer function $C(z)$ and (ii) based on causal blocks. According to $C(z)$, the resulting controller has a high order, although the positive aspect is that only a few coefficients of the numerator and denominator are non-zero. This results in a reduced number of multiplications and additions when implemented in a digital platform, which greatly reduces the computational load. For example, (5.11) shows the discrete transfer function of $C(z)$ when $f_o = 50\ Hz$ and $Q(z)$ is a 2^{nd} order FIR filter. The numerator and denominator coefficients are zero in the intervals $[b_6, b_N]$ and $[a_4, a_N]$, respectively. Therefore, if the coefficients are normalized with respect to b_0, only 13 multiplications and 12 additions are needed (per axis). This approach works well for the non-frequency-adaptive RC-IP, but a higher accuracy in the coefficients may be necessary to perform the frequency-adaptation. The fact of operating on all individual transfer functions until obtaining $C(z)$ leads to a loss of precision in the coefficients.

$$C(z) = \frac{b_{N+2} z^{-(N+2)} + b_{N+1} z^{-(N+1)} + b_5 z^{-5} + b_4 z^{-4} + b_3 z^{-3} + b_2 z^{-2} + b_1 z^{-1} + b_0}{a_{N+2} z^{-(N+2)} + a_{N+1} z^{-(N+1)} + a_3 z^{-3} + a_2 z^{-2} + a_1 z^{-1} + a_0} \tag{5.11}$$

Regarding the second option for implementing the RC-IP, Fig. 5.12 shows the block diagram of the frequency-adaptive RC-IP in discrete time based on causal blocks. The non-frequency-adaptive version does not contain the transfer function $L(z)$. The number of delays

C and M are chosen in such a way that each individual block in Fig. 5.12 is a causal block, so that their individual digital implementation is feasible. This implementation has two advantages: it is less prone to design errors because the operation of multiple transfer functions to obtain a single transfer function $C(z)$ is avoided and, on the other hand, it achieves a higher accuracy in its coefficients and, thus, lower steady-state error. The steady-state error is theoretically zero but, due to discretization effects, implementation issues, noise in the measurements and other sources of uncertainty this error is small but not exactly zero. This applies to any controller implemented in a digital platform.

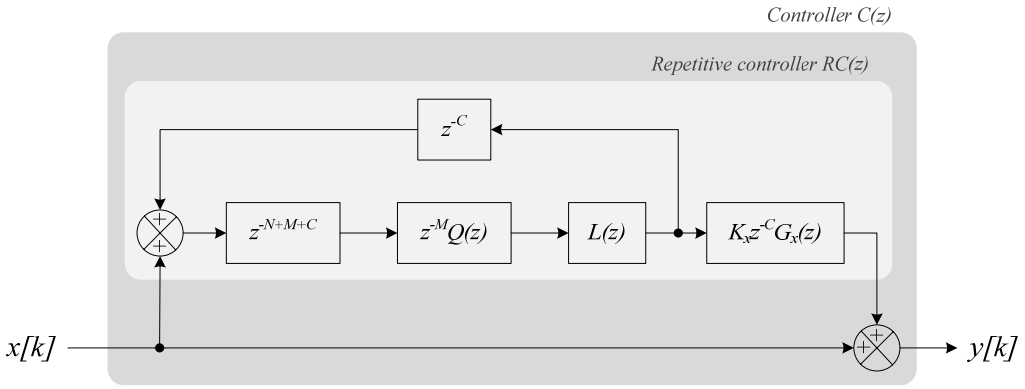

Fig. 5.12. Frequency-adaptive RC-IP in discrete time based on causal blocks.

When programming the controller, it is necessary to store a number of samples of the input and output signals that depends on N. The parameter N is fixed for the non-frequency-adaptive algorithm, but in the opposite case this results in buffers with variable size. If dynamic memory allocation wants to be avoided, the buffers must have a fixed length. They must have the largest estimated value, which is given by the estimated lowest frequency drift that could take place. In the case that N is less than this value, the remaining positions of the buffer are filled with zeros. The maximum length of the buffers depends on the maximum frequency drift to consider and available memory on the DSP.

The flowchart of the programming of the frequency-adaptive RC-IP based on causal blocks is shown in Fig. 5.13. The sampling frequency is defined by `FS`. Each of the causal blocks represented in Fig. 5.12 has been labeled with a number from 1 to 5, and their corresponding input and output variables are named as `input`*`BlockNumber`* (`input1` to `input5`) and `output`*`BlockNumber`* (`output1` to `output5`). An example of the programming in C-language is given in some steps of this flowchart. For example, regarding the calculation of the variable parameter l_e, a few lines of C-code show how to limit its value to avoid numerical instability of the algorithm. Besides, the usage of the constant `EPS`[1] in the calculation of the grid fundamental period T is generally advisable to avoid divisions by zero

[1] In MATLAB, the value of the constant EPS is the distance from 1.0 to the next largest double-precision number, that is EPS = 2^{-52}. This constant is defined with the same value in the programming of the algorithm in a DSP.

(when the divisor is a variable). The programming of each causal block is straightforward since they are based on a transfer function. The programming of the $L(z)$ block has been given as an example. It is of paramount importance to notice that the variables (buffers) have to be defined as *static* when they are going to be used to store data from previous iterations. Finally, the output of the plug-in repetitive controller (labeled as `outputRepetitiveController` in Fig. 5.13) can be employed as input to a precompensator, e.g. a PI controller.

If required, the parameter l_e does not have to be updated in each iteration of the control loop if the grid frequency is not expected to suffer fast variations. This will allow decreasing the execution time and will lead to smother variations in l_e.

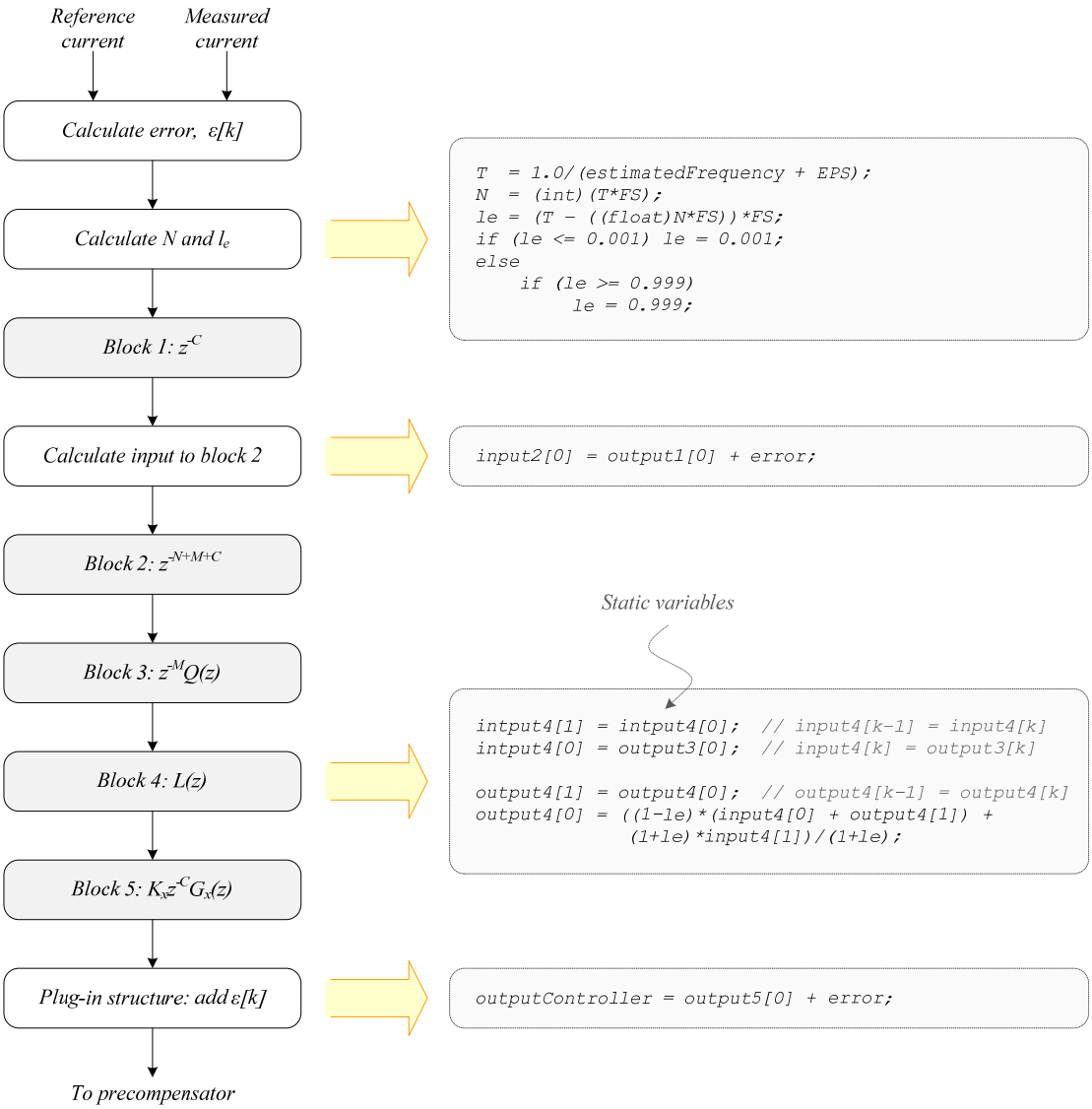

Fig. 5.13. Flowchart of the programming of the frequency-adaptive RC-IP based on causal blocks.

5.3. Repetitive Control based on Feedback and Feedforward Delay Paths (RC-FFDP).

5.3.1. Continuous-time domain.

Two different proposals of this type of repetitive controller are tackled in this section, namely, RC-FFDP1 (based on [Escobar*, et al.*, 2009]) and RC-FFDP2 (based on [Loh*, et al.*, 2008]).

The basis of the first one is found in [Escobar*, et al.*, 2007a]. The models shown in Fig. 5.14 were studied in first place where, depending on the configuration of the feedback and feedforward delay paths, they managed to compensate all harmonics (Fig. 5.14.a) or just the odd (Fig. 5.14.b). Their corresponding transfer functions are described by (5.12) and (5.13), respectively.

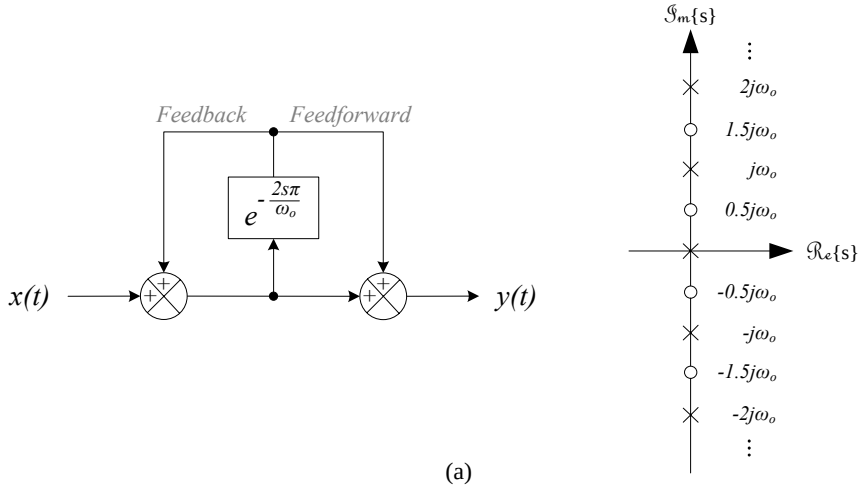

(a)

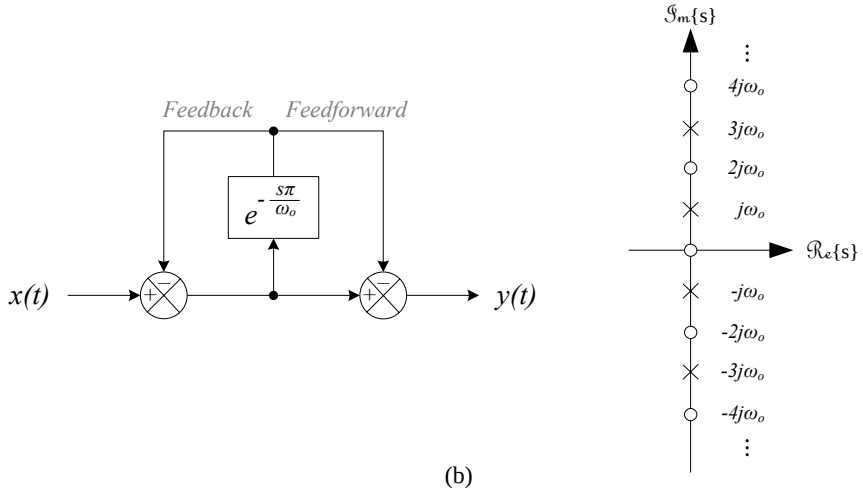

(b)

Fig. 5.14. Block diagram in continuous time and pole-zero map of (a) positive-feedback (all harmonics) repetitive controller with feedforward, and (b) negative feedback (odd harmonics) repetitive controller with feedforward.

$$C(s) = \frac{1 + e^{-\frac{2s\pi}{\omega_o}}}{1 - e^{-\frac{2s\pi}{\omega_o}}} \tag{5.12}$$

$$C(s) = \frac{1 - e^{-\frac{2s\pi}{\omega_o}}}{1 + e^{-\frac{2s\pi}{\omega_o}}} \tag{5.13}$$

Looking toward an implementation in balanced three-phase systems, a scheme able to compensate harmonics of order $6k \pm 1$ $(k \in \mathbb{Z})$ was designed in [Escobar*, et al.*, 2007b], as shown in Fig. 5.15. Its transfer function is shown in (5.14).

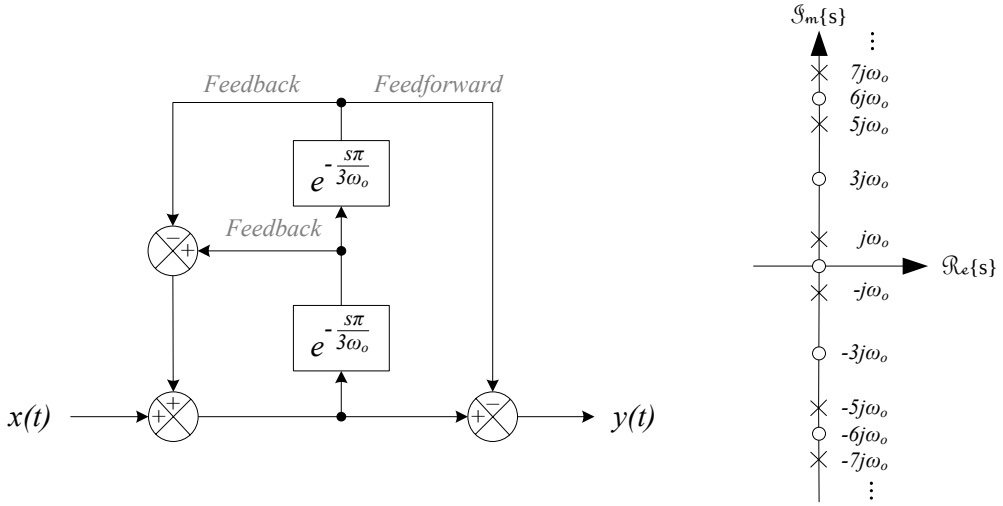

Fig. 5.15. Block diagram in continuous time and pole-zero map of the RC-FFDP1 for harmonics of order $6k \pm 1$.

$$C(s) = \frac{1 - e^{-2s\tau_d}}{1 + e^{-2s\tau_d} - e^{-s\tau_d}} \tag{5.14}$$

Some modifications were made to the original scheme of Fig. 5.15 for practical reasons. To limit the infinite gain at the resonant frequencies, and thus, to prevent instability problems, the authors proposed to add damping to all the poles and zeros by attaching gain factors to each delay block, K_1 and K_2 (with $K_1 = 2 - (1/K_2),\ 0 < K_1 < 1$ and, thus, $0.5 < K_2 < 1$). They have to be different to avoid shifting the resonant peaks with respect to the expected frequencies $(6k \pm 1)f_o$. This is not the case for the notches whose position is still at $3k\omega_o$. On the other hand, two low-pass filters are included in order to remove the noise introduced in the measurement process. They are considered to be of the form $Q(s) = 1/(\tau s + 1)$, where τ is the cutoff frequency. The resulting continuous time transfer function is described by (5.15).

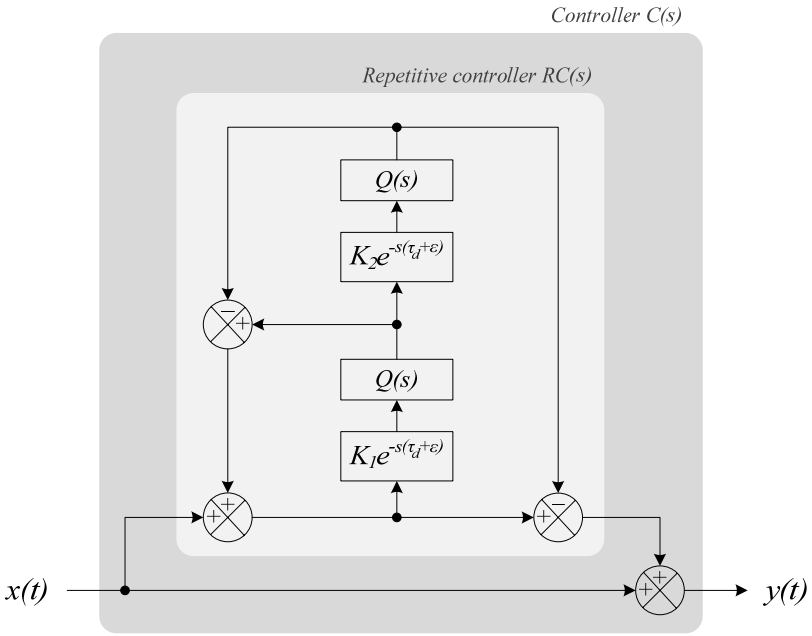

Fig. 5.16. RC-FFDP1 in continuous time.

$$C(s) = \frac{(\tau s + 1)^2 - K_1 K_2 e^{-2s(\tau_d+\varepsilon)}}{(\tau s + 1)^2 + K_1 K_2 e^{-2s(\tau_d+\varepsilon)} - (\tau s - 1) K_1 e^{-s(\tau_d+\varepsilon)}} \tag{5.15}$$

Fig. 5.17 shows a comparison of the ideal RC-FFDP1 and the modified scheme when $K_1 = 0.8889$, $K_2 = 0.9$ and τ takes the values of $\tau = 10^{-4}\ s$ and $\tau = 10^{-5}\ s$. The gain of the resonant peaks is lower as the gains K_1 and K_2 increase. It can be observed that the addition of low-pass filters not only restricts the bandwidth of the controller, but also introduces considerable phase shift inaccuracies at each $6k \pm 1$ harmonic. Furthermore, the phase shift varies nonlinearly [Escobar, *et al.*, 09]. To compensate this effect, the introduction of an increment ε in the delay time of each delay block was proposed.

The second proposal, RC-FFDP2, was studied in [Loh, *et al.*, 2008], where the authors gave it the name of "Time delay control". It is also based on feedback and feedforward delay paths as shown in Fig. 5.18 and it works in mixed reference frame. Its transfer function is shown in (5.16). The current controller is formed by a SOGI (see section 4.2) tuned to the grid fundamental harmonic and working in $\alpha\beta$-axes, plus the repetitive controller compensating the harmonics of order $6k$ ($k \in \mathbb{Z}$) and working in dq-axes. Note that the authors did not implement it as a plug-in controller but in parallel with the SOGI.

$$RC(s) = \frac{K\left(1 + K_f e^{-s\tau_d} Q(s)\right)}{1 - K_f e^{-s\tau_d} Q(s)} \tag{5.16}$$

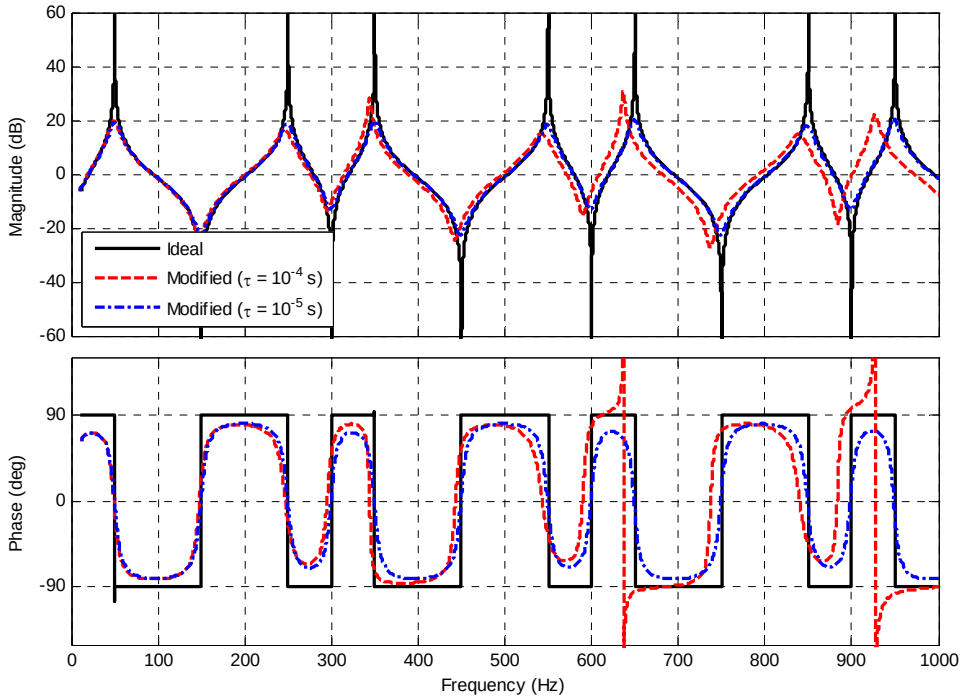

Fig. 5.17. Bode diagram of the ideal RC-FFDP1 in continuous time and the modified RC-FFDP1 when $\tau = 10^{-4}\ s$ and $\tau = 10^{-5}\ s$.

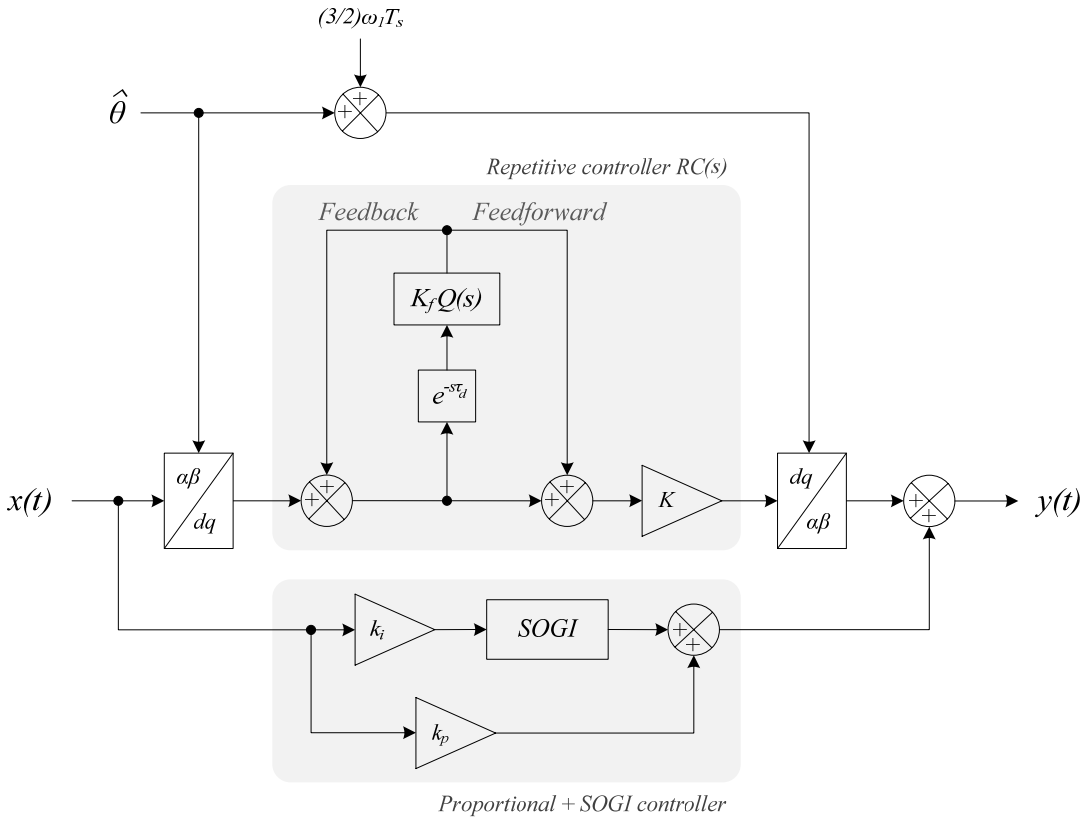

Fig. 5.18. RC-FFDP2 in continuous time.

For practical reasons, it also contains a gain K_f to add some damping and hence robustness to the control path. On the root locus, this means shifting the poles slightly to the left by σ, given that $K_f e^{-s\tau_d} = e^{-(s+\sigma)\tau_d}$ $\left(0 \leq K_f \leq 1\right)$. The gains at the resonant peaks are now not finite, but given by $\left(1 + K_f\right)/\left(1 - K_f\right)$.

The authors of [Loh*, et al.*, 2008] claimed that the basic schemes of RC-FFDP1 (Fig. 5.14), although proven to be effective, still face the complication of unintentional noise amplification caused by its implicit inclusion of an integrator. This is the reason why they made a different use of this "embedded" integrator, proving mathematically that it can be used for compensating all grid harmonic disturbances if the phase angle is synchronized with the distorted grid, including those with pulsations $+(6k-1)\omega_o$ and $-(6k+1)\omega_o$ (although at a reduced gain).

In contrast to RC-IP, these controllers do not depend on the plant model to adjust its parameters; they only depend on the grid frequency.

5.3.2. Discrete-time domain.

The RC-FFDP1 in discrete time is shown in Fig. 5.19, and its corresponding transfer function is described by (5.17). It consists of two blocks of time delay $d = \tau_d/T_s = 1/(6f_oT_s)$ arranged in two feedback paths and a feedforward path, plus two FIR filters $Q(z)$ (low pass filters). Linear-phase FIR filters were chosen to easily compensate the delay introduced by them. This delay is calculated as $\tau_{FIR} = (W/2) \cdot T_s$, i.e., it adds a delay of $W/2$ samples, so it is enough to introduce the term $W/2$ in both delay blocks to compensate the shift. Regarding their implementation, in [Escobar, *et al.*, 09] it was performed using the windowed method with a cutoff frequency $f_c = 1650\ Hz$, sampling frequency $f_s = 12\ kHz$ and order $W = 16$.

$$C(z) = \frac{1 - K_1K_2z^{-2(d-W/2)}Q^2(z)}{1 - K_1z^{-(d-W/2)}Q(z) + K_1K_2z^{-2(d-W/2)}Q^2(z)} \tag{5.17}$$

As for the second scheme, its discrete time version is shown in Fig. 5.20. It is characterized by the discrete transfer function of (5.18).

$$RC(z) = \frac{K\left(1 + K_fz^{-d}Q(z)\right)}{1 - K_fz^{-d}Q(z)} \tag{5.18}$$

A problem can arise in the digital implementation of the time delay τ_d as a delay block

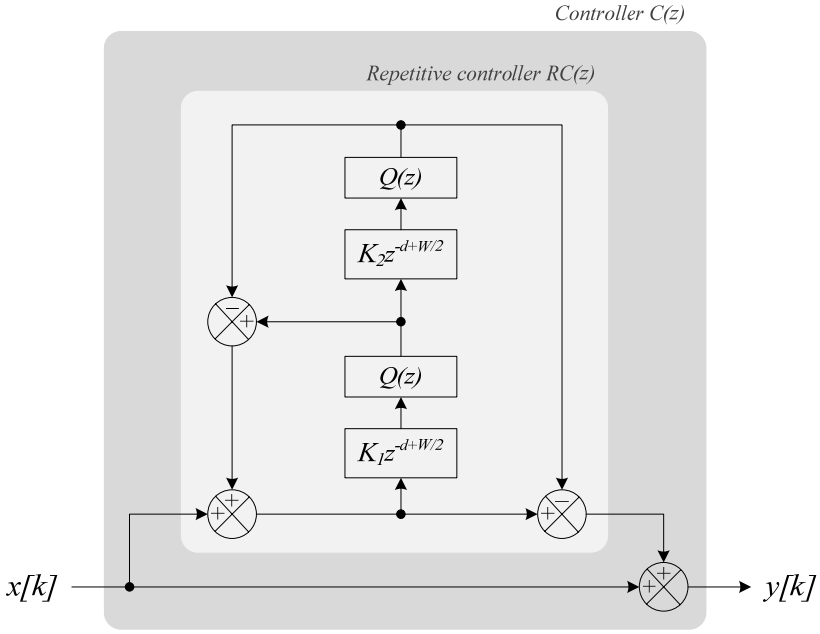

Fig. 5.19. RC-FFDP1 in discrete time.

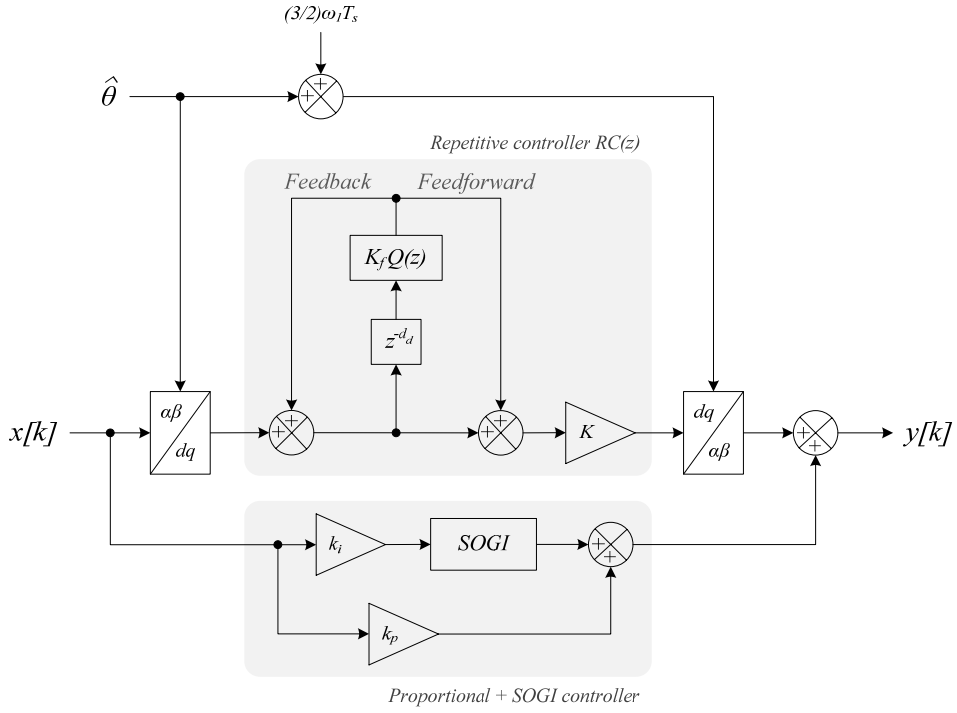

Fig. 5.20. RC-FFDP2 in discrete time.

z^{-d}. As already mentioned above, the parameter d is calculated as $d = \tau_d/T_s = 1/(6f_oT_s)$ and is required to be a natural number to implement it as a single delay block z^{-d}. Considering a grid frequency of $50\,Hz$, the necessary values of the sampling period T_s such that $d \in \mathbb{N}$ would be, for example, $83.33\,\mu s$ $(12\,kHz, d = 40)$, $98.04\,\mu s$ $(10.2\,kHz, d =$

34), etc. These are not typical values of T_s, and maybe the rest of the converter control is already designed for another T_s. Therefore, in practical cases is quite likely that $d \notin \mathbb{N}$.

The technique used in this Thesis to solve this problem is the Thiran method to model the decimal part of the delay d [Laakso*, et al.*, 1996]. This method is the simplest way to design an all-pass filter approximating a given fractional delay D. It is characterized by maximally flat group delay at the zero frequency [Oetken, 1979]. The coefficients are obtained from (5.19):

$$a_k = (-1)\binom{W}{k}\prod_{n=0}^{W}\frac{D-W+n}{D-W+k+n} \quad for \;\; k \in \mathbb{N} \tag{5.19}$$

where W is the filter order. In the case at hand, let us express d as a sum of an integer part (d_i) and a fractional part (d_f):

$$d = d_i + d_f \tag{5.20}$$

The fractional delay d_f is the one modeled with a Thiran filter, and its corresponding block z^{-d_f} is placed in series with z^{-d_i}. Since d_f is always less than 1, then $W = 1$. The calculation of the single coefficient is reduced to:

$$a_0 = \frac{1-d_f}{1+d_f} \tag{5.21}$$

and the approximated delay is calculated as:

$$z^{-d_f} \approx \frac{a_0 + z^{-1}}{1 + a_0 z^{-1}} \tag{5.22}$$

Consequently, the total delay z^{-d} can be approximated as shown in (5.23):

$$z^{-d} = z^{-d_i} z^{-d_f} \approx z^{-d_i}\frac{a_0 + z^{-1}}{1 + a_0 z^{-1}} \tag{5.23}$$

where the parameters d_i and a_0 are calculated offline. The block diagram of the repetitive controller $RC(z)$ from RC-FFDP2 (see Fig. 5.20) is represented in Fig. 5.21. It is now adapted to any sampling period T_s, regardless of whether the resulting delay is a natural number or not. An equivalent block diagram could be obtained for RC-FFDP1, applying Thiran to the decimal part of $d - W/2$.

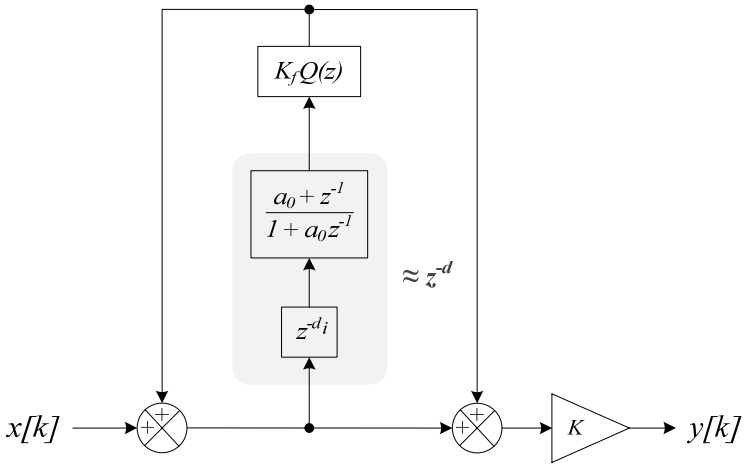

Fig. 5.21. Repetitive controller $RC(z)$ in RC-FFDP2, adapted to any sampling period T_s.

If the parameter d were approximated with Thiran instead of just the fractional part d_f, this would result in a controller with an order of almost the double. For instance, a sampling period of $T_s = 100\,\mu s$ yields $d = d_i + d_f = 33 + 1/3$, which results in $z^{-d_f} = z^{-1/3} \approx (0.5 + z^{-1})/(1 + 0.5z^{-1})$. If Thiran is applied to d, the resulting transfer function has order 34 and none of its coefficients is zero, neither in the numerator nor in the denominator. This is the reason why the controller order increases when including this transfer function. Despite the fact that using a larger number of coefficients to model the delay provides a higher similarity with the continuous time delay, the differences with using Thiran for the fractional part can be noticed only at high frequencies. However, at these frequencies the gain of the controller is considerably low due to the filter $Q(z)$ and the effect is negligible. Fig. 5.22 shows a detail of the magnitude diagram centered on $h = 19$ when the delay z^{-d} is approximated applying Thiran to d or to the fractional part d_f. Clearly, there is a slight displacement of the resonance peak but, due to the effect of the filter $Q(z)$, these peaks are not as selective as the frequency increases and the loss of gain is minimal.

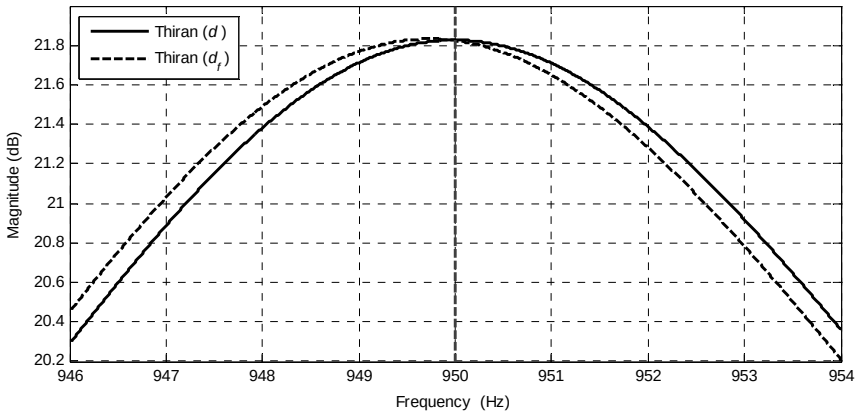

Fig. 5.22. Detail of the magnitude diagram of the RC-FFDP1 centered on *h = 19* when the delay z^{-d} is approximated applying Thiran to d or to the fractional part d_f.

5.3.3. Frequency-adaptive algorithm and computational burden.

The problem when designing a frequency-adaptive RC-FFDP is the same as when working with sampling periods that yield a non-natural number of delays (see previous section). This is solved in the same way, which is by using a first-order Thiran filter (Fig. 5.21). The delay $d - W/2$ in RC-FFDP1 (Fig. 5.19) or simply d in RC-FFDP2 (Fig. 5.20) is periodically updated during the execution of the control loop thank to a frequency-estimation method. This leads to an update of parameters d_i (see (5.20)) and a_0 (see (5.21)). The block diagram of the frequency-adaptive RC-FFDP2 is shown in Fig. 5.23, where f_{est} is the frequency obtained with a frequency-estimation method.

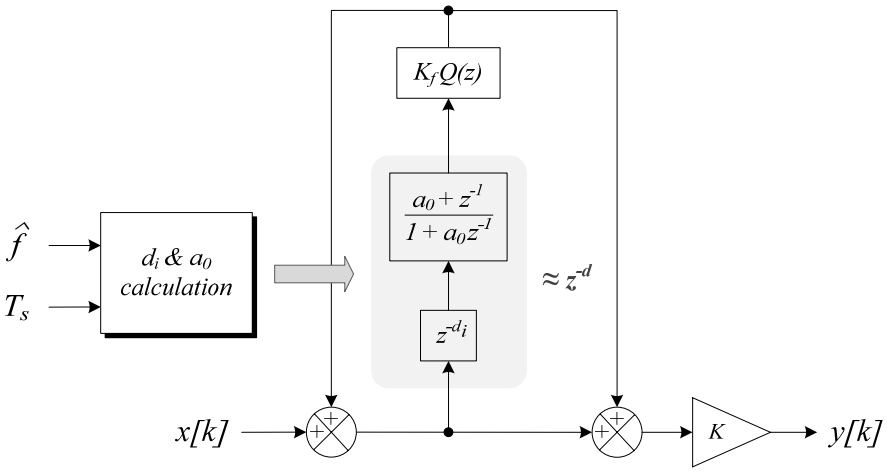

Fig. 5.23. Frequency-adaptive RC-FFDP2 in discrete time.

Concerning the computational burden, the transfer function of RC-FFDP1 has order 87 for $f_o = 50\ Hz$ and $T_s = 100\ \mu s$, and only a few of its coefficients are non-zero. Therefore, this controller has higher complexity and execution time than RC-IP. In the same conditions, the transfer function of RC-FFDP2 has order 42 and any of its coefficients are non-zero.

In order to establish a comparison with RC-IP in the same conditions of frequency and sampling period (see section 5.2.2), RC-FFDP1 needs to perform 350 multiplications and 349 additions, whereas RC-FFDP2 needs 162 multiplications and 161 additions (per axis).

Fig. 5.24a shows a possible block diagram for programming the frequency-adaptive RC-FFDP1. The delay z^{-d_i} has been split into two parts, one corresponding to the inherent delay due to the programming process (z^{-1}) and another corresponding to the remaining integer delay $\left(z^{-(d_i-1)}\right)$. The block *delayThiranFilter* applies this integer delay plus the Thiran filter and the FIR filter $\left(Q(z)\right)$, as represented in Fig. 5.24b.

According to the signals labeled in Fig. 5.24a, the flowchart of the programming of the

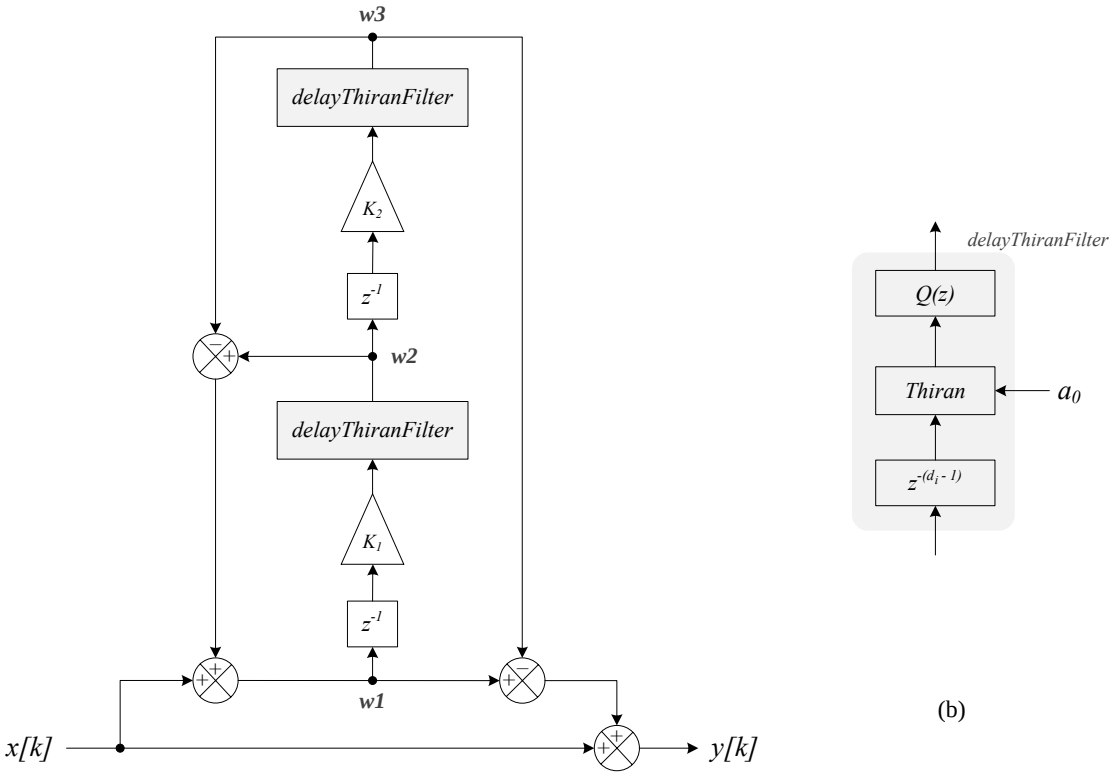

Fig. 5.24. (a) Block diagram used to program the frequency-adaptive RC-FFDP1; (b) inner structure of the block named *delayThiranFilter*.

frequency-adaptive RC-FFDP1 is shown in Fig. 5.25. The function `delayThiranFilter` receives as inputs a signal according to Fig. 5.24a, the number of integer delays $d_i - 1$ and the Thiran filter coefficient a_0. Regarding the variables employed, the element `[0]` refers to the actual state ($[k]$) whereas the element `[1]` refers to the previous state ($[k-1]$).

5.4. Repetitive Control based on Discrete Cosine Transform (RC-DCT).

5.4.1. Discrete-time domain.

This type of repetitive controller is based on "moving" or "running" Discrete Fourier Transform (DFT) filters with a window equal to one fundamental period. This is a FIR filter whose equation is [Mattavelli and Marafao, 2004; Rodríguez*, et al.*, 2010]:

$$F_{DFT}(z) = \frac{2}{N}\sum_{i=0}^{N-1}\left(\sum_{h\in N_h}\cos\left[\frac{2\pi}{N}h(i+N_a)\right]\right)\cdot z^{-i} \tag{5.24}$$

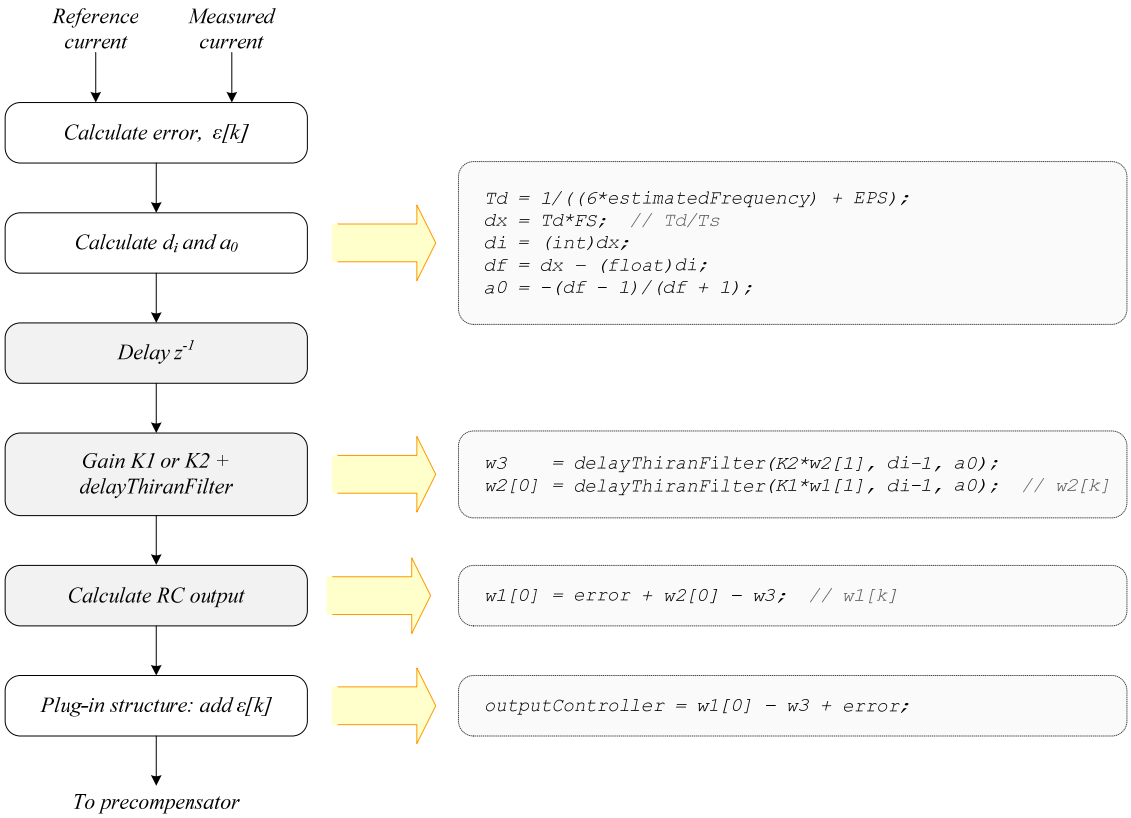

Fig. 5.25. Flowchart of the programming of the frequency-adaptive RC-FFDP1.

where $N = T/T_s$ is again the number of samples within one fundamental period, N_h is the set of selected harmonic frequencies and N_a is the number of leading steps determined to exactly track the reference. This is also called a Discrete Cosine Transform (DCT) filter, hence the name of this repetitive controller.

The internal structure of the RC-DCT is shown in Fig. 5.26, and it is formed by an N-point shift register, a block that performs the DCT and a delay of N_a steps. In order to recover zero phase shift of the loop gain at the desired frequencies and to stabilize the system against rounding and quantization errors introduced by the digital sampling process, a delay of N_a steps (equivalent to a leading phase shift) is then needed in the feedback path, applied by means of the z^{-N_a} block. This parameter is obtained by means of an optimization process during the simulation stage.

The DCT block can be seen as a pass-band FIR filter of N taps with unity gain at all selected harmonics of order h. The shift register is used to form the N-step input vector (w) necessary for the DCT block, which performs the following operations based on (5.24):

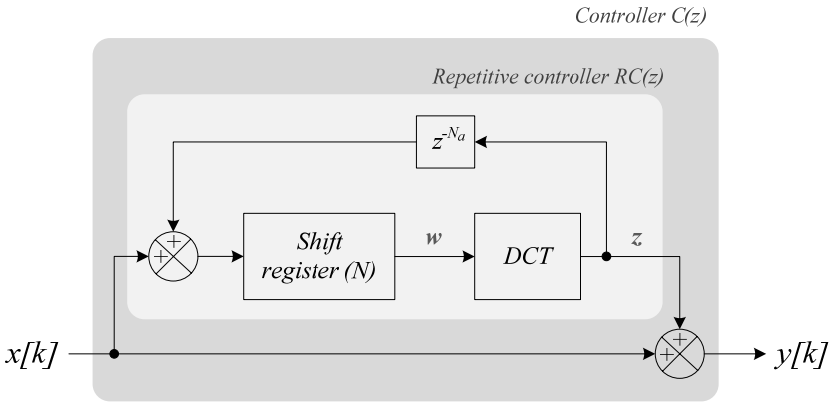

Fig. 5.26. Block diagram of the RC-DCT.

$$for\ (i = 0;\ i < N;\ i++)$$

$$dct[i] = \frac{2}{N} \sum_{h \in N_h} \cos\left(\frac{2\pi}{N} h(i + N_a)\right) \tag{5.25}$$

$$z = z + w[i] \cdot dct[i]$$

The most optimum option is to calculate the DCT coefficients offline. In this way, the computational complexity is not affected by an increase in the number of harmonics to be compensated. For example, Fig. 5.27 shows the Bode diagram of $RC(z)$ in Fig. 5.26 when compensating the harmonics 6^{th}, 12^{th} and 18^{th} in dq-frames. This controller presents the narrowest resonant peaks, i.e. it is very selective; on the other hand, one of its drawbacks is its high gain at the remaining frequencies, which can amplify noise and undesired perturbations.

5.4.2. Frequency-adaptive algorithm and computational burden.

As seen in Fig. 5.26, the RC-DCT algorithm needs a shift register of N positions to obtain the samples $w[k] \dots w[k-N]$ and multiply them by the N coefficients of the DCT. This number N can be a non-natural number when the grid frequency varies, being truncated in this case $(N_i = \lfloor N \rfloor = \lfloor T/T_s \rfloor \in \mathbb{N})$. To compensate the error introduced by this truncation, the order of the desired harmonics is recalculated with the estimated grid frequency $(\hat{f})$, and subsequently the DCT coefficients are recalculated to adapt the frequency spectrum of the RC-DCT.

When truncating the parameter N, the fundamental frequency that the controller is seeing is:

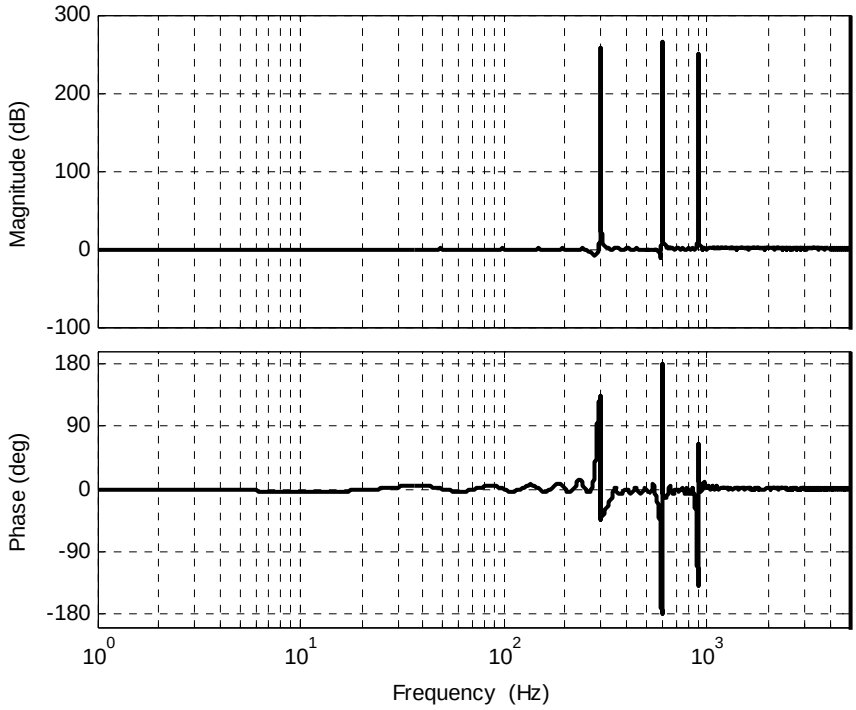

Fig. 5.27. Bode diagram of $RC(z)$ in Fig. 5.26 (RC-DCT).

$$f_o' = \frac{1}{T_s N_i} \tag{5.26}$$

With this frequency, the new harmonic order is calculated as:

$$h' = \frac{h\hat{f}}{f_o'} \tag{5.27}$$

where h is the original harmonic order. These orders are then applied to (5.24). This technique depends on the dynamics of the frequency estimation method.

This controller presents one of the highest computational loads. Under the same conditions in which RC-IP and RC-FFDP were compared, that is $f_o = 50\,Hz$ and $T_s = 100\,\mu s$, it takes 200 multiplications and 200 additions per axis. If this load is too high for the available resources of the processor, the periodic nature of the DCT coefficients can be exploited at the expense of reducing the accuracy of the algorithm. This is observed in Fig. 5.28, where the DCT coefficients are represented depending on the harmonics to be compensated. The coefficients have an even symmetry of period $2N/h_{low}$, where h_{low} is the lowest-order harmonic to be compensated, therefore it would be only necessary to calculate the first $\lfloor 2N/h_{low} \rfloor$ DCT coefficients. A lack of accuracy is obtained if this period is not a natural number.

Fig. 5.29 depicts the flowchart of the programming of the frequency-adaptive RC-DCT for $h = 6, 12$ and 18. This diagram includes C-code lines to calculate the DCT coefficients online, which are highly optimized. To avoid using trigonometric functions, the cosine function has been implemented by means of a look-up table of 1440 elements, i.e. with an accuracy of 0.25°. If required, the accuracy could be increased by using a look-up table with more elements (always multiple of 360).

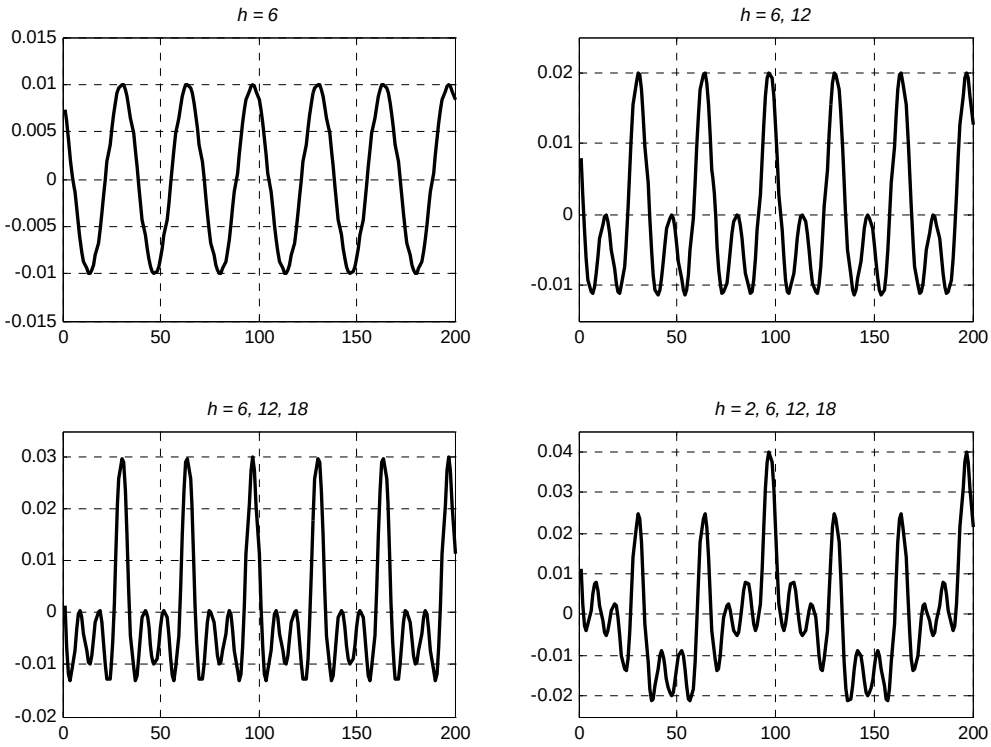

Fig. 5.28. Value of the DCT coefficients depending on the harmonics to be compensated. The *x*-axis has 200 points since the coefficients are calculated for $N = 200$ ($f_o = 50\ Hz,\ T_s = 100\ \mu s$).

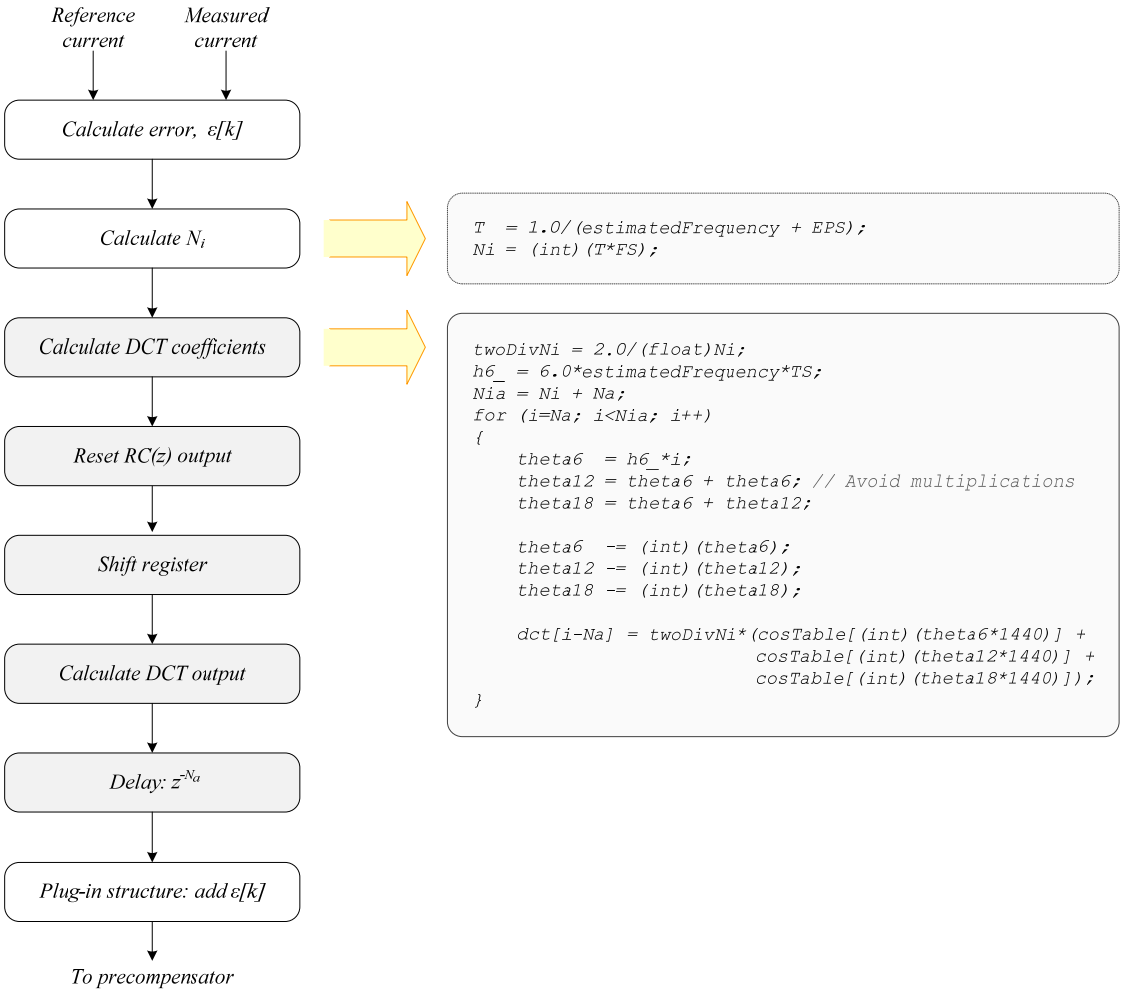

Fig. 5.29. Flowchart of the programming of the frequency-adaptive RC-DCT for $h = 6, 12, 18$.

5.5. Current control scheme.

Fig. 5.30 shows the current control scheme based on a plug-in repetitive controller. The current control structure has two control loops: the repetitive controller and the precompensator. This scheme is implemented in $\alpha\beta$-axes for RC-FFDP (5.30a), and in dq-axes for RC-DCT and RC-IP (Fig. 5.30b).

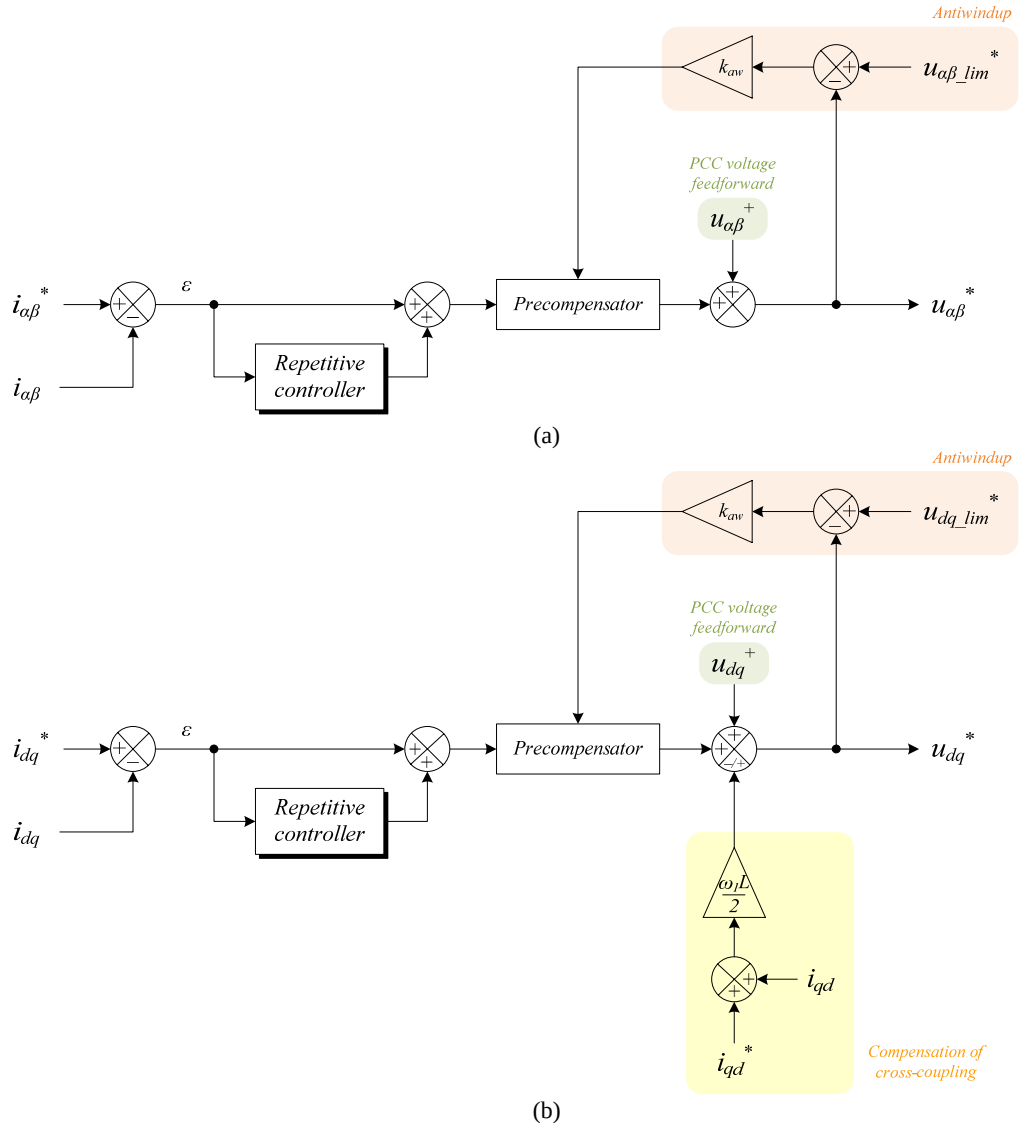

Fig. 5.30. Current control scheme based on repetitive controllers in (a) *αβ*-axes and (b) *dq*-axes.

Fig. 5.31 shows the Bode diagram of the open-loop transfer function based on RC-IP (binomial filter with order 2, which is referenced as *bin2*), RC-IP (Hamming-window filter with order 16, which is referenced as *ham16*), RC-DCT ($N_a = 5$), RC-FFDP1 and RC-FFDP2. The controllers RC-DCT and RC-IP show the lowest gain at the interharmonic frequencies, which will ensure a better noise rejection. Regarding the filter used in RC-IP, the gain at high frequencies with *ham16* is lower than *bin2*, although these frequencies are usually out of the operation range. Besides, the gain at the lower frequencies is higher with *ham16*, as explained in section 5.2.1. Therefore, higher harmonic tracking is achieved by *ham16*. RC-FFDP1 and RC-FFDP2 present a higher gain at the interharmonic frequencies and also a lower gain at the resonant frequencies. Thus, these controllers have not been tested in the experimental setup.

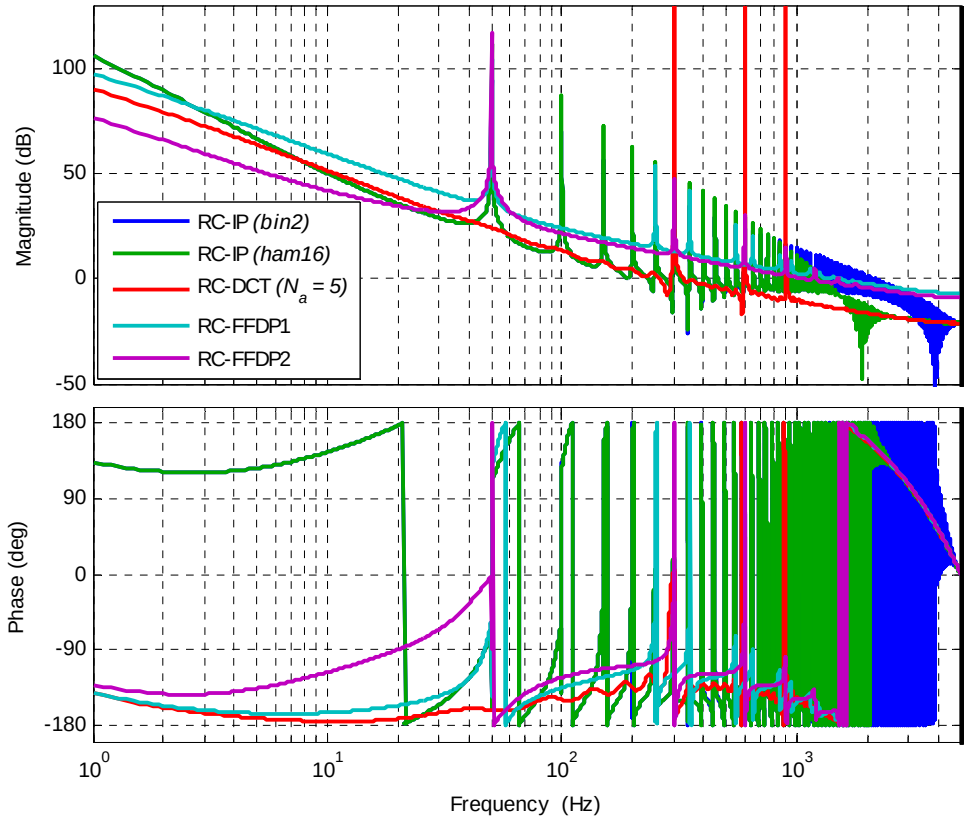

Fig. 5.31. Bode-diagram of the open-loop transfer function based on RC-IP (*bin2*), RC-IP (*ham16*), RC-DCT ($N_a = 5$), RC-FFDP1 and RC-FFDP2.

Fig. 5.32 and Fig. 5.33 shows the error signals in dq-axes and $\alpha\beta$-axes, respectively, after applying an amplitude jump of 150 % at $t = 0.5\ s$ to the harmonics (a) $h = 1$, (b) $h = 1, 5, 7$, (c) $h = 1, 11, 13$ and (d) $h = 1, 17, 19$. The amplitude level for each harmonic is $1/h\ p.u.$ These figures clearly show how RC-FFDP1 and RC-FFDP2 obtains higher steady-state error due to their higher gain at the interharmonic frequencies. Fig. 5.32 also shows that RC-DCT obtains one of the lowest settling times, as well as the loss of selectivity in all controllers as the harmonic frequency increases. The RC-DCT is the one with better performance at high frequencies since no filter is required to ensure its stability, and therefore it has higher gains. If required, this situation can be improved in RC-IP by modifying the cutoff frequency of the filter $Q(z)$ or adjusting the gain K_x. At medium frequencies, the Bode diagram shows that the interharmonic gain of RC-IP is even lower than RC-DCT.

The main performance and stability indicators are collected in Table 5.1. These values numerically verify what has been stated in the preceding paragraphs by means of the settling time, maximum overshoot and minimum gain and phase margins. The settling time has been calculated as the time after which the output remains within $\pm 2\%$ (when the input is a unity step). RC-FFDP1 and RC-FFDP2 are characterized by having the worst indicators, i.e. highest settling time, highest overshoot and critical stability margins. On the other hand, RC-DCT shows a better stability while having a slightly higher settling time than RC-IP.

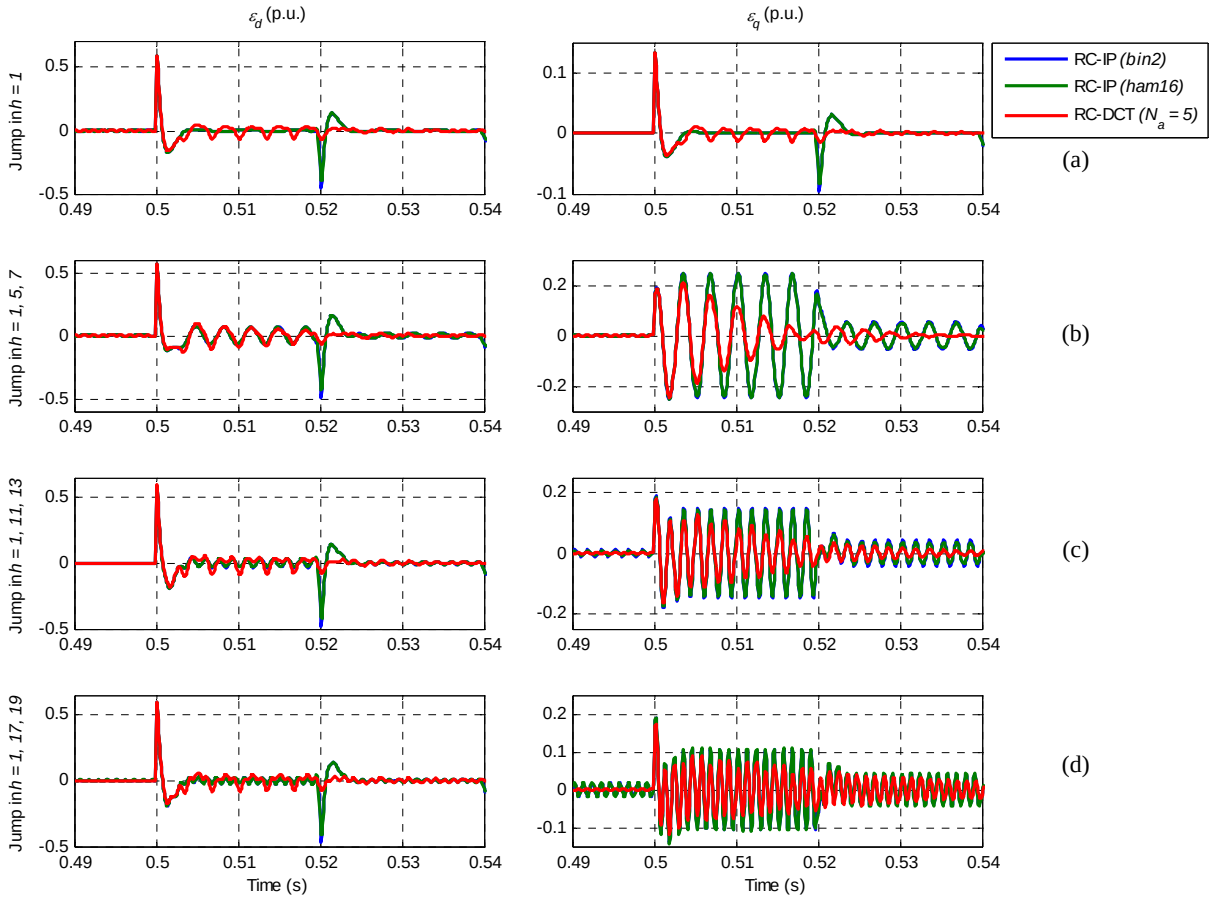

Fig. 5.32. Simulation results: error in *dq*-axes after applying an amplitude jump of 150 % at $t = 0.5\ s$ to the harmonics (a) $h = 1$, (b) $h = 1, 5, 7$, (c) $h = 1, 11, 13$ and (d) $h = 1, 17, 19$ to RC-IP (*bin2*), RC-IP (*ham16*) and RC-DCT ($N_a = 5$).

5.6. Conclusions.

Three structures to implement a repetitive controller have been analyzed and studied, namely, RC-IP, RC-FFDP and RC-DCT. Each of them presents different features in terms of stability, gain at harmonic and interharmonic frequencies and dynamic response. A frequency-adaptive scheme for each of these repetitive controllers has been studied, and a detailed analysis of their programming and computational burden has been provided.

Two different filters have been studied to assure the stability of RC-IP: a binominal FIR filter with order 2 (which is referenced as *bin2*) and a Hamming-window FIR filter with order 16 (which is referenced as *ham16*). In general terms, a better performance is obtained as the filter order increases at the expense of increasing the computational burden of the controller. Its frequency-adaptive algorithm has been studied based on the work [Roldán-Pérez, *et al.*, 2011].

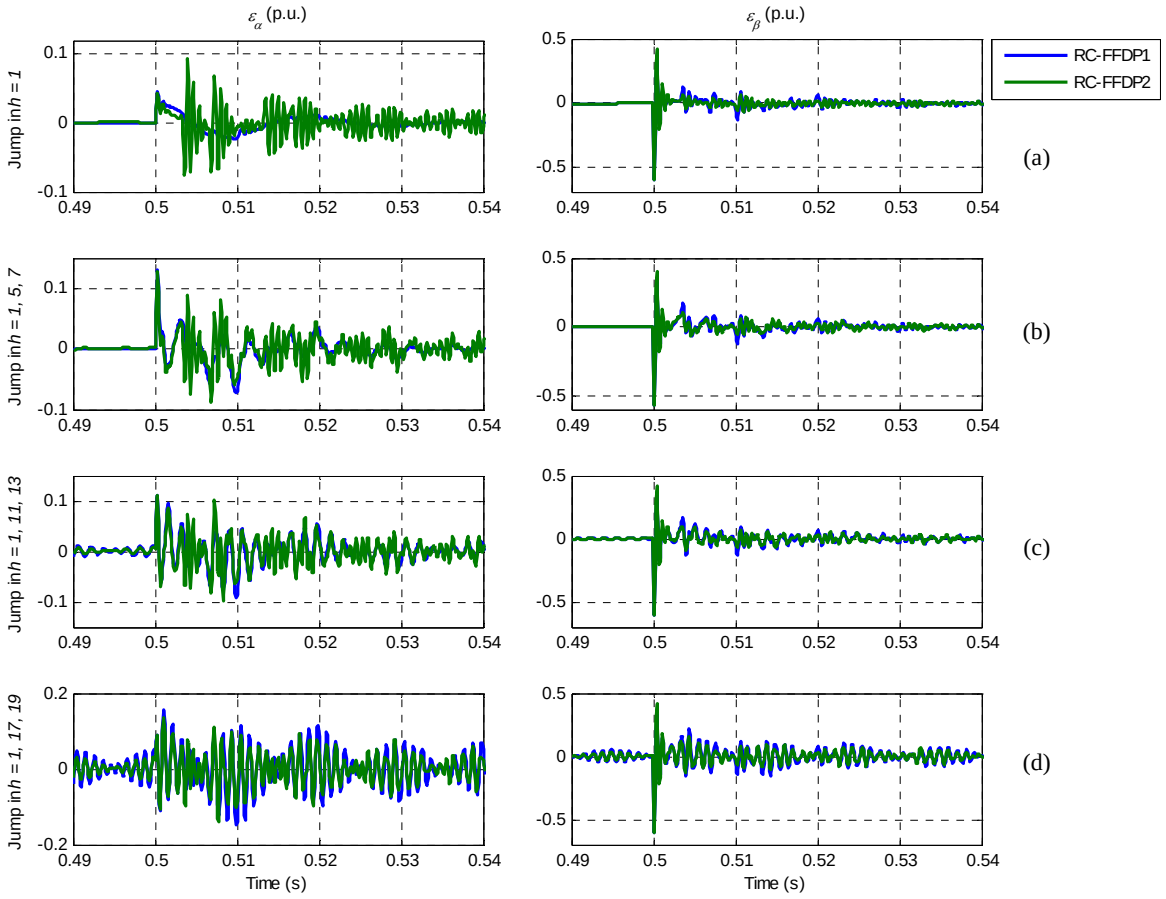

Fig. 5.33. Simulation results: error in $\alpha\beta$-axes after applying an amplitude jump of 150 % at $t = 0.5\ s$ to the harmonics (a) $h = 1$, (b) $h = 1, 5, 7$, (c) $h = 1, 11, 13$ and (d) $h = 1, 17, 19$ to RC-FFDP1 and RC-FFDP2.

TABLE 5.1. PERFORMANCE AND STABILITY INDICATORS OF THE CURRENT CONTROL SCHEME BASED ON REPETITIVE CONTROLLERS.

	RC-IP (bin2)	***RC-IP (ham16)***	***RC-DCT ($N_a = 5$)***	***RC-FFDP1***	***RC-FFDP2***
Settling time, t_s	23.41 ms	24.82 ms	37.5 ms	128 ms	52.8 ms
Maximum overshoot (%)	28.89 %	28.89 %	26.54 %	102.71 %	68.66 %
Minimum gain margin, GM (dB)	5.65 dB	5.67 dB	10.1 dB	0.164 dB	1.04 dB
Minimum phase margin, PM (°)	29.2°	29.1°	28.1°	1.16°	9°

The repetitive controllers based on FFDP show the highest steady-state error due to the poor characteristics of their Bode diagrams, i.e. they have the highest gains at the interharmonic frequencies and the lowest gains at the desired frequencies. A fine tuning of

their parameters could improve their performance. The problem related to the implementation of a non-natural number of delays has also been solved by means of a Thiran filter, which is useful both in its non-frequency-adaptive and frequency-adaptive version.

One of the main advantages of RC-DCT is that no additional filtering is needed to ensure its stability, which allows obtaining a higher gain at high frequencies. Besides, the harmonics to compensate can be selected manually, which do not increase the computational burden. The frequency-adaptive version of this controller has been proposed, and an example of the optimized C-code to compute its coefficients online has been shown to overcome the problem of its high computational load.

Therefore, the best performance is obtained by RC-IP and RC-DCT. RC-IP is more suitable for compensating harmonics of lower order than RC-DCT due to the lower gain at the interharmonic frequencies in this range, whereas RC-DCT present a very high gain at higher frequencies compared to RC-IP. If frequency-adaptation is required, a lower consumption of resources is accomplished by RC-IP.

6

PCC voltage control

After studying in depth the current control of a grid-connected VSC, the second control to analyze is the PCC voltage controller. The presence of an unbalanced voltage at the PCC results in the appearance of a negative sequence current component that deteriorates the control performance. STATCOMs are well-known to be a power application capable of carry out the PCC voltage regulation in distribution lines that may suffer from grid perturbations. This Thesis proposes a novel PCC voltage controller in synchronous reference frame to compensate an unbalanced PCC voltage by means of a STATCOM, allowing an independent control of both positive and negative voltage sequences. As mentioned in the state of the art in chapter 2, several works have been proposed in this line but they were not able to compensate an unbalance in the PCC voltage. Furthermore, this controller includes aspects as antiwindup and droop control to improve the control system performance.

6.1. Introduction.

The ongoing large-scale integration of wind energy into the power system demands the continuous revision of grid codes and power quality standards in order to fulfill restrictive constraints. Furthermore, most host utilities also require that wind farms must tolerate system disturbances [Piwko*, et al.*, 2006]. These requirements become of paramount importance in remote locations where the feeders are long and operated at a medium voltage level, providing a weak grid connection. The main feature of this type of connection is the increased voltage regulation sensitivity to changes in load [Ledesma*, et al.*, 2003]. Thus, the system's ability to regulate voltage at the PCC to the electrical system is a key factor for the successful operation of the wind farm [Farias*, et al.*, 2010], even in the face of voltage flicker caused by wind gusts or post fault electromechanical swings in the power grid [Piwko*, et al.*, 2006].

Nowadays, there are grid operators that allow providing unbalanced currents so that the power at the PCC remains constant. This is very useful in weak grids because it allows connecting all loads to a balanced PCC voltage, which is especially important for sensitive

loads that could disconnect if the AC voltage does not meet restrictive voltage standards.

This task can be accomplished by means of a STATCOM. The STATCOM is a VSC system whose prime function is to exchange reactive power with the host AC system [Yazdani and Iravani, 2010] and control the power factor. In a distribution system, it is mainly used for voltage regulation [Schauder*, et al.*, 1997]. This has a major application in weak grids, whose significant grid impedance may lead to large PCC voltage variations compared to that of strong grids. The general system under investigation is shown in Fig. 6.1. Several loads and wind farms are connected to the same PCC along with a STATCOM, which is in charge of regulating the PCC voltage. In this figure, L and R are the grid filter parameters, L_g and R_g are the grid impedance parameters, C_{DC1} and C_{DC2} are the DC-link capacitors and the STATCOM is a three-level NPC converter.

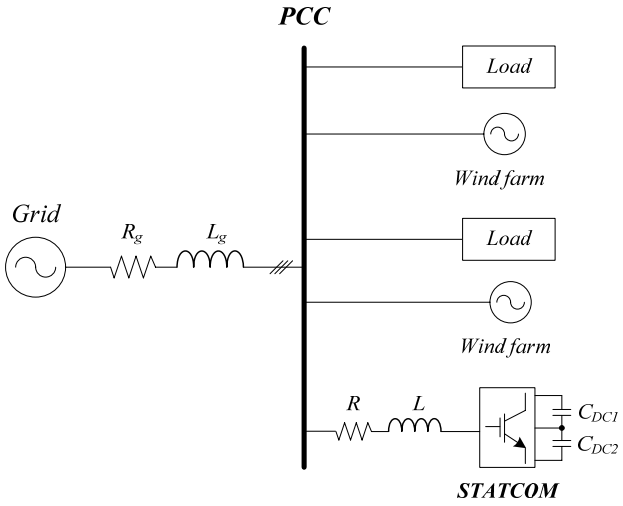

Fig. 6.1. Overview of the general system under investigation.

One of the most typical disturbances in power systems is an unbalance in the PCC voltage [Bollen, 2000]. It is the difference in the magnitudes of the phase (or line) voltages of a three-phase system. There is no standardized mathematical expression to quantify the unbalance of a three-phase system. Three definitions of unbalance are reviewed in [Pillay and Manyage, 2001], one was developed by NEMA (National Equipment Manufacturer's Association), another was developed by the IEEE and the other is the most common definition used by engineering community (the so-called *true definition*). The latter expresses the voltage unbalance factor (VUF) in percent as:

$$VUF(\%) = \frac{U^-}{U^+} \cdot 100 \tag{6.1}$$

where U^- is the rms value of the negative sequence component and U^+ is the rms value of the positive sequence component. An example of an unbalanced three-phase system with VUF equal to 8.33 % is shown in Fig. 6.2.

An unbalanced voltage has several negative effects. For instance, it reduces efficiency and can cause failure in induction machines [Lee, 1999]. It also produces negative effects on power electronic converters. The voltage unbalance can impair a PWM converter system because the input active and reactive power ripples are generated by the cross products of line currents and unbalanced voltages [Kang and Sul, 1997]. The grid synchronization algorithm has to be sufficiently fast and accurate to extract the positive and negative voltage sequences precisely, in order to generate the output current references. A PCC voltage controller is needed to cancel these harmful effects while allowing an independent control of positive and negative sequence components.

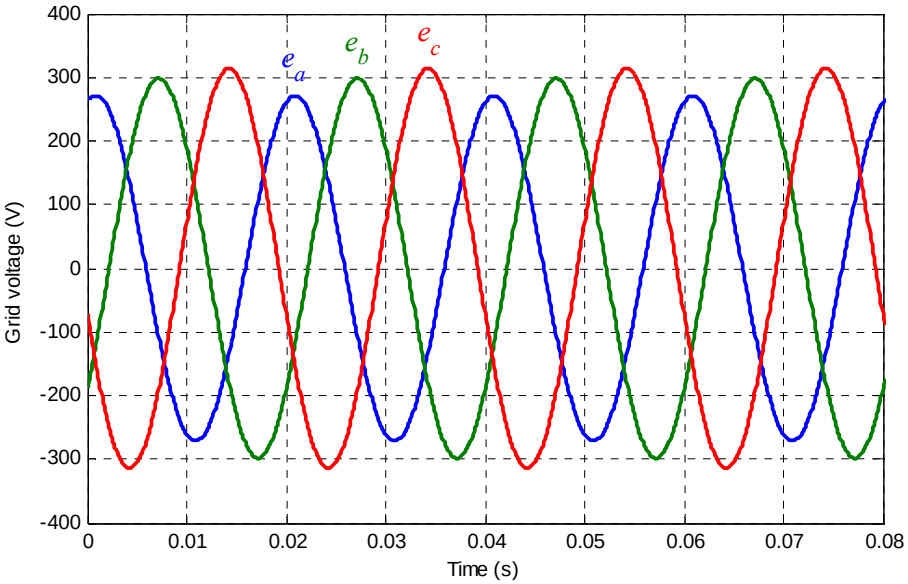

Fig. 6.2. Unbalanced grid voltage.

6.2. Grid modeling under unbalanced conditions.

A VSC can be represented as an ideal AC voltage source (per phase). Therefore, its connection to the grid can be depicted according to the scheme of Fig. 6.3, where L and R are the grid filter parameters, L_g and R_g are the grid impedance parameters, V is the VSC output voltage, U is the PCC voltage, E is the ideal grid voltage and $\vec{\imath}$ is the current flowing from the VSC to the grid.

It is well-known that any three-phase system can be split into the sum of three balanced systems, namely, positive, negative and zero sequences. A balanced three-phase system will be only composed of a positive sequence system. However, in real power systems several types of disturbances may affect the grid and give rise to the appearance of a negative

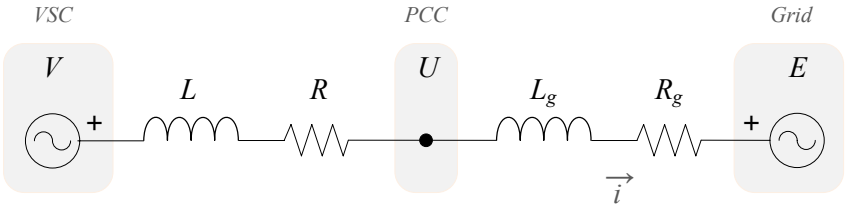

Fig. 6.3. Scheme of the connection of a VSC to the grid (per phase).

sequence system in addition to the positive sequence one. Zero sequence systems only appear in three-phase four-wire power systems [Akagi*, et al.*, 2007] and this case is not tackled in this paper, since a three-phase three-wire power system is considered.

In order to obtain a general model of the grid, valid for both balanced and unbalanced conditions, the scheme of Fig. 6.3 is considered. The grid model is calculated from the voltage equation between the points *U* (PCC) and *E* (ideal grid), which can be expressed in time domain and in synchronous reference frame (*dq*-axes) as shown in (6.2a) for positive sequence (superscript '+') and (6.2b) for negative sequence (superscript '-'). In these equations, ω_o is the fundamental angular frequency ($\omega_1 = 2\pi 50\ rad/s$). Each PCC voltage component is formed by the voltage drop across the grid filter, a cross-coupling term between axes and the ideal grid voltage.

$$\vec{u}^{+}(t) = R_g\vec{i}^{+}(t) + L_g\frac{d\vec{i}^{+}(t)}{dt} + j\omega_1 L_g\vec{i}^{+}(t) + \vec{e}^{+}(t) \tag{6.2a}$$

$$\vec{u}^{-}(t) = R_g\vec{i}^{-}(t) + L_g\frac{d\vec{i}^{-}(t)}{dt} - j\omega_1 L_g\vec{i}^{-}(t) + \vec{e}^{-}(t) \tag{6.2b}$$

Each of these voltages is separated into its *d* and *q* projections: positive sequence voltages u_d^+ and u_q^+ are shown in (6.3a) and (6.3b), whereas negative sequence voltages u_d^- and u_q^- are shown in (6.4a) and (6.4b). Grid resistance R_g is considered to be very small, therefore its contribution to the PCC voltage can be neglected (compared to the voltage drop across the grid filter inductance). Furthermore, the derivative of a constant signal (such as $\vec{i}$ in *dq*-axes) is zero. Note that u_d^+ is equal to zero (6.3a) because a Phase-Locked Loop (PLL) is used to synchronize the positive sequence PCC voltage vector ($\vec{u}^{+}$) with the *q*-axis, hence the projection of $\vec{u}^{+}$ on this axis is equal to its amplitude $\left(u_q^+ \equiv |\vec{u}^{+}|\right)$.

$$u_d^+ = 0 \tag{6.3a}$$

$$u_q^+ \approx \omega_1 L_g i_d^+ + e_q^+ \tag{6.3b}$$

$$u_d^- \approx \omega_1 L_g i_q^- + e_d^- \tag{6.4a}$$

$$u_q^- \approx -\omega_1 L_g i_d^- + e_q^- \tag{6.4b}$$

From the above equations it is straightforward to observe that each PCC voltage component is related to only one current component: u_q^+ and i_d^+, u_d^- and i_q^-, and u_q^- and i_d^-. Current component i_q^+ is related to the control of the DC-link voltage and does not directly influence on the PCC voltage level. Thus, three independent voltage controllers are needed for u_q^+, u_d^- and u_q^-. Since they are constant voltages, a PI controller is enough to ensure zero steady-state error. The plant models needed for the design of these controllers are shown in Fig. 6.4 for each component, based on (6.3b) and (6.4).

6.3. Control scheme.

The block diagram of the proposed control scheme is shown in Fig. 6.5. The high level control loop can be chosen between the *"Active and reactive power control"* block or the *"PCC voltage control and calculation of* i_q^{+*}*"* block. The following stage is the *dq* to *αβ* transformation and calculation of $i_{\alpha\beta}^*$ and, finally, the low level control loop is the current controller.

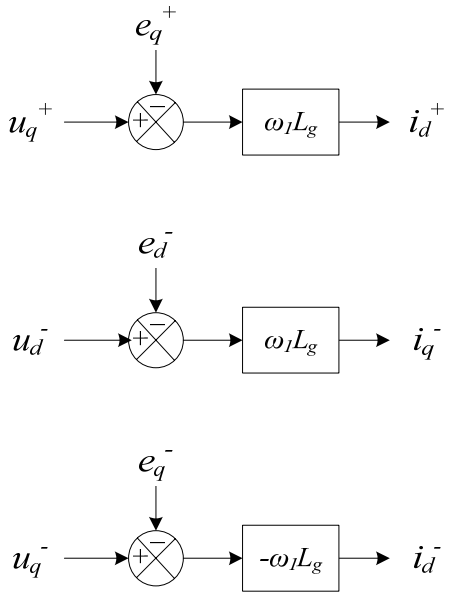

Fig. 6.4. Plant model of the PCC voltage control for each component in *dq*-axes .

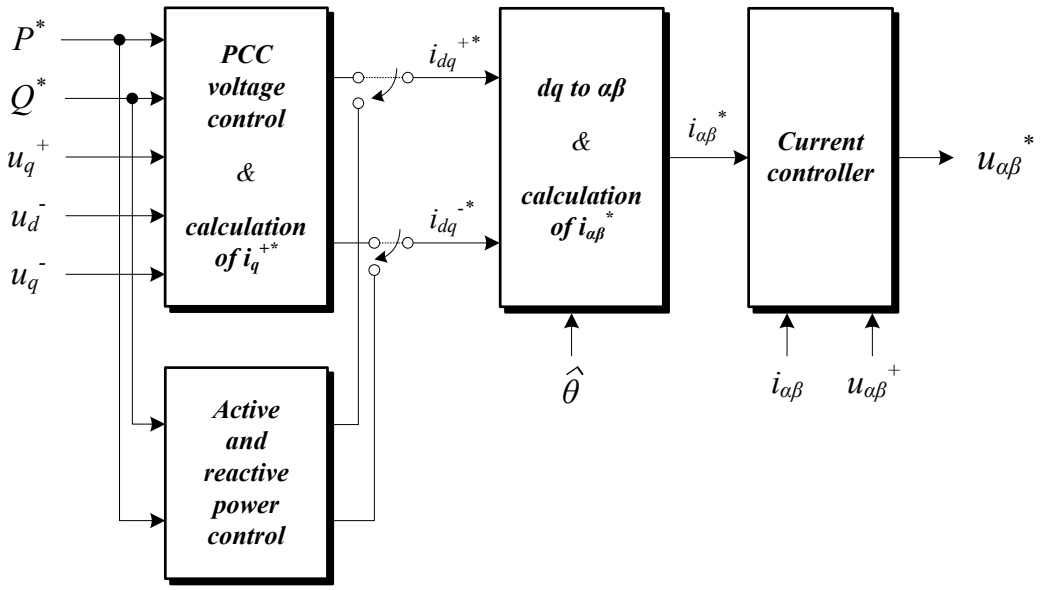

Fig. 6.5. Control scheme including the PCC voltage controller.

6.3.1. Active and reactive power control.

This controller is regulated by the equation system in (6.5). It relates active power, reactive power, PCC voltage and current in *dq*-axes and it is usually employed in active and reactive power control, as well as in power factor control. Active and reactive powers are divided into three parts: average power (P and Q), oscillating power with cosine terms ($P_{2\omega(c)}$ and $Q_{2\omega(c)}$) and oscillating power with sine terms ($P_{2\omega(s)}$ and $Q_{2\omega(s)}$). If grid conditions are balanced, these four oscillating powers are zero and there are only positive sequence voltages and currents. Multiplying by the inverse matrix, the corresponding expressions for the calculation of the reference currents are obtained (i_{dq}^{+} and i_{dq}^{-}). To do so, $P_{2\omega(c)}$ and $P_{2\omega(s)}$ are set to zero to compensate the unbalance caused by negative sequence voltage and $Q_{2\omega(c)}$ and $Q_{2\omega(s)}$ are not controlled, therefore their corresponding rows are eliminated from (6.5). Trying to control these oscillating reactive powers only deteriorates the control performance, therefore they are allowed to run freely.

$$\begin{bmatrix} P_0 \\ P_{2\omega(c)} \\ P_{2\omega(s)} \\ Q_0 \\ Q_{2\omega(c)} \\ Q_{2\omega(s)} \end{bmatrix} = \begin{bmatrix} u_d^+ & u_q^+ & u_d^- & u_q^- \\ u_d^- & u_q^- & u_d^+ & u_q^+ \\ u_q^- & -u_d^- & -u_q^+ & u_d^+ \\ u_q^+ & -u_d^+ & u_q^- & -u_d^- \\ u_q^- & -u_d^- & u_q^+ & -u_d^+ \\ -u_d^- & -u_q^- & u_d^+ & u_q^+ \end{bmatrix} \cdot \begin{bmatrix} i_d^+ \\ i_q^+ \\ i_d^- \\ i_q^- \end{bmatrix} \tag{6.5}$$

6.3.2. PCC voltage control.

The block diagram of the PCC voltage controller is shown in Fig. 6.6a and it is implemented in *dq*-axes. This stage is formed by three “individual voltage controllers” in parallel, whose outputs are i_d^{+*}, i_d^{-*} and i_q^{-*}, plus the calculation of i_q^{+*} by means of (6.6). This equation is obtained from (6.5). The minus sign that goes with u_q^+ is due to the current direction. These four outputs are the references for the current controller. In this figure, ε represents the error signal and the subscript ‘lim’ stands for ‘limited’.

$$i_q^{+*} = \frac{P^* u_q^+}{(u_d^-)^2 + \left(u_q^-\right)^2 - \left(u_q^+\right)^2} \tag{6.6}$$

The inner structure of each “individual voltage controller” is depicted in Fig. 6.6b. As mentioned, it is mainly formed by a PI controller with a forward Euler integrator. The constant δ is 1 for the voltage controllers of u_q^+ and u_d^-, and -1 for the voltage controller of u_q^- due to the minus sign in (6.4b). It is a first order system and, considering the cascaded system of Fig. 6.5, the tuning goal is to achieve a settling time larger than ten times the settling time of the current controller ($t_s|_{vc} > 10 \cdot t_s|_{cc}$, where t_s is the settling time, ‘vc’ means voltage control and ‘cc’ means current control). This constraint affects the position of the closed-loop pole introduced by the PI controller. The integral constant (k_i) helps achieve zero steady-state error in the event of model mismatch and disturbances. Therefore, the parameter tuning is focused on settling time and controller bandwidth. The resulting parameters are $k_p = 0.05$ and $k_i = 350$.

In order to prevent the windup of the integrator, an antiwindup mechanism has been added to each PI controller. It is characterized by the antiwindup constant, which has been set as $k_{aw} = 0.1$. High values for this parameter cause system instability. When using an antiwindup technique, an important detail to be taken into account is that its contribution should not be added to the integral branch of the PI controller until the whole control system starts. Otherwise, the control system would be forced to start with a non-zero error.

The linear operating range of a STATCOM with given maximum capacitive and inductive ratings can be extended if a regulation "droop" is allowed. Regulation "droop" means that the terminal voltage is allowed to be smaller than the nominal no-load value at full capacitive compensation and, conversely, it is allowed to be higher than the nominal value at full inductive compensation [Hingorani and Gyugyi, 2000]. It also ensures automatic load sharing with other voltage compensators. Perfect regulation (zero droop or slope) could result in poorly defined operating point, and a tendency of oscillation, if the system impedance exhibited a "flat" region (low impedance) in the operating frequency range of interest

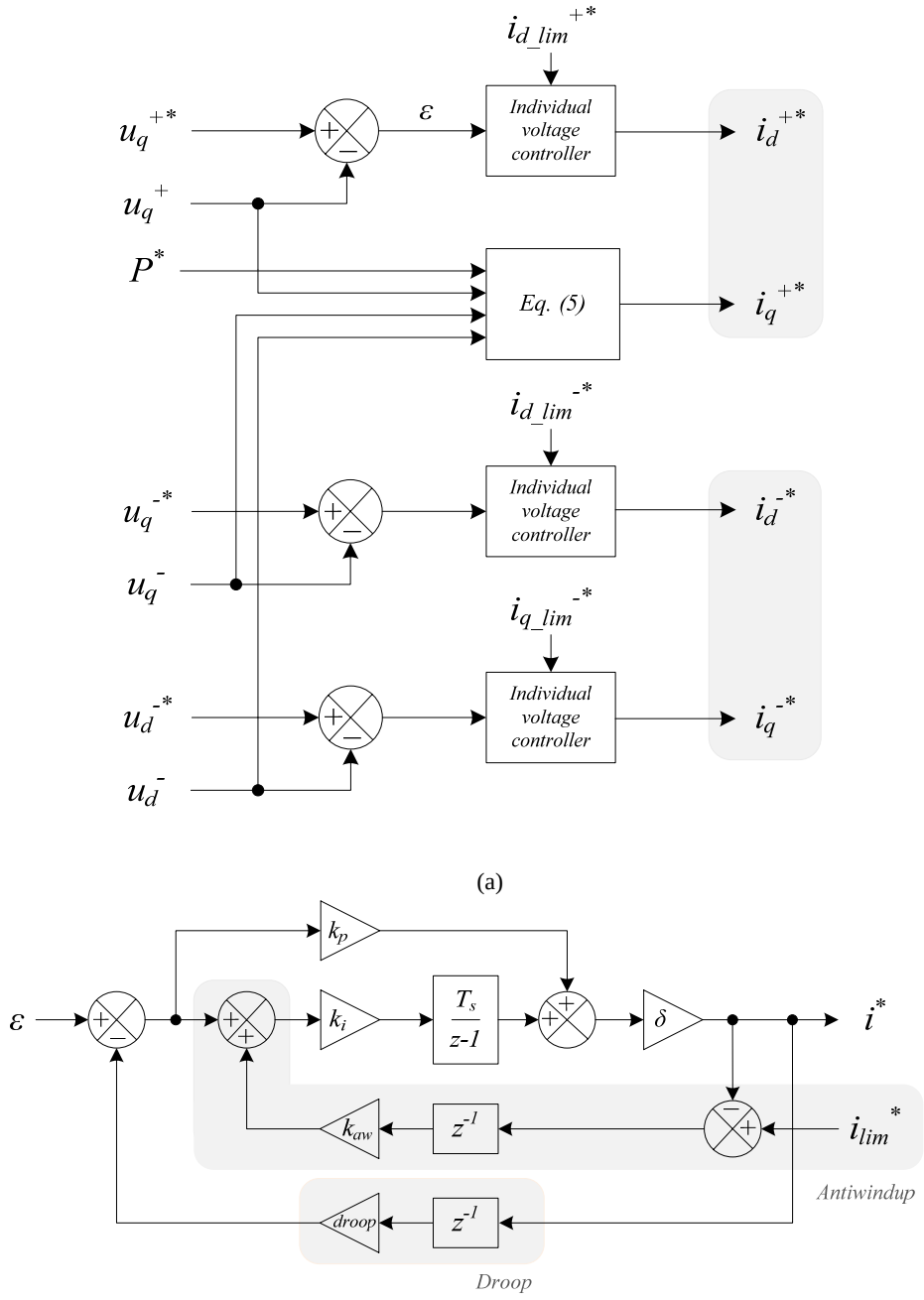

Fig. 6.6. (a) Block "*PCC voltage control & calculation of* i_q^{+*}" of Fig. 6.4; (b) block diagram of the "*individual voltage controller*".

[Hingorani and Gyugyi, 2000]. This droop control has been added to the voltage controller as shown in Fig. 6.6b, characterized by the constant $droop = 0.01$. Similarly to k_{aw}, high values for this parameter cause system instability.

The expression in (6) is obtained from (5).

6.3.3. *dq* to *αβ* transformation and calculation of *αβ*-axes reference current.

The outputs of the first stage of the control scheme are i_{dq}^{+*} and i_{dq}^{-*}. These current references have to be transformed to *αβ*-axes, since the current controller is implemented in stationary reference frame. The reason for this is that a resonant controller tuned at ω in *αβ*-axes is able to compensate both positive and negative sequences, whereas in *dq*-axes two controllers would be necessary, a PI controller and a resonant controller tuned at 2ω. The fact of increasing the number of controllers connected in parallel endangers the system stability and increases the settling time of the controller.

Positive and negative sequence current references in *αβ*-axes are calculated as shown in (6.7a) and (6.7b) for positive and negative sequence, respectively. The estimated phase angle $\hat{\theta}$ of the positive sequence PCC voltage vector is obtained with a PLL, whose bandwidth is set to $20\ Hz$. This results in a good tradeoff between selectivity, steady-state error and response speed.

$$\begin{bmatrix} i_{\alpha}^{+*} \\ i_{\beta}^{+*} \end{bmatrix} = \begin{bmatrix} cos\,\hat{\theta} & -sin\,\hat{\theta} \\ sin\,\hat{\theta} & cos\,\hat{\theta} \end{bmatrix} \cdot \begin{bmatrix} i_{d}^{+*} \\ i_{q}^{+*} \end{bmatrix} \tag{6.7a}$$

$$\begin{bmatrix} i_{\alpha}^{-*} \\ i_{\beta}^{-*} \end{bmatrix} = \begin{bmatrix} cos\,\hat{\theta} & sin\,\hat{\theta} \\ -sin\,\hat{\theta} & cos\,\hat{\theta} \end{bmatrix} \cdot \begin{bmatrix} i_{d}^{-*} \\ i_{q}^{-*} \end{bmatrix} \tag{6.7b}$$

Afterwards, the final current references are calculated according to (6.8a) and (6.8b).

$$i_{\alpha}^{*} = i_{\alpha}^{+*} + i_{\alpha}^{-*} \tag{6.8a}$$

$$i_{\beta}^{*} = i_{\beta}^{+*} + i_{\beta}^{-*} \tag{6.8b}$$

6.3.4. Current controller.

The third stage of the control scheme is the current controller. The harmonics present in power systems are those of order $6k \pm 1$ ($k \in \mathbb{Z}$), which turn into $6k$ ($k \in \mathbb{Z}$) when changing the reference frame from stationary to synchronous. This allows halving the number of resonant controllers needed in the current control [Bojoi*, et al.*, 2005]. Therefore, since harmonics 5^{th} (negative sequence) and 7^{th} (positive sequence) are usually present in the grid, the current control scheme of Fig. 6.7 has been implemented to obtain the simulation results. It consists of two resonant controllers tuned at ω and 6ω, based on SOGIs, a feedforward of the positive sequence PCC voltage and *αβ* to *dq* and *dq* to *αβ* transformations. A feedforward of the total PCC voltage (including negative sequence) would introduce non-desired

harmonics in the control. The error signals in $\alpha\beta$-axes and dq-axes are $\varepsilon_{\alpha\beta}$ and ε_{dq}, respectively.

To help decreasing the computational burden, the trigonometric functions involved by these transformations can be implemented by means of look-up tables if the digital platform has enough available memory.

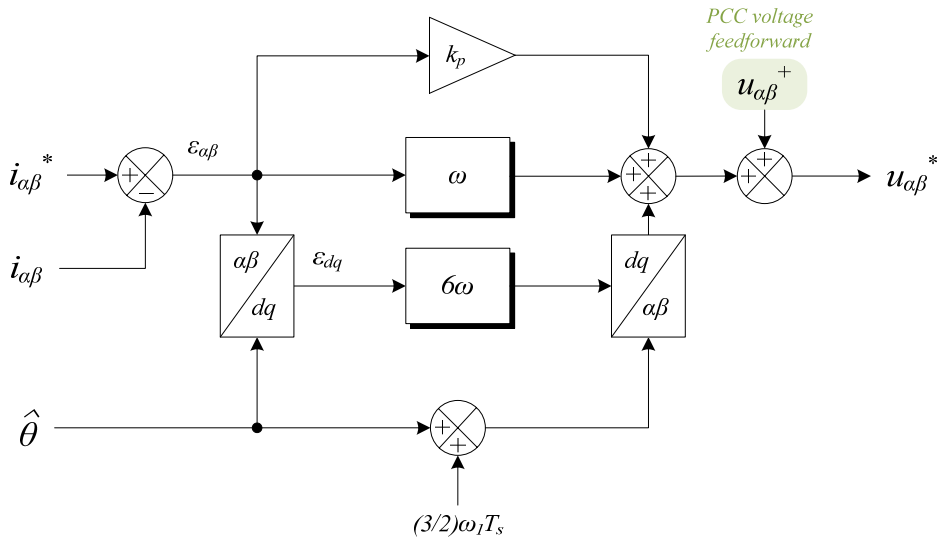

Fig. 6.7. Block diagram of the block “Current controller” of Fig. 6.4.

6.4. Online adaptation of the DC-link reference voltage.

To enable the power transfer between the grid and the DC-link capacitors, u_{DC} must be greater than $\sqrt{2}\,u_{LL}$, where u_{LL} is the line-to-line PCC voltage. When calculating the reference DC-link voltage, a safety margin Δu_{DC} is usually given to ensure the energy transfer in case of voltage fluctuations. This margin takes values from $20\ V$ to $30\ V$ in weak grids. Therefore, the calculation of u_{DC}^{*} is shown in (6.9).

$$u_{DC}^{*} \geq \sqrt{2}\,u_{LL} + \Delta u_{DC} \tag{6.9}$$

When the PCC voltage is expected to suffer large variations, as in the case of weak grids, u_{DC}^{*} should be recalculated online to adapt its value to the actual AC voltage. In this way, the modulation index is kept around its optimal value, i.e. $m_a \approx 1$. Otherwise, the modulation index will be altered, which can increase the converter power losses, modify the expected harmonic content and worsen the overall system performance [Wu, 2006].

6.5. Sampling mode when working with an L-filter.

One of the essential parts of the converter control is the synchronization system. The angle of the PCC voltage vector is derived from this. This angle would coincide with that of the grid voltage if it were an ideal grid. Generally, the impedance is neglected in terms of controller design, considering the voltage at the PCC as the system voltage [Cóbreces, 2009].

Blasko et al. [Blasko, *et al.*, 1998] established that the optimal moment to sample the currents are those in which the PWM carrier signal reaches its maximum and minimum value, as it is in those moments when the current ripple carries out its zero crossing. When working with an LCL-filter and a non-ideal grid, and sampling the PCC voltage at those same moments, the obtained PCC voltage in *dq*-axes corresponds to its actual value. However, this is not the same situation when working with an L-filter and a non-ideal grid. In this case, the PCC voltage presents a ripple in which two envelopes can be seen. By sampling synchronously with the sampling period of the currents, which is also the controller sampling period, the obtained PCC voltage corresponds to one of those envelopes, giving rise to incorrect projections of the PCC voltage on the *dq*-axes, see Figure 3.11a.

Briz et al. [Briz, *et al.*, 2010] posed two alternative methods to the method suggested by Blasko for sampling the currents, when the inverter is connected to a load whose natural frequency may be close to the sampling frequency. In such cases, the method based on the maximum and minimum points of the carrier signal introduces an error at the current fundamental frequency as well as aliasing problems. The methods the authors proposed were based on advancing the sampling instant and on multi-sampling per switching period.

The methods here studied for sampling the PCC voltage are similar to those shown in [Briz, *et al.*, 2010]. With the system configuration defined in Table 6.1, several methods for performing the PCC voltage sampling are shown in Fig. 6.8 [Huerta, 2009]:

- The previously mentioned sampling method synchronized with the current sampling, where the sampling period of the PCC voltage and the timer, T_{ss}, is equal to T_s (Fig. 6.9a);
- Sampling at the midpoint of T_s, with $T_{ss} = T_s$, which obtains a PCC voltage in *dq*-axes higher than the real value (Fig. 6.9b);
- Sampling shifted a time t_{ad} with respect to the sampling instants of the current, where $T_{ss} = T_s$ and where the voltage remains erroneous (Fig. 6.9c);
- Oversampling of two samples, synchronized with T_s, where $T_{ss} = T_s/2$ and for which the voltage remains slightly erroneous (Fig. 6.9d);
- Oversampling of three samples, synchronized with T_s, where $T_{ss} = T_s/3$ and for

which the voltage still remains slightly erroneous (Fig. 6.9e), and

- Oversampling of four samples, which obtains a correct PCC voltage in *dq*-axes (Fig. 6.9f).

TABLE 6.1 SYSTEM PARAMETERS WITH L-FILTER AND NON-IDEAL GRID.

S_{base}	$100\ kVA$
U_n	$398\ V$
ω_1	$2\pi 50\ Hz$
L	$1.5 \cdot 10^{-1}\ p.u.$
R	$2.3 \cdot 10^{-3}\ p.u.$
L_g	$5 \cdot 10^{-2}\ p.u.$
R_g	$6{,}3 \cdot 10^{-10}\ p.u.$
T_{sw}	$400\ \mu s$
T_s	$200\ \mu s$

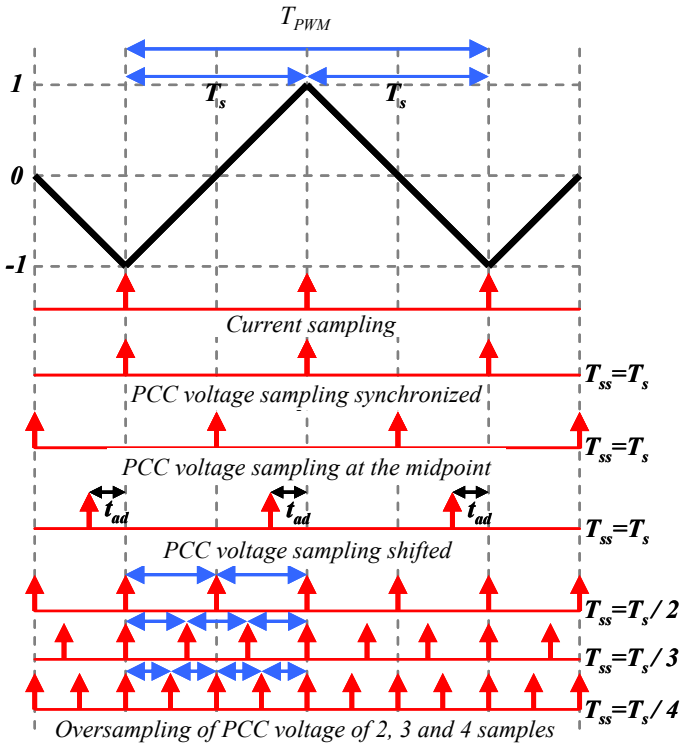

Fig. 6.8. Methods for performing the PCC voltage sampling [Huerta, 2009].

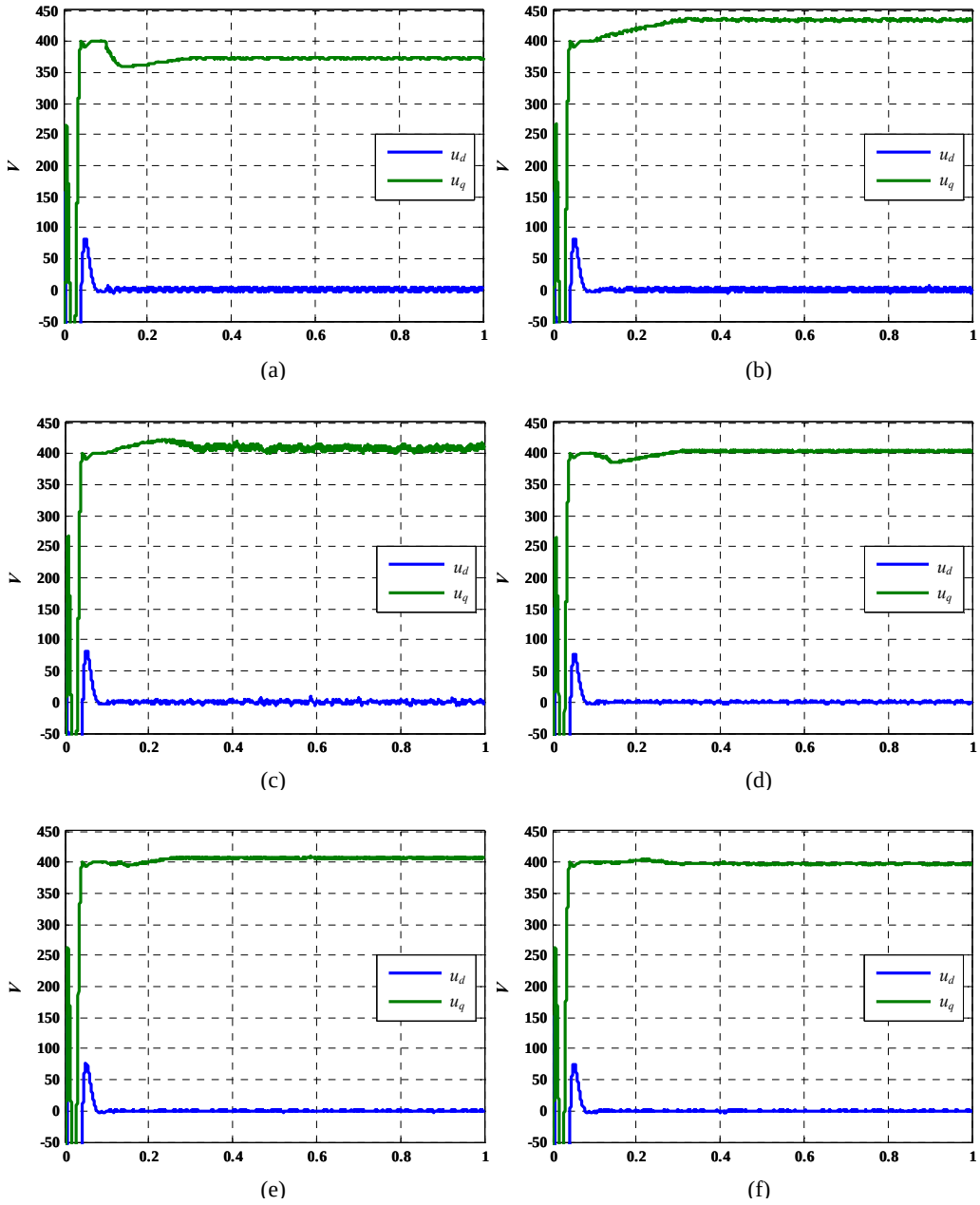

Fig. 6.9. Measured u_{dq} with (a) sampling synchronized, (b) sampling at the midpoint, (c) sampling shifted, (d) oversampling of two samples, (e) oversampling of three samples, and (f) oversampling of four samples.

6.6. Simulation results.

A simulation has been carried out with MATLAB/Simulink® in order to test the performance of the proposed voltage controller. The ideal grid voltage of Fig. 6.2 has been considered, with a grid impedance of $L_g = 0.25\ mH$ and $R_g = 0.5\ m\Omega$ (weak grid). The grid filter parameters are $L = 0.75\ mH$ and $R = 3.63\ m\Omega$. The NPC rated power is 100 kVAr and the DC-link capacitors have a value of $C_{DC1} = C_{DC2} = 4.5\ mF$. No load is connected to the PCC. The proposed voltage controller is enabled at t = 0.5 s.

Fig. 6.10 shows the temporary evolution of the PCC voltage in *abc*-axes. It presents a high ripple due to the high grid impedance. It is clear that, when the voltage control is enabled, the PCC voltage is balanced. This is corroborated by decomposing this voltage in their positive and negative sequences as shown in Fig. 6.11. The positive sequence u_{dq}^{+} remains the same because its reference voltage corresponds to the value it had before enabling the PCC voltage control. The negative sequence u_{dq}^{-} becomes almost zero since its reference voltage is set to zero for both *d* and *q* components, as well as the VUF.

The current flowing from the VSC to the grid is represented in Fig. 6.12 in *abc*-axes. Since no load is connected to the PCC, the current before enabling the voltage control is zero. Afterwards, the VSC provides an unbalanced current in order to compensate the negative sequence component.

Since the PCC voltage is no longer unbalanced due to the effect of the voltage controller, the unbalance now appears on the DC-link voltage (u_{DC}). Fig. 6.13a shows that a large oscillation appears in u_{DC} when compensating the negative sequence voltage, reaching nearly $\pm 125\,V$. Besides, the DC-link voltage unbalance, calculated as the difference between positive and negative DC-link voltages ($u_{DC}^{+} - u_{DC}^{-}$), is also increased. If the level of this oscillation is not permissible, the voltage reference for negative sequence voltage can be set with a value different from zero but still low enough to satisfy regulations when it comes to maximum PCC voltage unbalance. This would result in a reduction of u_{DC} oscillation and DC-link voltage unbalance.

Fig. 6.14 displays the reference currents in *dq* and *αβ*-axes. All of them are almost negligible before enabling the voltage control. Due to the negative sequence compensation, an oscillation of frequency $2f_1$ appears in i_q^{+*} (Fig. 6.14a). Notice how reference currents in *αβ*-axes ($i_{\alpha\beta}^{*}$, Fig. 6.14e) are unbalanced.

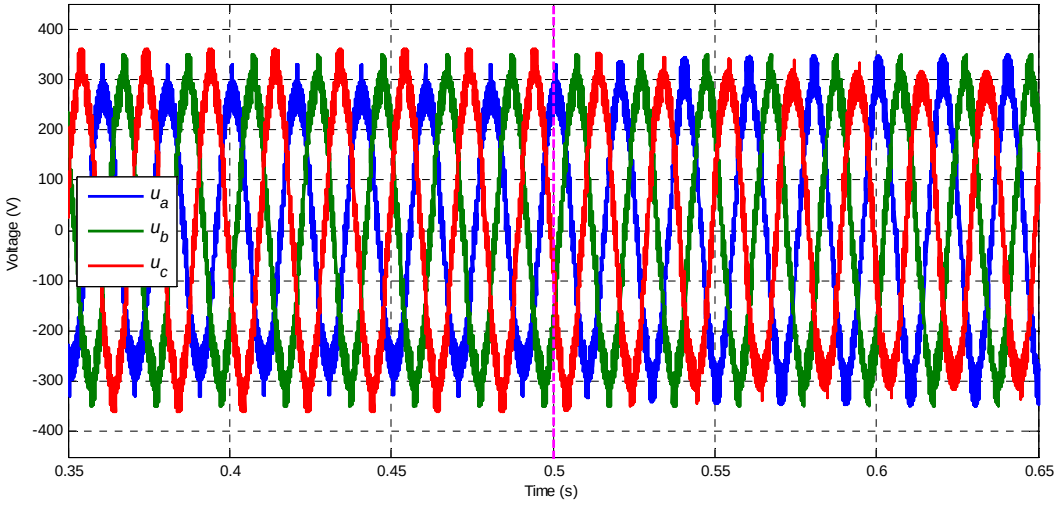

Fig. 6.10. PCC voltage.

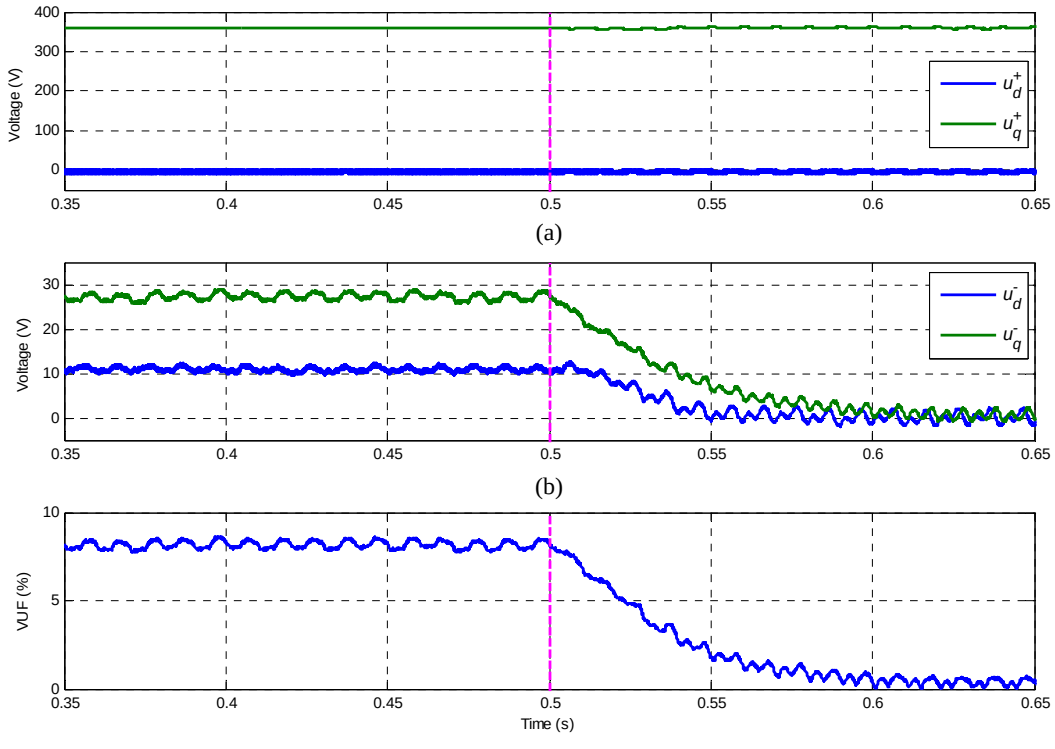

Fig. 6.11. PCC voltage (a) positive and (b) negative sequences in *dq*-axes; (c) VUF (%).

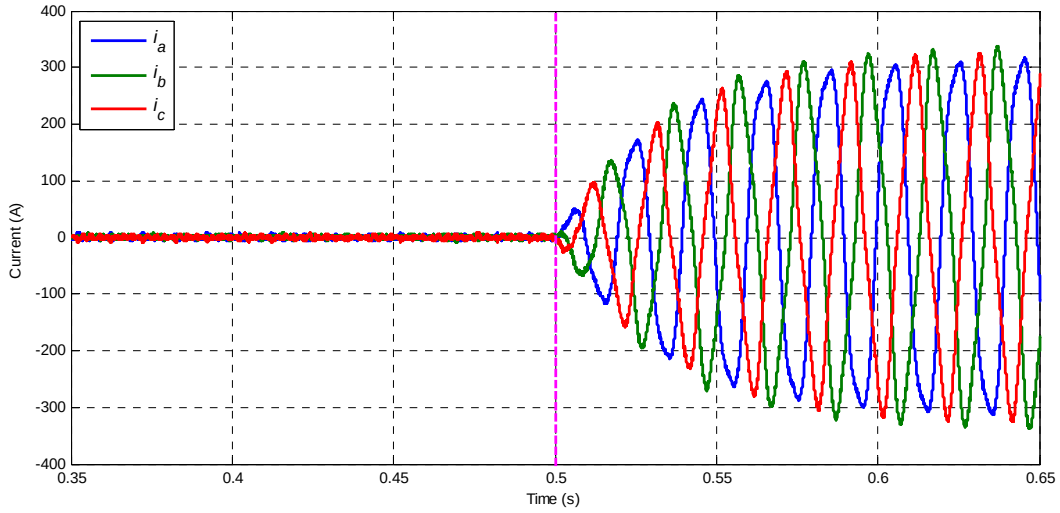

Fig. 6.12. PCC current.

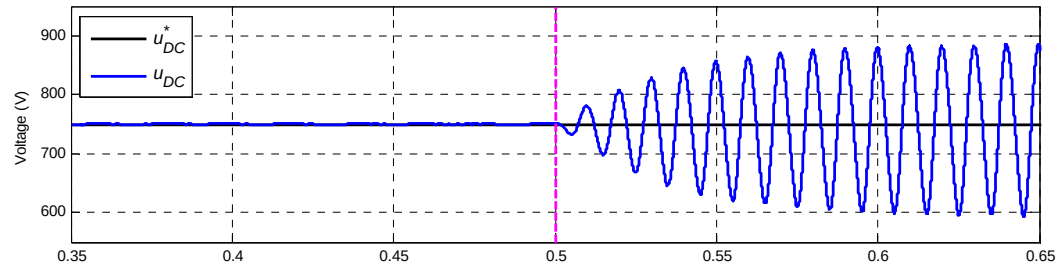

(a)

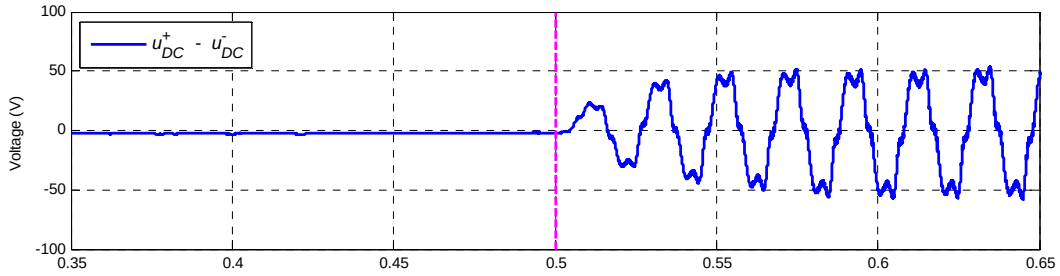

(b)

Fig. 6.13. (a) DC-link voltage and (b) DC-link voltage unbalance.

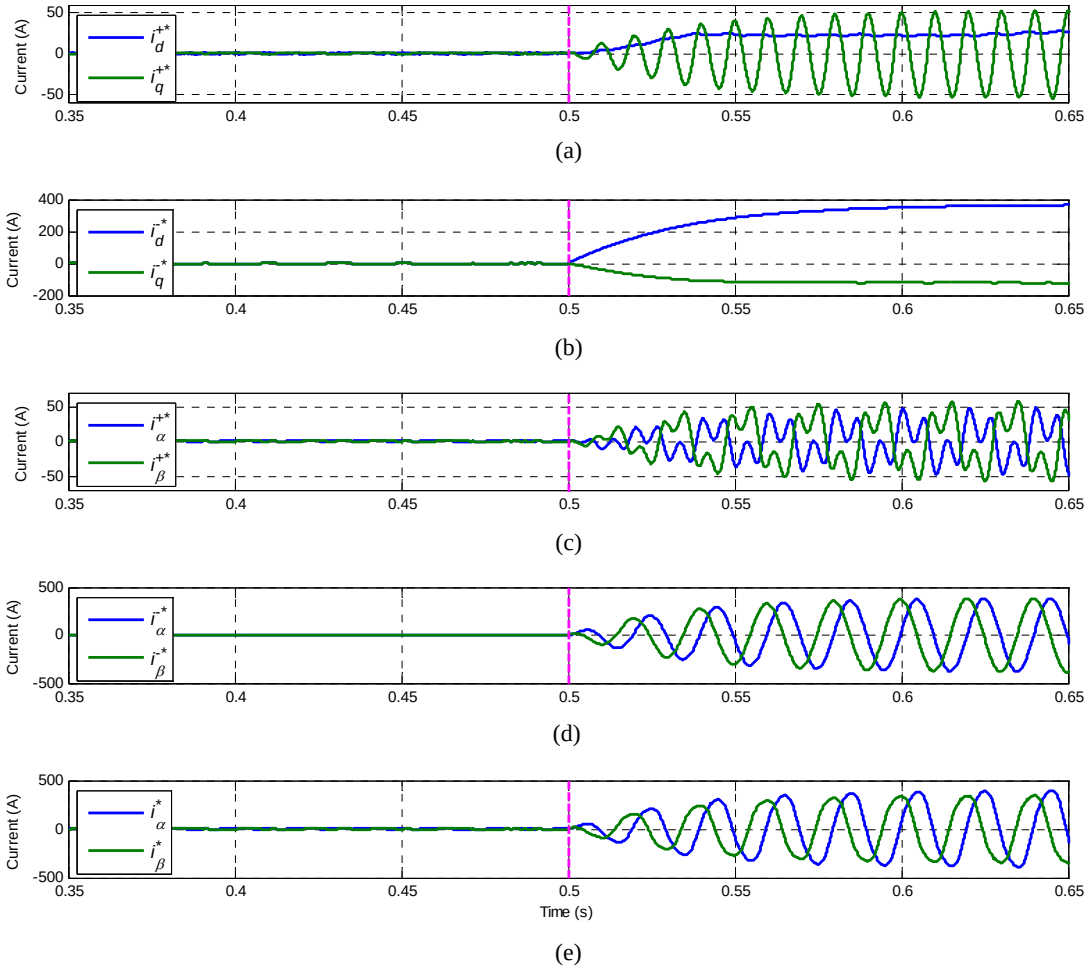

Fig. 6.14. (a) Positive sequence reference current in dq-axes, i_{dq}^{+*}; (b) negative sequence reference current in dq-axes, i_{dq}^{-*}; (c) positive sequence reference current in $\alpha\beta$-axes, $i_{\alpha\beta}^{+*}$; (d) negative sequence reference current in $\alpha\beta$-axes, $i_{\alpha\beta}^{-*}$; (e) reference current in $\alpha\beta$-axes, $i_{\alpha\beta}^{*}$.

6.7. Conclusions.

This chapter has proposed a PCC voltage controller in synchronous reference frame to compensate an unbalanced PCC voltage by means of a STATCOM, allowing an independent control of both positive and negative voltage sequences. To do so, the grid model has been studied under unbalanced conditions, showing the equations that relate voltage and current.

This voltage controller has been placed inside a control scheme to evaluate its performance by means of simulation results. These results have demonstrated the efficacy of this controller, managing to significantly reduce the oscillation present in the DC-link voltage.

However, due to the compensation of the PCC voltage negative sequence, an oscillation appears on the DC-link voltage, with frequency twice the fundamental grid frequency. The magnitude of this oscillation depends on the level of negative sequence. If the level of this

oscillation is not permissible, the voltage reference for negative sequence voltage can be set with a value different from zero but still low enough to satisfy regulations when it comes to maximum PCC voltage unbalance. This would result in a reduction of u_{DC} oscillation and DC-link voltage unbalance.

Experimental results have not been provided because the grid at our laboratory is not a weak grid and, even though this could be simulated by increasing the inductance in series with the VSC (thus, increasing the grid impedance), our three-level NPC converter has not been sized for compensating such unbalances.

7

Experimental results

This chapter collects the results of a series of experimental tests used to characterize the behavior of the current controllers studied and developed in this Thesis. These tests have been classified into (i) transient response, (ii) steady-state response and (iii) behavior under frequency jumps. To accomplish this characterization, several performance indicators have been defined, which will help establishing a comparison among the current controllers.

Secondly, computational load and execution time are analyzed. Special attention is paid to the implementation of repetitive controllers due to their criticality.

7.1. Performance indicators.

In this section, the definitions of some of the indicators used to assess the performance of a control system are described briefly. They have been categorized according to the type of response they analyze, namely, transient response and steady-state response.

7.1.1. Transient response.

- *Settling time.*

  The settling time (t_s) is the time after which the output remains within ± 2 % or ± 5 % of its final value, which is usually required to be small [Franklin*, et al.*, 1998]. In this Thesis, the definition of ± 2 % has been considered.

- *Maximum overshoot.*

  The maximum overshoot is the peak value divided by the final value, which should typically be 1.2 (20 %) or less.

7.1.2. Steady-state response.

- *Steady-state error.*

  The steady-state error is the difference between the desired value and the final value of the output. If the desired value of the output for a system is r (a constant) and the actual output is $y(t)$, the steady state error is defined as:

$$e_{ss} = \lim_{t\to\infty} \big(r - y(t)\big) \tag{7.1}$$

- *Total Harmonic Distortion (THD).*

  The THD is defined as the root mean square (RMS) value of the total harmonics of the signal, divided by the RMS value of its fundamental component. The THD is calculated as shown in (7.2), where h is the harmonic order and X_h is the RMS value of the signal evaluated at the harmonic h^{th}. Instead of calculating the RMS value for each harmonic, the numerator in (7.2) has been replaced by $X_{total} - X_1 - X_{DC}$, where X_{total} is the RMS value of the signal X, X_1 is the RMS value of the fundamental component and X_0 is the RMS value of the DC component.

$$THD_X = \frac{\sqrt{\sum_{h=2}^{\infty} X_h^2}}{X_1} \tag{7.2}$$

- *Weighted Total Harmonic Distortion (WTHD).*

  The WTHD is superior to the THD as a figure of merit for a non-sinusoidal converter waveform since the WTHD predicts the distortion in the current and subsequent additional losses which are typically the major issues in the application of such converters. The calculation of the WTHD is given by (7.3). The maximum harmonic order that has been taken into account is $h = 50$.

$$WTHD_X = \frac{\sqrt{\sum_{h=2}^{\infty} \left(\frac{X_h}{h}\right)^2}}{X_1} \tag{7.3}$$

7.2. Experimental setup.

The algorithms studied in this Thesis have been tested in the experimental setup of Fig. 7.1, and whose schematics are depicted in Fig. 7.3. Such experimental setup is composed of the following items:

- Grid parameters:
  - Base voltage: $U_{base} = 400\ V$,
  - Base frequency: $\omega_{base} = 2\pi 50\ rad/s$.
- Three-level Neutral Point Clamped (NPC) converter with the following parameters:
  - Rated apparent power: $S_n = 100\ kVA$,
  - Nominal voltage: $U_{nominal} = 400\ V$,
  - DC-link nominal voltage: $u_{DC} = 750\ V$,
  - DC-link maximum voltage: $u_{DC_{max}} \approx 1200\ V$,
  - DC-link capacitors: $C_{DC1} = C_{DC2} = 4.5\ mF$,
  - IGBTs: FD300R12KE3 and DF300R12KE3 (http://www.eupec.com)
  - Grid-filter: $L = 0.75\ mH$, $R = 3.63\ m\Omega$.
- Oscilloscope *Yokogawa DL750*:
  - Up to 16 channels,
  - 12 bit, 10 MS/s input modules.
- Programmable three-phase AC voltage source *Pacific Power 345-AMX*:
  - Two modules, master and slave, each of them with rated apparent power $S_n = 4.5\ kVA$.
  - Output frequency: $20 - 5000\ Hz$,
  - Phase voltage: $0 - 338\ V_{L-N}$ $(3\emptyset)$,
  - Line voltage: $0 - 585\ V_{L-L}$ $(3\emptyset)$.
- Control platform (Fig. 7.2):
  - Development board *TMS320C6713DSK* of DSP *TMS320C6713* from Texas Instruments (http://www.ti.com),
  - Development board *DIGILAB 2E* (http://www.digilentinc.com) of FPGA *SPARTAN 2E* from Xilinx (http://www.xilinx.com).

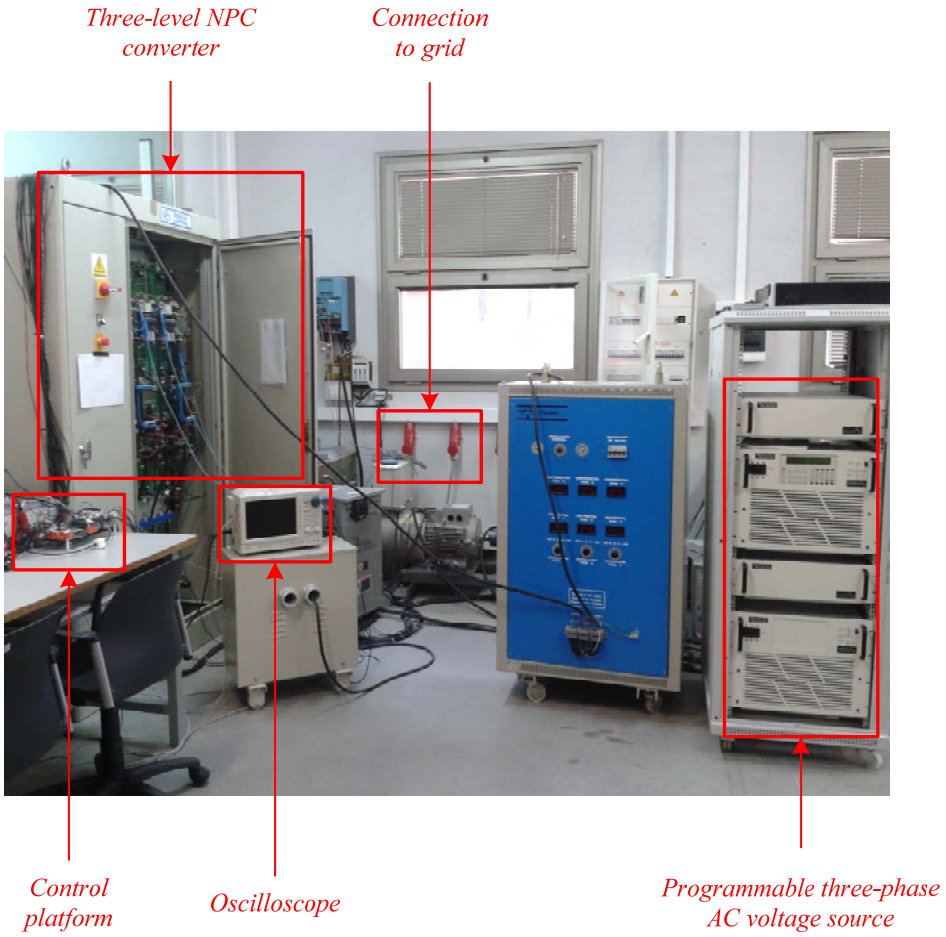

Fig. 7.1. Experimental setup.

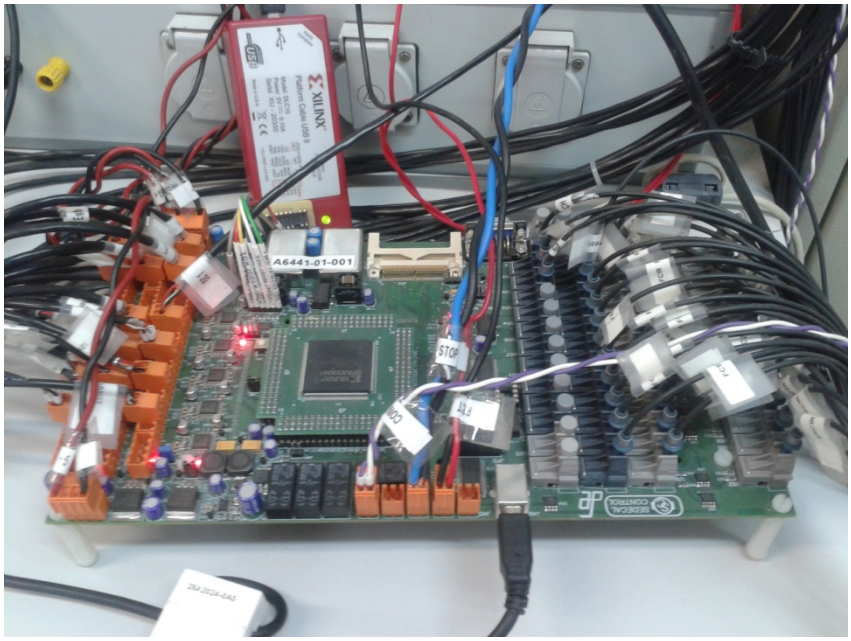

Fig. 7.2. Control platform.

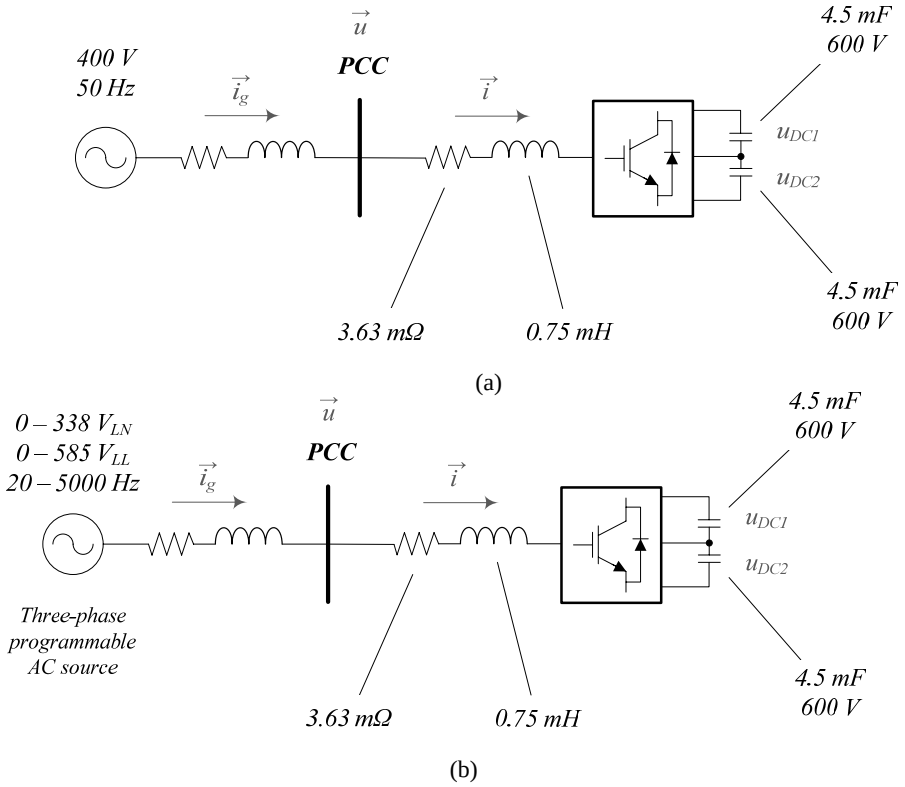

Fig. 7.3. Schematics of the experimental setup (a) connected to the laboratory grid and (b) connected to the three-phase programmable AC source.

7.3. Experimental tests.

Experimental tests carried out can be divided into three basic sets:

- *Characterization of transient response.*

  To make a comparison among the current control techniques studied in chapters 4 and 5, two abrupt steps in the reactive power reference have been applied, one from $+5$ to $+30\ kVAr$ and another from -5 to $-30\ kVAr$.

- *Characterization of steady-state response.*

  The steady-state response of the current controllers has been tested by analyzing the system performance when the reactive power reference is set to $Q^* = +30\ kVAr$. In these conditions, the harmonic compensation capabilities of the current controllers are compared.

- *Behavior under frequency jumps.*

  The grid-connection of the converter has been replaced by a connection to the programmable AC voltage source. This allows applying frequency jumps to the output waveform and selecting the desired voltage harmonics. Frequency jumps

from 50 to $45\,Hz$ and from 50 to $55\,Hz$ have been tested. Although grid frequency does not usually suffer as large drifts as the tested ones and, besides, grid codes indicate the disconnection of the converter from the grid in case of frequency drifts lower than these ones, the fact of the system being stable in such conditions is a great indicator of the robustness of the control. Moreover, this allows a better assessment of the usage of a frequency-adaptive controller and an evaluation its performance.

The tested current control techniques are the following:

- *Proportional (P) + resonant controllers tuned at* $h = 6, 12, 18$.
    - P + SOGI. The SOGI has been discretized with the methods FOH and TPW. Both non-frequency-adaptive and frequency-adaptive.
    - P + SOGI-LLN. The SOGI-LLN has been discretized with the methods FOH and TPW.
    - P + AFC.
- *Repetitive controllers.*
    - RC-DCT tuned at $h = 6, 12, 18$. The values of the parameter N_a which showed the best performance in simulation results were 4 and 5. Both non-frequency-adaptive and frequency-adaptive.
    - RC-IP. Two different implementations of the filter $Q(z)$ have been compared, binomial filter of order 2 (*bin2*) and Hamming-window filter of order 16 (*ham16*).

7.3.1. Connection to the laboratory grid.

7.3.1.1. Specifications of the laboratory grid.

The waveform of the typical PCC voltage at our laboratory when the VSC is not operating is depicted in Fig. 7.4a. It is characterized by a high level of harmonics 5^{th} and 7^{th}, as shown in its corresponding FFT. A third harmonic component also appears in the phase voltage, although it does not yield a potential difference. This is checked by analyzing the PCC line-to-line voltage shown in Fig. 7.4, in which the third harmonic no longer appears. The level of the significant harmonics present in the PCC phase voltage with respect to the fundamental component is shown in Table 7.1.

The measured PCC voltage is affected by aliasing. Furthermore, it is not possible to perform an oversampling of the PCC voltage due to the limitations of the DSP, so that the

measured voltage does not match exactly the real one. An error of few volts is then introduced. The grid synchronization algorithm should be implemented in a high-performance digital platform such as an FPGA, so that oversampling of the PCC voltage can be performed.

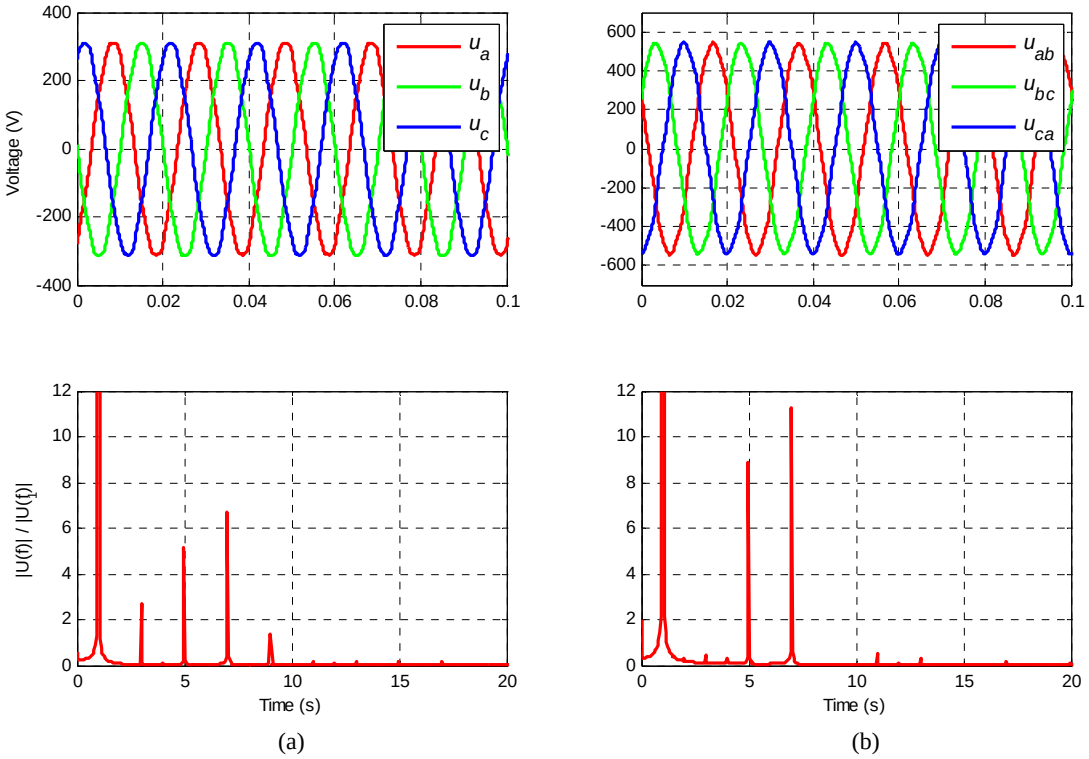

(a) (b)

Fig. 7.4. Measured waveform and FFT of the (a) PCC phase voltage and (b) PCC line-to-line voltage at our laboratory.

TABLE 7.1. LEVEL OF THE HARMONICS PRESENT IN THE GRID OF OUR LABORATORY.

Harmonic order	**5**	**7**	**11**	**13**	**17**	**19**
Level	1.6793 %	2.1526 %	0.0731 %	0.0584 %	0.0330 %	0.0257 %

7.3.1.2. Transient response.

7.3.1.2.1. Abrupt step in positive reactive power reference.

Fig. 7.5 to Fig. 7.7 collects the waveforms of the measured grid current when resonant control is employed to implement the current controller and when abrupt steps in the reactive power reference are applied: first from $+5$ to $+30$ $kVAr$ and then from $+30$ to $+5$ $kVAr$. In each graph, the two bottom waveforms are a zoom of the top waveform, each centered on each step, as marked on the main waveform by means of thin grey rectangles. Fig. 7.8 and Fig. 7.9 do the same with repetitive control.

SOGI (FOH)

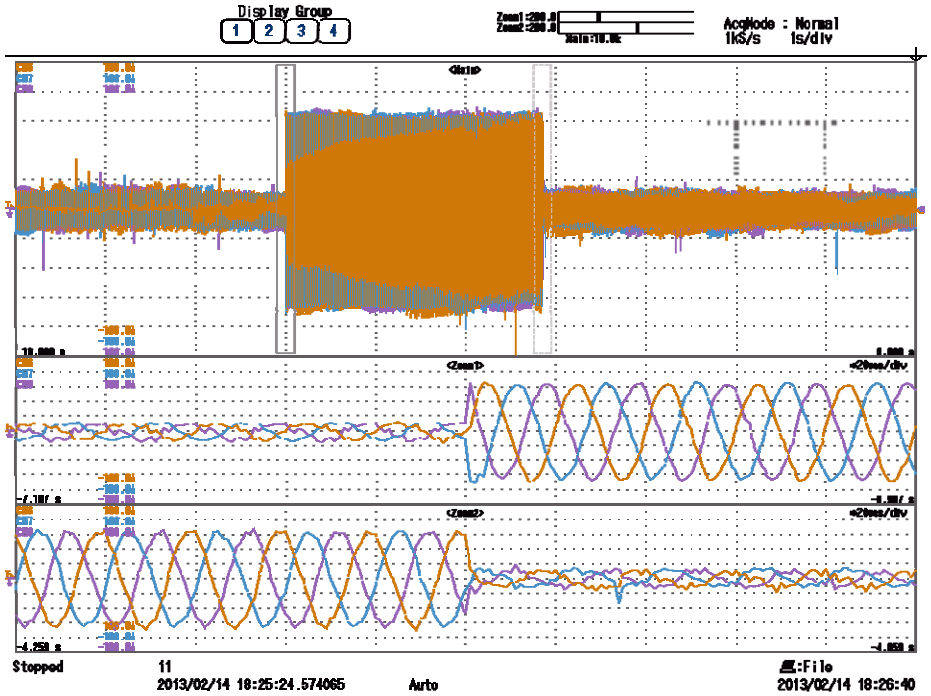

SOGI (TPW)

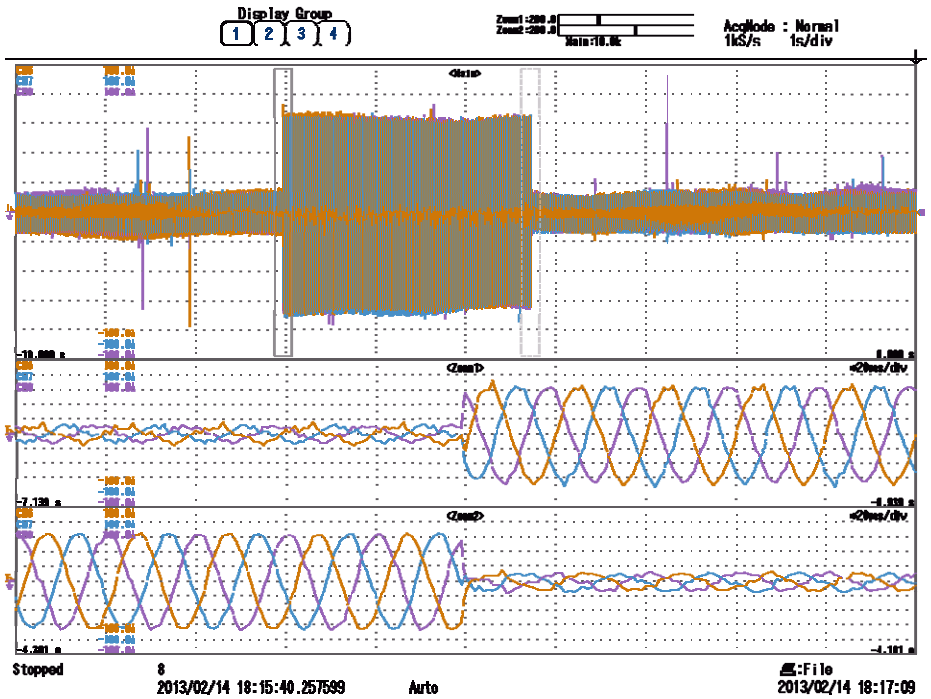

Fig. 7.5. Measured grid current when P + SOGI is applied and when abrupt steps in the reactive power reference are applied: (i) from +5 to +30 *kVAr* and (ii) from +30 to +5 *kVAr*. In each graph, the two bottom waveforms are a zoom of the top waveform, each centered on each step, as marked on the main waveform by means of grey rectangles.

SOGI-LLN (FOH)

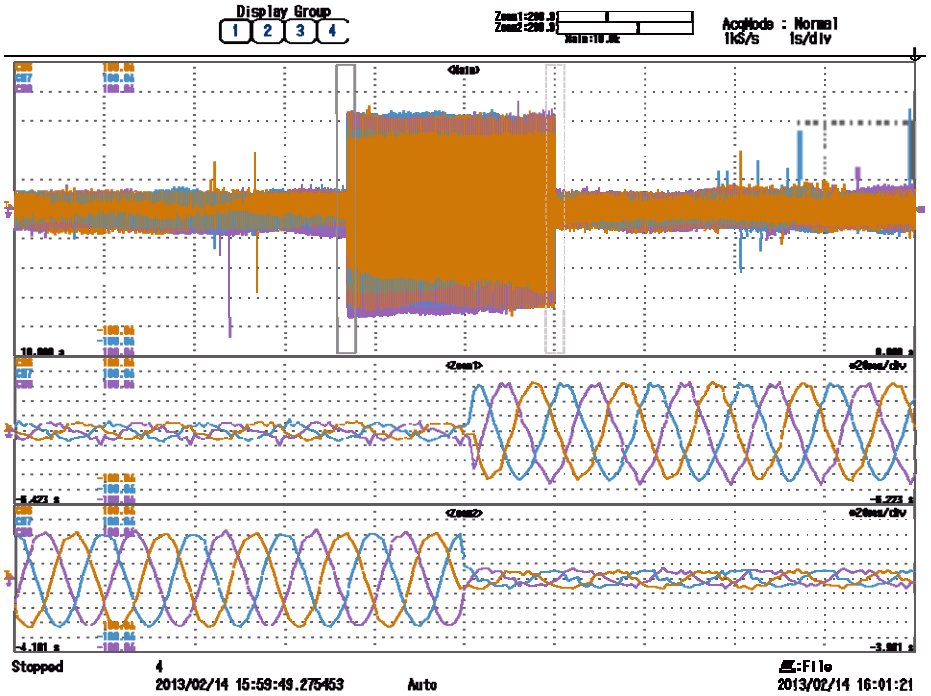

SOGI-LLN (TPW)

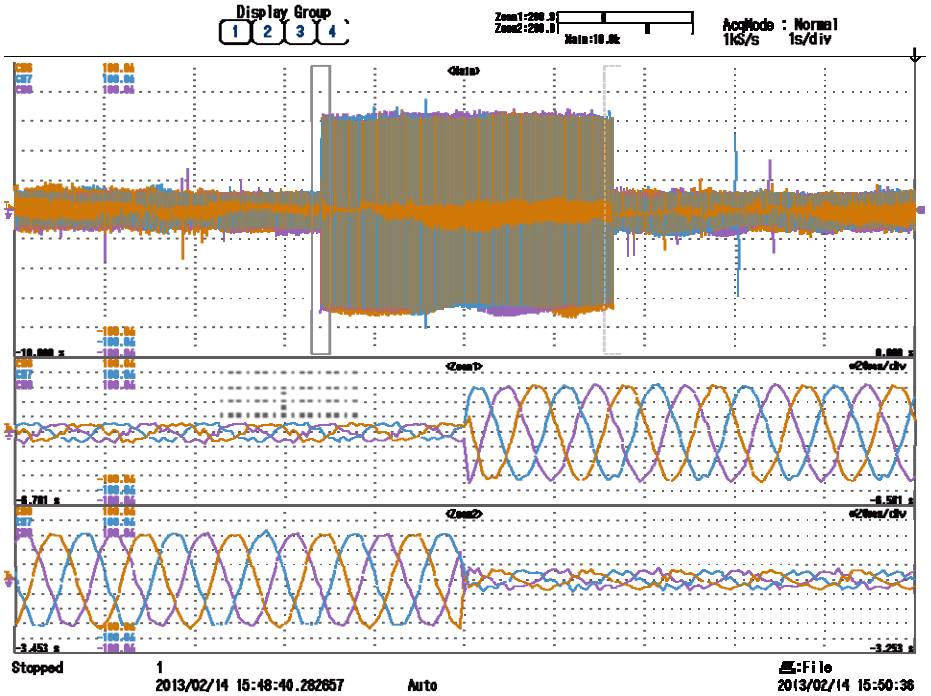

Fig. 7.6. Measured grid current when P + SOGI-LLN is applied and when abrupt steps in the reactive power reference are applied: (i) from +5 to +30 *kVAr* and (ii) from +30 to +5 *kVAr*. In each graph, the two bottom waveforms are a zoom of the top waveform, each centered on each step, as marked on the main waveform by means of grey rectangles.

AFC

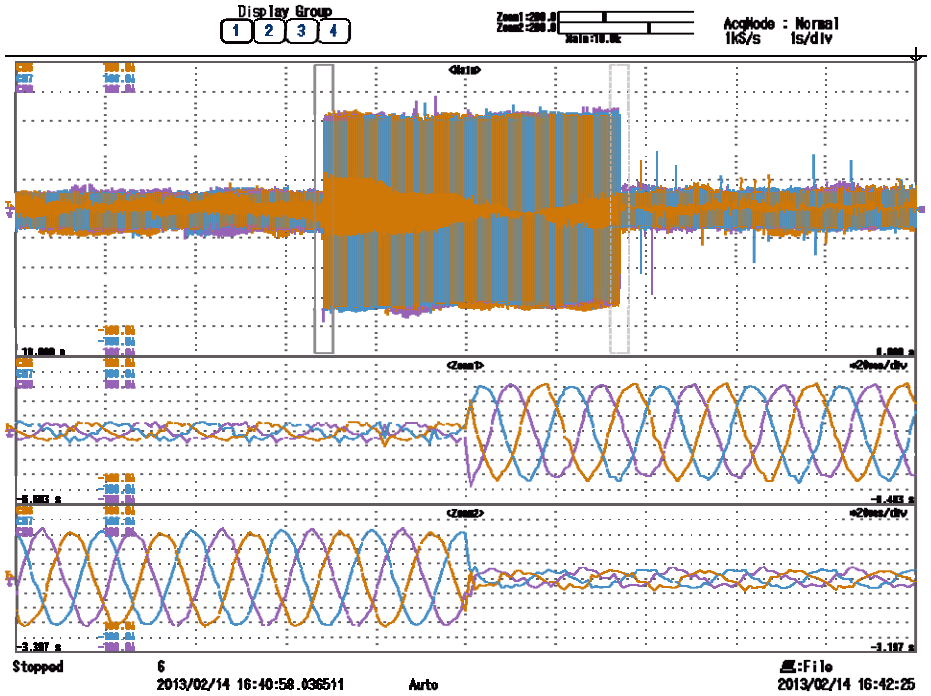

Fig. 7.7. Measured grid current when P + AFC is applied and when abrupt steps in the reactive power reference are applied: (i) from +5 to +30 *kVAr* and (ii) from +30 to +5 *kVAr*. The two bottom waveforms are a zoom of the top waveform, each centered on each step, as marked on the main waveform by means of grey rectangles.

RC-DCT ($N_a = 4$)

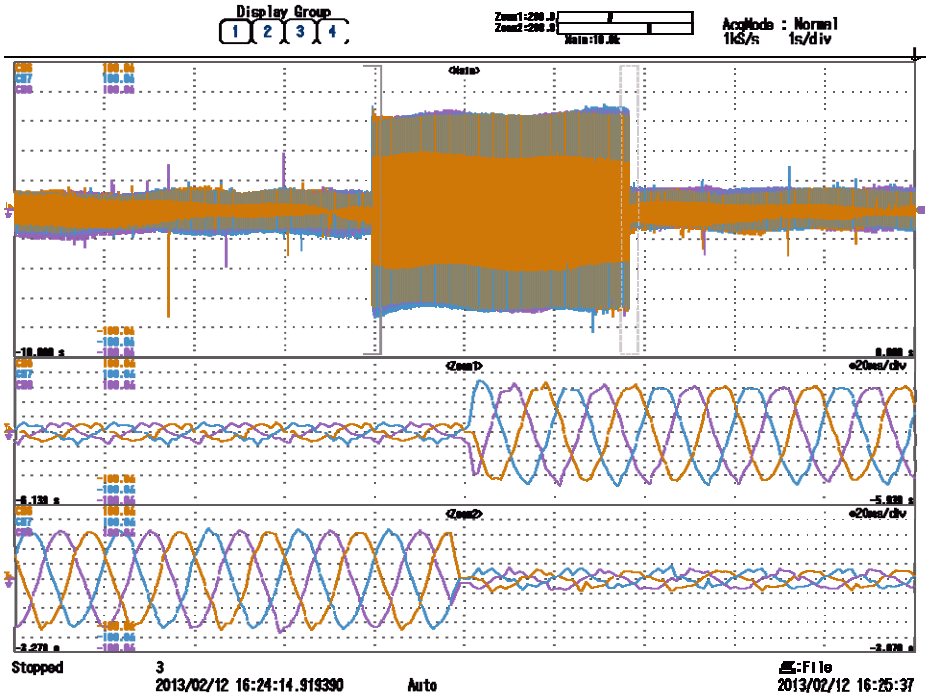

RC-DCT ($N_a = 5$)

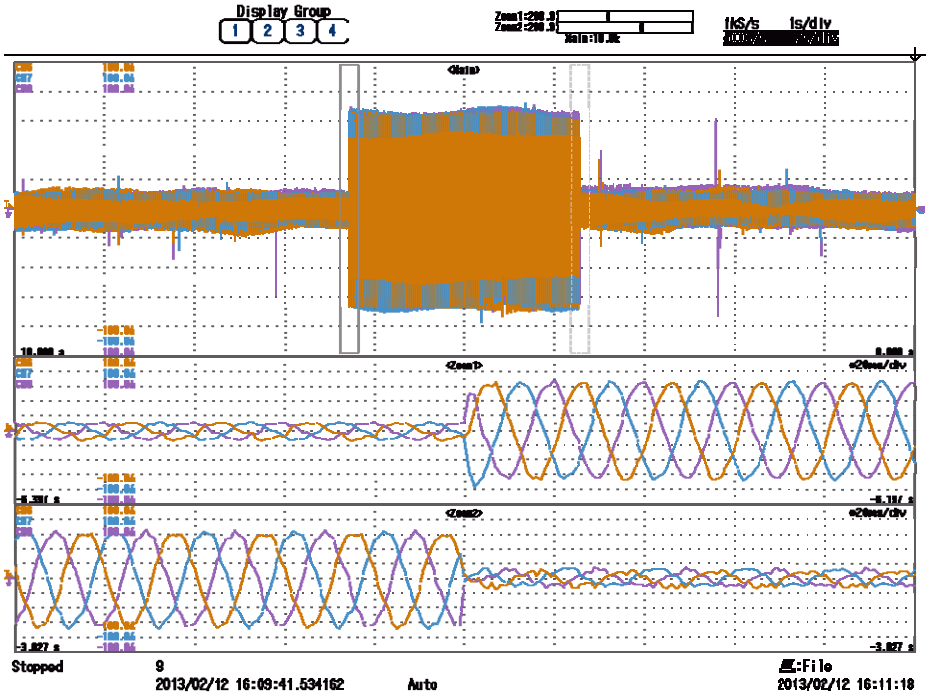

Fig. 7.8. Measured grid current when RC-DCT is applied and when abrupt steps in the reactive power reference are applied: (i) from +5 to +30 *kVAr* and (ii) from +30 to +5 *kVAr*. In each graph, the two bottom waveforms are a zoom of the top waveform, each centered on each step, as marked on the main waveform by means of grey rectangles.

RC-IP (bin2)

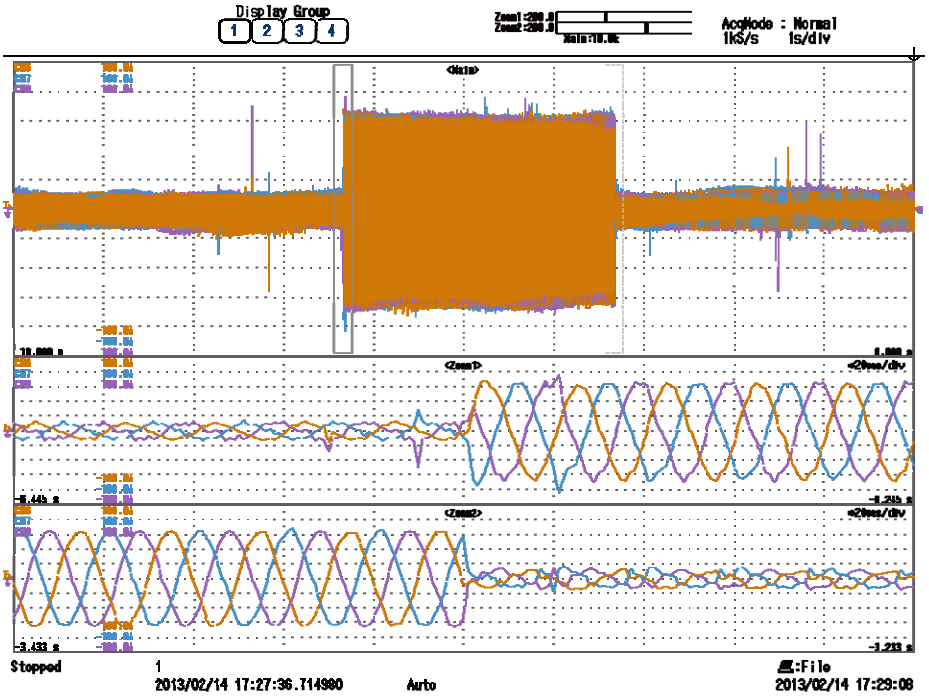

RC-IP (ham16)

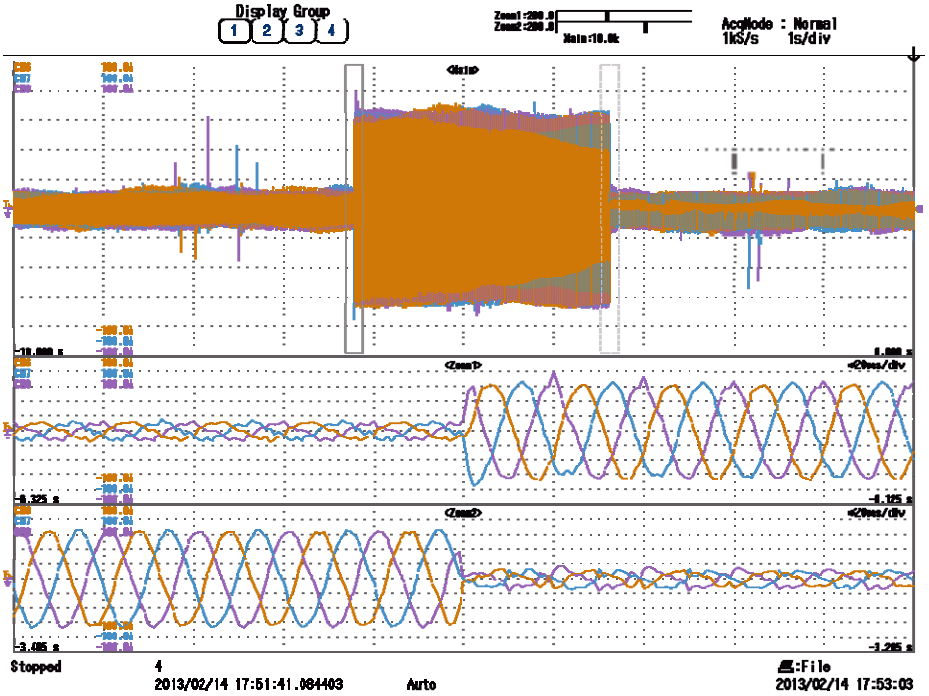

Fig. 7.9. Measured grid current when RC-IP is applied and when abrupt steps in the reactive power reference are applied: (i) from +5 to +30 *kVAr* and (ii) from +30 to +5 *kVAr*. In each graph, the two bottom waveforms are a zoom of the top waveform, each centered on each step, as marked on the main waveform by means of grey rectangles.

Fig. 7.10 compares the transient response of the aforementioned current control techniques when an abrupt step in the reactive power reference is applied from $+5$ to $+30$ *kVAr*. Although this is a step in a constant reference, this figure represents how the controllers that perform harmonic compensation affect the dynamics of the whole current controller. Therefore, the most significant parameter that can be drawn from this experimental test is the maximum overshoot, which is lower in the case of repetitive controllers, as shown in Table 7.2. In a practical case, references are always applied in an incremental way, so that the overshoot is minimized. Thus, this extreme situation would be avoided.

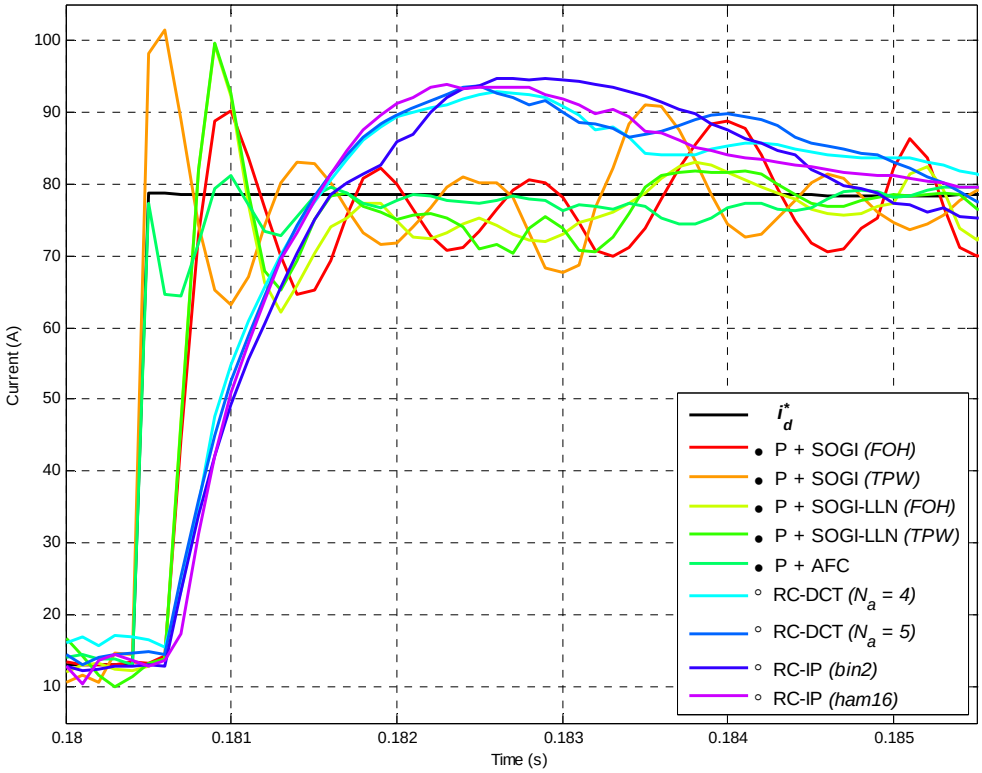

Fig. 7.10. Comparison of the transient response of the current control implemented with resonant and repetitive controllers when an abrupt step in the reactive power reference is applied: from $+5$ to $+30$ *kVAr*. The reactive current i_d is displayed.

TABLE 7.2. MAXIMUM OVERSHOOT OF THE CURRENT CONTROLLERS TUNED AT h = 6, 12 AND 18 WHEN A REACTIVE POWER STEP IS APPLIED.

Resonant controller	*Maximum overshoot*	*Repetitive controller*	*Maximum overshoot*
P + SOGI (FOH)	1.1479 (14.79 %)	***RC-DCT*** $(N_a = 4)$	1.1823 (18.23 %)
P + SOGI (TPW)	1.2904 (29.04 %)	***RC-DCT*** $(N_a = 5)$	1.1941 (19.41 %)
P + SOGI-LLN (FOH)	1.0583 (5.83 %)	***RC-IP (bin2)***	1.2062 (20.62 %)
P + SOGI-LLN (TPW)	1.2676 (26.76 %)	***RC-IP (ham16)***	1.1958 (19.58 %)
P + AFC	1.0341 (3.41 %)		

7.3.1.2.2. Abrupt step in negative reactive power reference.

Fig. 7.11 compares the transient response of the aforementioned current control techniques when an abrupt step in the reactive power reference is applied from -5 to -30 *kVAr*. Once again, the repetitive controllers show a lower overshoot and a larger settling time.

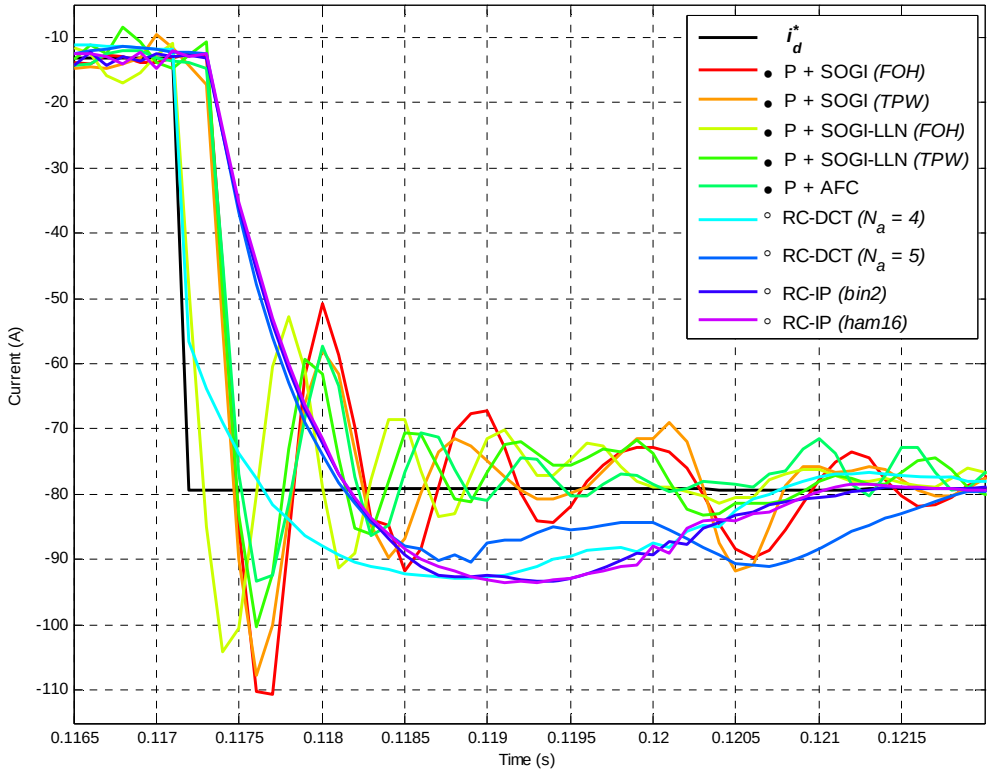

Fig. 7.11. Comparison of the transient response of the current control implemented with resonant and repetitive controllers when an abrupt step in the reactive power reference is applied: from -5 to -30 *kVAr*. The reactive current i_d is displayed.

7.3.1.3. Steady-state response.

The THD and WTHD obtained with each current controller is displayed in Fig. 7.12. This figure reveals that, since the harmonic content of the grid voltage is only significant at low-order harmonics, both THD and WTHD are decreased with all the controllers studied. The techniques that further decrease the harmonic distortion are SOGI-LLN, AFC and RC-IP.

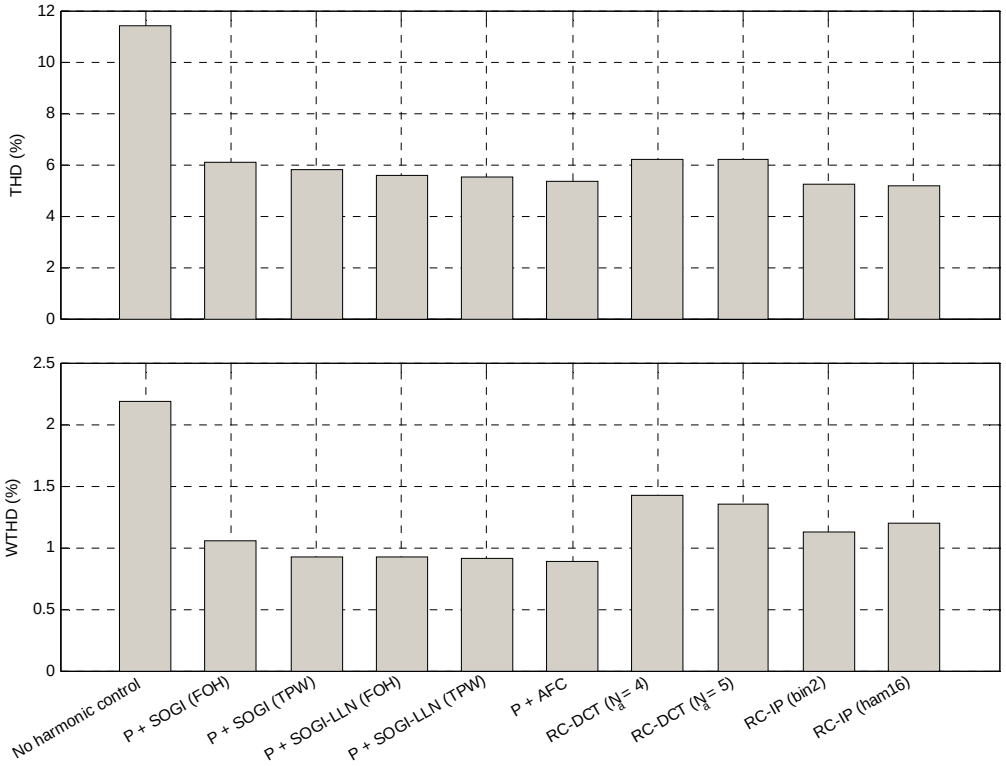

Fig. 7.12. Comparison of the THD and WTHD of the measured grid current with resonant and repetitive controllers.

7.3.2. Connection to the programmable three-phase AC voltage source.

7.3.2.1. Specifications of the AC output voltage.

The programmable AC voltage source allows setting the number and level of harmonics of the output waveform. The measured PCC phase voltage and its FFT after applying the selected pattern and when the VSC is not operating are shown in Fig. 7.13a. The level of the harmonics selected with respect to the fundamental component is shown in Table 7.3. The PCC line-to-line voltage and its FFT are represented in Fig. 7.13b.

TABLE 7.3. LEVEL OF THE HARMONICS PRESENT IN THE SPECIFIED OUTPUT VOLTAGE OF THE AC VOLTAGE SOURCE TO TEST THE FREQUENCY-ADAPTIVE ALGORITHMS.

Harmonic order	**5**	**7**	**11**	**13**	**17**	**19**
Level	1.9880 %	3.0485 %	1.5448 %	0.7221 %	0.0357 %	0.1096 %

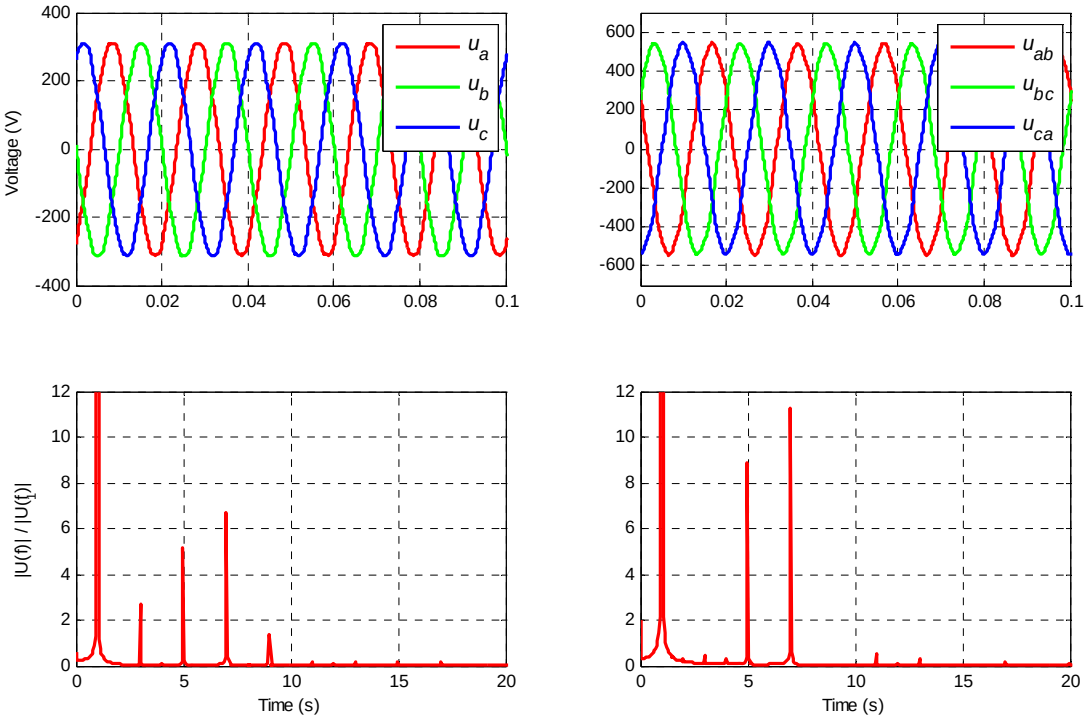

(a) (b)

Fig. 7.13. Measured waveform and FFT of the (a) PCC phase voltage and (b) PCC line-to-line voltage provided by the programmable three-phase AC voltage source.

7.3.2.2. Behavior under frequency jumps.

7.3.2.2.1. Frequency jump from 50 to 45 Hz.

Fig. 7.14 shows the grid frequency estimated with two methods: PLL (section 3.3.1) and FLL (section 3.3.2). A first-order filter with cutoff frequency $f_c = 1\,Hz$ is inserted at the output of the frequency estimator. This helps reducing the ripple in the estimated frequency and provides the current controller with a better and more accurate performance. This is also the reason of the slow transient between the initial and final value of the estimated grid frequency, which is marked within a pink line and a purple line.

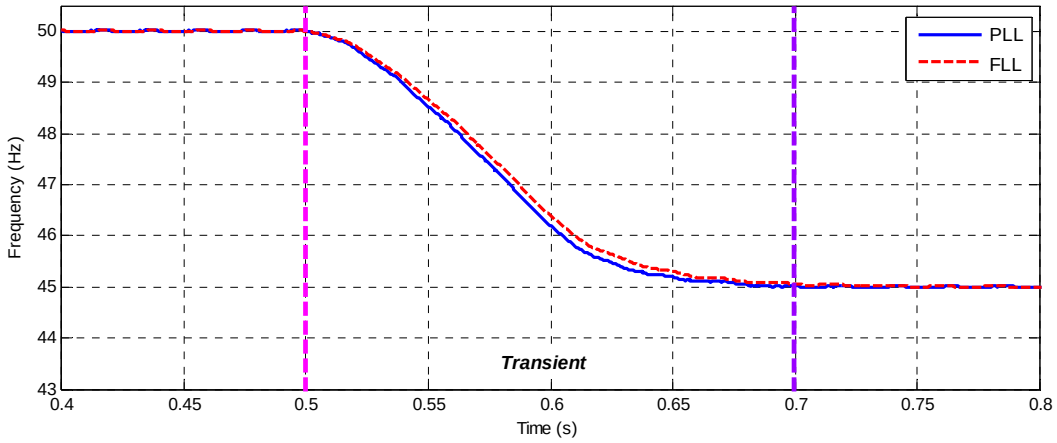

Fig. 7.14. Comparison of the grid frequency estimated with the PLL and the FLL when a frequency jump from 50 to 45 Hz is applied in the programmable three-phase AC voltage source. The pink and purple dashed lines show the beginning and the ending of the transient between both frequencies.

7.3.2.2.1.1. Results for P + SOGI.

The P + SOGI has been implemented in $\alpha\beta$-axes to run this test, and the TPW discretization has been chosen since it obtained the lowest THD (Fig. 7.12). Therefore, the PI controller has been replaced by a SOGI tuned at $h = 1$. Fig. 7.15 shows the α-component of the error of the non-frequency-adaptive and frequency-adaptive P + SOGI when the frequency jump of Fig. 7.14 is applied.

The FFT of the error signals of Fig. 7.15 are represented in Fig. 7.16. In the case of the non-frequency-adaptive algorithm, the fundamental harmonic suffers a great increase when changing the grid frequency due to the loss of selectivity, as well as the harmonics 5^{th} and 7^{th}. These harmonics are present in the PCC voltage and they experience a lack of rejection since the non-frequency-adaptive SOGI 6ω is not tuned according to the new grid frequency.

The recorded waveforms of the grid current are shown in Fig. 7.17.

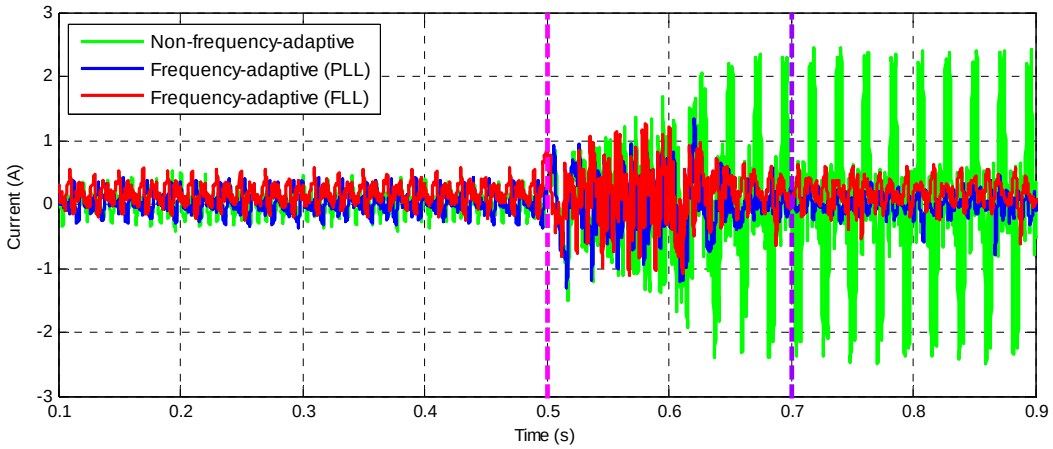

Fig. 7.15. α-component of the error signals of the non-frequency-adaptive and frequency-adaptive resonant controller based on P + SOGI ($h = 1, 6, 12, 18$) in $\alpha\beta$-axes when the frequency jump of Fig. 7.14 is applied.

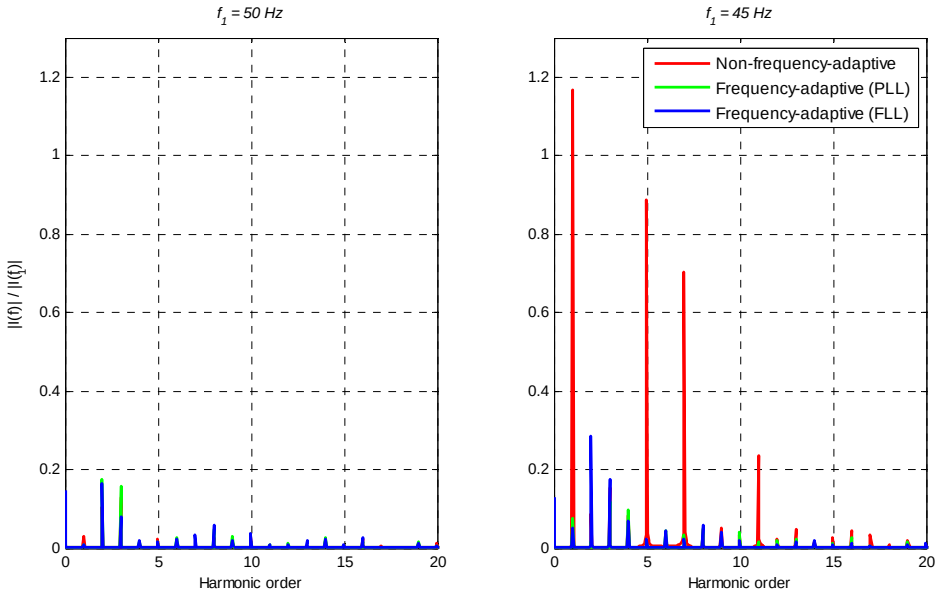

(a) (b)

Fig. 7.16. FFT of the error signal depicted in Fig. 7.15, corresponding to the non-frequency-adaptive and frequency-adaptive resonant controller based on P + SOGI ($h = 1, 6, 12, 18$) in $\alpha\beta$-axes, at the nominal frequencies of (a) 50 *Hz* and (b) 45 *Hz*.

Non-frequency-adaptive P + SOGI (TPW)

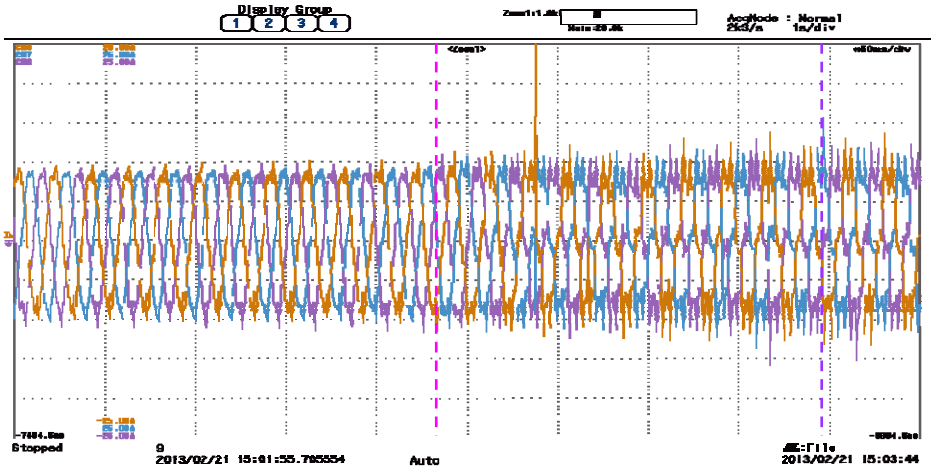

Frequency-adaptive (PLL) P + SOGI (TPW)

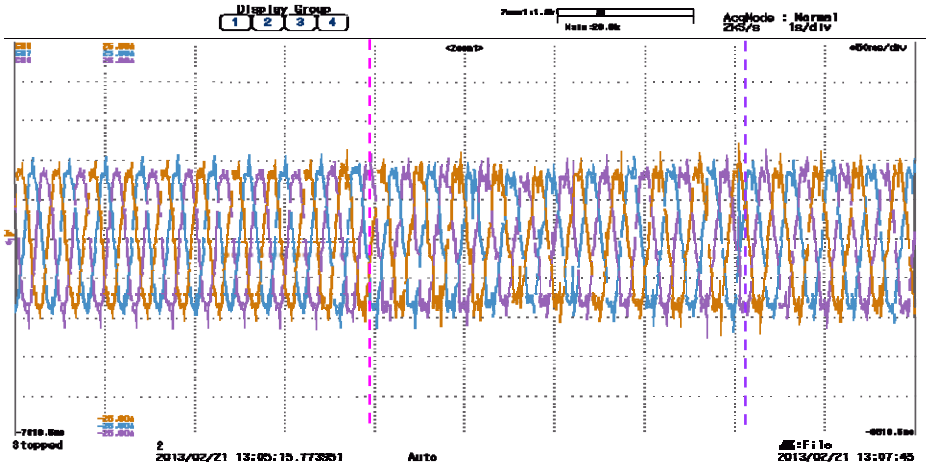

Frequency-adaptive (FLL) P + SOGI (TPW)

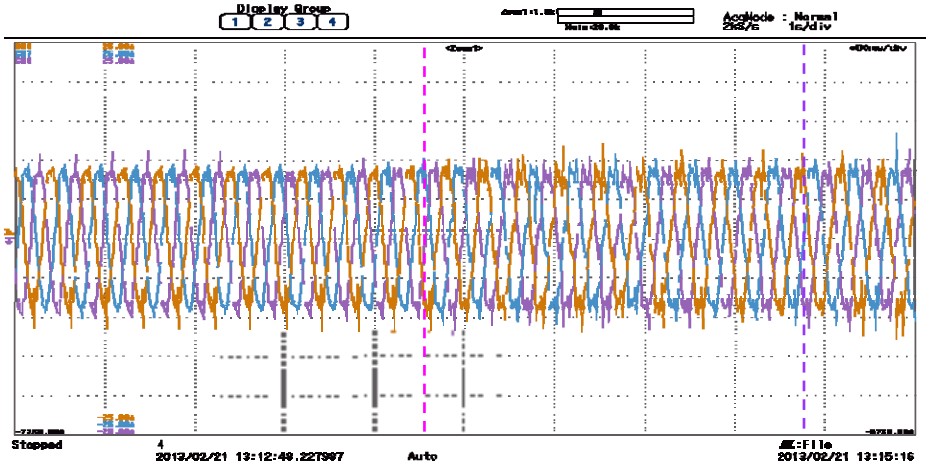

Fig. 7.17. Comparison of the measured grid current when applying the non-frequency adaptive and frequency-adaptive resonant controller based on P + SOGI ($h = 1, 6, 12, 18$) in $\alpha\beta$-axes and the frequency jump of Fig. 7.14 is applied.

7.3.2.2.1.2. Results for RC-DCT.

In this test, the parameter N_a has been set to 5. Fig. 7.18 shows the q-component of the error of the non-frequency-adaptive and frequency-adaptive RC-DCT when the frequency jump of Fig. 7.14 is applied.

The FFT of the error signals of Fig. 7.18 is represented in Fig. 7.19. In the case of the non-frequency-adaptive algorithm, a high level of harmonic 6th appears due to the lack of selectivity at this frequency, knowing that this controller is implemented in dq-axes and harmonics 5th and 7th turn into 6th. The grid current waveforms are shown in Fig. 7.20.

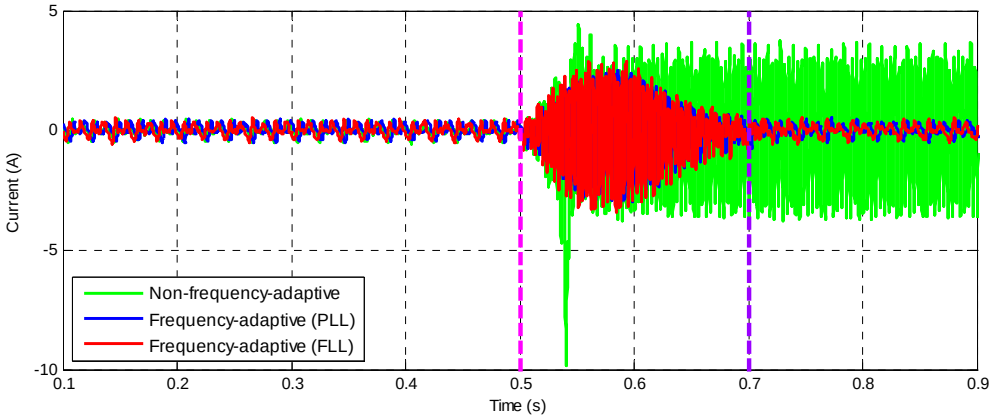

Fig. 7.18. q-component of the error signals of the non-frequency-adaptive and frequency-adaptive repetitive controller based on RC-DCT with $N_a = 5$ ($h = 6, 12, 18$) in dq-axes when the frequency jump of Fig. 7.14 is applied.

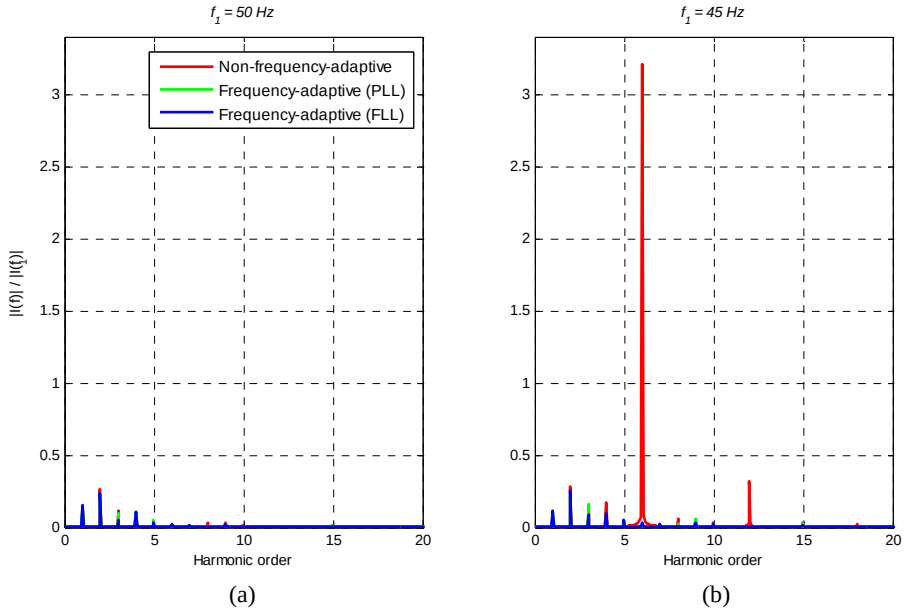

Fig. 7.19. FFT of the error signals depicted in Fig. 7.18, corresponding to the non-frequency-adaptive and frequency-adaptive repetitive controller based on RC-DCT with $N_a = 5$ ($h = 6, 12, 18$) in dq-axes, at the nominal frequencies of (a) 50 Hz and (b) 45 Hz.

Non-frequency-adaptive RC-DCT ($N_a = 5$)

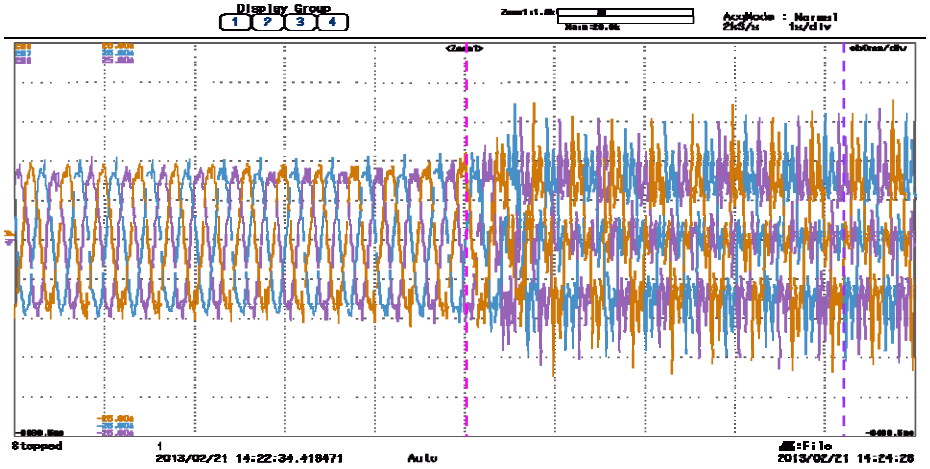

Frequency-adaptive (PLL) RC-DCT ($N_a = 5$)

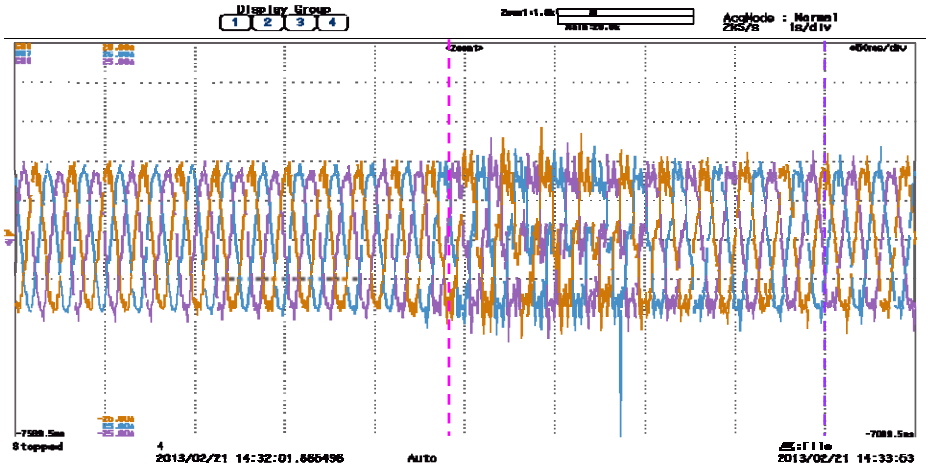

Frequency-adaptive (FLL) RC-DCT ($N_a = 5$)

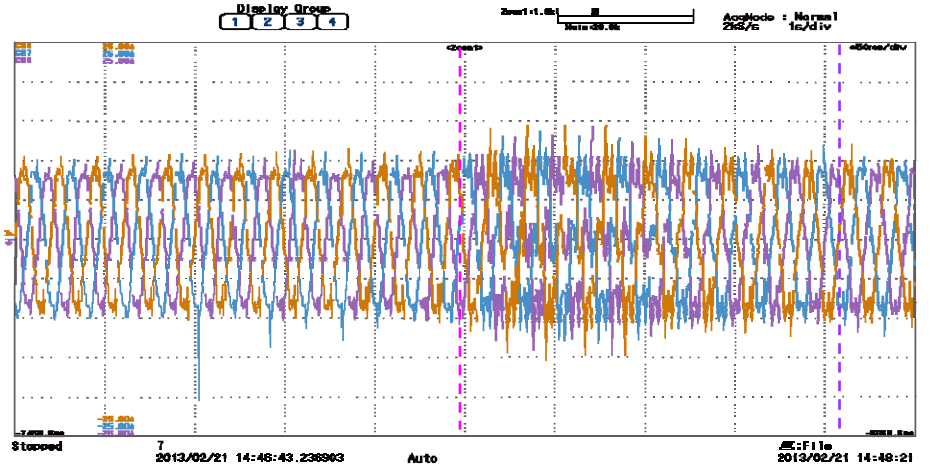

Fig. 7.20. Comparison of the measured grid current when applying the non-frequency adaptive and frequency-adaptive repetitive controller based on RC-DCT with $N_a = 5$ ($h = 6, 12, 18$) in dq-axes and the frequency jump of Fig. 7.14 is applied.

7.3.2.2.2. Frequency jump from 50 to 55 Hz.

Similarly to Fig. 7.14, Fig. 7.21 shows the grid frequency estimated with two methods: PLL and FLL. A first-order filter with cutoff frequency $f_c = 1\ Hz$ is inserted at the output of the frequency estimator. This helps reducing the ripple in the estimated frequency and provides the current controller with a better and more accurate performance. This is also the reason of the slow transient between the initial and final value of the estimated grid frequency, which is marked within a pink line and a purple line.

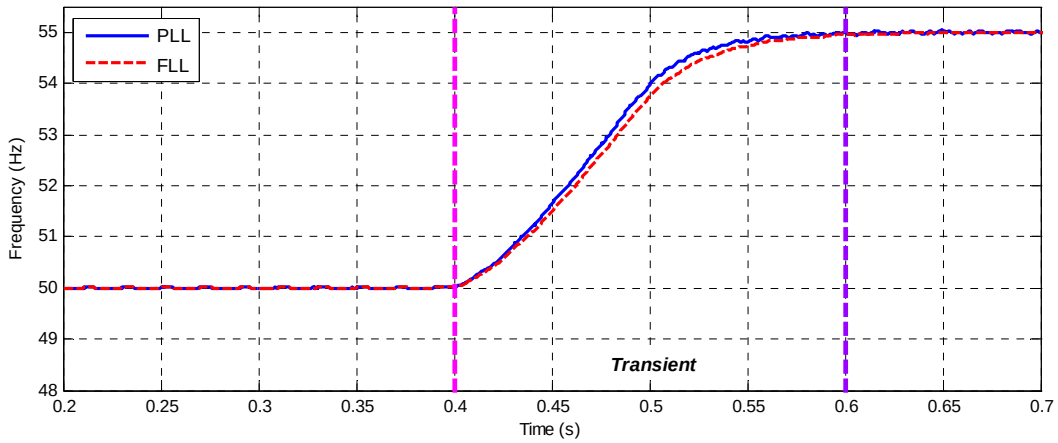

Fig. 7.21. Comparison of the grid frequency estimated with the PLL and the FLL when a frequency jump from 50 to 55 *Hz* is applied in the programmable three-phase AC voltage source. The pink and purple dashed lines show the beginning and the ending of the transient between both frequencies.

7.3.2.2.2.1. Results for P + SOGI.

Fig. 7.22 shows the α-component of the error of the non-frequency-adaptive and frequency-adaptive P + SOGI when the frequency jump of Fig. 7.14 is applied.

The FFT of the error signals of Fig. 7.22 is represented in Fig. 7.23. In the case of the non-frequency-adaptive algorithm, the effect of the lack of selectivity is even worse than when applying a negative frequency drift (to 45 *Hz*). Almost all low-order harmonics suffer an increase in their values, deteriorating the current control performance.

The recorded waveforms of the grid current are shown in Fig. 7.24.

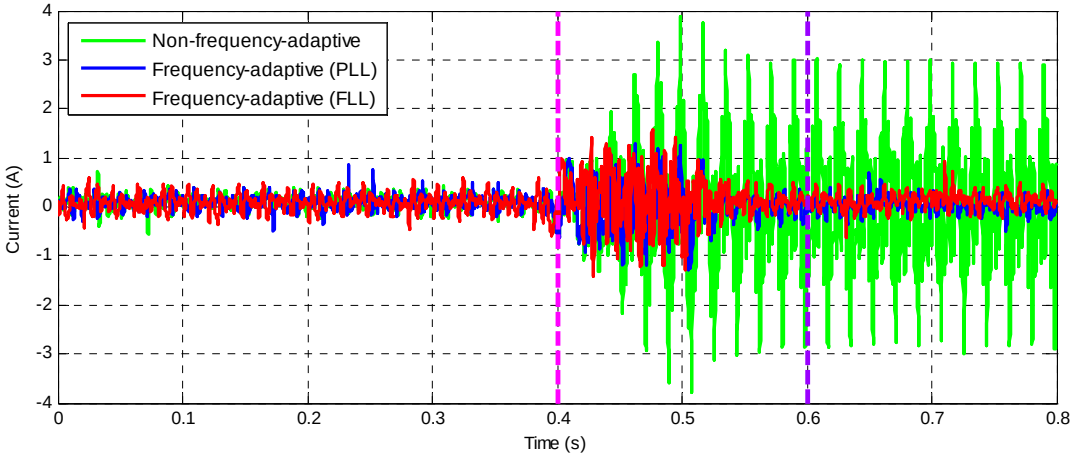

Fig. 7.22. α-component of the error signals of the non-frequency-adaptive and frequency-adaptive resonant controller based on P + SOGI ($h = 1, 6, 12, 18$) in $\alpha\beta$-axes when the frequency jump of Fig. 7.21 is applied.

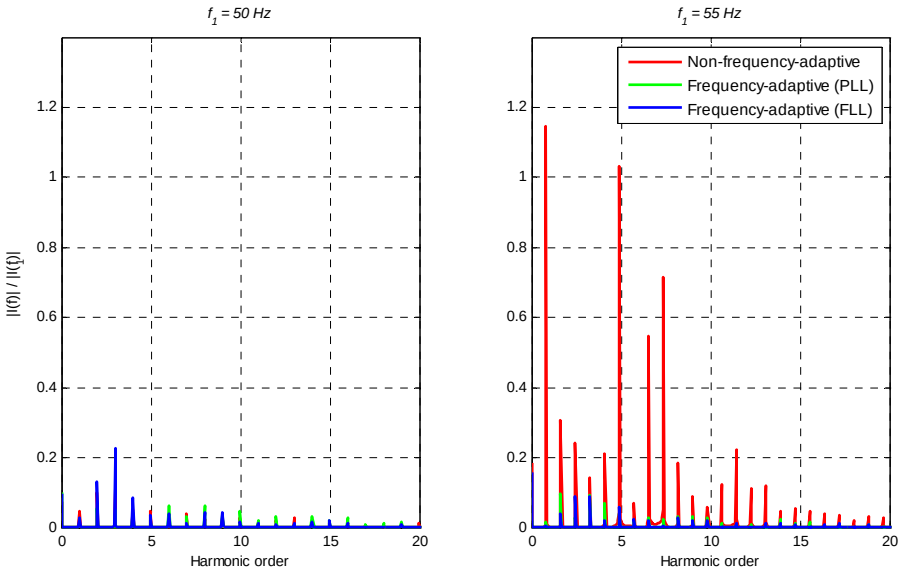

(a) (b)

Fig. 7.23. FFT of the error signals depicted in Fig. 7.22, corresponding to the non-frequency-adaptive and frequency-adaptive resonant controller based on P + SOGI ($h = 1, 6, 12, 18$) in $\alpha\beta$-axes, at the nominal frequencies of (a) 50 *Hz* and (b) 55 *Hz*.

Non-frequency-adaptive P + SOGI (TPW)

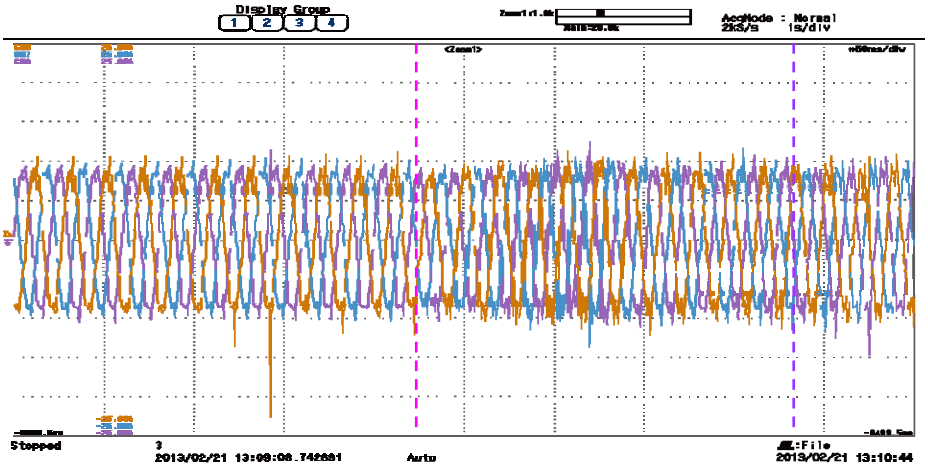

Frequency-adaptive (PLL) P + SOGI (TPW)

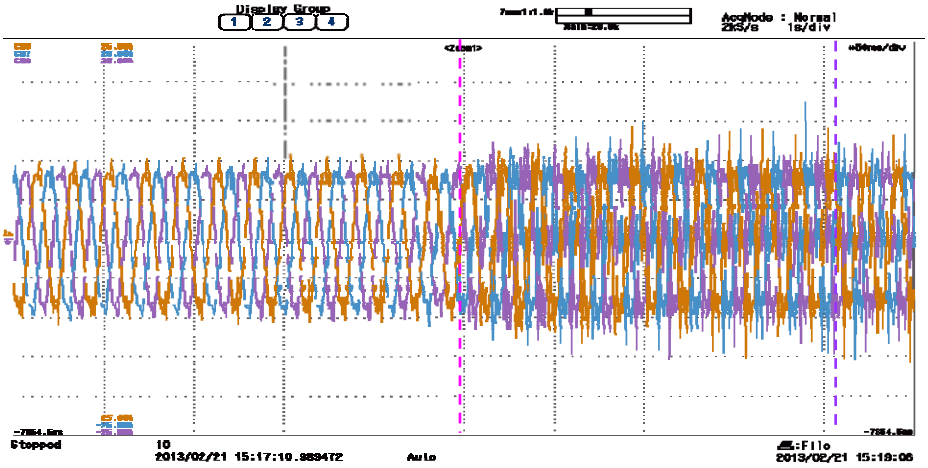

Frequency-adaptive (FLL) P + SOGI (TPW)

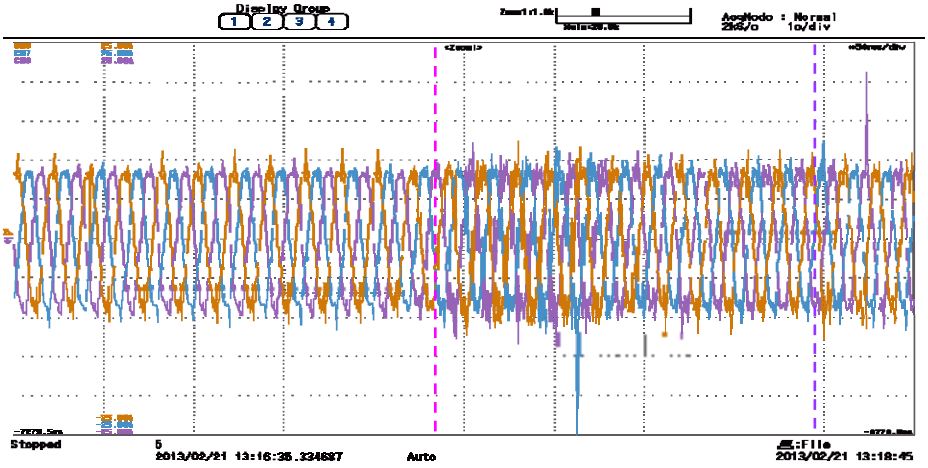

Fig. 7.24. Comparison of the measured grid current when applying the non-frequency adaptive and frequency-adaptive resonant controller based on P + SOGI ($h = 1, 6, 12, 18$) in $\alpha\beta$-axes and the frequency jump of Fig. 7.21 is applied.

7.3.2.2.2.2. Results for RC-DCT.

Fig. 7.25 shows the *q*-component of the error of the non-frequency-adaptive and frequency-adaptive RC-DCT when the frequency jump of Fig. 7.21 is applied.

The FFT of the error signals of Fig. 7.25 is represented in Fig. 7.26. In the case of the non-frequency-adaptive algorithm, an undesired 6th harmonic appears when changing the grid frequency. The recorded waveforms of the grid current are shown in Fig. 7.27.

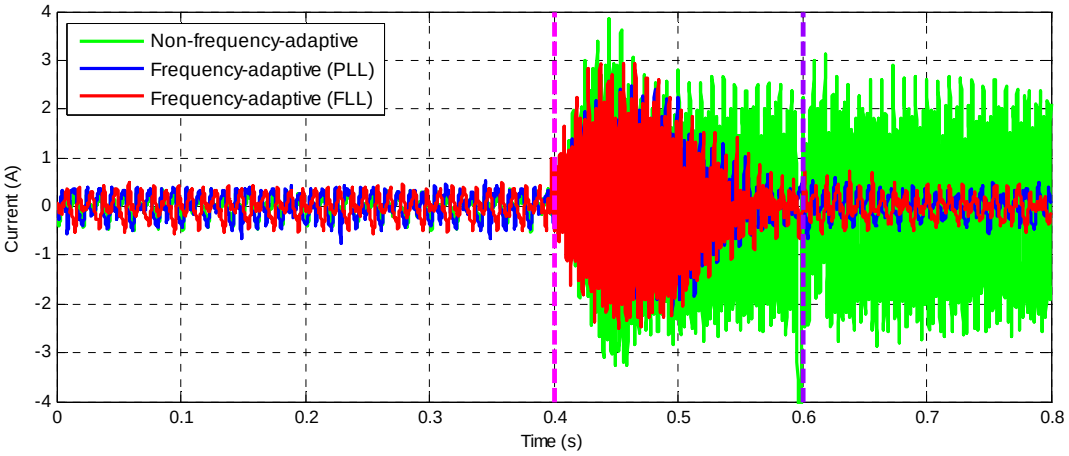

Fig. 7.25. *q*-component of the error signals of the non-frequency-adaptive and frequency-adaptive repetitive controller based on RC-DCT with $N_a = 5$ ($h = 6, 12, 18$) in *dq*-axes when the frequency jump of Fig. 7.21 is applied.

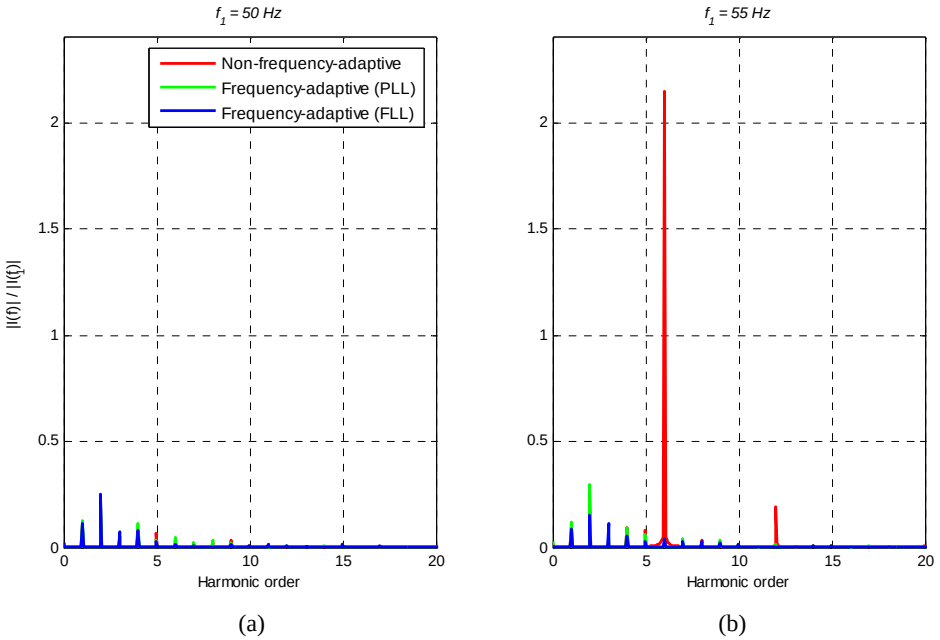

Fig. 7.26. FFT of the error signals depicted in Fig. 7.25, corresponding to the non-frequency-adaptive and frequency-adaptive repetitive controller based on RC-DCT with $N_a = 5$ ($h = 6, 12, 18$) in *dq*-axes, at the nominal frequencies of (a) 50 *Hz* and (b) 55 *Hz*.

Non-frequency-adaptive RC-DCT ($N_a = 5$)

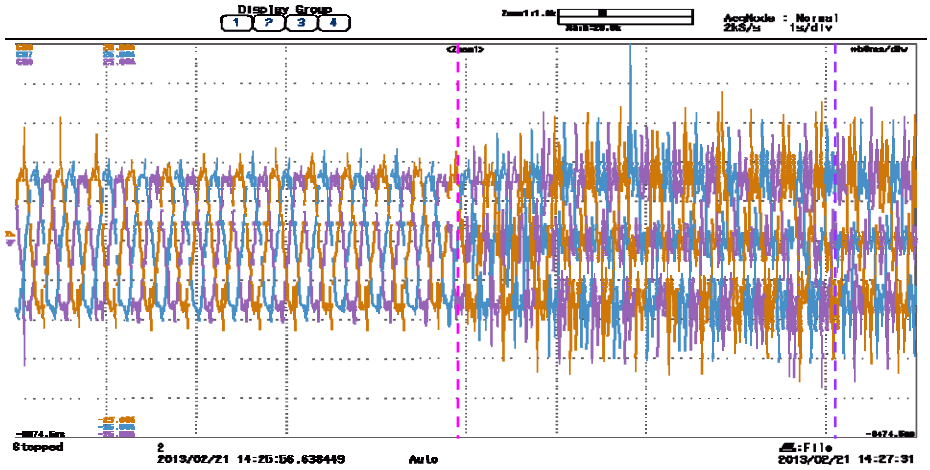

Frequency-adaptive (PLL) RC-DCT ($N_a = 5$)

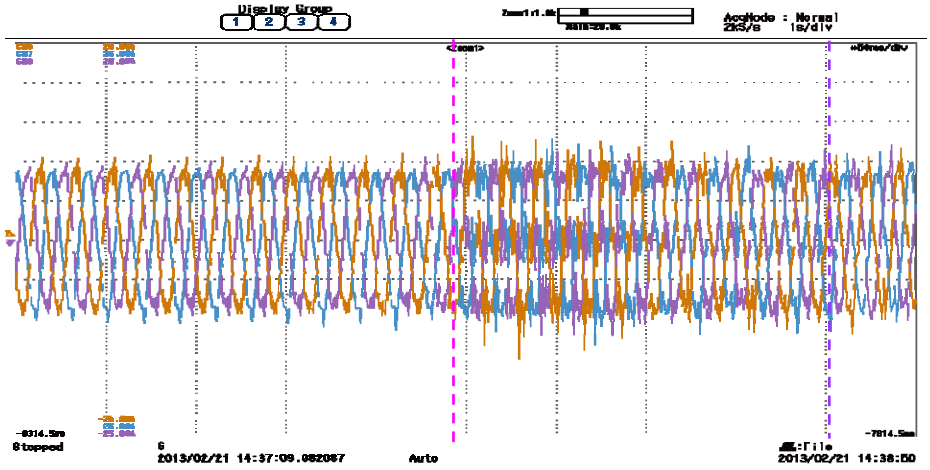

Frequency-adaptive (FLL) RC-DCT ($N_a = 5$)

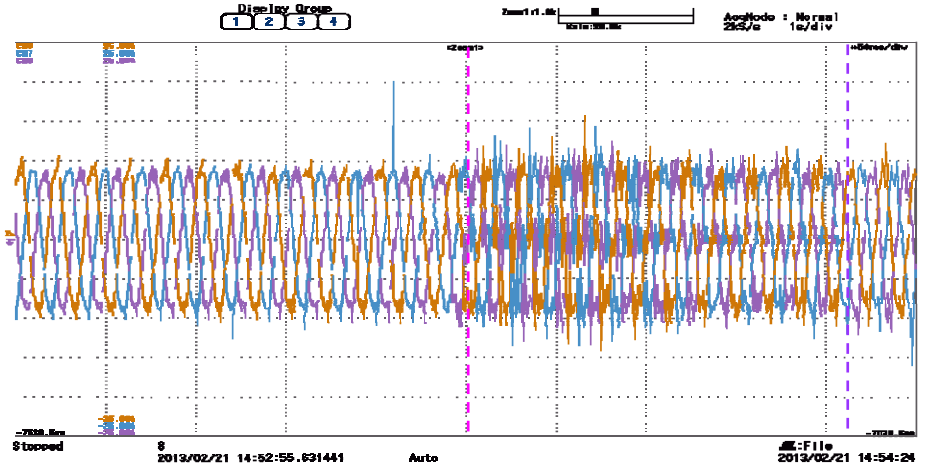

Fig. 7.27. Comparison of the measured grid current when applying the non-frequency adaptive and frequency-adaptive repetitive controller based on RC-DCT with $N_a = 5$ ($h = 6, 12, 18$) in dq-axes and the frequency jump of Fig. 7.21 is applied.

7.3.3. Execution time.

7.3.3.1. Analysis of the execution time of repetitive controllers.

The execution times of the current control based on repetitive controllers as well as the execution times corresponding to the operation of the shift registers and the multiplications & additions are shown in Fig. 7.28. These times have been obtaining by generating a digital grid voltage in the DSP instead of in the experimental setup. These data show that, in the case of non-frequency-adaptive controllers, the order of the controller (the length of the shift registers) is the parameter with the greatest influence in the execution time of the algorithm. Thus, RC-IP is the controller with the highest execution time. On the other hand, RC-FFDP1 is the controller with the lowest order, therefore it achieves the lowest execution time.

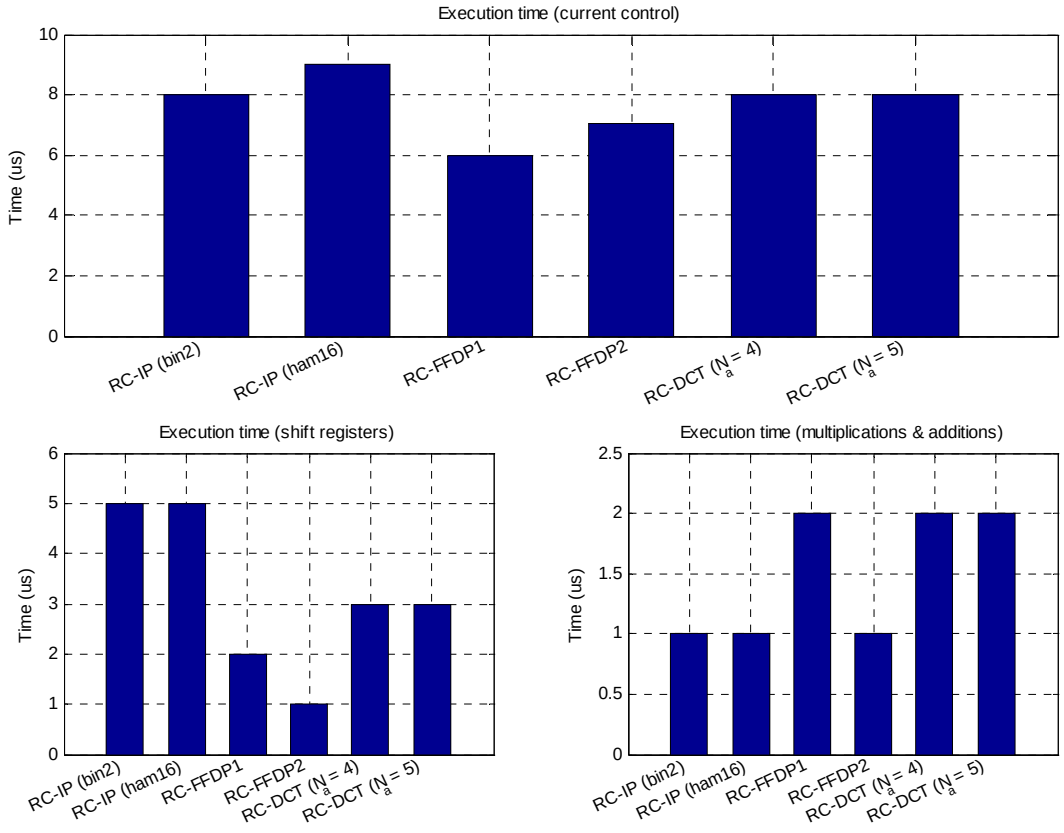

Fig. 7.28. Execution times of the current control, shift registers and multiplications & additions for repetitive controllers when the sampling period is $T_s = 100\ \mu s$.

7.3.3.2. Comparison of the execution time of all tested current controllers.

The execution time of the acquisition, communication and control of the converter has been measured for each current controller implemented. These execution times are collected

in Fig. 7.29. It is important to mention that the source code has been optimized in the *Build options* of the project in Code Composer Studio so that the code execution takes less time.

As expected, the control that obtains the highest execution time is based on the frequency-adaptive RC-DCT ($t_{exec}|_{RC-DCT} \approx 74\ \mu s$). The control based on the remaining controllers takes around $15 - 20\ \mu s$ less to execute. This would not be possible without applying the optimization options of Code Composer Studio and without having a well-depurated C-code.

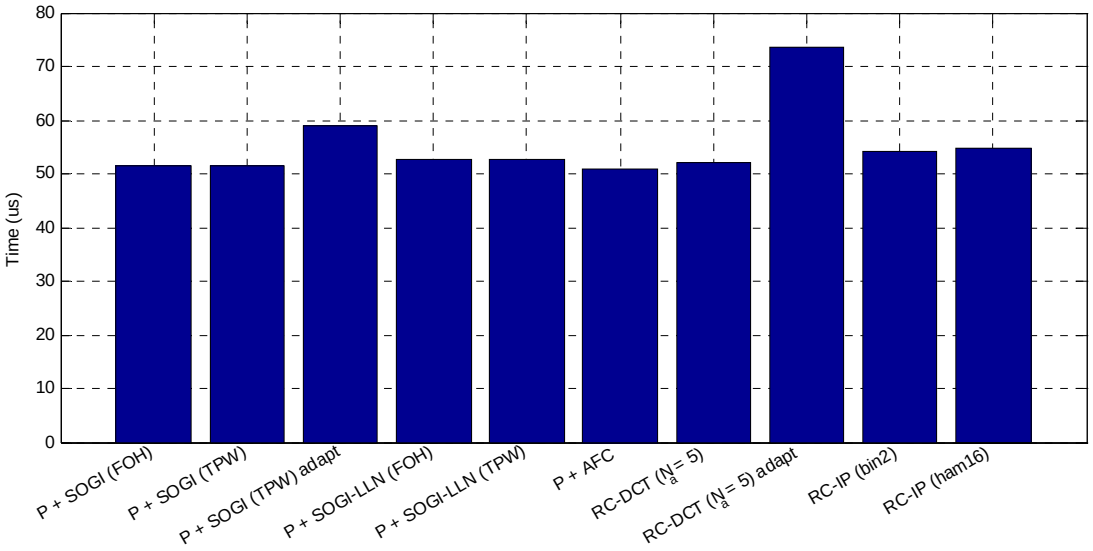

Fig. 7.29. Execution times of the control, communication and acquisition of the converter when the sampling period is $T_s = 100\ \mu s$.

7.4. Conclusions.

When deciding what current controller to choose, it is necessary to consider the purpose of the application. If it is only necessary to compensate for low-order harmonics, as in the case of the grid in our laboratory, it is sufficient to use a resonant controller. SOGI are SOGI-LLN have shown the best performance from the viewpoint of settling time. Provided that system stability is assured, SOGI-LLN arises as the desired option due to its low steady-state error and phase control capabilities. However, SOGI-LLN has one of the highest overshoots; hence if this is not permissible, AFC is a good tradeoff.

However, resonant control ceases to be a viable option when the number of harmonics to compensate starts to increase due to its problems with stability. Therefore, in this case it is advisable to opt for repetitive control. Among the different ways to implement it, RC-IP has shown the best performance in terms of response speed and steady-state error, but it is necessary to have a powerful digital processor to implement it.

If this is not possible due to the limited resources of the digital platform, RC-DCT would be a good compromise. However, in terms of implementation of frequency-adaptive algorithms, it is clear that it is compulsory to have a high performance processor to implement the frequency-adaptive RC-DCT.

Table 7.4 summarizes the results obtained during this chapter. In this table, FA stands for Frequency-Adaptive (algorithm) and NFA stands for Non-Frequency-Adaptive (algorithm).

TABLE 7.4. COMPARISON OF CURRENT CONTROLLERS BASED ON RESONANT AND REPETITIVE CONTROLLERS.

Current controller	***Overshoot***	***THD***	***WTHD***	***Execution time***	***Computational burden***	
					NFA	***FA***
P + SOGI (FOH)	14.79 %	6.09 %	1.06 %	51.4 μs	Very low	Low
P + SOGI (TPW)	29.04 %	5.79 %	0.927 %	51.4 μs	Very low	Low
P + SOGI-LLN (FOH)	5.83 %	5.55 %	0.925 %	52.8 μs	Very low	Very high
P + SOGI-LLN (TPW)	26.76 %	5.53 %	0.915 %	52.7 μs	Very low	Very high
P + AFC	3.41 %	5.37 %	0.884 %	50.8 μs	Very low	Low
RC-DCT ($N_a = 4$)	18.23 %	6.22 %	1.42 %	52 μs	Medium	High
RC-DCT ($N_a = 5$)	19.41 %	6.18 %	1.35 %	52 μs	Medium	High
RC-IP (bin2)	20.62 %	5.23 %	1.12 %	54.3 μs	Medium	High
RC-IP (ham16)	19.58 %	5.19 %	1.2 %	54.8 μs	Medium	High
RC-FFDP1	—	—	—	—	Medium	High
RC-FFDP2	—	—	—	—	Medium	High

8

Conclusions and future works

8.1. Conclusions.

This Thesis is focused on the field of cascade linear control systems applied to the control of VSCs connected in shunt with the grid through an L-filter, especially in connections to weak grids and in two topics: (i) tracking of grid current harmonics and rejection of grid voltage harmonics, and (ii) control of PCC voltage in an unbalanced condition. For this purpose, contributions to current control (implemented by means of resonant and repetitive controllers) and PCC voltage control have been made in this Thesis.

In first place, the general control scheme of a VSC connected in shunt with the grid through an L-filter has been analyzed, showing the possible controllers that it may contain and their function. Special attention has been given to the current controller. An exhaustive comparison of the main characteristics of a current controller implemented in $\alpha\beta$ and dq-axes has been carried out, yielding that the most suitable configuration for compensating the negative sequence caused by an unbalanced grid voltage is a resonant controller tuned at the fundamental grid frequency in $\alpha\beta$-axes.

The study of the calculation of reference currents has been focused on this type of current controller. The performance of four different methods of calculation of reference currents has been analyzed and compared, showing that the so-called *dq_4×4* achieves the best performance in terms of reduction of DC-link voltage oscillation and oscillating active power.

The performance of both resonant and repetitive controllers applied to grid-connected VSCs has been studied, tested and compared. Different discretization techniques have been applied to resonant control and their resulting characteristics have been studied in detail, showing that TPW and FOH methods obtain the discrete time models that better match the continuous time model. Both types of control have been implemented according to different structures. It has been verified that they are well suited to compensate harmonic currents due

to their optimum tracking and harmonic rejection capability.

Resonant controllers are an option with low computational burden and the preferable choice when the number of harmonics to compensate is low. Due to stability problems of the SOGI, other techniques that are able to perform a phase control have been studied: SOGI-LLN and AFC. Provided that system stability is assured, SOGI-LLN arises as the desired option due to its low steady-state error and phase control capabilities. However, SOGI-LLN has one of the highest overshoots; hence if this is not permissible, AFC is a good tradeoff. With regard to the implementation of the frequency-adaptive version of these controllers, SOGI-LLN is not a viable option due to the high complexity of the calculation of its parameters, whereas SOGI and AFC are simple to implement. They both entail the calculation of a few trigonometric operations, but it has been tested that they do not suppose a high consumption of resources and their digital implementation is feasible.

As the number of resonant controllers connected in parallel increases, the stability margin of the control system suffers a considerable reduction. Furthermore, the controllers that are designed by emulation, i.e. they are first designed in continuous time and then they are discretized, suffer a considerable decline in their selectivity.

Therefore, when a high number of harmonics must be compensated, it is advisable to opt for repetitive control. Among the different ways to implement it, RC-IP has shown the best performance in terms of response speed and steady-state error, but it is necessary to have a powerful digital processor to implement it. If this is not possible due to the limited resources of the digital platform, RC-DCT represents a good compromise. In general, repetitive controllers have a better capability to track and reject harmonics, but the computational load is larger than in the case of resonant controllers. For the case of RC-DCT, this computational load can be a bit smaller if the DCT coefficients are calculated offline, since they only depend on the harmonic order and the sampling period and they are not going to change during the execution of the control algorithm. As for the implementation of frequency-adaptive algorithms, it is clear that it is compulsory to have a high-performance processor to implement the frequency-adaptive RC-DCT. Basic guidelines for the programming of all frequency-adaptive repetitive controllers tackled in this Thesis have been provided.

Regarding the methods to perform grid synchronization and monitoring studied in chapter 3, an abrupt frequency jump of $\pm 5\ Hz$ has been applied to them to test their performance with a view to develop frequency-adaptive current controllers. Furthermore, a proper grid synchronization is also essential to develop control schemes that are able to work irrespective of the grid nominal frequency, i.e. in $50\ Hz$ or $60\ Hz$ grids. The KF has the largest overshoot and settling time; the EKF is an intermediate option in terms of response speed but it presents the highest noise in the estimated grid frequency; and the PLL and FLL have a very similar response, as well as showing the lowest overshoot and fastest response. Therefore, the grid

synchronization algorithms that have been implemented in the control platform of the experimental setup are the PLL-based (DSOGI-PLL) and FLL-based (DSOGI-FLL).

A novel PCC voltage controller in synchronous reference frame has been proposed in this Thesis to compensate an unbalanced PCC voltage by means of a STATCOM, allowing an independent control of both positive and negative voltage sequences. Simulation results have demonstrated the efficacy of this controller, managing to significantly reduce the negative sequence in the PCC voltage.

8.2. Future works.

The next research lines can be derived from the conclusions listed in the previous section.

8.2.1. Current control.

- Study of converter control techniques with low switching frequency. Due to advances in power electronics, the rated power that power devices can handle is growing fast. This trend is accompanied by a need to reduce power converter losses, which can be achieved by control techniques capable of working with low switching frequencies. To do so, it is necessary to study how the application of references is modified, study the maximum harmonic that the current controller is able to compensate according to sampling and switching frequencies, study possible modifications to modulation strategies, etc.
- Implementation of current controllers in high-performance digital platforms that allow using smaller sampling periods. This will improve the features of current controllers tuned to compensate high-order harmonics, especially in resonant controllers designed by emulation. This must be accompanied by the implementation of the grid synchronization algorithm in a platform such as an FPGA to perform the oversampling of the PCC voltage.
- Study of the application of the plug-in topology to resonant controllers, evaluating the improvements introduced by it and considering its application to the current control of grid-connected VSCs. This will be addressed by studying the characteristics of the resulting open-loop transfer functions, analyzing their transient and steady-state response and obtaining simulation and experimental results in the same setup used in this Thesis.
- Analysis of the stability and robustness of the current controllers tackled in this Thesis. Theoretically, techniques like Lyapunov, analysis through Nyquist diagrams, modification of plan parameters in simulations, etc. can be applied to establish a numerical comparison. Practically, the current controllers can be

designed for a plant model that does not match the real parameters.

- Application of all current controllers studied in this Thesis to the control of VSCs connected to the grid through an LCL-filter or even more advanced topologies, such as LLCL-filters.
- Study of the performance of the current controllers studied in this Thesis when the VSC is connected to the grid through a transformer. The magnetizing inductance of the transformer has to be taken into account, since it may endanger the internal stability of the control system. A transformer introduces a zero at the origin in the system, which may lead to problems when the current controller wants to be designed according to the inverse of the plant (to cancel its dynamics).
- Study of the effect of varying all possible parameters in the current controllers tackled in this Thesis in order to draw up a complete and exhaustive tuning guide depending on the specific control requirements. These parameters include proportional gains, integral gains, damping factors, phase shifts, etc.
- According to the work developed in [Huerta*, et al.*, 2011], the possibility of applying resonant and repetitive controllers to LQG servo controllers will be studied, analyzing their effect on the eigenvalues of the system.

8.2.2. PCC voltage control.

- Experimental testing of the PCC voltage controller to validate its efficiency and adjust the tuning of its parameters. A weak grid can be simulated by connecting an autotransformer between the laboratory grid and the VSC grid-filter, which allows selecting independent inductances for each phase. Therefore, the voltage drop in each inductance is different and an unbalanced PCC voltage is obtained. This will also allow a further study of the dynamics of PCC voltage controller depending on the grid conditions.
- Sizing of the VSC to compensate an unbalanced PCC voltage. For instance, the maximum DC voltage that the DC-link capacitors can handle will determine the maximum level of PCC voltage negative sequence that the VSC can compensate.
- Study of the behavior of weak grids and analyzing their effect on the dynamics of the plant in case of flickers, voltage dips, etc. Both small-signal and large-signal studies are required for this purpose. Study of the effect of grid impedances with variable inductance. This will allow developing improved PCC voltage controllers, studying possible cross-couplings between axes, etc. Furthermore, the PCC voltage controller proposed in this Thesis will be studied for the case of a VSC connected to the grid through an LCL-filter.
- Analysis of possible values for the droop control gain in the PCC voltage

controller under unbalanced conditions. The use of this droop control gain takes more importance when several VSCs are connected in shunt mode and the PCC voltage needs to be controlled.

References

H.Akagi, E. H. Watanabe, and M. Aredes. "Instantaneous power theory and applications to power conditioning," John Wiley & Sons, 2007, ISBN 9780470118924.

H.Akagi, "Active harmonic filters," *Proc.of the IEEE,* 2005, vol. 93, no. 12, pp. 2128-2141.

M.P.Bahrman and B.K.Johnson, "The ABCs of HVDC transmission technologies," *IEEE Power and Energy Magazine*, 2007, vol. 5, no. 2, pp. 32-44.

A.Bhattacharya, C.Chakraborty, and S.Bhattacharya, "Shunt compensation. Reviewing traditional methods of reference current generation," *IEEE Industrial Electronics Magazine*, 2009, vol. 3, no. 3, pp. 38-49.

F.Blaabjerg, R.Teodorescu, M.Liserre, and AV.Timbus, "Overview of Control and Grid Synchronization for Distributed Power Generation Systems," *IEEE Trans. Industrial Electronics*, 2006, vol. 53, no. 5, pp. 1398-1409.

V.Blasko, V.Kaura, and W.Niewiadomski, "Sampling of discontinuous voltage and current signals in electrical drives: a system approach," *IEEE Trans. Industry Applications*, 1998, vol. 34, no. 5, pp. 1123-1130.

M.Bodson, "Rejection of periodic disturbances of unknown and time-varying frequency," *International Journal of Adaptive Control and Signal Processing*, 2005, vol. 19, no. 2-3, pp. 67-88.

R.I.Bojoi, G.Griva, V.Bostan, M.Guerriero, F.Farina, and F.Profumo, "Current control strategy for power conditioners using sinusoidal signal integrators in synchronous reference frame," *IEEE Trans. Power Electronics*, 2005. vol. 20, no. 6, pp. 1402-1412.

M.H.J.Bollen, "Understanding power quality problems," IEEE press, vol. 3, 2000.

F.Briz, D.Díaz-Reigosa, M.W.Degner, P.García, and J.M.Guerrero, "Current sampling and measurement in PWM operated AC drives and power converters," *International Power Electronics Conference (IPEC'10)*, 2010, pp. 2753-2760.

H.L.Broberg and R.G.Molyet, "A new approach to phase cancellation in repetitive control," *Industry Applications Society Annual Meeting*, 1994, vol. 3, pp. 1766-1770.

H.L.Broberg and R.G.Molyet, "Reduction of repetitive errors in tracking of periodic signals: theory and application of repetitive control," *First IEEE Conference on Control Applications*, 1992, vol. 2, pp. 1116-1121.

E.J.Bueno, "Optimización del comportamiento de un convertidor de tres niveles NPC conectado a la red eléctrica," PhD thesis, University of Alcalá, Spain, 2005.

M.F.Byl, S.J.Ludwick, and D.L.Trumper, "A loop shaping perspective for tuning controllers with adaptive feedforward cancellation," *Precision Engineering*, 2005,1. vol. 29, no. 1, pp. 27-40.

E.Carroll,"High power active devices," 2005, ABB, Switzerland.

N.Celanovic, "Space vector modulation and control of multilevel converters," 2000.

G.W.Chang, "A new method for determining reference compensating currents of the three-phase shunt active power filter," *IEEE Power Engineering Review*, 2001, vol. 21, no. 3, pp. 63-65.

B.Chen and Y.Hsu, "A minimal harmonic controller for a STATCOM," *IEEE Trans. Industrial Electronics*, 2008, vol. 55, no. 2, pp. 655-664.

S.K.Chung, "Phase-locked loop for grid-connected three-phase power conversion systems," 2000, 147, 3, pp. 213-219.

S.Clifford, "Delivering energy and climate solutions," (EWEA 2007 annual report), 2007.

S.Cóbreces, "Optimization and analysis of the current control loop of VSCs connected to uncertain grids through LCL filters," PhD thesis, University of Alcala, Spain, 2009.

R.C.Dorf and R.H.Bishop,. "Modern control systems," 1991.

P.N.Enjeti and P.D.Ziogas, "Analysis of a static power converter under unbalance: a novel approach," *IEEE Trans. Industrial Electronics*, 1990, vol. 37, no. 1, pp. 91-93.

P.N.Enjeti, P.D.Ziogas, and M.Ehsani, "Unbalanced PWM converter analysis and corrective measures," *Industry Applications Society Annual Meeting*, 1989, vol.1, pp. 861-870.

G.Escobar, P.Mattavelli, and M.F.Martínez-Montejano, "Modifications to repetitive-based controllers using FIR filters for practical implementation," in *IECON '09. 35th Annual Conference of IEEE*, pp. 3246-3251.

G.Escobar, P.R.Martínez, and J.Leyva-Ramos, "Analog circuits to implement repetitive controllers with feedforward for harmonic compensation," *IEEE Trans. Industrial Electronics*, 2007(b), vol. 54, no. 1, pp. 567-573.

G.Escobar, A.A.Valdez, J.Leyva-Ramos, and P.Mattavelli, "Repetitive-based controller for a UPS inverter to compensate unbalance and harmonic distortion," *IEEE Trans. Industrial Electronics*, 2007(a), vol. 54, no. 1, pp. 504-510.

J.E.Farach, W.M.Grady, and A.Arapostathis, "An optimal procedure for placing sensors and estimating the locations of harmonic sources in power systems," *IEEE Trans. Power Delivery*, 1993, vol. 8, no. 3, pp. 1303-1310.

M.F.Farias, P.E.Battaiotto, and M.G.Cendoya, "Wind farm to weak-grid connection using UPQC custom power device," *IEEE International Conference on Industrial Technology*, 2010, pp. 1745-1750.

B.A.Francis and W.M.Wonham, "The internal model principle for linear multivariable regulators," *Applied Mathematics and Optimization*, 1975, vol. 2, no. 2, pp. 170-194.

G.F.Franklin, J.D.Powell, and M.L.Workman. "Digital control of dynamic systems," 1998, pp. 841.

A.García-Cerrada, O.Pinzón-Ardila, V.Feliú-Batlle, P.Roncero-Sánchez, and P.García-González, "Application of a repetitive controller for a three-phase active power filter," *IEEE Trans. Power Electronics*, 2007, vol. 22, no. 1, pp. 237-246.

A.García-Cerrada, P.Roncero-Sánchez, P.García-González, and V.Feliú-Batlle, "Detailed analysis of closed-loop control of output-voltage harmonics in voltage-source inverters," *Electric Power Applications*, 2004, vol. 151, no. 6, pp. 734-743.

A.A.Girgis, W.B.Chang, and E.B.Makram, "A digital recursive measurement scheme for online tracking of power system harmonics," *IEEE Trans. Power Delivery*, 1991, vol. 6, no. 3, pp. 1153-1160.

G.C.Goodwin, S.F.Graebe, and M.E.Salgado, "Control system design," 2001, vol. 240, Prentice Hall.

R.Griñó, R.Cardoner, R.Costa-Castelló, and E.Fossas, "Digital repetitive control of a three-phase four-wire shunt active filter," *IEEE Trans. Industrial Electronics*, 2007, vol. 54, no. 3, pp. 1495-1503.

R.Griñó and R.Costa-Castelló, "Digital repetitive plug-in controller for odd-harmonic periodic references and disturbances," *Automatica*, 2005, vol. 41, no. 1, pp. 153-157.

J.F.Gronquist, W.A.Sethares, F.L.Alvarado, and R.H.Lasseter, "Power oscillation damping control strategies for FACTS devices using locally measurable quantities," *IEEE Trans. Power Systems*, 1995, vol. 10, no. 3, pp. 1598-1605.

L.Gyugyi, C.D.Schauder, and K.K.Sen, "Static synchronous series compensator: a solid-state approach to the series compensation of transmission lines," *IEEE Trans. Power Delivery*, 1997, vol. 12, no. 1, pp. 406-417.

L.Gyugyi and E.C.Strycula, "Active ac power filters," IEEE IIAS annual meeting, 1976, pp. 529-535.

S.Hara, T.Omata, and M.Nakano, "Synthesis of repetitive control systems and its applications," *24th IEEE Conference on Decision and Control*, 1985, vol. 24, pp. 1387-1392.

S.Hara and Y.Yamamoto, "Stability of repetitive control systems," *24th IEEE Conference on Decision and Control*, 1985, vol. 24, pp. 326-327.

L.Harnefors and H.-.Nee, "Model-based current control of AC machines using the internal model control method," *IEEE Trans. Industry Applications*, 1998, vol. 34, no. 1, pp. 133-141.

G.Hillerström, "On repetitive control," PhD Thesis, 1994.

N.Hingorani and L.Gyugyi, "Understanding FACTS: concepts and technology of flexible AC transmission systems," 2000, ed. Mohamed El-Hawary, vol. 1.

N.G.Hingorani, "FACTS - Flexible AC transmission system," *International Conference on AC and DC Power Transmission*, 1991, pp. 1-7.

D.G.Holmes, T.A.Lipo, B.P.McGrath, and W.Y.Kong, "Optimized design of stationary frame three phase ac current regulators," *IEEE Trans. Power Electronics*, 2009, vol. 24, no. 11, pp. 2417-2426.

D.G.Holmes and T.A.Lipo. "Pulse width modulation for power converters. Principles and practice," 2003, 18, pp. 744.

F.Huerta, "Aplicación de técnicas de identificación y control multivariable en convertidores en fuente de tensión conectados a la red eléctrica," PhD Thesis, University of Alcalá, Spain, 2009.

F.Huerta, D.Pizarro, S.Cóbreces, F.J.Rodríguez, C.Girón, and A.Rodriguez, "LQG servo controller for the current control of LCL grid-connected Voltage-Source Converters," *IEEE Trans. Industrial Electronics*, 2012, vol. 59, no. 11, pp. 4272-4284

N.Hur, J.Jung, and K.Nam, "A fast dynamic DC-link power-balancing scheme for a PWM converter-inverter system," *IEEE Trans. Industrial Electronics*, 2001, vol. 48, no. 4, pp. 794-803.

T.Inoue, M.Nakano, and S.Iwai, "High accuracy control of servomechanism for repeated contouring," *Proc. 10th Annual Symposium on Incremental Motion Control Systems and Devices*, 1981, pp. 285-292.

T.Inoue, M.Nakano, T.Kubo, S.Matsumoto, and H.Baba, "High accuracy control of a proton synchrotron magnet power supply," *Proc. 8th World Congress of IFAC*, 1981, vol. 20, pp. 216-221.

S.J.Julier and J.K.Uhlmann, "New extension of the Kalman filter to nonlinear systems," *AeroSense'97. International Society for Optics and Photonics*, 1997, pp. 182-193.

J.Kang and S.Sul, "Control of unbalanced voltage PWM converter using instantaneous ripple power feedback," *Power Electronics Specialists Conference, (PESC'97)*, 1997, vol. 1, pp. 503-508.

M.P.Kazmierkowski and L.Malesani, "Current control techniques for three-phase voltage-source PWM converters: a survey," *IEEE Trans. Industrial Electronics*, 1998. vol. 45, no. 5, pp. 691-703.

P.Kundur. "Power system stability and control," 1994.

T.I.Laakso, V.Valimaki, M.Karjalainen, and U.K.Laine. "Splitting the unit delay," *Signal Processing Magazine*, 1996, vol. 13, no. 1, pp. 30-60.

P.Ledesma, J.Usaola, and J.L.Rodríguez, "Transient stability of a fixed speed wind farm," *Renewable Energy*, 2003, vol. 28, no. 9, pp. 1341-1355.

C.Lee, "Effects of unbalanced voltage on the operation performance of a three-phase induction motor," *IEEE Trans. Energy Conversion*, 1999, vol. 14, no. 2, pp. 202-208.

M.Lindgren. "Modeling and control of voltage source converters connected to the grid," PhD Thesis, Chalmers Umiversity of Technology, Sweden, 1998.

P.C.Loh, Y.Tang, F.Blaabjerg, and P.Wang, "Time delay control of power converters: Mixed frame and stationary-frame variants," *Applied Power Electronics Conference and Exposition (APEC'08)*, 2008, pp. 1181-1187.

S.J.Ludwick. "A rotary fast tool servo for diamond turning of asymmetric optics," PhD Thesis, Massachusetts Institute of Technology, USA, 1999.

H.Ma and A.A.Girgis, "Identification and tracking of harmonic sources in a power system using a Kalman filter," *IEEE Trans. Power Delivery*, 1996, vol. 11, no. 3, pp. 1659-1665.

S.Malo and R.Griñó, "Adaptive feed-forward cancellation control of a full-bridge DC-AC voltage inverter," *Proc. 17th IFAC World Congress*, 2008, vol. 17, no. 1, pp. 4571-4576.

P.Mattavelli, F.Polo, S.Sattin and, F.DaI Lago, "Dynamic improvement in UPS by means of control delay minimization," *Industry Applications Conference*, 2004, vol. 2, pp. 843-849.

P.Mattavelli and F.P.Marafao, "Repetitive-based control for selective harmonic compensation in active power filters," *IEEE Trans. Industrial Electronics*, 2004, vol. 51, no. 5, pp. 1018-1024.

P.Mattavelli, "A closed-loop selective harmonic compensation for active filters," *IEEE Trans. Industry Applications*, 2001, vol. 37, no. 1, pp. 81-89.

A.P.S.Meliopoulos, F.Zhang, and S.Zelingher, "Power system harmonic state estimation," *IEEE Trans. Power Delivery*, 1994, vol. 9, no. 3, pp. 1701-1709.

R.Mihalic, P.Zunko, I.Papic, and D.Povh, "Improvement of transient stability by insertion of FACTS devices," *IEEE Trans. Power Delivery*, 1996, vol. 11, pp. 521-525.

L.Moran, P.D.Ziogas, and G.Joos, "Design aspects of synchronous PWM rectifier-inverter systems under unbalanced input voltage conditions," *IEEE Trans. Industry Applications*, 1989, vol. 28, no. 6, pp. 1286-1293.

M.Nakano and S.Hara. "Microprocessor-based repetitive control," Springer Netherlands, 1986, pp. 279-296.

J.G.Nielsen, M.Newman, H.Nielsen, and F.Blaabjerg, "Control and testing of a dynamic voltage restorer (DVR) at medium voltage level," *IEEE Trans. Power Electronics*, 2004, vol. 19, no. 3, pp. 806-813.

J.G.Nielsen, F.Blaabjerg, and N.Mohan, "Control strategies for dynamic voltage restorer compensating voltage sags with phase jump," *Applied Power Electronics Conference and Exposition (APEC'01)*, 2001, vol. 2, pp. 1267-1273.

M.Noroozian, L.Angquist, M.Ghandhari, and G.Andersson, "Use of UPFC for optimal power flow control," *IEEE Trans. Power Delivery*, 1997, vol. 12, no. 4, pp. 1629-1634.

S.Norrga. "Power electronics for high voltage direct current (HVDC) applications," 2011.

G.Oetken. "A new approach for the design of digital interpolating filters," 1979, vol. 27, no. 6, pp. 637-643.

T.Omata, S.Hara, and M.Nakano, "Nonlinear repetitive control with application to trajectory control of manipulators," *Journal of Robotic systems*, 1987, vol. 4, no. 5, pp. 631-652.

R.Ottersten. "On control of back-to-back converters and sensorless induction machine drives," PhD Thesis, Chalmers Umiversity of Technology, Sweden, 2003.

E.Özdemir, M.Kale, and S.Özdemir, "Active power filter for power compensation under non-ideal mains voltages," *Proc. of the IEEE MED*, 2003.

P.Pillay and M.Manyage, "Definitions of voltage unbalance," *IEEE Power Engineering Review*, 2001, vol. 21, no. 5, pp. 50-51.

O.Pinzón-Ardila. "Compensación selectiva de armónicos mediante filtros activos de potencia," PhD Thesis, Universidad Pontificia de Comillas, Spain, 2007.

R.Piwko, N.Miller, J.Sánchez-Gasca, X.Yuan, R.Dai, and J.Lyons, "Integrating large wind farms into weak power grids with long transmission lines," *Power Electronics and Motion Control Conference (IPEMC'06)*, 2006, vol. 2, pp. 1-7.

M.Rizo, A.Rodríguez, F.J.Rodríguez, E.Bueno, and M.Liserre, "Different approaches of stationary reference frames saturators," *38th Annual Conference of Industrial Electronics (IECON'12)*, 2012, pp. 2245-2250.

A.Rodríguez, M.Moranchel, E.J.Bueno, and F.J.Rodríguez, "Tuning of resonant controllers applied to the current control of Voltage-Source Converters," *38th Annual Conference of Industrial Electronics (IECON'12)*, 2012, pp. 4463-4468.

A.Rodríguez, C.Girón, V.Sáez, M.Rizo, E.Bueno, and F.J.Rodríguez, "Analysis of repetitive-based controllers for selective harmonic compensation in active power filters," *36th Annual Conference of Industrial Electronics (IECON'10)*, 2010, pp. 2013-2018.

A.Rodríguez, C.Girón, M.Rizo, V.Sáez, E.Bueno, and F.J.Rodríguez, "Comparison of current controllers based on repetitive-based control and second order generalized integrators for active power filters," *35th Annual Conference of Industrial Electronics (IECON'09)*, 2009, pp. 3223-3228.

F.J.Rodríguez, E.Bueno, M.Aredes, L.G.B.Rolim, F.A.S.Neves, and M.C.Cavalcanti, "Discrete-time implementation of second order generalized integrators for grid converters," *34th Annual Conference of Industrial Electronics (IECON'08)*, 2008, pp. 176-181.

P.Rodríguez, A.Luna, M.Ciobotaru, R.Teodorescu, and F.Blaabjerg. "Advanced grid synchronization system for power converters under unbalanced and distorted operating conditions," 2006, pp. 5173-5178.

P.Rodríguez, A.Timbus, R.Teodorescu, M.Liserre, and F.Blaabjerg, "Reactive power control for improving wind turbine system behavior under grid faults," *IEEE Trans. Power Electronics*, 2009, vol. 24, no. 7, pp. 1798-1801.

P.Rodríguez, A.Luna, I.Candela, R.Teodorescu, and F.Blaabjerg, "Grid synchronization of power converters using multiple second order generalized integrators," *34th Annual Conference of Industrial Electronics (IECON'08)*, 2008, pp. 755-760.

P.Rodríguez, R.Teodorescu, I.Candela, A.V.Timbus, M.Liserre, and F.Blaabjerg, "New positive-sequence voltage detector for grid synchronization of power converters under faulty grid conditions," *Power Electronics Specialists Conference (PESC'06)*, 2006, pp. 1-7.

J.Roldán-Pérez, A.García-Cerrada, J.L.Zamora-Macho, P.Roncero-Sánchez, and E.Acha, "Adaptive repetitive controller for a three-phase dynamic voltage restorer," *International Conference on Power Engineering, Energy and Electrical Drives (POWERENG)*, 2011, pp. 1-6.

T.M.Rowan and R.J.Kerkman, "A new synchronous current regulator and an analysis of current-regulated PWM inverters," *IEEE Trans. Industry Applications*, 1986, vol. IA-22, no. 4, pp. 678-690.

G.Saccomando and J.Svensson, "Transient operation of grid-connected voltage source converter under unbalanced voltage conditions," *Industry Applications Conference*, 2001, vol. 4, pp. 2419-2424.

C.Schauder, M.Gernhardt, E.Stacey, T.Lemak, L.Gyugyi, T.W.Cease, and A.Edris, "Operation of ±100 MVAr TVA STATCON," *IEEE Trans. Power Delivery*, 1997, vol. 12, no. 4, pp. 1805-1811.

C.D.Schauder and R.Caddy, "Current control of voltage-source inverters for fast four-quadrant drive performance," *IEEE Trans. Industry Applications*, 1982, vol. IA-18, no. 2, pp. 163-171.

M.Sedighy, S.B.Dewan, and F.P.Dawson, "A robust digital current control method for active power filters," *IEEE Trans. Industry Applications*, 2000, vol. 36, no. 4, pp. 1158-1164.

S.Skogestad and I.Postlethwaite. "Multivariable feedback control analysis and design," 2005, pp. 574.

V.K.Sood, "HVDC and FACTS controllers: applications of static converters in power systems," Kluwer Academic Pub, 2004.

J.Svensson, M.Bongiorno, and A.Sannino, "Practical implementation of delayed signal cancellation method for phase-sequence separation," *IEEE Trans. Power Delivery*, 2007, vol. 22, no. 1, pp. 18-26.

R.Teodorescu, M.Liserre, and P.Rodríguez. "Grid converters for photovoltaic and wind power systems," 2011, vol. 29.

M.Tomizuka, T.-.Tsao, and K.-.Chew, "Discrete-time domain analysis and synthesis of repetitive controllers," *American Control Conference*, 1988, pp. 860-866.

M.Tomizuka, "Zero phase error tracking algorithm for digital control," *ASME Journal of Dynamic Systems Measurement and Control*, 1987, vol. 109, no. 1, pp. 65.

T.-.Tsao and M.Tomizuka, "Adaptive zero phase error tracking algorithm for digital control," *Journal of Dynamic Systems Measurement and Control*, 1987, vol. 109, no. 4, pp. 349-354.

A.Van Der Meulen and J.Maurin. "Current source inverter vs. voltage source inverter topology (Technical data TD02004004E)," 2010.

M.Vilathgamuwa, A.A.D.R.Perera, S.S.Choi, and K.J.Tseng, "Control of energy optimized dynamic voltage restorer," *25th Annual Conference of Industrial Electronics (IECON'99)*, 1999, vol. 2, pp. 873-878.

D.Vincenti and H.Jin, "A three-phase regulated PWM rectifier with on-line feedforward input unbalance correction," *IEEE Trans. Industrial Electronics*, 1994, vol. 41, no. 5, pp. 526-532.

G.Welch and G.Bishop, "An introduction to the Kalman filter".

B.Wu. "High-power converters and AC drives," 2006.

AYazdani and R.Iravani. "Voltage-Sourced Converters in power systems," 2010.

A.G.Yepes, F.D.Freijedo, J.Doval-Gandoy, O.López, J.Malvar, and P.Fernández-Comesaña, "Effects of discretization methods on the performance of resonant controllers," *IEEE Trans. Power Electronics*, 2010, vol. 25, no. 7, pp. 1692-1712.

X.Yuan, W.Merk, H.Stemmler, and J.Allmeling, "Stationary-frame generalized integrators for current control of active power filters with zero steady-state error for current harmonics," *IEEE Trans. Industry Applications*, 2002, vol. 38, no. 2, pp. 523-532.

X.Yuan, J.Allmeling, W.Merk, and H.Stemmler, "Stationary frame generalized integrators for current control of active power filters with zero steady state error for current harmonics of concern under unbalanced and distorted operation conditions," *Industry Applications Conference*, 2000, vol. 4, pp. 2143-2150.

N.R.Zargari and G.Joos, "Performance investigation of a current-controlled voltage-regulated PWM rectifier in rotating and stationary frames," *IEEE Trans. Industrial Electronics*, 1995, vol. 42, no. 4, pp. 396-401.

A.Zervos and C.Kjaer. "Wind energy scenarios up to 2030," 2008.

K.Zhou and D.Wang, "Unified robust zero-error tracking control of CVCF PWM converters," *IEEE Trans. Circuits and Systems I: Fundamental Theory and Applications*, 2002, vol. 49, no. 4, pp. 492-501.

K.Zhou and D.Wang, "Digital repetitive learning controller for three-phase CVCF PWM inverter," *IEEE Trans. Industrial Electronics*, 2001, vol. 48, no. 4, pp. 820-830.

D.N.Zmood and D.G.Holmes, "Stationary frame current regulation of PWM inverters with zero steady-state error," *IEEE Trans. Power Electronics*, 2003, vol. 18, no. 3, pp. 814-822.

D.N.Zmood, D.G.Holmes and G.H.Bode, "Frequency-domain analysis of three-phase linear current regulators," *IEEE Trans. Industry Applications*, 2001, vol. 37, no. 2, pp. 601-610.